Modeling of structural integrity of aged low alloy steels using non-local mechanics

MAGNUS BOÅSEN

Akademisk avhandling som med tillstånd av Kungliga Tekniska Högskolan i Stockholm framläggs till offentlig granskning för avläggande av teknologie doktorsexamen fredagen den 18 september 2020 kl. 10.00 i Ångdomen, Osquars backe 31, Stockholm.

Academic Dissertation which, with due permission of the KTH Royal Institute of Technology, is submitted for public defence for the Degree of Doctor of Philosophy on Friday the 18th of September at 10:00 in Ångdomen, Osquars backe 31, Stockholm.

Doctoral Thesis in Solid Mechanics
KTH Royal Institute of Technology
Stockholm, Sweden 2020

ISBN 978-91-7873-603-4
TRITA-SCI-FOU 2020:024

Printed by: Universitetsservice US-AB, Sweden 2020

Till mina eviga förebilder
Vanja och Curt Boåsen,
Lena Lindström,
mor och far
samt ljuset i mitt liv
Sofia Boåsen

Abstract

Ageing of low alloy steels affects the structural integrity assessment as it most commonly causes embrittlement and a hardening of the material. This is due to the evolution of the microstructure during operation in the specific application. In nuclear applications, the most common causes of ageing of low alloy steels are irradiation and thermal ageing. Embrittlement in this type of materials is generally divided into hardening and non-hardening embrittlement. The formation of clusters or precipitates of solute atoms typically cause the former, and the weakening of grain boundaries generally cause the latter. This thesis is devoted to the development of models that can be used to describe the material properties of aged low alloy steels in terms of plastic properties and fracture toughness, and to the study of the effects of thermal ageing on the mechanical properties of a low alloy steel.

In *Paper I*, a strain gradient plasticity framework is applied in order to capture length scale effects. The constitutive length scale is assumed to be related to the dislocation mean free path and the changes it undergoes during plastic deformation. Several evolution laws for the length scale were developed and implemented in a FEM-code. This was used to solve a test problem in order to probe the effects of the length scale evolution. All length scale evolution laws considered in this study results in a decreasing length scale, which causes an overall softening in cases where the strain gradient dominates the solution. The results are in tentative agreement with phenomena of strain localization that occurs in highly irradiated materials.

In *Paper II*, a scalar stress measure for cleavage fracture is developed and generalized, here called the effective normal stress measure. This is used in a non-local weakest link model which is applied to two datasets from literature in order to study the effects of the effective normal stress measure, as well as to experiments considering four-point bending of specimens containing a semi-elliptical surface crack. The model is shown to reproduce the failure probability of all considered datasets, i.e. well capable of transferring toughness information between different geometries.

In *Paper III*, a thermally aged weld from the Ringhals nuclear power plant is studied experimentally and compared to a reference material using fracture toughness testing. The main objective of the study was to investigate the effect of thermal ageing on the cleavage or brittle fracture toughness, with a specific focus on the effect of crack tip constraint. The testing showed that thermal ageing had enabled brittle fracture initiation from grain boundaries, resulting in a bimodal toughness distribution due to multiple mechanisms for brittle fracture initiation.

In *Paper IV*, the non-local weakest link model in *Paper II* is further developed to account for multiple mechanism brittle fracture. The model is developed for brittle fracture initiation from grain boundaries and second phase particles. The grain boundary mechanism is inferred from simulations of polycrystalline aggregates using crystal plasticity. When applied to the experimental results of *Paper III*, the model is able to describe the fracture toughness distribution with a remarkable accuracy.

Sammanfattning

Åldring av låglegerade stål påverkar utvärderingen av en komponents strukturella integritet eftersom det vanligtvis ger en påföljande försprödning och härdning av materialet. Detta är på grund av hur materialets mikrostruktur utvecklas under drift i specifika användningsområden. Inom kärnteknisk användning är den vanligaste orsaken till åldring av låglegerade stål antingen bestrålning eller termisk åldring. Försprödning i denna typ av material delas vanligtvis upp i härdande och icke-härdande försprödning. Bildandet av kluster eller utskiljningar av legeringsämnen orsakar typiskt den förstnämnda typen, medans den andra orsakas generellt av försvagade korngränser. Den här avhandlingen ägnas till utvecklingen av modeller som kan användas för att beskriva de mekaniska egenskaperna hos åldrade låglegerade stål i termer av de plastiska egenskaperna och brottseghet, samt undersökningar av termisk åldring av låglegerade stål.

I *Artikel I*, används en plasticitetsteori baserad på både den plastiska töjningen samt dess gradient för att kunna fånga längdskalebeteenden. Längdskalan i teorin antas vara relaterad till dislokationernas medelfria väg och förändringen den genomgår vid plastisk deformation. Flera utvecklingslagar för längdskalan har analyserats och implementerats i en finita element kod. Denna implementering har använts för att lösa ett testproblem med syfte att undersöka effekterna av utvecklingen hos längdskalan. Alla utvecklingslagar som presenteras i artikeln ger en minskande längdskala. Fenomenet leder till ett övergripande mjuknande vid fall där den plastiska töjningsgradienten har stor inverkan på lösningen. Resultaten är i preliminär överenstämmelse med de typer av lokalisering av plastisk töjning som observerats i starkt bestrålade material.

I *Artikel II* utvecklas ett generaliserat spänningsmått i syfte att beskriva klyvbrott, här benämnt effektivt normalspänningsmått. Detta har använts i samband med en icke-lokal svagaste länk modell, som har applicerats på två experimentella studier från den öppna litteraturen i syfte att studera effekterna av det effektiva normalspänningsmåttet. Utöver detta presenteras även nya experiment på ytspruckna provstavar under fyrpunktsböj. I artikeln visas att modellen återskapar sannolikheten för brott för alla undersökta experimentuppställningar, d.v.s. modellen visas vara väl duglig för att överföra brottseghet mellan geometrier.

I *Artikel III* undersöks ett termiskt åldrat svetsgods från Ringhals kärnkraftverk experimentellt genom brottseghetsprovning och jämförs mot ett referensmaterial. Det huvudsakliga målet med studien har varit att undersöka effekten av termisk åldring på den spröda brottsegheten med ett specifikt fokus på effekten av *crack tip constraint*. Provningen påvisade att den termiska åldringen möjliggjorde initiering av sprödbrott från korngränser, med en påföljande bimodal brottseghetsfördelning på grund av initiering av sprödbrott från flera mekanismer

I *Artikel IV* vidareutvecklas den icke-lokala svagaste länk modell som presenterades i *Artikel II* till att ta hänsyn till flera mekanismer för sprödbrottsinitiering, mer specifikt, initiering från korngränser och sekundärfas partiklar. Mekanismen som beskriver korngränsbrott har tagits fram genom att studera polykristaller med hjälp av kristallplasticitet. När modellen appliceras på de experimentella resultaten från *Artikel III* lyckas den återge brottseghetsfördelningen särdeles väl.

Acknowledgements

The work presented in this thesis has been carried out at Solid Mechanics, KTH Royal Institute of Technology, Stockholm between April 2016 and May 2020. The work has been funded by the Swedish Radiation Safety Authority SSM, the Swedish Centre for Nuclear Technology SKC, and Nordic nuclear safety research NKS. All sources of funding are gratefully acknowledged.

It is hard to accurately define what makes a good teacher, but somehow you will always know when you have had one. I know that I have had several during my studies at KTH, without them I would not be who I am today. Three specific teachers that I would like to acknowledge are my supervisors. My main supervisor Pål Efsing has a great mind and a big heart – together we shaped this project into what is presented in this thesis and through this became good friends – and for his support I am grateful. My co-supervisors Carl Dahlberg and Jonas Faleskog served as mentors within their respective and shared fields, for their support I am grateful.

Over the course of my time at the department, I met colleagues and students who have made a lasting impression on me. I would like to acknowledge my office mate, Carl-Magnus Everitt, for providing friendly support and enduring my ramblings. I would also like to mention my good friend Armin Halilović whom I met during my first day at the Department of Solid Mechanics, since then we have been good friends, for which I am grateful.

Collaboration with the very competent Kristina Lindgren has been a great opportunity, which has developed my skills and way of thinking of the micro- and nanostructure of materials.

This project has received a great deal of attention and support within the materials groups of the nuclear power plants in Sweden. This has afforded me opportunities otherwise unattainable in an academic environment. Specifically, I would like to acknowledge Ringhals AB for supplying material and being a constant sounding board for ideas. Greatly acknowledged is Jenny Roudén for always answering my questions, calls, and reading my paper drafts. Also acknowledged at Ringhals are: Björn Forsgren, Johan Blomström, Kerstin Richnau, Per Waernqvist, Fredrik Andreasson, and Per Nilsson. For their support I am grateful.

The experimental effort in Paper III of this thesis would not have been made possible without the continuous support of Martin Öberg. His availability is greatly acknowledged and I am grateful for his mentorship and forbearance. Also, when conducting experiments there is a constant need for workshop manufacturing or adjustments. For this, I would like to acknowledge Göran Rådberg and Jörgen Jansson for their helpfulness and availability.

Furthermore, I would like to acknowledge Ulla Ehrnstén and Marketta Mattila for the micro- and macrographs of the welds presented within the thesis.

Stockholm, May 2020
Magnus Boåsen

List of appended papers

Paper I: *Evolution of the length scale in strain gradient plasticity*

Carl F.O. Dahlberg and Magnus Boåsen
International Journal of Plasticity, vol. 112, 2019, p.220-241

Paper II: *A generalized probabilistic model for cleavage fracture with a length scale - Influence of stress state and application to surface cracked experiments*

Magnus Boåsen, Mateusz Stec, Pål Efsing, Jonas Faleskog
Engineering Fracture Mechanics, *vol*. 214, 2019, *p*.590-608

Paper III: *Analysis of thermal embrittlement of a low alloy steel weldment using fracture toughness and microstructural investigations*

Magnus Boåsen, Kristina Lindgren, Martin Öberg, Mattias Thuvander, Jonas Faleskog, Pål Efsing

TRITA-SCI-RAP 2020:004. *Solid Mechanics, KTH Royal Institute of Technology, Stockholm, Sweden.*

Paper IV: *A weakest link model for multiple mechanism brittle fracture – Model development and application*

Magnus Boåsen, Carl F.O. Dahlberg, Pål Efsing, Jonas Faleskog

TRITA-SCI-RAP 2020:005. *Solid Mechanics, KTH Royal Institute of Technology, Stockholm, Sweden.*

In addition to the appended papers, the work has resulted in the following publications:

On flux effects in a low alloy steel from a Swedish reactor pressure vessel
Magnus Boåsen, Pål Efsing, Ulla Ehrnstén
Journal of Nuclear Materials, vol. 484, 2017, p.110-119

Evolution of precipitation in reactor pressure steel welds under neutron irradiation
Kristina Lindgren, Magnus Boåsen, Krystyna Stiller, Pål Efsing, Mattias Thuvander
Journal of Nuclear Materials, vol. 488, 2017, p.222-230

Cluster formation in in-service thermally aged pressurizer welds
Kristina Lindgren, Magnus Boåsen, Krystyna Stiller, Pål Efsing, Mattias Thuvander
Journal of Nuclear Materials, vol. 504, 2018, p.23-28

Thermal ageing of low alloy steel weldments from a Swedish nuclear power plant – a study of mechanical properties
Magnus Boåsen, Kristina Lindgren, Jenny Rouden, Martin Öberg, Jonas Faleskog, Mattias Thuvander, Pål Efsing
Fontevraud 9, conference proceedings and presentation, 2018, Avignon, France

Thermal ageing of low alloy steel weldments from a Swedish nuclear power plant – the evolution of the microstructure
Kristina Lindgren, Magnus Boåsen, Krystyna Stiller, Pål Efsing, Mattias Thuvander
Fontevraud 9, conference proceedings, 2018, Avignon, France

Contribution to the papers

The author's contributions to the appended papers are as follows:

Paper I:
Boåsen derived and proposed assumptions for several of the evolution laws presented in the paper. All the numerical implementation and about half of all the simulations were carried out by Boåsen. In the writing process, Boåsen was active in finding relevant references and wrote about half of the paper.

Paper II:
Boåsen wrote the program code used for all the post-processing described in the paper. The effective normal stress measure was derived by Boåsen. All the used finite element models were created and run by Boåsen. In the writing process, Boåsen wrote most of the paper.

Paper III:
Boåsen planned the experiments and the manufacturing, as well as executing the experiments and the analysis. The manuscript was written mostly by Boåsen. Dr. Lindgren carried out the nanostructural investigations and analysis.

Paper IV:
Boåsen identified the necessary modeling framework needed and derived the multiple mechanism weakest link model. Boåsen came up with the idea to utilize crystal plastic modeling to infer the g_1-function and subsequently the analytical model. Boåsen implemented the porous plastic Gurson model together with Faleskog. Boåsen carried out all modeling and analysis. Boåsen wrote the paper.

Contents

1. Introduction

The importance of electrical power to the development of society cannot be overstated. Production of electricity comes in many forms and is largely dependent on natural resources such as oil, coal, rivers, biomass and fissile material, and to a minor extent on sun and wind. The dependence on fossil fuels (oil, coal) for production of electricity results in the release of large quantities of CO_2. A greenhouse gas, CO_2 contributes to climate change through the greenhouse effect as well as other types of altered environmental conditions, such as those brought forth by e.g. ocean acidification. Nuclear power can be used as a stable source of electricity production (as opposed to intermittent sources such as wind and solar) with very little CO_2 generated per TWh of electricity produced compared to other sources. As electrical power increases the standard of living in societies around the world, it could be of interest to understand the impact from different energy sources on life itself. One study estimates the mortality in terms of loss of human life per TWh of produced electricity for nuclear power to be 0.01, which in the same study is compared to solar which has a doubled mortality rate and wind with a tripled mortality rate in relation to nuclear [1]. Another study compares nuclear to fossil-based power generation, where the mortality rate of coal power in Europe is 387 times higher than that of nuclear [2].

Sweden obtains a large share (40 % [3]) of its electricity from nuclear power. Some of the Swedish reactors are coming close to the end of their originally designed life-times and will face decommissioning, and some of the reactors are undergoing life extension programs. It is therefore especially important to understand the effects of long-term operation on the materials used in the reactors. For instance, the reactor pressure vessel is made from welded plates and/or forgings of low alloy steel. Low alloy steels are alloys containing primarily iron (Fe) and low amounts of alloying elements (1.5-5 %), typically Mn, Si, Ni, Mo, Cr and V. The reactor pressure vessel is subjected to neutron irradiation originating from the core, and an operating temperature of ~290 ˚C. This environment causes the low alloy steel and its weldments to become embrittled due to ageing, which reduces the size of the operating window in terms of pressure and temperature, as well as the operating limits and design transients. Therefore, regular safety assessments at timed intervals are conducted in order to ensure maintained operability of the reactor. It is also important to realize that replacement of a reactor pressure vessel is very complicated and very costly.

1.1. Aims of this study

This thesis is the culmination of a PhD-project with the aim of studying the effects of ageing on the mechanical properties of low alloy steels in nuclear reactors. The work has included study and development of modeling concepts and frameworks for modeling the ageing effects on low alloy steels, and an experimental investigation of thermal ageing of a pressurizer from a pressurized water reactor. The thesis contains four papers, with the first two presenting two possible modeling pathways for studying ageing induced effects on the relevant mechanical properties of low alloy steels. The latter two are concerned with an experimental program and the modeling of fracture toughness tests of aged low alloy steel weldments.

1.2. Structure

The thesis is outlined as follows; Section 2 presents a general review of the most pertinent effects of ageing with respect to micro- and nanostructure as well as key effects related to mechanical properties and embrittlement. Its purpose is to put the appended papers in the correct context. Section 3 contains a short review of the key aspects related to the first two appended papers as well as an excerpt of key results. Section 4 is concerned with the content of Paper III, where an experimental series of a thermally aged material is tested and compared to the results of a reference material from the same test series. Section 5 is relevant to Paper IV, where a modeling framework for multiple mechanism brittle fracture is presented and applied to the test results of Paper III. Section 6 presents some possible considerations for future work.

2. On the ageing effects on the mechanical properties of low alloy steels

2.1. Low alloy steel and associated weld metal

Reactor pressure vessels are commonly made from low alloy steels which have a ferritic or ferritic/bainitic microstructure and are chosen due to their good mechanical properties, e.g. fracture toughness. However, the fracture toughness of these steels exhibits a strong temperature dependence. At low temperatures, ferritic steels are brittle and have a failure mode commonly called cleavage fracture. This type of fracture is typically initiated due to slip induced cracking of a second phase particle, which nucleates a micro crack that starts propagating dynamically [4], [5]. In order for such a micro crack to develop into a critical cleavage crack, it must propagate across microstructural obstacles such as high angle grain boundaries [6], [7], [8]. For this to happen, the micro crack needs to have been nucleated in a region where the stress is high enough over a sufficiently large distance [9], [10]. If all obstacles in the vicinity of the initial crack nucleus can be overcome, the crack develops into a macroscopic cleavage crack which results in a drastic failure. At increasing temperature, the material becomes more ductile, until eventually the cleavage failure mode is suppressed. This suppression is accompanied by a shift to a ductile failure mode, which becomes dominant. This transition is called the ductile-to-brittle transition and is commonly defined by the temperature at which the transition is occurring. This temperature is typically determined from one of two methods, the older method being impact testing, where the temperature at 41 J of absorbed energy, T_{41J}, is used to define the transition. The more recent method relies on fracture toughness testing according to the master curve methodology to determine the reference temperature T_0, which is the temperature at which the median fracture toughness is 100 $\mathrm{MPa}\sqrt{\mathrm{m}}$ [11]. The typical result of both methods is used to illustrate the ductile-to-brittle transition in Figure 1.

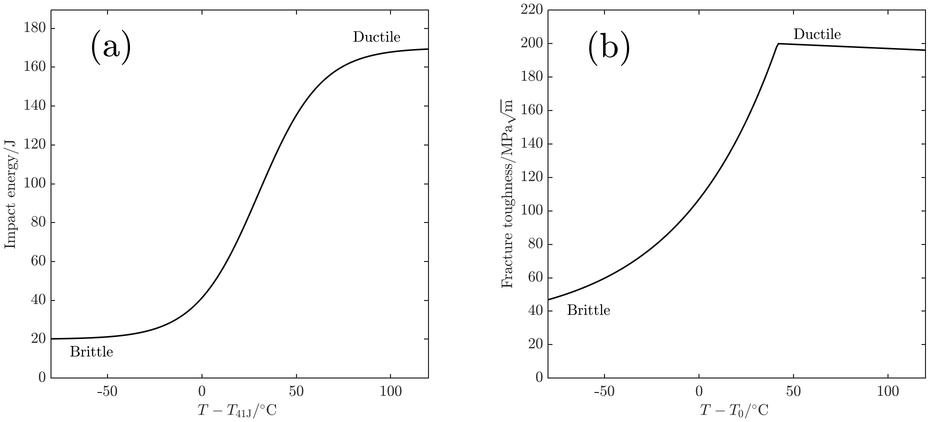

Figure 1. Illustration of the ductile-to-brittle transition for a typical low alloy steel as measured by (a) Charpy impact testing, and (b) fracture mechanical testing through the master curve methodology.

The multi-layer weld metal of reactor pressure vessels made from low alloy steel will obtain a ferritic or ferritic/bainitic microstructure similarly to the plates and forgings and therefore also exhibits the same type of temperature dependent fracture modes. Typically, a weld in a reactor pressure vessel consists of roughly 280 layers; each layer is called a weld bead, which gives rise to a complex microstructure. This complexity lies in the grain structure, which is different compared to that of the plates or forgings due to the nature of welding. As a weld bead solidifies, a dendritic grain structure emerges transverse to the welding direction. As the multi-layer weld is built up, subsequent weld beads will be laid on top of the already existing beads, thus effectively heat treating the upper part of the weld bead below. This gives rise to a region with smaller equiaxed grains in the bead below due to recrystallization from the locally increased temperature. As this process continues, the weld will achieve a microstructure that has regions of dendritic grains, regions with finer grains that have been reheated once and regions that have been reheated several times. These variations in the microstructure can be clearly seen in the macrograph in Figure 2. The micrograph in Figure 3 shows a detailed image of region 2 in Figure 2, illustrating the reheated region between two weld beads containing an equiaxed grain structure. This varying microstructure of welds gives rise to mechanical properties that vary dependent on position.

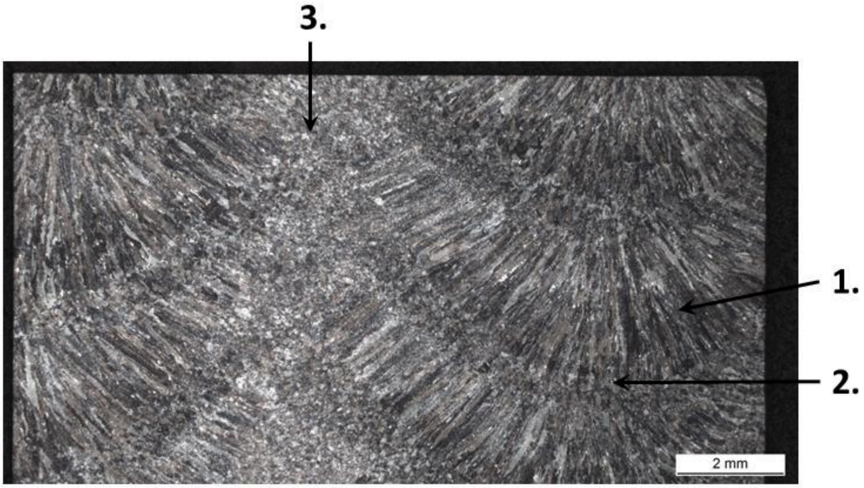

1. Dendritic region, 2. Reheated region, 3. Twice reheated region

Figure 2. Weld macrograph displaying the grain microstructure characteristic to multi-layer welds. Image courtesy of Ulla Ehrnstén.

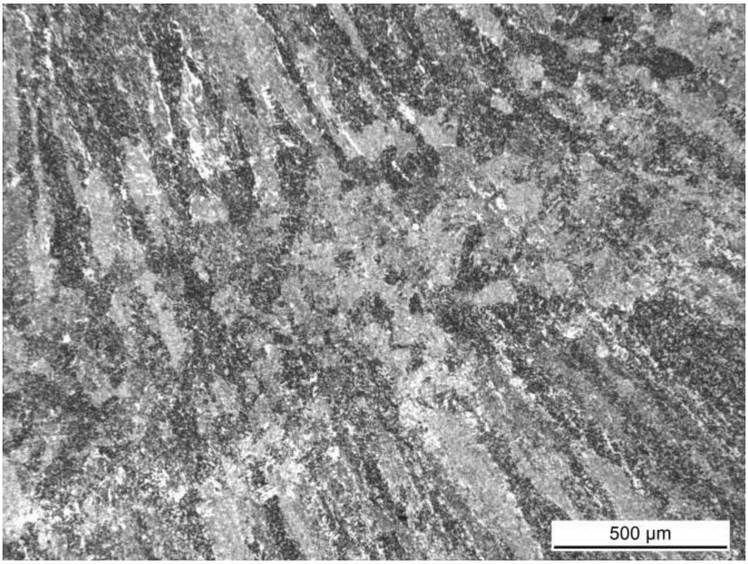

Figure 3. Micrograph displaying the region containing equiaxed grains between regions of dendritic grains. Image courtesy of Ulla Ehrnstén.

2.2. Ageing of low alloy steels

The ageing of low alloys steels due to neutron irradiation and thermal ageing is seen in changes of the mechanical properties due to alterations in the micro- and nanostructure of the metal. Ageing is commonly referred to as embrittlement due to a decrease in toughness of the material. The word ageing will be used alongside with and encompasses embrittlement throughout this thesis.

In general terms it can be said that ageing affects the plastic properties and causes an embrittlement of the material. This emerges as an increase in yield strength, a decreased work hardening slope and a shift in the transition temperature from lower to higher. Changes in the plastic properties of the material are due to the formation of microstructural features such as solute clusters (which may become precipitates) and in the case of irradiation, also matrix damage. In the case of irradiation ageing of the Swedish reactors Ringhals units 3 and 4 (R3 and R4), the shift in mechanical properties was larger than expected. There was also no evidence of any embrittlement saturation, which has been suggested from observations in other cases of irradiated steels where Cu was the main embrittling solute. The alloying content of the weld metal in R3 and R4 is high in Mn and Ni (~1.5 %) and rather low in Cu (0.05 %) and P (0.015 %). Under irradiation, this gives rise to the formation of evenly distributed solute clusters containing primarily Mn, Ni and low amounts of Cu [12], [13], [14]. Matrix damage can emerge under irradiation in the form of vacancy or interstitial clusters, i.e. nano sized voids and dislocation loop-like structures [15], [16]. These types of features all act to increase the resistance to dislocation motion, thus changing the plastic properties of the material.

Investigations of the weld metal (submerged arc weld) of the replaced pressurizer in the Ringhals unit 4 reactor system indicated a large degree of embrittlement and hardening relative to what was expected. The weld metal in this component has similar alloying content to the welds of the reactor pressure vessel, but the operating temperature is at 345 ˚C (cf. ~290 ˚C) and it is not subjected to neutron irradiation. Solute clusters were found using atom probe tomography situated primarily on dislocations and grain boundaries [17]. The difference between thermally aged and neutron irradiated steels can be explained by how solutes segregate and form clusters during irradiation versus in purely thermal conditions. Solute atoms such as the ones found in the clusters are dragged by interstitials and vacancies towards sinks where solute clusters will form, i.e. dislocations, grain boundaries and radiation induced defects such as nano sized voids or dislocation loops [18], [19]. During irradiation, there exists a flux of both interstitials and vacancies due to the interaction between neutrons and the lattice. In the absence of irradiation, i.e. pure thermal conditions, the number of vacancies outnumber the interstitials due to a lower thermal activation energy barrier of vacancies. Thus, at thermal conditions, the alloying elements will be dragged by vacancies to existing sinks such as dislocations and grain boundaries, which offers an explanation to why solute clusters have been observed there in the thermally aged welds from the Ringhals pressurizer. In contrast, evenly distributed clusters were found in the irradiated R3 and R4 welds, where evenly distributed sinks appear due to the interaction between the neutrons and the lattice. The difference in the nanostructure between irradiated weld metal from the Ringhals 4 reactor pressure vessel and the thermally aged pressurizer is illustrated in Figure 4, where more clusters are evident in the irradiated material due to the radiation induced defects.

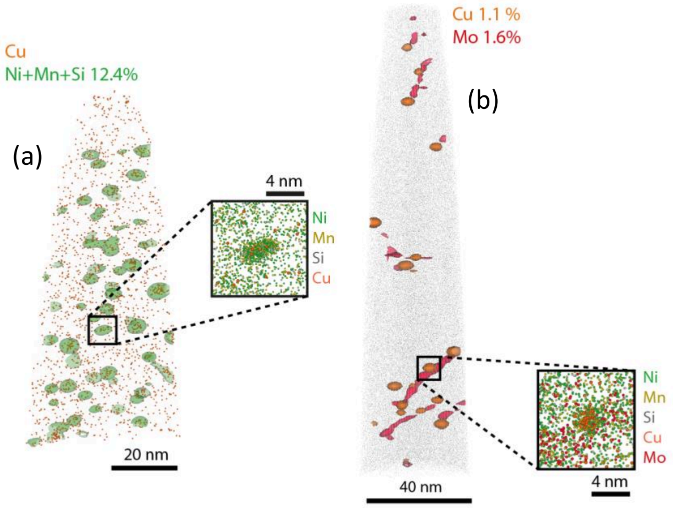

Figure 4. Atom Probe Tomography reconstruction of the nanostructure of (a) irradiated weld metal, and (b) thermally aged weld metal. Image courtesy of Dr. Kristina Lindgren.

As briefly mentioned above, plastic properties are altered due to the formation of the solute clusters. The effects of irradiation on the plastic properties of structural nuclear materials have been observed to cause an increase in yield strength along with a decreased work hardening and in cases of very high irradiation dose, a yield point drop (drop in stress level post initial yielding). For instance, in a study by Farell et al. [20] tensile testing of highly irradiated BCC (low alloy steel), FCC and HCP materials revealed a significantly increased yield stress coupled with a drop in stress right after the yield point and a reduced ductility in the studied materials. This phenomenon has been observed in several material systems and states. For example, in a study by Cotrell and Stokes [21], aluminum (FCC) was studied where a sharp yield point drop was observed after pre-straining at a low temperature with resumed straining at a higher temperature. Luft [22] noted similar phenomena of yield point drop along with work softening when studying precipitation hardened molybdenum and quenched or neutron irradiated metals (both BCC and FCC). The mechanism behind the yield point drop in aged reactor structural alloys is linked to dislocation channel deformation, where plastic deformation concentrates in distinct bands in the microstructure [20], [22]. Inside these bands, also called *clear bands*, the irradiation induced obstacles to dislocation motion have been cleared away by previous dislocation motion. Thus, the resistance to dislocation motion is significantly lower compared to the surrounding material, and therefore plastic deformation tends to localize there.

Embrittlement of low alloy steels appears as a lowered toughness and an increased ductile-to-brittle transition temperature due to ageing. Embrittlement is commonly divided into two categories, hardening and non-hardening embrittlement. The former is due to an increase in yield strength that gives higher stresses ahead of a crack front, *ceteris paribus,* and thus higher probability of a micro crack reaching a critical state for brittle cleavage fracture. This example of how hardening affects embrittlement is somewhat simplified, since other factors affecting the cleavage properties could change at the same time due to ageing. In a publication by Sokolov et al. [23] irradiation embrittlement of a reactor pressure vessel weld metal was studied through the use of fracture, impact and tensile testing. The study revealed a shift of $\Delta T_0 = 165$ ˚C accompanied with an increase in room temperature yield strength of $\Delta\sigma_y = 226$ MPa. In the paper it was also shown how the ductile *J-R* curve was lowered due to irradiation. The latter, non-hardening embrittlement, works by increasing the probability of failure by brittle fracture without the formation of features which impede dislocation motion (not causing hardening). This type of embrittlement is caused by the introduction of a second source of micro crack nucleation sites: grain boundaries weakened due to segregation of impurity elements, increasing the probability for brittle intergranular failure. In the extensive review of intergranular failure in steels by Briant and Banerji [24], it is noted that some distinguishable phenomena appear to be related to intergranular failure. One being that segregation of elements from groups IV-VI in the periodic system appears to yield the most potent grain boundary embrittlement, which is also mentioned by McMahon [25]. These groups include elements such as Si, Sn, P and S, which are not uncommon impurities or alloying elements in the steels of interest. As an example, in a study by Shtrombakh et al. [26] thermal ageing after exposure times up to ~200 000 h of several Russian reactor pressure vessel steels were investigated. It was found that ageing only affected the weld metal with a rather high Ni content, and that the embrittlement was mainly due to impurity segregation resulting in intergranular fracture, i.e. non-hardening embrittlement.

3. Modeling concepts of ageing effects

This section presents the proposed framework for modeling ageing induced changes to the mechanical properties of low alloy steels.

3.1. Hardening and changes of plastic properties

As outlined in Section 2.2, significant changes to the plastic properties emerge as a consequence of the ageing of structural nuclear alloys, such as low alloy steels. Since these changes emerge due to the formation of microstructural features that affect the dislocation motion and overall dislocation behavior, strain gradient plasticity (SGP) theory was chosen for building a modeling framework capable of retracing the main characteristics of ageing induced changes of the plastic properties. SGP offers a way of introducing a size dependent plastic constitutive behavior by allowing the plastic strain gradient to carry constitutive information. The SGP formulation considered here was developed by Gudmundson [27] and is a higher order continuum theory where the plastic strain gradient contributes to the work per unit volume along with the plastic and elastic strains. The internal virtual work in a volume can be expressed as

$$\delta w_i = \int_V \left[\sigma_{ij} \delta\varepsilon_{ij}^{\mathrm{e}} + q_{ij} \delta\varepsilon_{ij}^{\mathrm{p}} + m_{ijk} \delta\eta_{ijk}^{\mathrm{p}} \right] dV, \tag{1}$$

where q_{ij} and m_{ijk} are higher order stress tensors, which are work conjugated to the plastic strain $\delta\varepsilon_{ij}^{\mathrm{p}}$ and the plastic strain gradient $\delta\eta_{ijk}^{\mathrm{p}} \equiv \delta\left(\partial\varepsilon_{ij}^{\mathrm{p}} / \partial x_k\right)$, respectively. The corresponding strong form of (1) are two sets of equilibrium equations

$$\begin{aligned} &\frac{\partial \sigma_{ij}}{\partial x_j} = 0, \\ &\frac{\partial m_{ijk}}{\partial x_k} + s_{ij} - q_{ij} = 0, \end{aligned} \tag{2}$$

where s_{ij} denotes the deviatoric part of σ_{ij}.

The Cauchy stress tensor σ_{ij} and the elastic strain $\varepsilon_{ij}^{\mathrm{e}}$ are related through the standard isotropic Hooke's law. Effective scalar measures of stress and plastic strain are defined analogously to J_2-plasticity, which is a formulation for plastic deformation assuming that all plastic deformation is deviatoric in nature, i.e. only undergoes shape change, no volume change. The effective stress Σ and strain rate $\dot{E}^{\mathrm{p}}$ are expressed as

$$\Sigma = \sqrt{\frac{3}{2}\left(q_{ij}q_{ij} + \frac{m_{ijk}m_{ijk}}{l^2}\right)}, \quad \dot{E}^{\mathrm{p}} = \sqrt{\frac{2}{3}\left(\dot{\varepsilon}_{ij}^{\mathrm{p}}\dot{\varepsilon}_{ij}^{\mathrm{p}} + l^2\dot{\eta}_{ijk}^{\mathrm{p}}\dot{\eta}_{ijk}^{\mathrm{p}}\right)}, \tag{3}$$

where l is the intrinsic constitutive length scale, which will be further addressed below. Following from this formalism, effective scalar measures of the plastic strain increment and strain gradient increment can be expressed as

$$\dot{\varepsilon}^{\mathrm{p}} = \sqrt{\frac{2}{3}\dot{\varepsilon}_{ij}^{\mathrm{p}}\dot{\varepsilon}_{ij}^{\mathrm{p}}}, \quad \dot{\eta}^{\mathrm{p}} = \sqrt{\frac{2}{3}\dot{\eta}_{ijk}^{\mathrm{p}}\dot{\eta}_{ijk}^{\mathrm{p}}}. \tag{4}$$

The current framework would lead to an indeterminacy of the higher order stresses if a rate-independent plastic constitutive model were to be used. Instead, a viscoplastic model is used and the plastic flow rules are expressed as

$$\dot{\varepsilon}_{ij}^{\mathrm{p}} = \dot{\varepsilon}_0\frac{3q_{ij}}{2\Sigma}\Phi\left(\Sigma, \sigma_{\mathrm{f}}\right), \quad \dot{\eta}_{ijk}^{\mathrm{p}} = \dot{\varepsilon}_0\frac{3m_{ijk}}{2l^2\Sigma}\Phi\left(\Sigma, \sigma_{\mathrm{f}}\right), \tag{5}$$

where the $\dot{\varepsilon}_0$ is a reference strain rate and σ_{f} is the material flow stress. The viscoplastic potential Φ was chosen to be a Ramberg-Osgood type function as

$$\Phi\left(\Sigma, \sigma_f\right) = \frac{\Sigma}{\sigma_{\mathrm{f}}}\zeta + \left(\frac{\Sigma}{\sigma_{\mathrm{f}}}\right)^n, \tag{6}$$

where the parameter $\zeta > 0$, but $<< 1$, is necessary from a numerical point of view and can be interpreted as the inverse of the initial resistance to plastic flow. The parameter was set to $\zeta = 10^{-9}$, and it only influences the solution (to a small extent) before initial yielding. It should be noted that a rate-independent behavior can be achieved from (6) if the exponent n is chosen to be a sufficiently large number.

The length scale introduced in (3) controls the influence of the plastic strain gradient on the constitutive response. This type of modeling is also called non-local continuum modeling, since the constitutive behavior at a point (local) is informed by its surrounding state (non-local) through the length scale and plastic strain gradient. For instance, if the plastic strain is allowed to vary over a region the size of the length scale or smaller, the response will be significantly affected. If the opposite occurs, the solution starts approaching the classical continuum J_2-plasticity response. As the length scale in this theory is only related to the plastic constitutive behavior, attempts can be made to relate this to the dislocation microstructure of materials of interest. In the study presented in Paper I of this thesis, it is assumed that the length scale l should be related to the dislocation mean free path and the changes it undergoes during plastic deformation. This is done by allowing the length scale to evolve with plastic deformation.

Patterning of the dislocation microstructure is of interest for the modeling of ageing effects on the plastic properties of structural alloys used in nuclear applications. As a starting point for this, Holt's [28] relation for dislocation cell size as a function of dislocation density was used

$$\Lambda = \frac{A}{\sqrt{\rho}}, \tag{7}$$

where Λ is the wavelength representing the average dislocation cell diameter, ρ is the dislocation density, and A is a non-dimensional material parameter. By differentiation of (7), and assuming equivalence between the changes in this microstructural length scale and the constitutive length scale $\mathrm{d}\Lambda = \mathrm{d}l$, a general evolution law for l can be expressed as

$$\mathrm{d}l = -\frac{l^3}{2A^2}\mathrm{d}\rho. \tag{8}$$

As the above outlined theory is an isotropic small strain plasticity framework, it is not possible to reliably compute a dislocation density based on the available fields. However, the effective measures of strain and strain gradient defined in (3) and (4) may serve as isotropic proxies for the dislocation densities with the addition of a few assumptions.

One example of how an evolution law for the length scale was developed is given here; others were also derived and are detailed in Paper I of this thesis. A common assumption about the dislocation density is that the total density is the sum of geometrically necessary dislocations (GND) and statistically stored dislocations (SSD) as $\rho = \rho^{\mathrm{G}} + \rho^{\mathrm{S}}$. However, as noted by Ashby [29], this is an oversimplification that should mainly be valid at small dislocation densities as the presence of ρ^{G} will accelerate the accumulation of ρ^{S}. Nevertheless, incrementally, such an addition of densities should be a valid assumption, i.e. $\mathrm{d}\rho = \mathrm{d}\rho^{\mathrm{G}} + \mathrm{d}\rho^{\mathrm{S}}$. Following arguments by Devincre et al. [30] and Ashby [29], reasonable relations for the GND and SSD densities could be written as

$$\mathrm{d}\rho^{\mathrm{G}} = \frac{1}{b}\mathrm{d}\eta^{\mathrm{p}}, \ \mathrm{d}\rho^{\mathrm{S}} = \frac{1}{bl}\mathrm{d}\varepsilon^{\mathrm{p}}, \tag{9}$$

where dynamic recovery effects on $\mathrm{d}\rho^{\mathrm{S}}$ are neglected, and *b* is the Burger's vector. By using this in (8) the following evolution law for the constitutive length scale is found

$$\mathrm{d}l = -\frac{l^3}{2A^2 b}\left(\mathrm{d}\eta^{\mathrm{p}} + \frac{\mathrm{d}\varepsilon^{\mathrm{p}}}{l}\right) = -Cl^3\left(\mathrm{d}\eta^{\mathrm{p}} + \frac{\mathrm{d}\varepsilon^{\mathrm{p}}}{l}\right), \tag{10}$$

where C is a parameter the physical dimension of 1/length that sets the strength of the length scale evolution.

A consequence of (10) is that the length scale will decrease and asymptotically approach $l = 0$. This indicates that the dislocation density would tend towards infinity, which is physically unreasonable. It could also be noted that if the dislocation density is allowed to increase indefinitely, then the crystalline base structure of the material would become increasingly more amorphous, where one could start to argue about the definition of a dislocation. Due to these reasons, a saturation length scale was introduced, which is related to the maximum dislocation density that can be achieved under plastic deformation. This comes into the evolution law as

$$\mathrm{d}l = -C\left(l - l_{\mathrm{sat}}\right)^{3}\left(\mathrm{d}\eta^{\mathrm{p}} + \frac{\mathrm{d}\varepsilon^{\mathrm{p}}}{l - l_{\mathrm{sat}}}\right), \tag{11}$$

where l_{sat} is the saturation length scale. The main effect of this is that the length scale would asymptotically reach l_{sat} instead of 0, thereby bounding the length scale evolution.

As a test problem to study the effects of the length scale evolution, a pure bending problem was solved using a 2D-plane strain finite element code. This problem was chosen because it gives a well-defined strain gradient through the geometry using only displacement boundary conditions and has a thorough analytical foundation. All boundaries except at the applied displacement are traction free, considering both higher and lower order tractions. The problem was solved using one column of elements and by enforcing pure bending, such that the deformation follows standard small strain Euler-Bernoulli beam theory, i.e. plane cross sections remain plane. For the flow stress of the material, a power law hardening model was used. An illustration of the bending problem and the finite element model along with the displacement boundary conditions used can be seen in Figure 5.

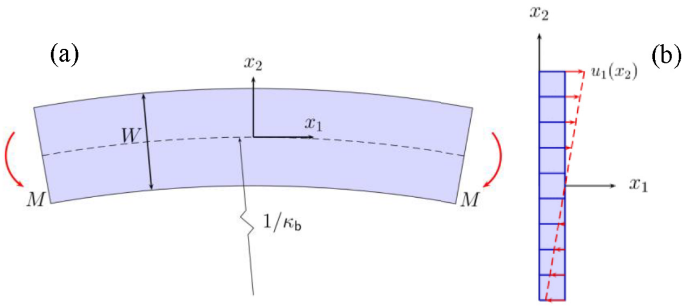

Figure 5. (a) Illustration of the pure bending problem, (b) illustration of finite element discretization and displacement boundary conditions

In Figure 6, the resulting normalized bending moment is shown as a function of the normalized curvature for two different beam thicknesses and different values of the evolution parameter C for the evolution law in (11). The main characteristics of the SGP model are unaffected by the evolving length scale, i.e. a smaller geometrical size produces a stronger response, which presents as a higher yield point. The upper family of curves in Figure 6 represents a beam with $W/l_0 = 3$ where the length scale evolution has distinct effects and the lower family of curves corresponds to a thicker beam with $W/l_0 = 12$ where the effects are less dramatic. Also included is the local theory solution where $W/l_0 \to \infty$ as a dotted line. It can be seen in Figure 6 that the length scale evolution combined with the size effects from the SGP theory results in an increase in the yield strength and a decrease in hardening, and in the more extreme cases also a yield point drop and a significant reduction in the rate of work hardening. This can be explained by the fact that as the length scale reduces, a *loss of non-locality* occurs, which locally, pushes the SGP solution towards the local theory solution. This effect will naturally vary throughout the thickness of the beam due to the variation of the plastic strain and strain gradient. With the formulation in (11) the length scale changes drastically towards the free edge, thus effectively reducing the normal stress at large values of x_2, resulting in a significant reduction of the bending moment due to a reduced length scale.

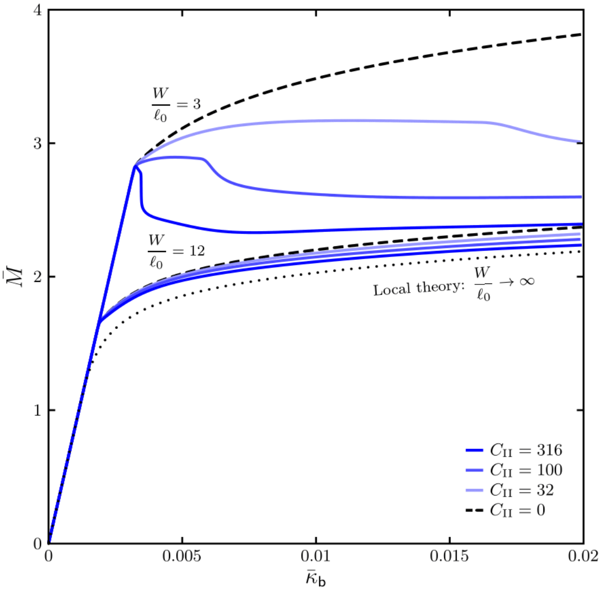

Figure 6. Normalized bending moment versus normalized bending curvature. The two families of curves represent different beam thicknesses. Reference gradient plasticity solutions are presented as dashed lines and the standard J_2-plasticity solution is presented as the dotted line.
The parameter C is normalized by l_0^{-1}, i.e. initial length scale.

These effects on the overall moment-curvature response are in tentative agreement with the general ageing effects that can be seen in low alloy steels and other structural alloys in nuclear applications. However, it is judged that this type of modeling needs far more attention before predictive modeling of effects of actual material ageing on the plastic properties can be carried out for practical purposes.

3.2. Single mechanism weakest link modeling of cleavage fracture

Transferability in fracture mechanics connects the toughness information from laboratory tested specimens to that of an actual defect in a component, such as the reactor pressure vessel. One of the main concerns of this transferability problem is the crack tip constraint, which in part is a geometrical phenomenon, but also an effect of the plastic properties of the material. Crack tip constraint can, in somewhat simplified terms, be explained as the ability to preserve the self-similar stress field ahead of the crack tip. A state of high constraint preserves the high stress state a head of the crack front, resulting in a conservative estimate of the fracture toughness. A state of low constraint will cause a breakdown of the self-similar stress fields through large scale yielding and thus result in higher fracture toughness. Usually, fracture tests are conducted using deeply cracked bend specimens that produce a state of high constraint, while actual defects are typically loaded in tension that generally produces a state of lower constraint. The transferability between the two is not trivial. The cleavage fracture process is strongly dependent on the susceptibility of micro crack nucleation and propagation. As this process is inherently probabilistic in nature, a probabilistic model was chosen as a viable modeling pathway for embrittlement. In Paper II of this thesis, a study is presented, where it is shown that the model of choice is capable of transferring the fracture toughness from high and low constraint laboratory tests to several geometries where loss of constraint occurs. In particular, it is shown that the model can reproduce the failure probability of surface cracked specimens with defects that geometrically resemble those of an actual reactor pressure vessel. In addition to this, we also develop a generalized scalar normal stress measure to be applied in conjunction with the non-local stress tensor. In Paper IV of this thesis, the model will be extended to incorporate the effects of multiple mechanisms of brittle fracture initiation.

The model chosen for modeling failure by brittle cleavage fracture is the model developed by Kroon and Faleskog [10]. This model assumes a weakest link mechanism for cleavage fracture. The basic assumptions of weakest link modeling of cleavage fracture are: (*i*) the total volume, V, of the considered structure can be divided into smaller elements of infinitesimal size where total failure will occur if one of these elements fail. (*ii*) the probability of failure of an element $\mathrm{d}P_\mathrm{f}$, depends on the stress and strain state in the element, and linearly on the volume of the element. Thus $\mathrm{d}P_\mathrm{f} = h(\sigma, \varepsilon)\, \mathrm{d}V/V_0$, where $h(\sigma, \varepsilon)$ is a function describing the random behavior associated with the micro mechanisms of the cleavage event, and V_0 is a reference volume that needs to be chosen together with $h(\sigma, \varepsilon)$. (*iii*) statistical independence of the critical state of the hazard function is assumed between the elements comprising the structure. The model in [10] is based on the assumption that cleavage fracture only occurs due to the simultaneous fulfilment of the statistically independent plastic strain based micro crack nucleation relation and a stress based propagation criterion. The model is outlined as follows, the cumulative probability of failure by cleavage fracture can be expressed as

$$P_\mathrm{f} = 1 - \exp\left(-\int_V h_\mathrm{max} \frac{\mathrm{d}V}{V_0} \right), \tag{12}$$

where h_max is the maximum value of the random function experienced throughout the loading history, V is the volume of the structure, and V_0 is the reference volume. The microstructural process of cleavage fracture comes in as the hazard function $h = h\left(\varepsilon_\mathrm{e}^\mathrm{p}, \bar{\sigma}\right)$, which is chosen as

$$\begin{aligned} &h\left(\varepsilon_\mathrm{e}^\mathrm{p}, \bar{\sigma}\right) = h_1\left(\varepsilon_\mathrm{e}^\mathrm{p}\right) h_2\left(\bar{\sigma}\right), \\ &h_1\left(\varepsilon_\mathrm{e}^\mathrm{p}\right) = c\varepsilon_\mathrm{e}^\mathrm{p}, \\ &h_2 = \begin{cases} \exp\left(-\left(\dfrac{\eta \sigma_\mathrm{th}}{\bar{\sigma}} \right)^2 \right) - \exp\left(-\eta^2\right), \text{ for } \bar{\sigma} > \sigma_\mathrm{th}, \\ 0, \text{ for } \bar{\sigma} < \sigma_\mathrm{th}. \end{cases} \end{aligned} \tag{13}$$

In (13), $\varepsilon_{\mathrm{e}}^{\mathrm{p}}$ is the effective plastic strain, $\bar{\sigma}$ is a non-local measure of stress, c, σ_{th} and η are material parameters, where the influence of η has in practical applications been observed to be weak. In Paper II of this thesis, a great deal of time has been devoted to the development of a generalized form of $\bar{\sigma}$.

The scalar non-local stress $\bar{\sigma}$ is attributed significance as it represents the condition that the stress field must be high enough over a sufficiently large volume. The non-local stress is a scalar measure, which is constructed from the non-local stress tensor defined according to the integral

$$\bar{\sigma}_{ij} = \frac{1}{V_{\mathrm{L}}} \int_{V_{\mathrm{L}}} \sigma_{ij} \left(\hat{X}_k - X_k \right) \mathrm{d}\hat{V}, \tag{14}$$

where $\mathbf{X}$ are the coordinates at the center of V_{L}, the volume over which the stress tensor is averaged. From $\bar{\sigma}_{ij}$ the non-local principal stresses $\left(\bar{\sigma}_{\mathrm{I}}, \bar{\sigma}_{\mathrm{II}}, \bar{\sigma}_{\mathrm{III}}\right)$ are calculated. A generalized effective normal stress measure can be constructed from the normal stress acting on a plane. The normal stress on a plane defined by the polar angle φ and the azimuthal angle θ from the principal stress system can be expressed as

$$\bar{\sigma}_{\mathrm{n}} \left(\varphi, \theta\right) = \bar{\sigma}_{\mathrm{I}} \cos^2 \varphi + \bar{\sigma}_{\mathrm{II}} \sin^2 \varphi \cos^2 \theta + \bar{\sigma}_{\mathrm{III}} \sin^2 \varphi \sin^2 \theta. \tag{15}$$

Integration of (15) combined with a stress distribution function $\rho\left(\varphi, \theta\right)$ over the unit sphere results in an averaged weighted normal stress as

$$\bar{\sigma} = \frac{1}{4\pi} \int_0^{2\pi} \int_0^{\pi} \bar{\sigma}_{\mathrm{n}} \left(\varphi, \theta\right) \rho\left(\varphi, \theta\right) \sin\varphi \, \mathrm{d}\varphi \, \mathrm{d}\theta. \tag{16}$$

By choosing $\rho\left(\varphi, \theta\right)$ to unity, the integral in (16) evaluates to the mean stress $\bar{\sigma}_{\mathrm{m}} = \left(\bar{\sigma}_{\mathrm{I}} + \bar{\sigma}_{\mathrm{II}} + \bar{\sigma}_{\mathrm{III}}\right)/3$. However, the stress distribution function $\rho\left(\varphi, \theta\right)$ can be chosen more carefully and should for physical reasons satisfy

$$\frac{1}{4\pi} \int_0^{2\pi} \int_0^{\pi} \rho\left(\varphi, \theta\right) \sin\varphi \mathrm{d}\varphi \mathrm{d}\theta = 1. \tag{17}$$

Choosing $\rho\left(\varphi,\,\theta\right)$ to only depend on the polar angle φ as

$$\rho\left(\varphi\right)=\left(n+1\right)\cos^{n}\varphi \quad \text{where } n\geq 0, \tag{18}$$

the integral presented in (16) evaluates to

$$\bar{\sigma}=\frac{\left(n+1\right)\bar{\sigma}_{\mathrm{I}}+\bar{\sigma}_{\mathrm{II}}+\bar{\sigma}_{\mathrm{III}}}{n+3}. \tag{19}$$

This is a non-local stress measure that is able to express a state of normal stress over the volume V_{L}, ranging from the mean stress $\bar{\sigma}_{\mathrm{m}}$ when $n=0$ to the maximum principal stress $\bar{\sigma}_{\mathrm{I}}$ when $n\rightarrow\infty$.

Micro cracks will not always nucleate on a cleavage plane aligned with the axis of the maximum principal stress. Therefore, the measure of effective normal stress in (19) can be interpreted as a phenomenological way of treating the potential triggering of cleavage initiation from a distribution of variously oriented micro cracks and associated cleavage planes. A visualization of the effective normal stress measure can be seen in Figure 7.

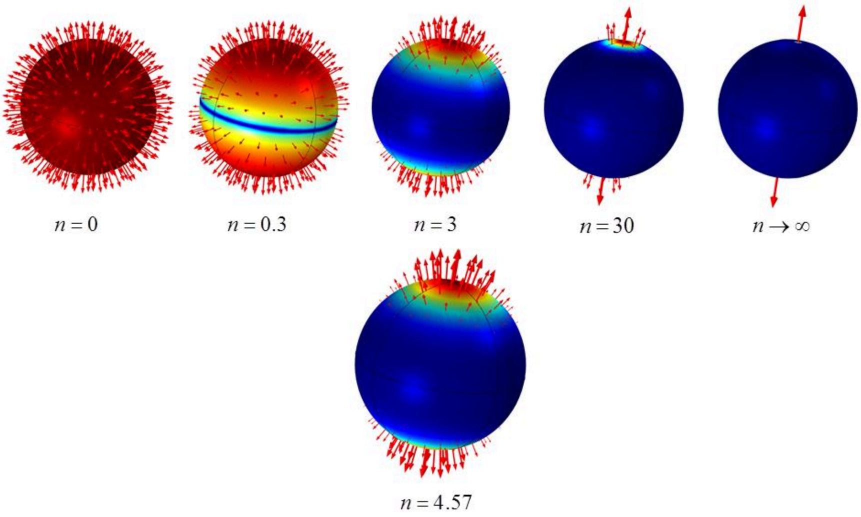

$n=0$ $\quad$ $n=0.3$ $\quad$ $n=3$ $\quad$ $n=30$ $\quad$ $n\rightarrow\infty$

$n=4.57$

Figure 7. Visualization of how the effective normal stress changes with the parameter n. Note that the mean stress is obtained when $n = 0$ and the maximum principal stress when $n \rightarrow \infty$.

In Paper II of this thesis, the model outlined above was applied to two data sets pertaining to loss of constraint and is shown to reproduce the effects of constraint on the cleavage fracture toughness of low alloy steels. In Figure 8, an example of calibration and validation of model parameters as well as the influence of the effective normal stress parameter n on the failure probability of SEN(B)-specimens (three-point bend) can be seen.

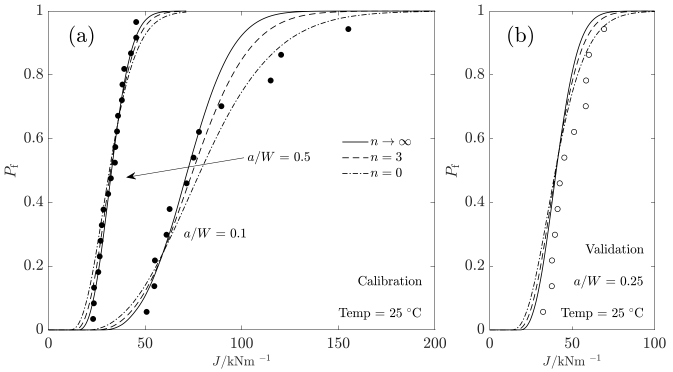

Figure 8. Predicted failure probability of SEN(B) specimens as solid lines tested at room temperature. (a) Subsets where $a/W = \{0.5, 0.1\}$ used for calibration of model parameters, (b) Subset where a/W = 0.25 used for validation of the probabilistic model. Rank probabilities from experiments as circles.

By applying the model to four-point bending experiments of surface cracked specimens containing a semi-elliptical crack, the failure predictions in Figure 9 result. The predictions presented in Figure 9 are all judged to be satisfactory, however, the results for $n = 0$ are slightly better than for $n \to \infty$.

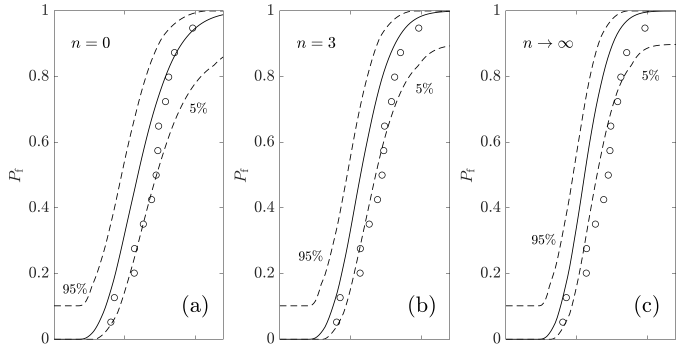

Figure 9. Predicted failure probability of the surface cracked four-point bending experiments as solid lines for different values of the effective normal stress parameter n. Dashed lines represent the 90 % confidence limits for the rank probabilites (a) $n = 0$, (b) $n = 3$, and (c) $n \to \infty$. Rank probabilities from experiments as circles.

4. Fracture toughness of a thermally aged low alloy steel weld

The assessment of the structural integrity of any structure made from a ferritic steel requires knowledge of the ductile-to-brittle transition temperature and the related fracture toughness. Typically, this is inferred from laboratory tests, where a conservative high constraint fracture toughness is determined. As stated in Section 3.2, a pertinent issue in the transferability between laboratory tests and the structural integrity of the component is crack tip constraint. With this in mind, research interest was spurred to investigate the effects of ageing on the constraint effect of a low alloy steel.

It was judged that the optimal way to investigate the constraint effect on the fracture toughness would be to include geometries where the crack tip constraint varies, such as three point bend specimens, SEN(B), with different crack to width ratios, e.g. $a/W = \{0.5 \text{ and } 0.1\}$. The deeply cracked specimen creates a state of high constraint, which gives a conservative estimate of the fracture toughness, and the shallowly cracked specimen results in a state of low crack tip constraint. The observation of any differences between two materials in the constraint effect is most effectively carried out by testing a set of high and low constraint specimens at a single temperature per material. The temperature for each material needs to be chosen so that the high constraint fracture toughness of the materials coincides. This experimental procedure makes it straightforward to observe any difference in the sensitivity to crack tip constraint, i.e. any difference in the crack tip constraint effect on the fracture toughness.

Paper III of this thesis presents an investigation where two low alloy steel welds from the Ringhals nuclear power plant in Sweden have been tested according to the outline above. The materials used in the testing included one thermally aged weld from an replaced pressurizer (PRZ) from unit 4 subjected to 345 ˚C for 215 000 h. The other weld from an exchanged reactor pressure vessel head (RPVH) from unit 3 subjected to 310-315 ˚C for 176 000 h was used as a reference, where the effects of thermal ageing were considered to be negligible in comparison to the pressurizer material. The reason that material subjected to operating temperatures had to be used as a reference material was that no archive material was available for the pressurizer welds. The reference material was chosen on account of being very similar in its as-manufactured mechanical properties, such as yield strength and the ductile-to-brittle transition temperature, and also having similar chemical composition to the pressurizer material. The aged material is denoted *R4PRZ* and the reference material is denoted *R3RPVH*.

Testing was conducted by carrying out a pre-series in order to determine the T_0 of each material, from which the test temperatures could be chosen in order to obtain the same high constraint fracture toughness. All tests of high constraint specimens carried out in this investigation, i.e. pre-series and the single temperature tests can be seen in Figure 10, where also the master curve temperature prediction is presented. It is clear that the thermally aged R4PRZ with a T_0 = -33 ˚C is more brittle than R3RPVH with a T_0 = -78 ˚C.

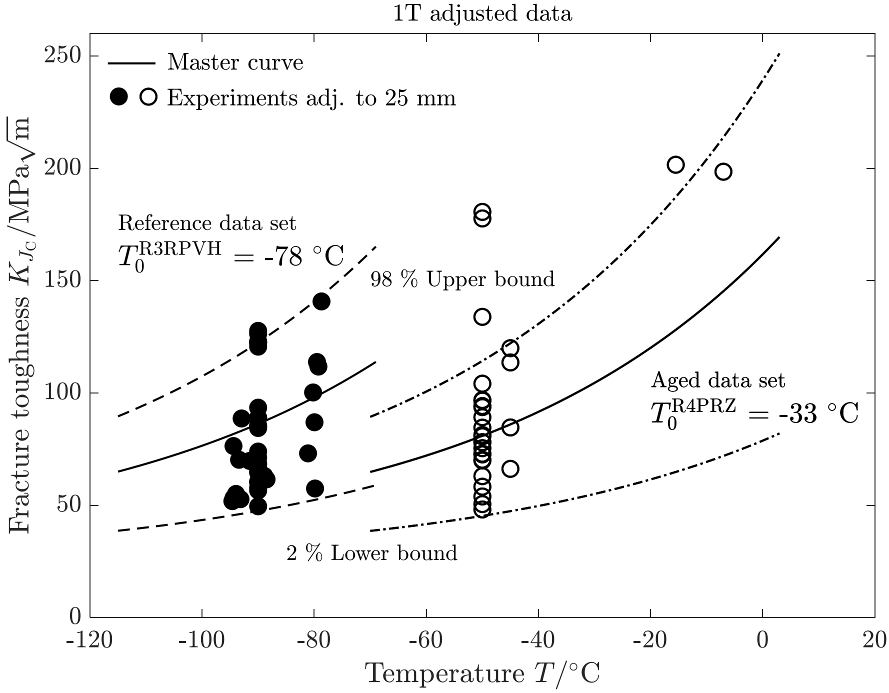

Figure 10. Fracture toughness of individual specimens belonging to both R3RPVH and R4PRZ against testing temperature, and the predicted temperature dependence from the master curve model.

Regarding the results of the single temperature investigation of the constraint effect on fracture toughness, the ranked probability of the R4PRZ tests presents itself as a bimodal toughness distribution as seen in Figure 11, where the effects are most obvious for the shallowly cracked specimens. The specimens containing the shallow cracks present a wide range of fracture toughness. The most brittle specimens display the same toughness as the specimens in the high constraint data set, while in the same data set there are specimens that are subject to significant ductile crack growth before the final brittle failure, displaying a fracture toughness ranging from 9.6 kN/m to 785 kN/m. The results from the reference, R3RPVH, show no traces of any bimodality, being unimodal as would be expected from an as-manufactured ferritic steel, i.e. exhibiting very low to no embrittlement.

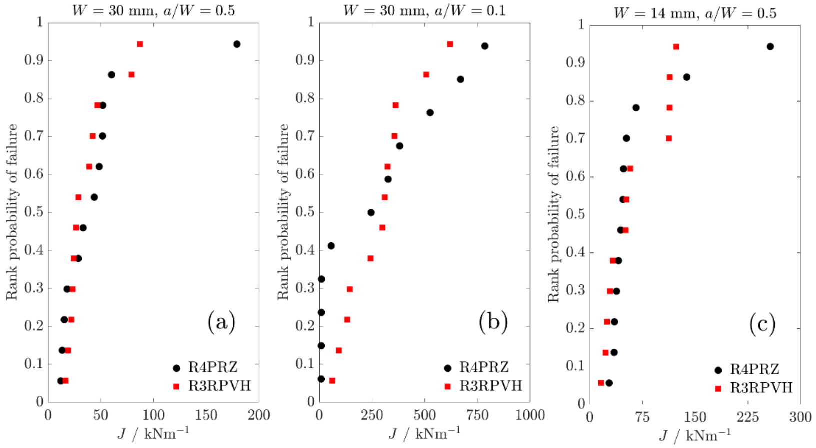

Figure 11. Rank probabilities for the fracture tests of R4PRZ at the test temperature -50 ˚C. (a) Data sets where $W = 30$ mm and $a/W = \{0.5, 0.1\}$. (b) Data set where $W = 14$ mm and $a/W = 0.5$.

Fractographical investigations of the thermally aged R4PRZ unraveled that the low toughness specimens in Figure 11 were subject to brittle fracture initiation stemming from grain boundaries, while the higher toughness specimens displayed a mixture of initiation from second phase particles and grain boundaries. Examples of fractographical images from the investigation can be seen in Figure 12-13. Investigations of the fracture surfaces of R3RPVH were also conducted. It was found that the brittle fracture initiation could be traced back to second phase particles, and that most of the fracture morphology was transgranular with small traces of intergranular fracture in the low toughness specimens.

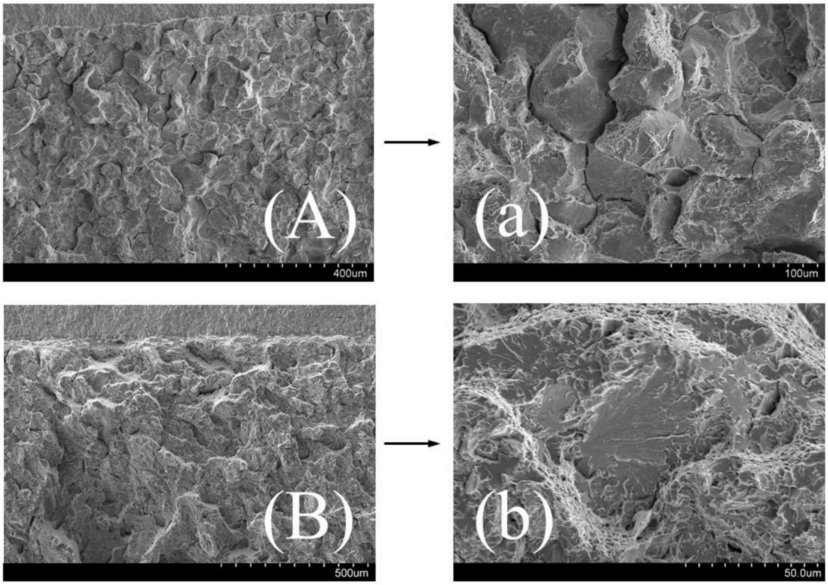

Figure 12. Fractography of deeply cracked specimens ($a/W = 0.5$) from the R4PRZ data set. Specimen {(A), (a)} fractured at a *low* toughness of $K_{JC} = 52$ MPa$\sqrt{\text{m}}$, displays intergranular fracture, note secondary cracks in (a). Specimen {(B), (b)} fractured at a *higher* toughness of $K_{JC} = 108$ MPa$\sqrt{\text{m}}$, displays transgranular fracture, probable initation point in (b).

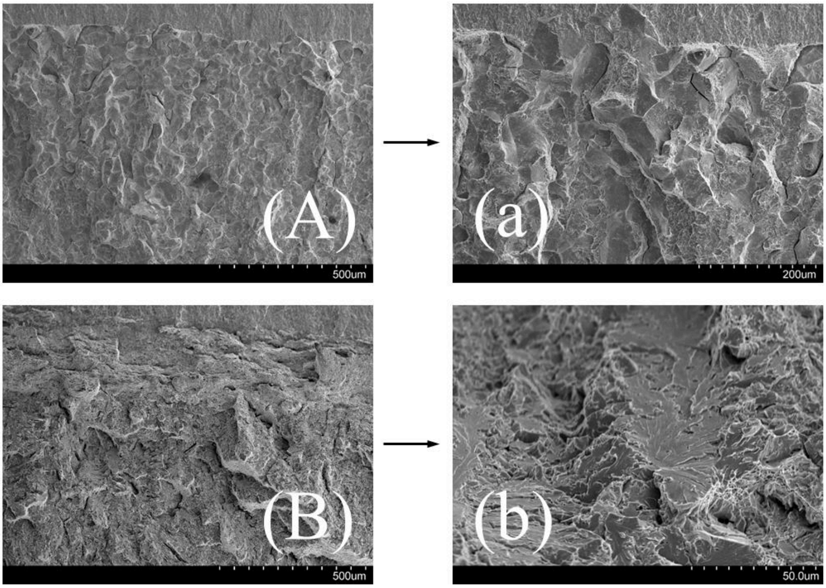

Figure 13. Fractography of shallowly cracked specimens ($a/W = 0.1$) from the R4PRZ data set. Specimen {(A), (a)} fractured at a *low* toughness of $K_{JC} = 50$ MPa$\sqrt{\text{m}}$, displays intergranular fracture, note secondary cracks in (a). Specimen {(B), (b)} fractured at a *higher* toughness of $K_{JC} = 270$ MPa$\sqrt{\text{m}}$, displays transgranular fracture, probable initation point in (b).

Uniaxial tensile testing of the materials investigated in this study indicates that both materials have been subject to hardening during operation. A comparison can be seen in Table 1, where the as-manufactured check-in data is comparted to the results of this study. Hardening due to ageing is commonly ascribed to the formation of solute clusters or fine scale precipitates during operation, which act as obstacles to dislocation motion. Both materials were investigated using APT, where clusters were found present in both materials; however to a far greater extent in the thermally aged R4PRZ than in the reference R3RPVH.

Table 1. Comparison between check-in yield strength and the results obtained in this investigation.

R_{p02}/MPa	Check-in	Current	Difference
R4PRZ	579	656	62
R3RPVH	575	637	77

The thermally aged steel from the Ringhals unit 4 pressurizer appears from this study to have been subjected to both non-hardening as well as hardening embrittlement. This is evidenced by the emergence of a second mode of brittle fracture initiation from grain boundaries besides initiation from second phase particles, resulting in a bimodal fracture toughness distribution. The hardening contribution is obvious in the results of the mechanical properties, which connects to the emergence of solute clusters in the microstructure.

The main finding of this study is that the ageing of low alloy steels may act to suppress the conventional constraint effect on fracture toughness. That is, the additional conservatism that the constraint effect supplies appears to, in part, have disappeared due to the emergence of the intergranular failure mechanism. This effect of ageing has not been observed elsewhere, to the best of the author’s knowledge. Therefore, it is deemed pertinent for the community of structural integrity engineers to further pursue similar investigations of aged low alloy steels.

5. Multiple mechanism weakest link modeling of brittle fracture

The results presented in Section 4 initiated a modeling effort with the purpose of creating a micromechanically informed probabilistic model with multiple failure mechanisms. This was carried out by expanding upon the weakest link framework presented in Section 3.2 and has been documented in Paper IV of this thesis, a short summary of which is given below.

By assuming that brittle failure is governed by a weakest link mechanism and that in each sub volume there are two (or more) different mechanisms that can initiate brittle failure, it follows that the micro crack that develops into a self-sustaining macro crack will stem from either the one or the other mechanism, i.e. it can only have one origin. Mathematically this can be derived by assuming statistical independence or mutual exclusivity. Here, mutual exclusivity has been used and is expressed as as $P(A \cup B) = P(A) + P(B),$ where A and B corresponds to the two mechanisms, which results in an expression for the probability of failure as

$$P_{\mathrm{f}} = 1 - \exp\left(-\left(h^{\mathrm{A}} + h^{\mathrm{b}}\right) \frac{\mathrm{d}V}{V_0} \right), \tag{20}$$

where h^{A} and h^{B} are the hazard functions for the micro mechanisms of failure. More specifically, particle initiated transgranular and grain boundary initiated intergranular failure. In Section 3.2, the corresponding expression to Eq. (20) was calculated by evaluating the maximum value of h throughout the loading history. This methodology was renewed with interpreting the first part, h_1, comprised in the hazard function, $h = h_1(\varepsilon_{\mathrm{p}}) h_2(\bar{\sigma})$, as the number of micro cracks computed by integrating the rate of micro crack nucleation $g_1$as

$$h_1 = \int_0^{\varepsilon_{\mathrm{p}}} g_1\left(\varepsilon_{\mathrm{p}}\right) \mathrm{d}\varepsilon_{\mathrm{p}}. \tag{21}$$

The result of this is that the hazard function will be computed as

$$h^i = \int_0^{\varepsilon_{\mathrm{p}}} g_1^i\left(\varepsilon_{\mathrm{p}}\right) h_2^i\left(\bar{\sigma}\left(\varepsilon_{\mathrm{p}}\right)\right) \mathrm{d}\varepsilon_{\mathrm{p}}, \tag{22}$$

where the function h_2 is carried forward from the framework in Section 3.2 and corresponds to the fraction of the total number of nucleated micro cracks that can be regarded as potential triggering sites for macroscopic brittle fracture. Superscript i denotes the mechanism represented by the hazard function, i.e. grain boundary or particle-controlled failure. In Section 3.2, the model was developed and validated against experiments of brittle fracture tests where initiation occurred from second phase particles. In the formulation of that model, a linear $h_1(\varepsilon_\mathrm{p})$-function was used, which in the framework presented here, corresponds to a g_1-function that is constant. However, no previous experience with how to incorporate grain boundary failure in this framework exists.

With the purpose of making an informed choice of the g_1-function corresponding to the grain boundary mechanism of brittle fracture, crystal plasticity models analogous to the different zones of a weld microstructure were considered. The models used can be seen in Figure 14, where sub figures (a) and (b) are meant to represent the equiaxed regions of a weld microstructure, while (c) and (d) are made to represent the dendritic regions.

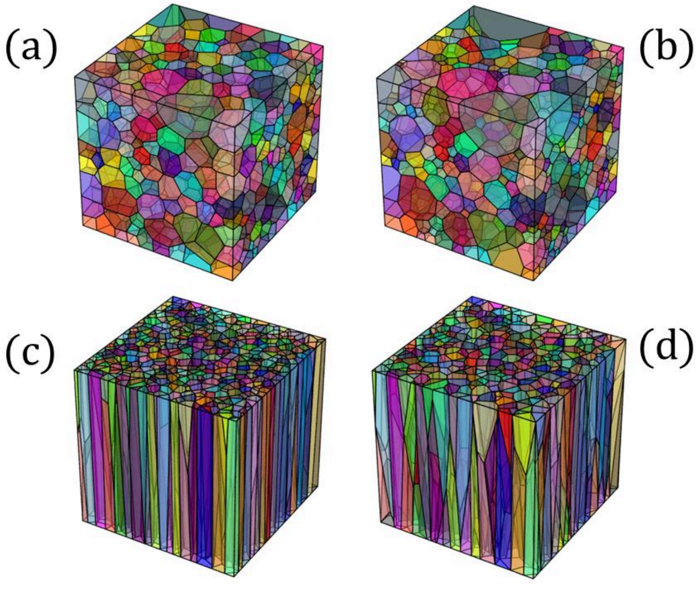

Figure 14. Tesselations of grain structures. (a) and (b) corresponds to the equiaxed grain structures. (c) and (d) correspond to the dendritic grain structures.

The models were solved by supplying boundary conditions through nonlinear kinematic constraints that would yield a constant stress triaxiality $T = (\sigma_{\mathrm{I}} + \sigma_{\mathrm{II}} + \sigma_{\mathrm{III}})/(3\sigma_{\mathrm{e}})$ and Lode parameter $L = (2\sigma_{\mathrm{II}} - \sigma_{\mathrm{I}} - \sigma_{\mathrm{III}})/(\sigma_{\mathrm{I}} - \sigma_{\mathrm{III}})$ through the loading history. In the post-processing of the analysis, the average normal stress acting over each grain boundary has been computed and compared to a critical stress according to a Griffith criterion. If a grain boundary is considered critical, it will be accumulated at that specific time step and not considered for failure in further post-processing.

The models were solved for stress triaxialities in the range $T = \{2.35, 2.2, 2.05, 1.9, 1.75\}$ and for a single Lode parameter value of $L = -0.25$, as the importance of the Lode parameter was early on found to be insignificant. The key result from the crystal analysis can be seen in Figure 15, where the fraction of critical grain boundaries is presented as a function of plastic strain which corresponds to the h_1-function given in (21) and was used to infer the g_1-function. In the analysis of the stress state that emerges in the grain boundaries, it was found that the global stress state is the dominating factor that determines the local grain boundary stress state. This allows for the construction of an analytical model in the same spirit as the crystal model.

In the analytical model of grain boundary failure, the principal stresses are computed from the stress triaxiality and the Lode parameter that together gives the characteristic of the stress state. The effective stress was computed from a flow stress relation, where the plastic strain becomes the loading parameter. This makes it possible to write the stress state as

$$\begin{aligned}\sigma_{\mathrm{I}} &= \sigma_{\mathrm{e}}\left(T + \frac{3-L}{3\sqrt{L^2+3}}\right),\\ \sigma_{\mathrm{II}} &= \sigma_{\mathrm{e}}\left(T + \frac{2L}{3\sqrt{L^2+3}}\right),\\ \sigma_{\mathrm{III}} &= \sigma_{\mathrm{e}}\left(T - \frac{3+L}{3\sqrt{L^2+3}}\right).\end{aligned} \tag{23}$$

The number of grain boundaries were set to 5000, the normals were randomly drawn to be uniformly distributed across the unit sphere, and the grain boundary areas were randomly drawn from a log-normal distribution to yield an area distribution akin to the crystal models. In all other regards, the analysis is the same as in the crystal models. Some results from the analytical model are presented and compared to the crystal models in Figure 15, where it can clearly be seen that the analytical model can reproduce the behavior of the crystal model.

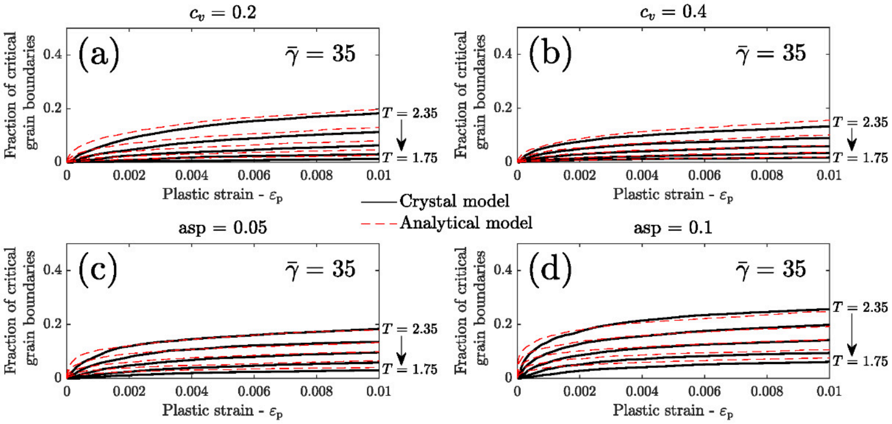

Figure 15. Comparison of the accumulated number fraction of critical grain boundaries between analytical model and the crystal models pertaining to the equiaxed grain structures in (a) and (b), and the dendritic grain structures in (c) and (d). Each line represents a solution where the stress triaxiality T belongs to the set {2.35, 2.2, 2.05, 1.9, 1.75}.

From the results of the crystal and analytical models, two candidates for the g_1-function were constructed as

$$g_1 = \frac{c}{\varepsilon_0\left(1+\dfrac{\varepsilon^{\mathrm{p}}}{\varepsilon_0}\right)}, \tag{24}$$

where ε^{p} is the equivalent plastic strain and

$$g_1 = \begin{cases} \dfrac{c}{\varepsilon_0\left(1+\dfrac{\varepsilon^{\mathrm{p}}}{\varepsilon_0}\right)}\left(T-T_{\mathrm{th}}\right)^2 \ \text{ for } \ T>T_{\mathrm{th}}, \\ 0 \ \text{ for } \ T \le T_{\mathrm{th}}. \end{cases} \tag{25}$$

Here, T is the stress triaxiality and the parameter T_{th} acts as a threshold for the stress triaxiality. The functions presented in Eqs. (24) and (25) could be fitted to the results of the crystal model and the analytical model, respectively, both with a R^2 above 0.99.

Concerning the application of the weakest link model to the fracture toughness tests presented in Section 4 and Paper III of this thesis, i.e. the constraint sensitivity tests of the reference and thermally aged materials. The reference material, which presents a unimodal fracture toughness distribution, is well described by a single mechanism weakest link framework using a constant g_1-function. Predictions of the failure probability of the sets used for parameter estimation and validation can be seen in Figure 16. Clearly, the model is able to predict the fracture toughness distribution with varying constraint and specimen size.

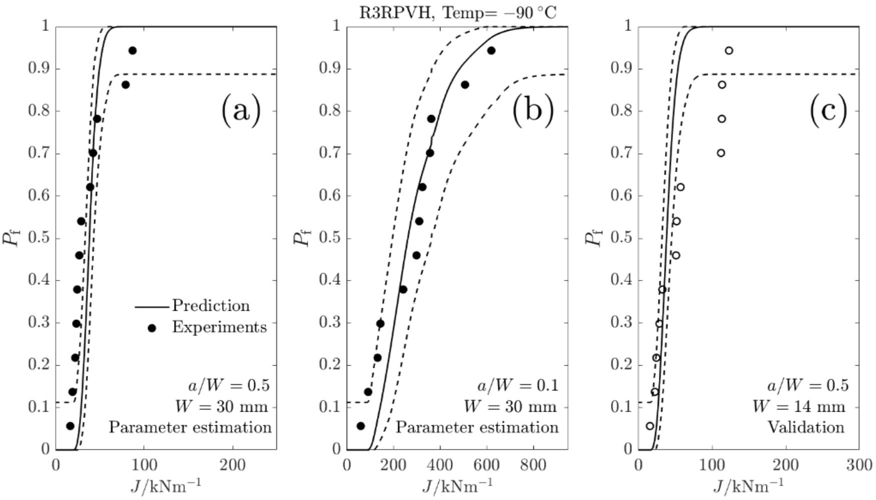

Figure 16. Comparison of the predicted failure probability with rank probabilities for the fracture tests (circles) of the reference material R3RPVH data set tested at a temperature -90 ˚C. (a) subset where $a/W = 0.5$ and $W = 30$ mm, (b) subset where $a/W = 0.1$ and $W = 30$ mm, and (c) subset where $a/W = 0.5$ and $W = 14$ mm. Subsets (a) and (b) were used for parameter estimation, subset (c) were used as validation of model predictions.

The application of the multiple mechanism weakest link model can be seen in Figure 17, where the predictions of the failure probability of the sets used for parameter estimation and validation are presented. Figure 18 shows the same data including an illustration of the underlying brittle fracture mechanisms. The multiple mechanism weakest link model is able to reproduce the fracture toughness distribution with a remarkable accuracy, both in terms of the constraint effect and the size effect. Regarding the choice of g_1 for the brittle fracture mechanism, of the two functions presented in Eqs. (24) and (25), the resulting failure prediction for the data set at hand is more or less the same regardless of which function is used. This may be due to the possibility of the difference in the stress triaxiality being too narrow between the geometries used for parameter investigation and model validation.

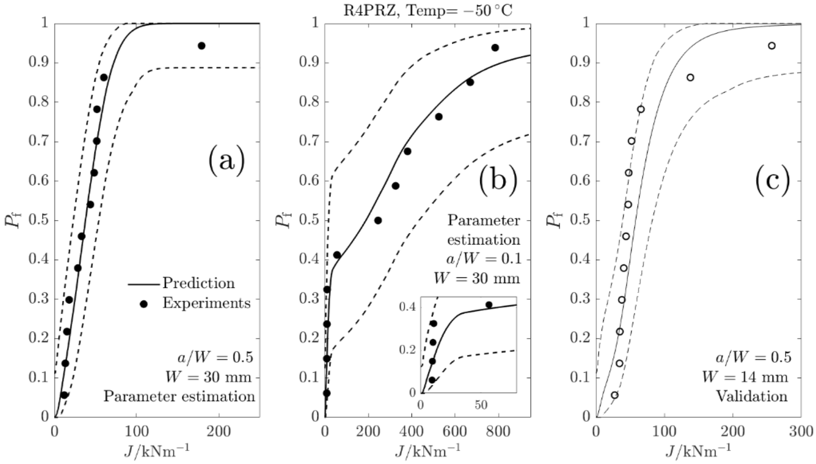

Figure 17. Comparison of the predicted failure probability with rank probabilities for the fracture tests (circles) of the reference material R4PRZ data set tested at a temperature -50 ˚C. (a) subset where *a*/*W* = 0.5 and *W* = 30 mm, (b) subset where *a*/*W* = 0.1 and *W* = 30 mm, and (c) subset where *a*/*W* = 0.5 and *W* = 14 mm. Subsets (a) and (b) were used for parameter estimation, subset (c) was used as validation of model predictions. Note, in (b) figure inset shows steep initial region of model prediction.

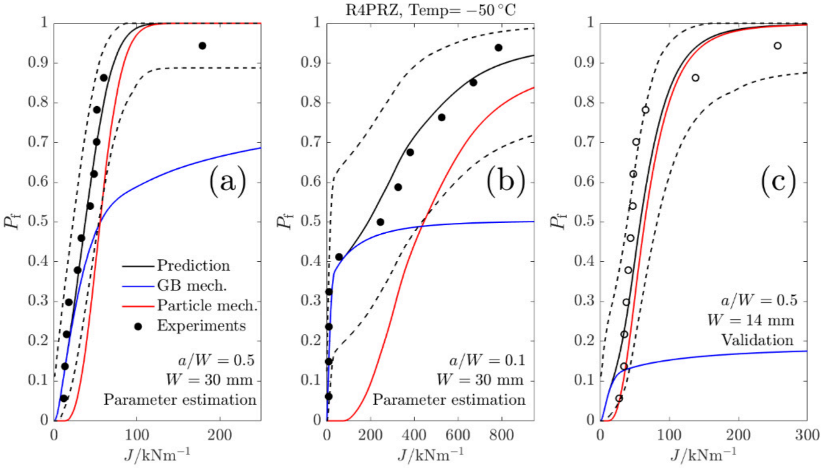

Figure 18. Comparison of the predicted failure probability with rank probabilities for the fracture tests (circles) of the reference material R4PRZ data set tested at a temperature -50 ˚C. Shown here are also the individual mechanisms calculated as if being single mechanism predictions. Note that the individual mechanisms as illustrated here do not sum up to the actual multi mechanism prediction since they are computed as single mechanism predictions and are for illustration purposes only.

6. Future work

The culmination of the work in this thesis is the multiple mechanism weakest link model. The model in itself contains some previously verified and some brand new elements. As presented, the model appears to work on the current data set at hand, however, further model development in tandem with experimental investigations is deemed necessary to further reinforce confidence in the model. Experiments where the fracture mechanisms could be separated more clearly would be a good starting point. This would enable improved understanding of the micro mechanism of failure, which could then be used to reshape or verify the basis of the model assumptions.

The temperature dependence of the mechanisms of brittle fracture initiation and their interactions is something that has been left out in the studies of this thesis. If experiments where the fracture mechanisms could be isolated could be devised, it would also be of great interest to study the temperature dependence of the two mechanisms.

Research on the interplay between ageing and ductile fracture mechanisms is also judged to be an area where future efforts could be placed.

Bibliography

[1] B. K. Sovacool, R. Andersen, S. Sorensen, K. Sorensen, V. Tienda, A. Vainorius, O. Marc Schirach och F. Bjørn-Thygesen, ”Balancing safety with sustainability: assessing the risk of accidents for modern low-carbon energy systems,” *Journal of Cleaner Production,* vol. 112, pp. 3952-3965, 2016.

[2] P. A. Kharecha och J. E. Hansen, ”Prevented Mortality and Greenhouse Gas Emissions from Historical and Projected Nuclear Power,” *Environmental Science and Technology,* vol. 47, nr 9, pp. 4889-4895, 2013.

[3] Statistiska Centralbyrån SCB, ”scb.se,” SCB, 30 November 2018. [Online]. Available: https://www.scb.se/hitta-statistik/sverige-i-siffror/miljo/elektricitet-i-sverige/. [Använd 27 May 2020].

[4] P. Bowen, S. G. Druce och J. F. Knott, ”Micromechanical modelling of fracture toughness,” *Acta Metallurgica,* vol. 35, nr 7, pp. 1735-1746, 1987.

[5] P. Bowen , S. G. Druce och J. F. Knott, ”Effects of microstructure on cleavage fracture in pressure vessel steel,” *Acta Metallurgica,* vol. 34, nr 6, pp. 1121-1131, 1986.

[6] Y. Qiao och A. Argon, ”Cleavage crack-growth resistance of grain boundaries in polycrystalline Fe-2%Si alloy: experiments and modeling,” *Mechanics of Materials,* vol. 35, pp. 129-154, 2003.

[7] Y. Qiao och A. Argon, ”Cleavage cracking resistance of high angle grain boundaries in FE-3%Si alloy,” *Mechanics of Materials,* vol. 35, pp. 313-331, 2003.

[8] A. Lambert-Perlade, A. Gourgues, J. Besson, T. Sturel och A. Pineau, ”An enhanced probabilistic model for cleavage fracture assessment accounting for local constraint effects,” *Metallurgical and Materials Transactions A,* vol. 35A, pp. 1039-1053, 2004.

[9] R. O. Ritchie, J. F. Knott och J. R. Rice, ”On the relationship between critical tensile stress and fracture toughness in mild steel,” *Journal of the Mechanics and Physics of Solids,* vol. 21, pp. 395-410, 1973.

[10] M. Kroon och J. Faleskog, ”A probabilistic model for cleavage fracture with a length scale - influence of material parameters and constraint,” *International Journal of Fracture,* vol. 118, pp. 99-118, 2002.

[11] ASTM International, ”E1921-15 Standard Test Method for Determination of Reference Temperature T0 for Ferritic steels in the Transition Range,” ASTM International, West Conshohocken, 2016.

[12] M. K. Miller, K. A. Powers, R. K. Nanstad och P. Efsing, ”Atom probe tomography characterizations of high nickel, low copper surveillance RPV welds irradiated to high fluences,” *Journal of Nuclear Materials,* vol. 437, pp. 107-115, 2013.

[13] K. Lindgren, M. Boåsen , K. Stiller, P. Efsing och M. Thuvander, ”Evolution of precipitation in reactor pressure vessel steel welds under neutron irradiation,” *Journal of Nuclear Materials,* vol. 488, pp. 222-230, 2017.

[14] K. Lindgren, ”Effects of Irradiation and Thermal Ageing on the Nanoscale Chemistry of Steel Welds,” Chalmers University of Technology, Gothenburg, 2018.

[15] D. Terentyev, X. He, G. Bonny, A. Bakaev, E. Shurkin och L. Malerba, ”Hardening due to dislocation loop damage in RPV model alloys: Role of Mn segregation,” *Journal of Nuclear Materials,* vol. 457, pp. 173-181, 2015.

[16] F. Bergner, F. Gillemot, M. Hernández-Mayoral, M. Serrano, G. Török, A. Ulbricht och E. Altstadt, ”Contributions of Cu-rich clusters, dislocation loops and nanovoids to the irradiation-induced hardening of Cu-bearing low-Ni reactor pressure vessel sttels,” *Journal of Nuclear Materials,* vol. 461, pp. 37-44, 2015.

[17] K. Lindgren, M. Boåsen, K. Stiller, P. Efsing och M. Thuvander, ”Cluster formation in in-service thermally aged pressurizer welds,” *Journal of Nuclear Materials,* vol. 504, pp. 23-28, 2018.

[18] L. Messina, M. Nastar, T. Garnier, C. Domain och P. Olsson, ”Exact ab initio transport coefficients in bcc FE-X (X = CR, Cu, Mn, Ni, P, Si) dilute alloys,” *Physical Review B,* vol. 90, p. 104203, 2014.

[19] L. Messina, M. Nastar, N. Sandberg och P. Olsson, ”Systematic electronic-structure investigation of substitutional impurity diffusion and flux coupling in bcc iron,” *Physical Review B,* vol. 32, p. 184302, 2016.

[20] K. Farrel, T. S. Byun och N. Hashimoto, ”Deformation mode maps for tensile deformation of neutron-irradiated structural alloys,” *Journal of Nuclear Materials,* vol. 335, pp. 471-486, 2004.

[21] A. H. Cottrell och R. J. Stokes, ”Effects of Temperature on the Plastic Properties of Aluminium Crystals,” *Proceedings of the Royal Society of London. Series A, Mathematical and Physical Sciences,* vol. 233, pp. 17-34, 1955.

[22] A. Luft, ”Microstructural processes of plastic instabilities in strengthened metals,” *Progress in Materials Science,* vol. 35, pp. 97-204, 1991.

[23] M. A. Sokolov, R. K. Nanstad och M. K. Miller, ”Fracture Toughness and Atom Probe Characterization of a Highly Embrittled RPV weld,” *Journal of ASTM International,* vol. 1, pp. 123-137, 2004.

[24] C. L. Briant och S. K. Banerji, ”Intergranular failure in steel: the role of grain boundary composition,” *International Metal Reviews,* pp. 164-199, 1978.

[25] C. J. McMahon, ”Intergranular Fracture in Steels,” *Materials Science and Engineering,* vol. 25, pp. 233-239, 1976.

[26] Y. I. Shtrombakh, B. A. Gurovich, E. A. Kuleshova, D. A. Maltsev, S. V. Fedotova och A. A. Chernobaeva, ”Thermal ageing mechanisms of VVER-1000 reactor pressure vessel steels,” *Journal of Nuclear Materials,* vol. 452, pp. 348-358, 2014.

[27] P. Gudmundson, ”A unified treatment of strain gradient plasticity,” *Journal of the Mechanics and Physics of Solids,* vol. 52, pp. 1379-1406, 2004.

[28] D. L. Holt, ”Dislocation cell formation in metals,” *Journal of Applied Physics,* vol. 41, pp. 3197-3201, 1970.

[29] M. F. Asbby, ”Deformation of plastically non-homogeneous materials,” *Philisophical Magazine,* vol. 21, pp. 399-424, 1970.

[30] B. Devincre, T. Hoc och L. Kubin, ”Dislocation mean free paths and strain hardening of crystals,” *Science,* vol. 320, pp. 1745-1748, 2008.

[31] Intergovernmental Panel on Climate Change (IPCC), ”Global Warming of 1.5 ˚C,” IPCC, Geneva, 2018.

[32] C. F. O. Dahlberg och J. Faleskog , ”Strain gradient plasticity analysis of the influence of grain size and distribution on the yield strength in polycrystals,” *European Journal of Mechanics A/Solids,* vol. 44, pp. 1-16, 2014.

[33] H. Nakata, K. Fuji, K. Fukuya, R. Kasada och A. Kimura, ”Grain Boundary Phosphorus Segregation in Thermally Aged Low Alloy Steelsw,” *Journal of Nuclear Science and Technology,* vol. 43, nr 7, pp. 785-793, 2006.

[34] A. Andrieu, A. Pineau, P. Joly, F. Roch och D. Ryckelynck, ”Influence of P and C intergranular segregation during manufacturing and ageing on the fracture toughness of nuclear pressure vessel steels,” *Procedia Materials Science,* vol. 3, pp. 655-660, 2014.

[35] E. D. Hondros och M. P. Seah, ”The Theory of Grain Boundary Segregation in Terms of Surface Adsorption Analogues,” *Metallurgical Transactions A,* vol. 8A, pp. 1363-13771, 1977.

[36] A. Pineau, A. Benzerga och T. Pardoen, ”Failure of metals I: Brittle and ductile failure,” *Acta Materialia,* vol. 104, pp. 424-483, 2016.

Summary of appended papers

Paper I: Evolution of the length scale in strain gradient plasticity

In this paper we assume a microstructural interpretation of the length scale in strain gradient plasticity theory. The length scale is assumed to relate to the dislocation spacing and the changes it undergoes during plastic deformation. From a relation between the dislocation cell size and the dislocation density an evolution law for the constitutive length scale as function of dislocation density has been derived. From this, several different evolution laws based on the available plastic strain field variables were derived and implemented in a 2D plane strain finite element code. This has been used to solve a test problem of pure bending, where the effects of the length scale evolution have been explored. Key results are that the strengthening effect of strain gradient plasticity is unaffected but that a decreased hardening is obtained and that in cases of strong evolution, a yield point drop phenomenon results.

Paper II: A generalized probabilistic model for cleavage fracture with a length scale - Influence of stress state and application to surface cracked experiments

In this paper we use a non-local weakest link model to study the effects of the stress measure used to model failure by cleavage fracture. We develop an effective normal stress measure capable of describing a state of generalized normal stress between the mean stress and the maximum principal stress, with a continuous transition in between. The model is applied to two experimental datasets from literature, as well as experiments on surface cracked specimens containing a semi-elliptical crack. The model is shown to be well capable of handling different kinds of crack tip constraint when predicting the cumulative probability of failure by cleavage fracture.

Paper III: Analysis of thermal embrittlement of a low alloy steel weldment using fracture toughness and microstructural investigations

In this paper we have conducted fracture toughness tests with the primary objective of investigating the influence of thermal ageing on the constraint effect on fracture toughness. Testing has been conducted on an in-service thermally aged weld metal from a replaced pressurizer from the Ringhals nuclear power plant and compared with a reference material from the same power plant. Atom Probe Tomography has also been carried out to investigate the effects of ageing on the nanostructure of the material. A key result is that a second brittle fracture mode from grain boundaries is introduced due to ageing besides the typical initiation from second phase particles. This alters the fracture toughness distribution so that a bimodality appears. The intergranular fracture mode is associated with very brittle behavior and partly cancels out the constraint effect on the fracture toughness.

Paper IV: A weakest link model for multiple mechanism brittle fracture – Model development and application

In this paper we develop a weakest link framework capable of handling brittle failure from two mechanisms, intergranular and transgranular failure. The expression for the probability of failure is derived from an assumption of mutual exclusivity, i.e. the final failure must stem from a unique mechanism. The mechanism for transgranular failure is used from previous studies, while the intergranular mechanism is inferred from micro mechanical analysis of polycrystalline aggregates using crystal plasticity. The fracture modeling itself has been carried out using a porous plastic Gurson model in order to accurately resolve the mechanical fields of the growing crack prior to the final brittle fracture. The influence of the ductile process on the brittle failure probability is also included. Key results include the accurate prediction of the fracture toughness distribution using the micro mechanically informed weakest link model, and a significant size effect of the intergranular mechanism that may lead to non-conservatism of small specimens.

Paper I

International Journal of Plasticity 112 (2019) 220–241

Contents lists available at ScienceDirect

International Journal of Plasticity

journal homepage: www.elsevier.com/locate/ijplas

Evolution of the length scale in strain gradient plasticity

Carl F.O. Dahlberg*, Magnus Boåsen

Department of Solid Mechanics, KTH Royal Institute of Technology, Teknikringen 8D, SE-100 44, Stockholm, Sweden

ARTICLE INFO

Keywords:
Length scale evolution
Strain gradient plasticity
Size effects
Dislocation mean free path
Dislocation microstructure

ABSTRACT

An equivalence is assumed between a microstructural length scale related to dislocation density and the constitutive length scale parameter in phenomenological strain gradient plasticity. An evolution law is formed on an incremental basis for the constitutive length scale parameter. Specific evolution equations are established through interpretations of the relation between changes in dislocation densities and increments in plastic strain and strain gradient. The length scale evolution has been implemented in a 2D-plane strain finite element method (FEM) code, which has been used to study a beam in pure bending. The main effect of the length scale evolution on the response of the beam is a decreased strain hardening, which in cases of small beam thicknesses even leads to a strain softening behavior. An intense plastic strain gradient may develop close to the neutral axis and can be interpreted as a pile-up of dislocations. The effects of the length scale evolution on the mechanical fields are compared with respect to the choice of length evolution equation.

1. Introduction

Plastic deformation of crystalline solids is generally entailed by a work hardening and the emergence of significant changes in dislocation microstructure. The interplay of these three; plastic deformation, work hardening, and dislocation microstructure, is strongly coupled, extends over several orders of magnitude in size and has been extensively studied. During the last century, several investigations have been conducted on the resulting fields due to the collective interactions of dislocations and their influence on the macroscopic mechanical properties. A fundamental relation for relating mechanical properties to dislocation microstructure is Taylor's relationship between flow stress on a slip plane and dislocation density $\tau = \alpha\mu b\sqrt{\rho}$, where μ is the shear modulus, b is the Burgers vector, and α is a non-dimensional material parameter relating the flow stress to the dislocation density, per the classical findings in Taylor (1934a, b).

As plastic deformation increases, patterning in the dislocation microstructure has been observed to emerge and develop into features such as dislocation cells and dislocation channels, see for instance Jakobsen et al. (2006). The formation of cells and their size was theoretically studied in Holt (1970) where the basis of the analysis lies in the minimization of the elastic energy of an array of dislocations, arriving at an expression for the cell diameter given by the wavelength

$$\Lambda = \frac{A}{\sqrt{\rho}}, \tag{1}$$

with A as a non-dimensional material parameter. Experimental studies on dislocation cell formation have observed cell sizes that scale well with the theoretical relation in (1) resulting in $A = 2...30$, see Koneva et al. (2008), Öztop (2011) and Oudriss and Feaugas

---

[*] Corresponding author.
E-mail address: carldahl@kth.se (C.F.O. Dahlberg).

https://doi.org/10.1016/j.ijplas.2018.08.016
Received 19 February 2018; Received in revised form 30 August 2018; Accepted 31 August 2018

(2016) for observations with both transmission electron microscopy (TEM) and scanning electron microscopy (SEM) of this. The relation between strength and dislocation density in single crystals is reported in El-Awady (2014) where several experiments are summarized and the deformation mechanisms are highlighted.

A critical review of experiments showing a size-dependent strength of metals can be found in Dunstan and Bushby (2013, 2014) where the authors argue that e.g. the Hall–Petch relation is an emergent phenomenon of more fundamental underlying scaling properties of crystals undergoing plastic deformation. One of the conclusions they reach is that the scaling exponent (usually taken to be $-1/2$) should be viewed with some caution since the experimental data can be made to fit equally well with several other values of the exponent. This is clearly an interesting observation but here we propose another interpretation of this discrepancy; that a universal scaling law cannot be constructed since the appropriate length scale that should go into such a law is not a constant but rather evolves with plastic deformation.

There are several microstructural length scales pertinent to plastic deformation. At the smallest scale, the lattice spacing is the fundamental dimension of a crystal but a more recognizable quantity at this scale is the magnitude of the Burgers vector, on the order of a few Å. Several other length scales related to the dynamics and interactions of a few dislocations are dislocation core diameter, stacking fault width (i.e. the width of a partial dislocation) and the related width of twinning bands. Clusters of dislocations may self-organize into quasi-periodic spatial distributions as vein patches, persistent slip bands, walls, cells, and channels (see Castelluccio and McDowell (2017)), each with a characteristic width, length or spacing. For plasticity there are also several important length scales that are associated with the microstructure; spinodal decomposition introduces a periodic variation in composition (e.g. Zhou et al. (2017)), the spacing of radiation-induced clusters, second phase particle diameter and their spacing, grain size, void diameter and their spacing. Loading can further introduce zones of intense plastic deformation with a well-defined dimension such as the crack tip plastic zone size, indentation depth, damage and/or fracture process zone size, and width of localization and shear bands.

Plasticity is a macroscopic manifestation of dislocation motion, nucleation, and annihilation. The dynamics of dislocation motion depends strongly on the dislocation mean free path, L. Even in standard engineering applications L can span several orders of magnitude and will affect both hardening and the emergence of dislocation microstructure. This emphasizes plasticity as a true multiscale problem where relevant size considerations can range from the atomic scale up to at least the millimeter scale, i.e. spanning 6–7 orders of magnitude in linear dimension, e.g. illustrated in Wang et al. (2018) for an additively manufactured steel. The discussion of length scales in plasticity have been related to geometrically necessary dislocations (GND) and the Burgers vector in many publications, for instance Gao and Huang (2003) where most of the understanding from the latter half of the previous century is well summarized.

In a recent paper Liu and Dunstan (2017) investigates the length scale that appears in several gradient extended theories and seek to give a more physical basis for it. Abu Al-Rub and Voyiadjis (2006) suggested a gradient plasticity length scale that increases linearly with accumulated plastic strain. Together with a lower order gradient enhanced theory, it was shown to be able to fit the bending moment versus curvature experiments of Stölken and Evans (1998). To accomplish this the initial yield stress had to be used as a fitting parameter instead of the plastic length scale. A variable length scale is further discussed by Evans and Hutchinson (2009) where possible interpretations of the length scale and its strain dependence is covered in some detail. They note that the best fit value of a constant length scale of either a lower order theory (Nix and Gao (1998)) or a higher order theory (Fleck and Hutchinson (2001)) differs considerably when fitting to micro bend tests and that both theories cannot fully reproduce the experimental data. A better match with experiments is attained by proposing a length scale that increases with accumulated plastic strain as $\ell_{\mathsf{FH}}(\varepsilon^{\mathsf{p}}) = \ell_0(1 + a_0\varepsilon^{\mathsf{p}}/\varepsilon_0)$ where $\ell_0 = 2$ μm, $a_0 = 0.2$, and ε_0 is the initial yield strain. However, they also note that a more physically motivated interpretation of the length scale is that it should be proportional to the effective spacing between obstacles to dislocation motion. This would imply a length scale that reduces with increased straining, or rather with increased accumulation of dislocations.

In two recent papers Petryk and Stupkiewicz (2016a, b) derive an elegant, and surprisingly simple, incremental gradient-enhanced plasticity theory for single crystals, similar in spirit to Nix and Gao (1998), where contributions from plastic strain gradients enter into the hardening relation. A physically motivated and variable characteristic length scale of plastic deformation is defined, and appears almost as a by-product of their formulation, solely in terms of classic quantities that are well known to the Materials Science community. This length scale will evolve with deformation as the crystal work hardens and is expressed as a function of resolved shear stress and hardening rate. The present paper will present a small strain isotropic strain gradient plasticity (SGP) theory specifically developed to account for an evolving plastic length scale. A reader familiar with the derivation in Petryk and Stupkiewicz (2016a) will recognize some of the initial arguments but the present formulation soon diverges as we formulate incremental evolution equations for the length scale based on plastic strain and the gradients thereof. The authors of this paper would, however, like to direct attention to these two papers and specifically the first paper which, in the introduction, contains a concise and very well written overview of the subject at hand.

Stölken and Evans (1998) performed pure bending experiments to measure the plastic length scale and also discussed the possibility of it varying with applied strain but noted that their experimental accuracy would not admit determination of a non-constant length scale. Additional constant curvature thin foil bending experiments can be found in Moreau et al. (2005) and Ehrler et al. (2008). Further experimental work on small-scale bending has mainly been conducted on micro-cantilever beams (MCB). In Motz et al. (2008) single crystal Cu MCB are investigated both experimentally and by 3D discrete dislocation dynamics simulations. Their results show a beam thickness dependent size effect on the yield stress (with scaling exponent either -0.74 or -1.1 depending on the fitting function) and also a strong effect on the subsequent hardening rate. The conclusion is that the accumulation of GND is the main culprit together with observations of so-called pile-ups of dislocations around the neutral axis of the beam. The pile-up around the neutral axis was specifically investigated in Kapp et al. (2015) where significant effects on back-stress evolution and hardening rate were observed due to the severity of the pile-ups. Another set of single crystal Cu MCB is reported on in Demir et al. (2010) where the influence of dislocation source starvation is argued to lead to a mean-field breakdown phenomenon to explain very moderate initial strengthening in thin beams. This mean-field breakdown is defined in terms of a microstructure correlation length thus introducing yet another relevant length measure in small-scale plasticity. In Tarleton et al. (2015) a flow stress size effect with scaling exponent of around -1 is found from a discrete dislocation study of MCB where a strong source density dependence is noted along with the formation and location of soft pile-ups.

The main goal of this paper is to present an extension to the Gudmundson (2004) SGP theory to allow for an evolution of the intrinsic length scale. We assume an equivalence between some microstructural length scale and the intrinsic constitutive length scale. This assumption is then used to derive an evolution law for the constitutive length scale from a standpoint of dislocation accumulation and spatial self-organization. A set of evolution laws are constructed in terms of the principal fields in SGP depending on how a dislocation density is interpreted in relation to these field variables. The extension is implemented in a finite element (FE) code based on the work presented in Dahlberg and Faleskog (2013), which has been previously used to study size effects in Dahlberg et al. (2013); Dahlberg and Faleskog (2014). Implications of the proposed theoretical extension are investigated by numerical solutions to the problem of plane strain pure bending.

The paper is outlined as follows: Section 2 contains a basis for the strain gradient formulation utilized in this paper. Section 3 presents the assumptions for, and derivation of, the length scale evolution equations, along with an outline of the FE implementation. Section 4 contains a numerical example of plane strain pure bending that has been solved using a fully implicit 2D plane strain FE scheme. The results are discussed in Section 5 and the paper is concluded in Section 6.

2. Isotropic strain gradient plasticity

The SGP formulation developed in Gudmundson (2004) is a higher order continuum theory where the plastic strain gradients contribute to the work per unit volume along with the plastic and elastic strains. The internal virtual work in a volume can be expressed as

$$\delta w_i = \int_V \left[\sigma_{ij}\delta\varepsilon_{ij}^{\mathrm{e}} + q_{ij}\delta\varepsilon_{ij}^{\mathrm{p}} + m_{ijk}\delta\eta_{ijk}^{\mathrm{p}} \right] \mathrm{d}V, \tag{2}$$

where q_{ij} and m_{ijk} are higher order stresses work conjugated to the plastic strain $\varepsilon_{ij}^{\mathrm{p}}$ and the plastic strain gradient $\eta_{ijk}^{\mathrm{p}} \equiv \varepsilon_{ij,k}^{\mathrm{p}}$, respectively. The corresponding strong form of (2) is two sets of equilibrium equations

$$\sigma_{ij,j} = 0 \tag{3}$$

and

$$m_{ijk,k} + s_{ij} - q_{ij} = 0, \tag{4}$$

where s_{ij} denotes the deviatoric part of σ_{ij}.

The Cauchy stress σ_{ij} and the elastic strain $\varepsilon_{ij}^{\mathrm{e}}$ are related constitutively through the standard isotropic Hooke's law. Effective scalar measures of stress and plastic strain are defined analogously to J_2 -plasticity, and in accordance to that plastic deformation is regarded to be purely dissipative. A good example of how energetic contributions can be included in the constitutive description can be found in Niordson and Legarth (2010). Here we neglect all such effects and emphasize that neither $\varepsilon_{ij}^{\mathrm{p}}$ nor η_{ijk}^{p} contributes to a free energy. Plastic processes are considered purely dissipative and the dissipation in a point must be non-negative, which leads to

$$\Sigma\dot{E}^{\mathrm{p}} = q_{ij}\dot{\varepsilon}_{ij}^{\mathrm{p}} + m_{ijk}\dot{\eta}_{ijk}^{\mathrm{p}} \geq 0, \tag{5}$$

where Σ and $\dot{E}^{\mathrm{p}}$ are the effective scalar measures of stress and plastic strain rate. The effective stress and strain are defined in accordance with (5) and are expressed as

$$\Sigma = \sqrt{\frac{3}{2}\left(q_{ij}q_{ij} + \frac{m_{ijk}m_{ijk}}{\ell^2} \right)}, \tag{6}$$

$$\dot{E}^{\mathrm{p}} = \sqrt{\frac{2}{3}\left(\dot{\varepsilon}_{ij}^{\mathrm{p}}\dot{\varepsilon}_{ij}^{\mathrm{p}} + \ell^2\dot{\eta}_{ijk}^{\mathrm{p}}\dot{\eta}_{ijk}^{\mathrm{p}} \right)}, \tag{7}$$

where ℓ is the intrinsic constitutive length scale. Following from this formalism, effective scalar measures of the plastic strain and strain gradient can be expressed as

$$\dot{\varepsilon}^{\mathrm{p}} = \sqrt{\frac{2}{3}\dot{\varepsilon}_{ij}^{\mathrm{p}}\dot{\varepsilon}_{ij}^{\mathrm{p}}}, \tag{8}$$

$$\dot{\eta}^{\mathrm{p}} = \sqrt{\frac{2}{3}\dot{\eta}_{ijk}^{\mathrm{p}}\dot{\eta}_{ijk}^{\mathrm{p}}}. \tag{9}$$

The current framework would lead to an elastic indeterminacy of the higher order stresses if a rate-independent plastic constitutive model were to be used. Instead, a viscoplastic model is utilized to describe the plastic constitutive behavior in which the plastic flow rules are expressed as

$$\dot{\varepsilon}^{\mathrm{p}}_{ij} = \dot{\varepsilon}^{\mathrm{p}}_{0}\frac{3q_{ij}}{2\Sigma}\Phi(\Sigma,\sigma_{\mathrm{f}}), \tag{10}$$

$$\dot{\eta}^{\mathrm{p}}_{ijk} = \dot{\varepsilon}^{\mathrm{p}}_{0}\frac{3m_{ijk}}{2\ell^{2}\Sigma}\Phi(\Sigma,\sigma_{\mathrm{f}}). \tag{11}$$

where $\dot{\varepsilon}^{\mathrm{p}}_{0}$ is the reference strain rate. The viscoplastic potential Φ is chosen to be a Ramberg-Osgood type function as

$$\Phi(\Sigma,\sigma_{f}) = \frac{\Sigma}{\sigma_{\mathrm{f}}}\zeta + \left(\frac{\Sigma}{\sigma_{\mathrm{f}}}\right)^{n}, \tag{12}$$

where the parameter $\zeta \neq 0$, but $\ll 1$, is necessary from a numerical point of view and can be interpreted as the inverse of the initial resistance to plastic flow. The parameter is set to $\zeta = 10^{-9}$ and only influences the solution (to a small extent) before initial yield. The flow stress is given by a power law hardening

$$\sigma_{\mathrm{f}} = \sigma_{0}\left(1 + \frac{E^{\mathrm{p}}}{\varepsilon_{0}}\right)^{m}, \tag{13}$$

where ε_0 is taken as the strain at yield in uniaxial tension, σ_0/E where σ_0 and E denote the standard uniaxial yield stress and Young's modulus, respectively.

3. Evolution law for the length scale

During plastic deformation, changes in the dislocation microstructure will lead to subsequent changes in some microstructural length scale as discussed in Section 1 above. Following this, and assuming equivalence between the changes in this microstructural length scale and the intrinsic constitutive length scale $\Lambda = \ell$, a general evolution law for the constitutive length scale can be derived from (1). By differentiation of (1) the evolution of the constitutive length scale in terms of incremental change of dislocation density can be found to be

$$\mathrm{d}\ell = \frac{-\ell^{3}}{2A^{2}}\mathrm{d}\rho. \tag{14}$$

In this study, an isotropic small strain plasticity framework is employed, and therefore it is not possible to reliably compute a dislocation density based on the available fields. However, the effective measures defined in (7), (8) and (9) may serve as isotropic proxies for the dislocation densities through a few different assumptions. From the general evolution law in (14) we proceed to construct specific evolution equations. Several possible interpretations of $\mathrm{d}\rho$ will be proposed which then lead to different evolution equations for the length scale.

3.1. The GND approach

The results in Kysar et al. (2010) and Öztop (2011) indicates that the microstructural length scale should evolve with the GND density. Thus, letting $\mathrm{d}\rho = \mathrm{d}\rho^{\mathrm{G}}$ in (14) leads to the need to specify $\mathrm{d}\rho^{\mathrm{G}}$ in terms of the available fields. By following Ashby (1970), where the geometrically necessary dislocations are related to the plastic strain gradient $\rho^{\mathrm{G}} = \frac{1}{b}\eta^{\mathrm{p}}$, a substitute for dislocation density suitable for use in the current framework can be written on incremental form

$$\mathrm{d}\rho^{\mathrm{G}} = \frac{1}{b}\mathrm{d}\eta^{\mathrm{p}}, \tag{15}$$

where b is the magnitude of Burgers vector. Substituting (15) into (14) gives

$$\mathrm{d}\ell = \frac{-\ell^{3}}{2A^{2}b}\mathrm{d}\eta^{\mathrm{p}} = -C_{\mathrm{I}}\ell^{3}\mathrm{d}\eta^{\mathrm{p}}, \tag{16}$$

where $C_{\mathrm{I}} = (2A^{2}b)^{-1}$ is a constant with the physical dimension of 1/length. With a typical Burgers vector magnitude of $b = 0.25$ nm and A in the range $2 \ldots 30$ the value of C_{I} is found to be $500 \ldots 2$ $\mu\mathrm{m}^{-1}$.

3.2. The incrementally additive approach

In the classic Taylor-hardening equation, $\tau = \alpha\mu b\sqrt{\rho}$, the dislocation density is usually considered to be additively decomposed, e.g. Ashby (1970), into GND and statistically stored dislocations (SSD) contributions, $\rho = \rho^{\mathrm{G}} + \rho^{\mathrm{S}}$. As noted by Ashby, this additive split is an oversimplification that should mainly be valid at small densities as the presence of ρ^{G} will accelerate the accumulation of ρ^{S}. However, incrementally such an addition of densities, i.e. $\mathrm{d}\rho = \mathrm{d}\rho^{\mathrm{G}} + \mathrm{d}\rho^{\mathrm{S}}$, should be a valid assumption.

In this approach, the GND contribution is also assumed to be given by (15) above. A reasonable assumption for the SSD component is that it evolves with the accumulation of equivalent plastic strain. Several dimensionally admissible, and simple, expressions for this can be constructed. For example, in Devincre et al. (2008), the statistical net storage rate of dislocations on a slip system i is given as

$$\frac{\mathrm{d}\rho^i}{\mathrm{d}\gamma^i} = \frac{1}{b}\left(\frac{1}{L^i} - y\rho^i\right), \tag{17}$$

where γ^i is the plastic slip, L^i is the dislocation mean free path and the $y\rho^i$ term models dynamic recovery. If, in the above equation, the dynamic recovery is neglected (i.e. letting $y = 0$), the plastic slip is interpreted as its isotropic counterpart and the dislocation mean free path is equated to the length scale the following expression results

$$\mathrm{d}\rho^{\mathrm{S}} = \frac{1}{b\ell}\mathrm{d}\varepsilon^{\mathrm{p}}. \tag{18}$$

A similar relation was given by Ashby (1970) as

$$\mathrm{d}\rho^{\mathrm{S}} = \frac{4}{b\lambda^{\mathrm{S}}}\mathrm{d}\gamma \tag{19}$$

where λ^{S} was noted to vary with applied shear strain. We will here refrain from drawing any far-reaching connections between the lengths scale L_i in (17) and λ^{S} in (19) but it is tempting to interpret them both as emergent manifestations of the same microstructural length scales.

Substituting (15) and (18) into (14) gives

$$\mathrm{d}\ell = \frac{-\ell^3}{2A^2b}\left(\mathrm{d}\eta^{\mathrm{p}} + \frac{\mathrm{d}\varepsilon^{\mathrm{p}}}{\ell}\right) = -C_{\mathrm{II}}\ell^3\left(\mathrm{d}\eta^{\mathrm{p}} + \frac{\mathrm{d}\varepsilon^{\mathrm{p}}}{\ell}\right), \tag{20}$$

where it should be noted that the constant $C_{\mathrm{II}} = C_{\mathrm{I}}$ from Section 3.1 above. In (20) the relative influence of $\mathrm{d}\eta^{\mathrm{p}}$ and $\mathrm{d}\varepsilon^{\mathrm{p}}$ will evolve with the deformation such that as ℓ decreases the relative influence of $\mathrm{d}\varepsilon^{\mathrm{p}}$ on $\mathrm{d}\ell$ will increase.

As stated above it should be emphasized that several other possible functional forms can be constructed for (18) from a physical dimension argument. The constant b can be substituted for ℓ or vice versa or either of them (or both) can be substituted for some other relevant parameter with the physical dimension of length.

In addition to the expression above we also propose a slightly modified, and admittedly ad-hoc, version of the evolution equation on the form

$$\mathrm{d}\ell = -C_{\mathrm{II}}\ell^3\left(\theta^{\mathrm{G}}\,\mathrm{d}\eta^{\mathrm{p}} + \theta^{\mathrm{S}}\,\frac{\mathrm{d}\varepsilon^{\mathrm{p}}}{\ell}\right), \tag{21}$$

where θ^{G} and θ^{S} are dimensionless parameters setting the relative influence of the gradient and the strain term, respectively. Setting $\theta^{\mathrm{G}} = 0$ and $\theta^{\mathrm{S}} \neq 0$ leads to an evolution equation that only depends on the plastic strain. The case $\theta^{\mathrm{G}} = 0$ and $\theta^{\mathrm{S}} = 1$ give

$$\mathrm{d}\ell = -C_{\mathrm{ii}}\ell^2\mathrm{d}\varepsilon^{\mathrm{p}}, \tag{22}$$

that will be used below to highlight the influence of the gradient term. The constant $C_{\mathrm{ii}} = C_{\mathrm{II}}$, and the lower case i:s are here only used to indicate that it is used in conjunction with this modified version of (20). Setting $\theta^{\mathrm{S}} < 0$ gives a situation where the length scale will increase with plastic deformation. This bears some similarity to what was proposed by Voyiadjis and Abu Al-Rub (2005) and Evans and Hutchinson (2009), however, there the length scale was given as a function of the accumulated plastic strain. The incremental evolution proposed here would in such a case lead to a possible unbounded growth of the length scale, which would be nonphysical and will not be further pursued here.

3.3. The phenomenological approach

In contrast to the two preceding approaches, we now propose a purely phenomenological approach where we remain agnostic as to the actual microstructural processes. Here ρ is interpreted to be an isotropic scalar measure of plastic deformation with no other significance attached to it. In this case, it is reasonable to assume that any measure of plastic deformation could be a valid substitute in (14). In isotropic SGP the gradient enhanced effective strain (7) is a candidate and thus we propose $\mathrm{d}\rho = c\,\mathrm{d}E^{\mathrm{p}}$ where c is a parameter of physical dimension 1/area.

There are many possible ways to choose the parameter c. Here three different choices will be given without any motivation. The first choice is $c = 1/b^2$ which gives

$$\mathrm{d}\rho = \frac{1}{b^2}\mathrm{d}E^{\mathrm{p}} \quad \Rightarrow \quad \mathrm{d}\ell = -C_{\mathrm{III}}\ell^3\mathrm{d}E^{\mathrm{p}}, \tag{23}$$

alternatively $c = 1/(b\ell)$ gives

$$\mathrm{d}\rho = \frac{1}{b\ell}\mathrm{d}E^{\mathrm{p}} \quad \Rightarrow \quad \mathrm{d}\ell = -C_{\mathrm{IV}}\ell^2\mathrm{d}E^{\mathrm{p}}, \tag{24}$$

and finally taking $c = 1/\ell^2$ leads to

$$\mathrm{d}\rho = \frac{1}{\ell^2}\mathrm{d}E^{\mathrm{p}} \quad \Rightarrow \quad \mathrm{d}\ell = -C_{\mathrm{V}}\ell\mathrm{d}E^{\mathrm{p}}. \tag{25}$$

Previously the parameter b has been identified, by its common interpretation, as the magnitude of the Burgers vector. In light of the crystallographic agnosticism espoused in this section, this might seem like an unreasonable interpretation and an incoherent mixing of scales and mechanisms. It is, therefore, best to think of b as a phenomenological fitting parameter here (or perhaps rather the resulting C-parameters). However, if one were to assign b as the Burgers vector magnitude then it can be noted that $C_{\mathrm{IV}} = C_{\mathrm{I}}$ from above. It can also be noted that $C_{\mathrm{V}} = 1/(2A^2)$ and thus directly given from experiments that measure A. The evolution laws in (23) and (25) are only given here for completeness and will not be covered in further detail in this paper.

3.4. Saturation length scale

A consequence of (14) is that the length scale will decrease, from some initial value ℓ_0, and asymptotically approach $\ell = 0$ as the dislocation density increases. It can be argued that since the length scale is supposed to be a measurable and microstructurally meaningful quantity it should not vanish. From relation (1) it can also be seen that the microstructural length scale cannot tend to zero since that would imply a dislocation density that tends to infinity. Electron backscatter diffraction (EBSD) measurements of dislocation density on plastically deformed metal specimens (e.g. a Ni single crystal in Kysar et al. (2010); Dahlberg et al. (2014), an Al bicrystal in Dahlberg et al. (2017), a Cu polycrystal in Jiang et al. (2013) and a Ti-alloy polycrystal in Littlewood et al. (2011)) all typically observe a maximum density on the order of $10^{15} - 10^{16}\ \mathrm{m}^{-2}$. A maximum in the attainable dislocation density in a material should translate to a minimum in possible values for the microstructural length scale, here denoted as the *saturation length scale* $\ell_{\mathrm{sat}} < \ell_0$.

The evolution equations in (16), (20), (22) and (24) will be modified to include the saturation length scale. An effective length scale that is the difference between the microstructural and the saturation length scale is defined, $\ell_{\mathrm{eff}} = \ell - \ell_{\mathrm{sat}}$, and substituted for the length scale in the evolution law. The evolution equations, to be used in Section 4 below, are thus modified so that equation (16) now reads

$$d\ell = -C_{\mathrm{I}}(\ell - \ell_{\mathrm{sat}})^3 d\eta^{\mathrm{p}}, \tag{26}$$

evolution equation (20) becomes

$$d\ell = -C_{\mathrm{II}}(\ell - \ell_{\mathrm{sat}})^3\left(d\eta^{\mathrm{p}} + \frac{d\varepsilon^{\mathrm{p}}}{\ell - \ell_{\mathrm{sat}}}\right), \tag{27}$$

similarly for (22) as

$$d\ell = -C_{\mathrm{ii}}(\ell - \ell_{\mathrm{sat}})^2 d\varepsilon^{\mathrm{p}}, \tag{28}$$

and finally (24) is written as

$$d\ell = -C_{\mathrm{IV}}(\ell - \ell_{\mathrm{sat}})^2 dE^{\mathrm{p}}. \tag{29}$$

3.5. Modification of the isotropic SGP model

The in-house plane strain FEM implementation (see Dahlberg and Faleskog (2013) for details) of the isotropic SGP theory in Section 2 has been modified to include the evolution equations proposed above. The main differences to the previous implementation are:

1. Each material point (i.e. Gauss point) is supplied with an initial material length scale ℓ_0 as opposed to a constant ℓ used previously.
2. The material length scale ℓ is treated as an internal variable similar to E^{p}.
3. A nonlinear equation solver is implemented to solve the evolution equation for a length scale increment $d\ell$, consistent with the Euler-backward approach, given increments in plastic strain, $d\varepsilon^{\mathrm{p}}$, and plastic strain gradients, $d\eta^{\mathrm{p}}$.
4. The plastic part of the consistent tangent stiffness will get additional contributions.

Details of the implementation can be found in the Appendix.

4. Numerical solutions to a pure bending problem

In order to illustrate the implications of the proposed theoretical extension numerical solutions to plane strain pure bending are presented. In all examples the normalized elastic modulus is $E/\sigma_0 = 800$, and Poisson's ratio is $\nu = 0.3$, the power law hardening exponent is $m = 0.1$, the rate exponent is set to $n = 200$ to approach rate independent behavior and loading is introduced by quasi-static displacement rates.

The problem is modeled by a single column of N_{elem} 2D plane strain elements along the x_2-axis. The number of elements was $N_{\mathrm{elem}} = 601$ unless otherwise specified. The elements are square and equal in size so that the width of the column is $B = W/N_{\mathrm{elem}}$. Loading is introduced by prescribing a displacement such that the column deforms according to standard small strain Euler–Bernoulli beam theory (i.e. plane cross sections remain plane), see Fig. 1(b). Since the governing theory is of higher order, boundary conditions on either plastic strain or its conjugated traction need to be prescribed. Here the top and bottom surfaces of the beam are assumed to be traction free, $\sigma_{ij}n_j = 0$ and $m_{ijk}n_k = 0$ where n_k is the normal vector on the top and bottom surface. This condition implies that there can be no plastic strain gradients when approaching the free surface. If framed in the context of dislocation motion and

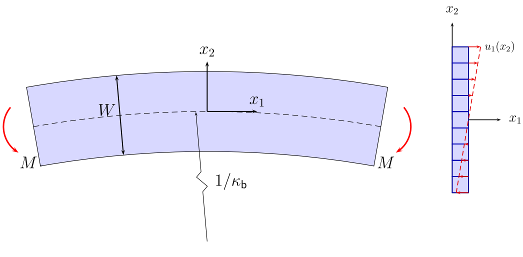

(a) (b)

Fig. 1. (a) Illustration of the pure bending problem where κ_{b} is the applied curvature and M is the resulting bending moment. (b) Illustration of FE discretization and applied displacement boundary condition for small strain pure bending. The number of elements indicated in (b) is just an illustration and the actual number of elements was 601.

accumulation this implies that dislocations are free to exit the surface and can therefore not pile up, i.e. $\rho^{\mathrm{G}} = 0$ there.

If the normal strain in the outermost fiber of the beam is denoted ε_{11} then the bending curvature is $\kappa_{\mathrm{b}} = 2\varepsilon_{11}/W$. Results will be presented in normalized curvature $\bar{\kappa}_{\mathrm{b}} = \kappa_{\mathrm{b}} W/2 = \varepsilon_{11}$. The resulting bending moment (per unit thickness) can be calculated as

$$M = \frac{\sigma_0 W^2}{4}\int_{-1}^{1} \bar{\sigma}_{11}\bar{x}_2 \mathrm{d}\bar{x}_2, \tag{30}$$

where $\bar{\sigma}_{11} = \sigma_{11}/\sigma_0$ and $\bar{x}_2 = 2x_2/W$. The bending moment will be presented normalized as $\overline{M} = 6M/(\sigma_0 W^2)$, i.e. normalized by the standard beam theory bending moment at initial yielding.

Results from thin beam bending using SGP without any evolution laws will be given in Section 4.1 and briefly discussed to set the scene. In Section 4.2 the general features of the proposed theory will be presented for one of the evolution equations. In Section 4.3 the consequence of the different evolution equations will be shown and in Section 4.4 two of the equations will be compared regarding an emergent feature of the solution.

Note that the evolution parameters C_{I}, C_{II} and C_{IV} all have physical dimension 1/length and attains the same value from the derivation. In the following sections a normalization with ℓ_0^{-1} is implied in figure legends but not explicitly stated to avoid cluttering.

4.1. The pure bending problem and gradient plasticity

Before delving into the solution details due to the proposed evolution laws in Section 3 it is worthwhile to first review some specifics of the pure bending problem solved with J_2 theory and the SGP theory of Gudmundson (2004). Thin foil bending has been analyzed previously in the context of gradient extended theories, obviously motivated by the experiments in Stölken and Evans (1998). The evolution of plastic strain through the thickness is covered in Peerlings (2007) and Niordson (2008) with a focus on how to treat the elastic-plastic boundary and higher order boundary conditions. In Idiart et al. (2009) the problem is used to distinguish between two different versions of SGP and some details of the solution fields are compared. More recently Martínez-Pañeda et al. (2016) investigated the role of both thickness and length of the foil using a distortion gradient plasticity theory.

To highlight all the intricacies of an SGP solution in one figure is not possible due to the complexity added by the non-standard terms. We, therefore, show the consequences of SGP in terms of a more familiar quantity; the elastic strain rate $\dot{\varepsilon}_{11}^{\mathrm{e}}$ normalized by the total strain rate $\dot{\varepsilon}_{11}^{\mathrm{tot}}$. Due to the boundary conditions the total strain rate varies linearly with $\bar{x}_2$. If the ratio $\dot{\varepsilon}_{11}^{\mathrm{e}}/\dot{\varepsilon}_{11}^{\mathrm{tot}} = 1$ this implies that a point is deforming by elastic straining only. Conversely, if the ratio $\dot{\varepsilon}_{11}^{\mathrm{e}}/\dot{\varepsilon}_{11}^{\mathrm{tot}} \approx 0$ then deformation is proceeding mainly by plastic straining (since $\dot{\varepsilon}_{11}^{\mathrm{tot}} = \dot{\varepsilon}_{11}^{\mathrm{e}} + \dot{\varepsilon}_{11}^{\mathrm{p}}$). In Fig. 2 this ratio is plotted for 5 different solutions as a contour plot where the vertical corresponds to the through-thickness direction, $0 < \bar{x}_2 \leq 1$, and the horizontal direction maps to load history, i.e. curvature increases from left to right.

In Fig. 2 a deep red color corresponds to elastic straining, sky blue is almost purely plastic straining and the darker blue appearing in (b)-(e) indicates some amount of elastic unloading, i.e. $\dot{\varepsilon}_{11}^{\mathrm{e}}/\dot{\varepsilon}_{11}^{\mathrm{tot}} < 0$. The J_2 solution is shown in Fig. 2(a) where the elastic-plastic boundary is clearly delineated and follows a $1/\bar{\kappa}_{\mathrm{b}}$ function, cf. Fig. 2 in Peerlings (2007). An SGP solution with $W/\ell_0 = 48$ is shown in Fig. 2(b) where the elastic-plastic boundary is more diffuse but follows the same general shape as in Fig. 2(a). It should be noted that yielding is now initiated in a region instead of just at the outermost fiber and that initial yielding is delayed compared to the local theory (indicated by the dashed black line). The SGP strengthening effect on M is small for $W/\ell_0 \gg 1$ and the available incremental work ($M\mathrm{d}\kappa_{\mathrm{b}}$) is almost the same as for the local theory. Since a larger region is actively yielding, the plastic dissipation is increased and is accommodated energetically by elastic unloading in a small region. The location and maximum intensity of this unloading are indicated by red arrow annotations in Fig. 2(b)–(e). When the thickness of the beam is reduced, the SGP strengthening effect can be seen by more pronounced delays in initial yielding. A more diffuse transition from elastic to plastic deformation is also associated with decreasing beam thickness. It should also be noted that the region of gross plastic flow will reach the neutral axis at some finite curvature, cf. Fig. 3 in Peerlings (2007). For the thinnest beam, $W/\ell_0 = 3$, in Fig. 2(e) the whole cross-section yields almost simultaneously and the comparatively small value of $W/\ell_0 = 3$ constrains the development of strong plastic strain gradients. Moment

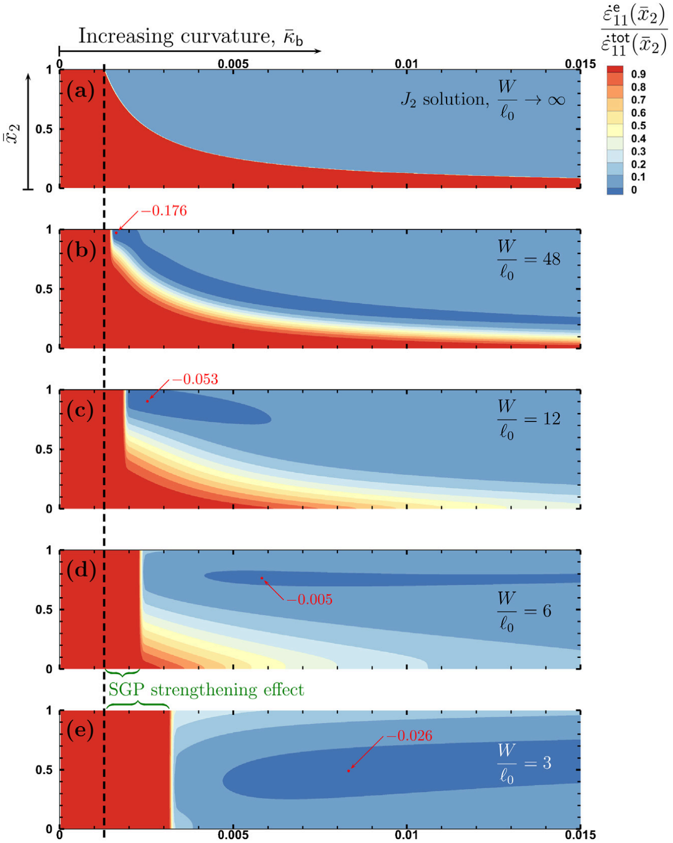

Fig. 2. Proportion of elastic straining, from neutral axis to free edge (vertically) over the load history (horizontally). Position and value of the most intense unloading (i.e. the largest negative magnitude) is indicated by arrow annotations in red. In (a) the local J_2 solution is shown and in (b)–(e) SGP solutions for progressively thinner beams. The dashed vertical line indicates the curvature at which yielding initiates in the local theory. (For interpretation of the references to color in this figure legend, the reader is referred to the Web version of this article.)

versus curvature response for (a), (c) and (e) can be seen in Fig. 3.

4.2. General solution features

The implications of an evolving length scale will here be presented using (27) where the length scale evolves with both effective plastic strain and effective plastic strain gradient. Results will be presented to highlight the effects of beam thickness W/ℓ_0 in combination with the magnitude of the length scale evolution by different values of the parameter C_{II}.

In Fig. 3 the normalized bending moment versus normalized curvature is shown for two different problem sizes that were chosen because they illustrate the combined effect of beam thickness and length evolution. The upper family of curves represents a beam with $W/\ell_0 = 3$ where the evolution of ℓ has obvious effects and the lower family of curves correspond to a thicker beam with $W/\ell_0 = 12$ for which the effects are much less dramatic. For both beam thicknesses, a reference solution is given as a dashed black line that corresponds to the solution with a constant material length scale $\ell = \ell_0$. The dotted black line is the local theory solution when the beam thickness $W/\ell_0 \to \infty$. The length scale evolution is controlled by the parameter $C_{\text{II}}/\ell_0^{-1} = 32,\ 100,\ 316$ and shown for both problem sizes in increasingly deeper shades of blue.

The effect of the length scale evolution is much more pronounced for the thinner beam ($W/\ell_0 = 3$), even for low values of C_{II}, due to the fact that the SGP formulation have a larger influence at thinner beam thicknesses, as can be seen by comparing the two dashed curves to the dotted local theory solution. One effect of an evolving length scale that is evident in all solutions is a reduction in

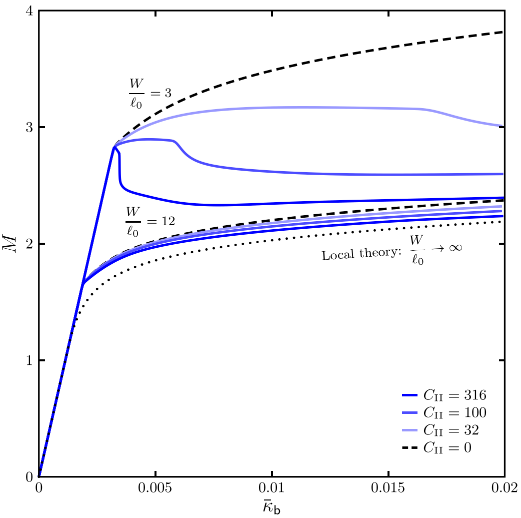

Fig. 3. Normalized bending moment versus normalized curvature. The two curve families represent two different beam thicknesses according to the annotations. Reference solutions for gradient plasticity with a constant length scale are given as dashed black lines and the local (scale invariant) solution is the dotted black line.

hardening which in the case of the thinner beam even leads to a gradual softening. In the thinner beam, a second phenomenon is evident where a sharper drop in load-bearing capacity is seen for all three curves. This feature is most accentuated in the curve with the highest C_{II} where a precipitous drop occurs almost immediately after initial yielding. The accelerated softening is due to the development of localized intense plastic strain gradients bounding a central region with interrupted plastic flow forming a band centered on the neutral axis of the beam. The specific details of which will be discussed in Section 4.2.1 and Section 4.2.2 below. Following the rapid softening the beam enters a deformation stage with more moderate softening that eventually leads to hardening due to a competition between length scale evolution and plastic strain hardening.

4.2.1. Details of solution fields

In this section the details of the plastic strain component $\varepsilon^{\mathrm{p}}_{11}$, Cauchy stress component σ_{11} and length scale ℓ will be presented in different shades of blue for four different values of $C_{\mathrm{II}}/\ell_0^{-1} = 32,\ 100,\ 316,\ 1000$ and where the case $C_{\mathrm{II}}/\ell_0^{-1} = 0$ is included as a reference gradient plasticity solution represented by a dashed black line. All solutions are for a beam with thickness $W/\ell_0 = 6$, i.e. in between the two cases presented above, and $\ell_{\mathrm{sat}}/\ell_0 = 0.05$. The solutions show the state at a normalized curvature $\bar{\kappa}_{\mathrm{b}} = 0.015 = 12\varepsilon_0$.

In Fig. 4 the plastic strain component $\varepsilon^{\mathrm{p}}_{11}$ is plotted through the thickness of the beam. All solutions have zero plastic strain at the neutral axis ($\bar{x}_2 = 0$) and are anti-symmetrical about this point. Three regions of the beam can be identified: (*i*) a central region around the neutral axis of width *d*, (*ii*) an intermediate region and (*iii*) a region close to the free surface. The insert in Fig. 4 illustrates the behavior in region (*i*) where the plastic strain may suffer a discontinuity during loading due to the length scale evolution. Any subsequent increase in loading after this discontinuity has formed will not increase the plastic strain inside the region and it is therefore denoted the region of *interrupted plastic straining*. For $C_{\mathrm{II}}/\ell_0^{-1} = 1000$ and $C_{\mathrm{II}}/\ell_0^{-1} = 316$ this region is already well-developed with an obvious jump in plastic strain. In the case of $C_{\mathrm{II}}/\ell_0^{-1} = 100$, a smaller bump is observable at $\bar{x}_2 = 0.047$ indicating the initial stages of the formation of the interrupted plastic strain region. Formation of this region and its width *d* will be further analyzed in Section 4.4 below.

The outermost region (*iii*) close to the free surface is in all cases influenced by the constraint that the plastic strain gradient must tend to zero as the free surface is approached. The influence of this constraint extends into the beam a distance that is on the order of ℓ in that region. Comparing the extent of this region in the dashed reference case to the curve for $C_{\mathrm{II}}/\ell_0^{-1} = 1000$ one can surmise that the local value of ℓ should be much smaller in the latter case, as will be seen in Fig. 5 below.

The intermediate region (*ii*) outside the central region is characterized by plastic strain distributions that do not differ significantly from each other, independent of the value of C_{II} and are also similar to the reference gradient plasticity solution without a length scale evolution. This region is also characterized by an almost constant plastic strain gradient.

In Fig. 5 the local value of the length scale is presented for the four different values on the evolution parameter. The reference case with a constant $\ell = \ell_0$ is omitted from Fig. 5 as the length scale remains unchanged throughout the loading history, and the dotted line at $\ell/\ell_0 = 0.05$ indicates the saturation length. At the neutral axis the plastic strain is zero so there the reduction in ℓ directly reflects the accumulation of η^{p}. An obvious difference between $C_{\mathrm{II}}/\ell_0^{-1} = 32$ and the three other curves can be seen in that the beam

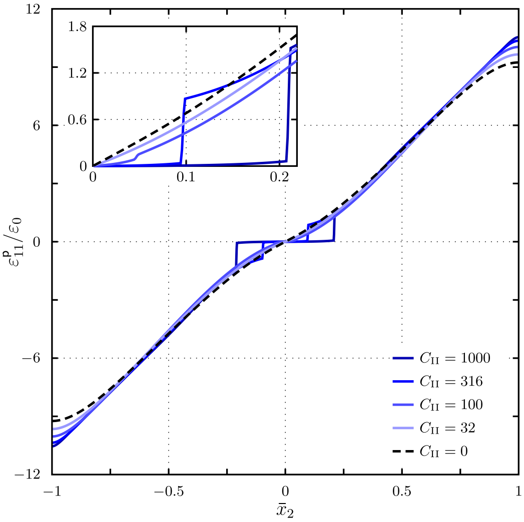

Fig. 4. Plastic strain versus normalized thickness coordinate presented for different values of the evolution parameter C_{II}. Dashed black line represents gradient plasticity reference solution with a constant length scale. Insert illustrates a zoom over the region in which the band of interrupted plastic deformation appears. For all curves $W/\ell_0 = 6$, $\ell_{\mathrm{sat}}/\ell_0 = 0.05$ and $\bar{\kappa}_{\mathrm{b}} = 0.015$.

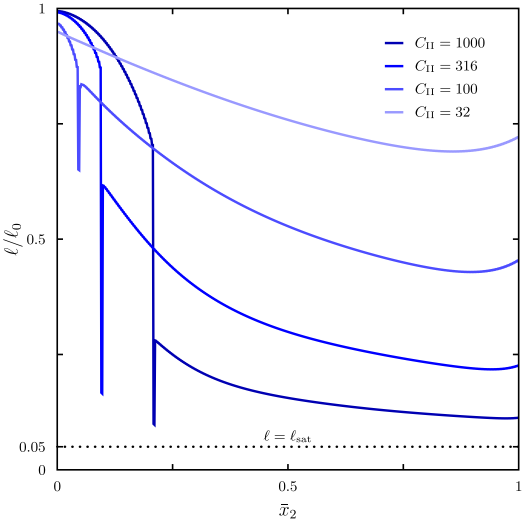

Fig. 5. Constitutive length scale versus normalized thickness coordinate presented for different values of the evolution parameter C_{II}. Dotted black line represents the saturation length scale used in the simulations. Note that only results for half of the beam thickness are presented as the solution is symmetric about $\bar{x}_2 = 0$. For all curves $W/\ell_0 = 6$, $\ell_{\mathrm{sat}}/\ell_0 = 0.05$ and $\bar{\kappa}_{\mathrm{b}} = 0.015$.

with the least evolution has not entered into a state where the band of interrupted plastic straining (*i*) has developed and consequently only region (*ii*) and (*iii*) are present. For the other three cases region (*i*) is characterized by a steep reduction in ℓ that terminates at a precipitous drop only to immediately rise sharply again. The position of this spike corresponds to the boundary between region (*i*) and (*ii*). This sharp drop, and subsequent almost equally sharp rise, in ℓ, is due to the fact that at this boundary,

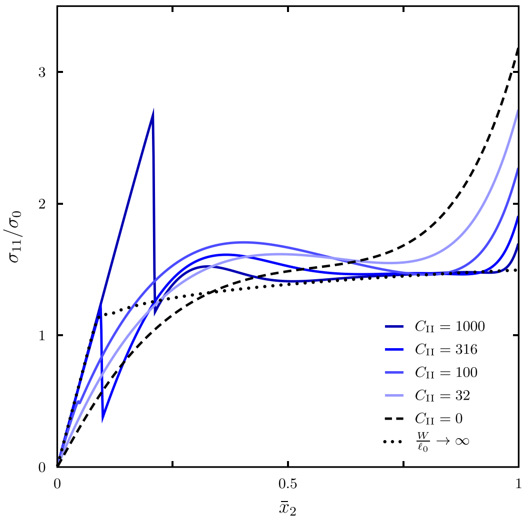

Fig. 6. Cauchy stress versus normalized thickness coordinate presented for different values of the evolution parameter C_{II}. Dashed black line represents gradient plasticity reference solution with a constant length scale. Note that only results for half of the beam thickness are presented as the solution is anti–symmetric about $\bar{x}_2 = 0$. For all curves $\ell_{\mathrm{sat}}/\ell_0 = 0.05$ and $\bar{\kappa}_{\mathrm{b}} = 0.015$. All curves are for $W/\ell_0 = 6$ except the dotted local theory solution.

because of the plastic strain jump, a strong gradient has to develop and that in turn accelerates the length scale evolution.

In all cases region (*ii*) is characterized by decreasing ℓ as $\bar{x}_2$ increases, reflecting the increased plastic strain accumulation further from the neutral axis. The upward bend in region (*iii*) is due to a less severe length evolution there because of the reduction of the plastic strain gradient as the free surface is approached (where it becomes zero). It should be emphasized that region (*iii*) is not a consequence of the length scale evolution but appear due to the gradient plasticity formulation and the boundary conditions. The formation of region (*i*) however is a direct consequence of the proposed length scale evolution extension to gradient plasticity.

The normal stress distribution, σ_{11}, is anti-symmetric about $\bar{x}_2 = 0$, and only half of the solution is presented in Fig. 6. As opposed to the previous plots in this section (Figs. 4 and 5) here the local theory solution ($W/\ell_0 \to \infty$) is included as a dotted line for comparison. The softening effect of the length scale evolution can now be explained by comparing the stress distributions to the bending moment (30) where it is obvious that a greater stress close to the edges of the beam will have a large influence on the moment response. It is, therefore, the stress state in region (*iii*) that dominates the behavior in Fig. 3.

In region (*i*) it can be seen that the stress increases linearly from the neutral axis. This is a consequence of the interrupted plastic straining. Once this region forms and plastic deformation stops, all imposed straining there will necessarily be elastic strain. If the width, *d*, is large the stress in region (*i*) will reach large values due to elasticity, as is apparent in the peak for $C_{\mathrm{II}}/\ell_0^{-1} = 1000$. At the boundary between (*i*) and (*ii*), the stress suffers a discontinuity which is initially mild but will become more conspicuous with increased loading.

The stress states in Fig. 6 illustrates how a phenomenon develops that we have elected to designate a *loss of non-locality*. When the length scale decreases in a significant portion of the beam the solution there will tend towards the local theory solution as the ratio W/ℓ increases locally. The most pronounced indication of this is the relatively flat portion of the curve for $C_{\mathrm{II}}/\ell_0^{-1} = 1000$, in a large part of region (*ii*), where the stress state is almost identical to the local theory solution.

4.2.2. Load history evolution of solution fields

This section details how the solution fields develop with loading as ℓ evolves. In Fig. 7 the proportion of elastic straining (cf. Fig. 2) is shown for the beam with $W/\ell_0 = 6$. For purpose of comparison, results from the solution with constant $\ell = \ell_0$ is shown in Fig. 7(a). Results for a beam with $C_{\mathrm{II}}/\ell_0^{-1} = 32$ is shown in Fig. 7(b). The main difference is that the beam experiences more plastic straining in the upper half of the domain (closer to the free surface) and slightly more elastic straining closer to the neutral axis of the beam. The region of elastic unloading is larger and initiates earlier. Increased plastic straining gives a corresponding decrease of elastic strains and therefore a reduction of the stress. When this happens in the outer parts of the beam the bending moment is affected and is the reason for the reduced moment response in beams with a moderate length evolution (e.g. all the curves for $W/\ell_0 = 12$ and the initial portions of the curves for $W/\ell_0 = 3$ in Fig. 3). In figures (c)-(e) progressively larger values of the evolution parameter are used, as noted by the annotations in the top right corner of each plot. The situation is initially similar to the solution in (b) but the difference from the state in (a) becomes more and more pronounced as C_{II} increases. In (c)-(e) it can be seen how the

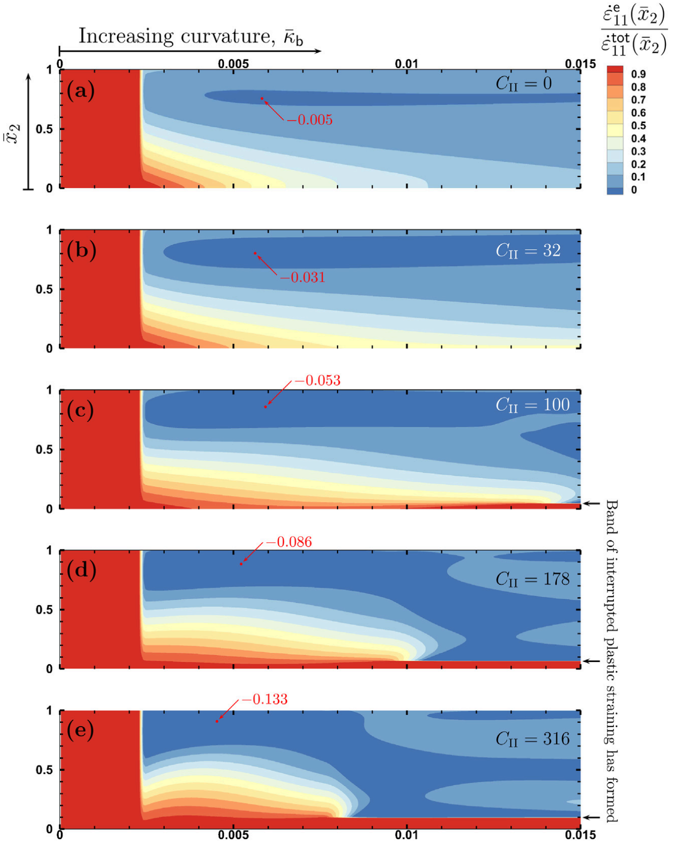

Fig. 7. Proportion of elastic straining, from neutral axis to free edge (vertically) over the load history (horizontally). Position and value of the most intense unloading (i.e. the largest negative magnitude) is indicated by arrow annotations in red. All cases shown are for beams of thickness $W/\ell_0 = 6$. In (a) the “reference” SGP solution with $\ell = \ell_0$ is shown and in (b)–(e) the evolution is progressively more intense, according to the annotations. (For interpretation of the references to color in this figure legend, the reader is referred to the Web version of this article.)

region of interrupted plastic straining forms at load levels of $\bar{\kappa}_b = 0.0138,\ 0.0095,\ 0.0077$ for the cases in (c), (d) and (e), respectively. A consequence of the formation of the band of interrupted plastic straining is that large regions outside of the band will experience elastic unloading, as indicated by the regions of dark blue expanding towards the neutral axis. This unloading is what produces the more pronounced drop in bending moment. After the band formation, some details of the solution are to a limited extent mesh dependent which is further discussed in Section 5.

In Fig. 8 further details of the plastic strain distribution, strain gradient field and the length scale are plotted at six different levels of increasing curvature. To demonstrate the effects of the length scale evolution on a problem where strain gradient effects are pronounced the solution is presented for a beam with thickness $W/\ell_0 = 3$ and with evolution parameter $C_{II}/\ell_0^{-1} = 100$. The results illustrate how the aforementioned fields develop with increasing deformation during the drop in the moment–curvature response shown in Fig. 3 and in detail in Fig. 8(a) below. The most distinct feature to note is the development of a band around the neutral axis where further plastic straining is interrupted as seen in Fig. 8(b), also noted in Section 4.2.1. Formation of this band occurs during the post-peak to drop part of the load history, indicated by the second, third and fourth markers from the left in Fig. 8(a). The band is delineated by a cusp-like peak in the plastic strain gradient, in Fig. 8(c), that emerges as a consequence of a feedback mechanism. The plastic strain distribution, from the neutral layer to the free edge, can be seen to describe a kind of sigmoid shape. This implies that the maximum value of η^p cannot be found at the neutral layer but must be located further out towards the edges of the beam. As the deformation progresses, the plastic strain develops more (relative to the applied strain) further out in the beam, as indicated by e.g. the contour gradients in Fig. 2(e), thereby maintaining and amplifying the shape of the plastic strain distribution. As the gradient

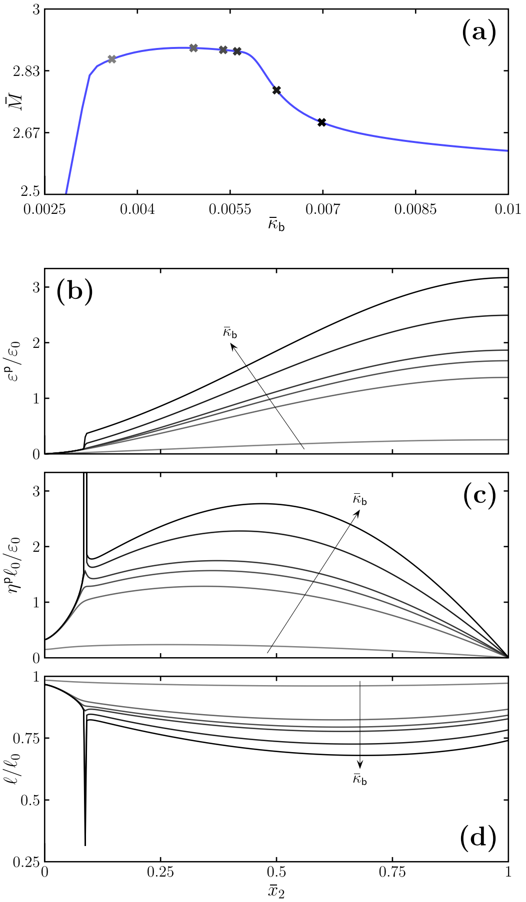

Fig. 8. (a) Detail of moment–curvature load history with markers in different shades of grey corresponding to the load levels in (b)–(d). Effect of load history on (b) effective plastic strain, (c) effective plastic strain gradient and (d) length scale. Note that in (b)–(d) only half of the solution is shown due to symmetry. (For interpretation of the references to color in this figure legend, the reader is referred to the Web version of this article.)

increases, the length scale is reduced which in turn means that it becomes energetically favorable to further increase the gradient instead of accumulating plastic strain to hold back the gradient. This mechanism then further strengthens itself in a feedback loop until it is eventually limited by ℓ approaching ℓ_{sat} and the diminished $\mathrm{d}\ell$ that implies. The same type of behavior is present in the thicker beams as well but there the moving elastic-plastic boundary complicates the analysis.

Another noteworthy feature is that the width of the band, *d*, stays constant once the band has formed and that further plastic strain accumulation occurs solely outside the band. The length scale evolution is illustrated in Fig. 8(d), which in the middle of the beam ($\bar{x}_2 \approx 0$) will be almost purely driven by the development of the plastic strain gradient, while at the edge of the beam the evolution will be purely driven by plastic strain, and in the region between, a combination of the two will contribute to the changes in length scale.

4.3. Different evolution equations

As elaborated on in Section 3, several evolution equations can be constructed on the basis of the coupling between plastic strain, plastic strain gradient, and dislocation densities. In this section, results are presented for the moment–curvature response of a material obeying the length scale evolution presented in (26), (27), (29) and (28). These four equations have the same evolution

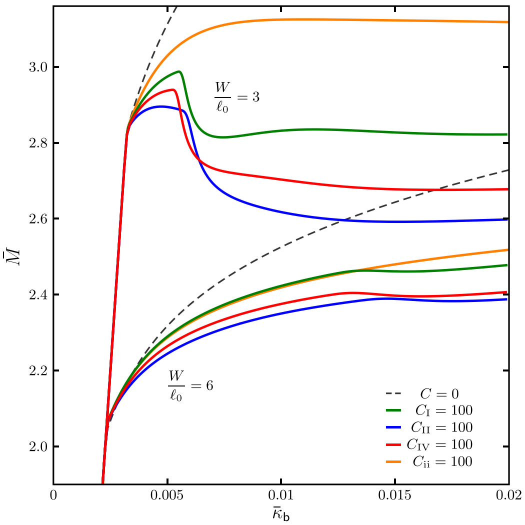

Fig. 9. Effect of length scale evolution equation on moment versus curvature response. Two families of curves representing $W/\ell_0 = 3,\ 6$ are presented for which four different evolution equations have been used. Green represents the GND–approach, blue the incrementally additive approach, red the phenomenological approach and orange the modified version where the length scale evolves only with the increment of plastic strain. The dashed lines corresponds to solutions with $\ell = \ell_0$. (For interpretation of the references to color in this figure legend, the reader is referred to the Web version of this article.)

parameter $C = (2A^2b)^{-1}$, making the solutions comparable in terms of the effect of the length scale evolution.

In Fig. 9 the effect of the choice of evolution equation on the moment–curvature response is presented by two families of curves representing the beam thicknesses $W/\ell_0 = 3$ and $W/\ell_0 = 6$ with the evolution parameter set to $C/\ell_0^{-1} = 100$. The curves are presented with color coding indicating the underlying evolution equation used for that specific solution, where green corresponds to (26), blue to (27), red to (29) and orange to (28). The main characteristics of the moment–curvature response are rather similar for the first three of the proposed models that all include contributions from the plastic strain gradient. When the length evolution is governed only by the accumulation of plastic strain (28) the response is markedly different. The difference is most apparent in the thinner beam, $W/\ell_0 = 3$, where it can be seen that the sharp drop in bending moment does not develop. This is because the band of interrupted plastic straining does not form when the length evolves only with plastic strain. Consequently, the feedback mechanism that leads to the limited localization in η^p is not triggered and large-scale elastic unloading is therefore avoided. All models do however exhibit a reduced moment response compared to the constant length scale SGP solutions (shown in the figure as dashed lines).

Limiting the discussion to the three evolution laws with an explicit gradient dependence, then the GND-approach (green) gives a stiffer response than the other two evolution equations (red and blue). This is due to the imposed boundary conditions at the edge of the beam, where the plastic strain gradient is zero, leading to an unchanged length scale at the edge and thus a preserved non-locality. This, in turn leads, to higher Cauchy stresses, as illustrated by the dashed black line in Fig. 6, thereby increasing the bending moment in comparison to the other models. The length evolution due to the incrementally additive approach (blue) and the phenomenological approach (red) both have a dependence on the plastic strain. They therefore experience a loss of non-locality at the edge of the beam and consequently a weaker response than that of the GND-approach.

The length scale at external load level $\bar{\kappa}_\mathrm{b} = 0.015$ is shown in Fig. 10 with preserved color coding (cf. Fig. 9) but with dashed lines for beams of thickness $W/\ell_0 = 3$ and solid lines for $W/\ell_0 = 6$. One noteworthy feature is that all models except the GND-approach reaches the same value for ℓ at the edge of the beam. This is due to the fact that there the gradient of plastic strain is zero and therefore only the effective plastic strain contributes to the length scale evolution. This is also the reason why the GND-approach does not show any change in length scale at the edge.

Another feature that differs between the solutions is the width of the band of interrupted plastic straining. The band attains the same width when the length scale evolves according to the GND- and the phenomenological approach, as can be seen by the red and green curve overlap in Fig. 10 at the spike-like part of the solution. The solutions for the incrementally additive approach attains a width that is, slightly, larger for both the $W/\ell_0 = 3$ and $W/\ell_0 = 6$ beams. Also, as discussed above, the modified evolution equation (orange) does not produce a spike in the length scale. The absence of the spike is indicating that this type of evolution does not lead to the region of interrupted plastic straining.

Contour plots of the relative elastic straining (in the same fashion as Figs. 2 and 7) are shown in Fig. 11 for a beam with thickness $W/\ell_0 = 6$. Results from all four length scale evolution laws above are presented. Again, the first three evolution laws show similar

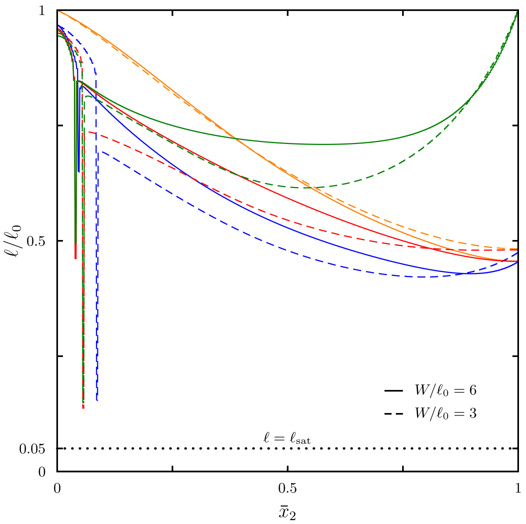

Fig. 10. Effect of choice of length scale evolution equation on the length scale. Two families of curves representing $W/\ell_0 = 3,\ 6$ are presented for which four different evolution equations have been used. Green represents the GND–approach, blue the incrementally additive approach, red the phenomenological approach and orange the modified version where the length scale evolves only with the increment of plastic strain. Note that only results for half of the beam thickness are presented as the solution is symmetric about $\bar{x}_2 = 0$. (For interpretation of the references to color in this figure legend, the reader is referred to the Web version of this article.)

behavior with the formation of the band of interrupted plastic straining and the associated widening of the elastic unloading region. The band forms earlier, at about $\bar{\kappa}_{\mathrm{b}} = 0.0125$, for both the GND model in Fig. 11(a) and the phenomenological approach in Fig. 11(c) than at $\bar{\kappa}_{\mathrm{b}} = 0.0138$ for the incrementally additive in Fig. 11(b). As mentioned earlier the specific details of the field after this event is subject to some mesh sensitivity but the general features are not dependent on the discretization. The unchanged length scale (preserved non-locality) close to the edge of the beam for the GND-approach prevents the elastic unloading to extend all the way to $\bar{x}_2 = 1$ in Fig. 11(a). In Fig. 11(d) the solution for the modified law is shown and the absence of the interrupted plastic straining is the most distinguishing feature as compared to the other three solutions.

4.4. Band of interrupted plastic straining

As have been noted in Section 4.2.1, Section 4.2.2 and Section 4.3 a distinct region centered around the neutral axis may form where plastic straining is interrupted, as opposed to the non-local reference solution where significantly larger plastic strains develop in the same region. The width of this band remains constant once formed and is related to the size of the problem and the evolution parameter C. As discussed above in Section 4.2.2 the band only forms when the evolution equation for ℓ has an explicit dependence on $d\eta^{\mathrm{p}}$. The width is dependent on the plastic strain gradient field as it develops after initial yielding. For thinner beams, this development can be quite different due to interactions with the free boundary, as can be seen by comparing the solution in Fig. 2(d) to Fig. 2(e). In Fig. 12 the effect of the evolution parameter on the width of this band is presented for the evolution equations in (26) and (27).

For the beams with thickness $W/\ell_0 = 6$ and 5, the normalized width of the band, d/W, is increasing with larger values of the evolution parameter C as seen in Fig. 12. However, for the thinner beams $W/\ell_0 = 4$ and 3, the width is increasing at small values of the evolution parameter, reaching a maximum and then decreases with larger values of C as seen in the results for $W/\ell_0 = 3$. For the beam with $W/\ell_0 = 4$, the decrease is not apparent but rather reaches what appears to be a plateau (Fig. 12, Top). The non-monotonic behavior for thinner beams is due to the distribution of plastic strain gradients and their development early in the plastic straining regime of the load history, as discussed above.

5. Discussion and summary of results

Before a discussion about the results, it is important to remember that the presented theory is isotropic. One should therefore not draw too far-reaching and quantitative conclusions regarding the details of the solution fields. Or how they correspond to microstructural features, e.g. dislocation cell formation. If a similar approach would be implemented in a strain gradient crystal plasticity framework (e.g. Gurtin et al. (2007); Gurtin (2008)) the details of the solutions would of course differ. It would then also be possible

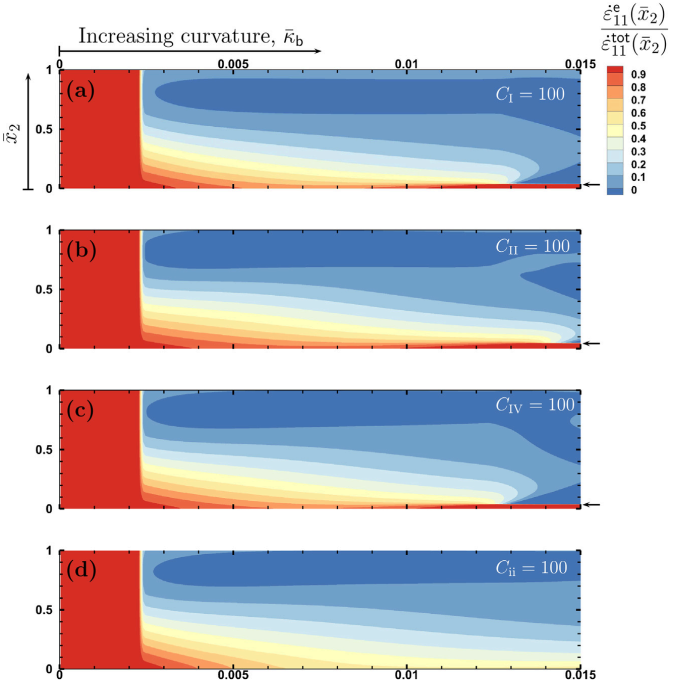

Fig. 11. Proportion of elastic straining, from neutral axis to free edge (vertically) over the load history (horizontally), for the four different evolution equations. All cases shown are for beams of thickness $W/\ell_0 = 6$. (a) shows the GND-approach, (b) the incrementally additive, (c) the phenomenological model and in (d) the modified version where evolution is due only to plastic strain.

to make more direct statements about emergent features in the microstructure. However, there are many similarities in the governing equations and boundary conditions between the isotropic and crystal SGP theories and it is reasonable to expect that the quantitative aspects of the corresponding solution fields would remain.

A short overview of the steps taken to construct the evolution equations is given below and the motivation behind them are then summarized.

1. Equating the length scale in SGP, ℓ, to the length that appears from expressions on the form $\rho^{-1/2}$ leads to a relation between $d\ell$ and $d\rho$
2. Assumptions on how $d\rho$ could be interpreted and what the continuum field proxies should be in the isotropic SGP framework
   a. GND approach where $d\rho = d\rho^G$ and $d\rho^G \propto d\eta^p$
   b. Incrementally additive approach where $d\rho = d\rho^G + d\rho^S$ and $d\rho^S \propto d\varepsilon^p$
   c. Phenomenological approach where $d\rho \propto dE^p$
   d. A modified version of the approach in b where $d\rho \propto d\varepsilon^p$

The assumption behind 2a above is motivated by the experiments in Kysar et al. (2010) and Öztop (2011) where the diameter of dislocation cells was found to be inversely proportional to the square root of the density of GNDs in the cell walls. The SSD density was not measured in those experiments and therefore a conservative approach is to neglect them. On the other hand, by following Holt (1970) and Ashby (1970) the SSD-contribution should not be ignored and are therefore included, leading to approach 2b. On the aggregate level the dislocation density is a measure of plastic deformation (or vice versa) and in isotropic SGP the gradient enhanced effective plastic strain plays this role. Therefore, by remaining agnostic about the mechanisms we propose the connection in 2c. This approach can also be motivated by considering Taylor's hardening equation and comparing it to the proposed hardening relation in SGP where the effective measure enters as the internal variable. A modification of the approach in 2b leads to a general evolution law where contributions from $d\varepsilon^p$ and $d\eta^p$ are weighted differently. From that, if the gradient contribution is ignored, the evolution equation in 2d results.

A general class of effective measures in SGP was suggested in Fleck and Hutchinson (1997) and explored in Evans and Hutchinson

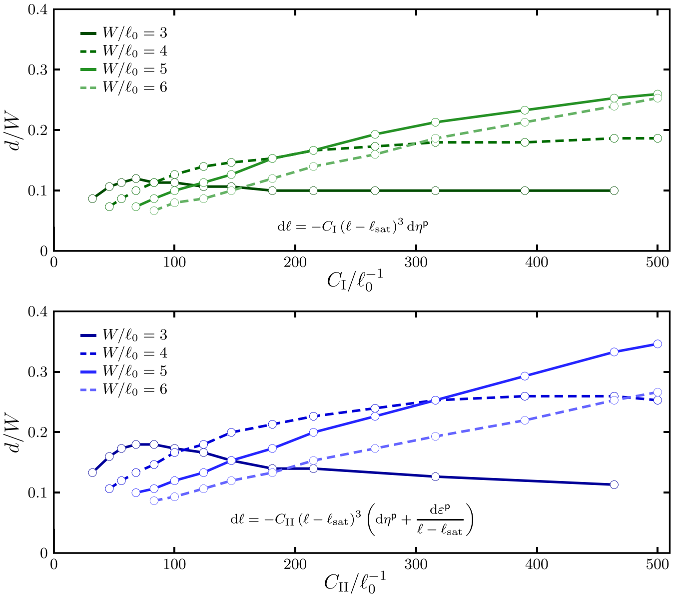

Fig. 12. Width of band of interrupted plastic straining versus evolution parameter C for different beam thicknesses W/ℓ_0. Top: GND-approach. Bottom: incrementally additive approach.

(2009) with further numerical consideration for an incremental and full tensorial case in Dahlberg and Faleskog (2013). Schematically an increment of the gradient enhanced effective strain can be written

$$\mathrm{d}E^{\mathrm{p}} = [(\mathrm{d}\varepsilon^{\mathrm{p}})^{\mu} + (\ell\mathrm{d}\eta^{\mathrm{p}})^{\mu}]^{1/\mu}. \tag{31}$$

If the parameter $\mu = 2$ then the present formulation in Section 2 is retained. It has been suggested (e.g. Fleck and Hutchinson (1997) and Evans and Hutchinson (2009)) that $\mu = 1$ is a more physically reasonable choice based on dislocation arguments. In connection with the evolution laws presented here, it can be noted that if $\mu = 1$ then (20) and (24) would coincide. There is not enough experimental data to point to or rule out, any of the proposed models based on the analysis performed here. Since the evolution equations presented in Section 3.3 are derived on a purely phenomenological basis it can be argued that they should be considered the least physically reasonable. Some relations between the proposed models and experimental observations will be covered in Section 5.1 and Section 5.2 below.

While connecting the increments $\mathrm{d}\varepsilon^{\mathrm{p}}$ and $\mathrm{d}\eta^{\mathrm{p}}$ to the accumulation of lengths of dislocation lines per unit volume, i.e. the dislocation density, a number of details and mechanisms have been neglected. As already noted in Section 3.2 we completely disregard dynamic recovery to get to an expression where $\mathrm{d}\rho^{\mathrm{S}} \propto \mathrm{d}\varepsilon^{\mathrm{p}}$. Since both $\mathrm{d}\varepsilon^{\mathrm{p}} \geq 0$ and $\mathrm{d}\eta^{\mathrm{p}} \geq 0$ the proposed evolution laws will always give $\mathrm{d}\ell \leq 0$. As it is known that dislocations may annihilate and thereby locally reduce the dislocation density it can be concluded that the proposed models also neglect annihilation. To include this would, at the least, require the introduction of effective increments that can be negative. A suggestion would be to allow the gradient increment to become negative if the plastic strain state tends to become more homogeneous. Here we have only considered monotonic loads so this should not influence our results.

In Section 4 the length scale evolution leads to a reduction in hardening as well as a gradual softening, and in the more extreme cases to a precipitous yield point drop. The latter two of these cases can be achieved by a strong evolution (high values of C) combined with a problem where pronounced gradients prevail, i.e. small beam thicknesses. In the solutions presented here, the larger values of C have mainly been used to demonstrate how this affects the solution in terms of the strain fields and the resulting global response. Making contact with experiments, one will notice that most experimentally motivated values of C/ℓ_0^{-1} are less than 100 (experimental measurements of A are discussed in Section 1 and values of C are given in Section 3.1), i.e. smaller than the largest value studied in this paper of $C/\ell_0^{-1} = 1000$. Here we have tacitly assumed that ℓ_0 should be on the order of about 1 μm. In the preceding analysis, we used ℓ_0 as the unit length with which all other lengths are compared (attaching no explicit length measure to it).

One interesting feature of the proposed length evolution is the band of interrupted plastic straining. This band does not develop in the reference solution (gradient plasticity with constant length scale parameter) or when the evolution of ℓ only depends on the accumulation of plastic strain. The formation of the band is driven by the plastic strain gradient and its development in conjunction with the evolving length scale. Invoking the assumption used in Section 3.1 relating η^{p} to ρ^{G} the development of a sharp peak in plastic strain gradients corresponds to a pile-up of GND around the neutral axis, in tentative agreement with experimental observations.

A reduction in ℓ in a region means that within that region the governing equations will become less non-local. The solution will tend towards a behavior that is more akin to the local theory solution, hence the terminology *loss of non-locality*. The effective measure of plastic deformation that enters into the hardening law, E^{p}, will be more controlled by the plastic strain, and less so by the gradients of plastic strain. This implies that, as noted by Ashby (1970), a population of ρ^{G} should accelerate the accumulation of ρ^{S} and thereby leading to a larger proportion of the hardening being due to ρ^{S} at later stages of deformation.

For the largest values on C, the Cauchy stresses inside the band of interrupted plastic straining, will become very large, as seen in Fig. 6. This is due to the displacement control to enforce an Euler-Bernoulli beam subjected to pure bending. Prescribing a linearly varying displacement imposes a linearly varying total strain distribution. This results in large Cauchy stresses due to elasticity when the plastic straining is interrupted inside the band. For the most intense cases of length scale evolution the stress state will reach unreasonably large values. This again indicates that the largest values of C investigated here are probably nonphysical and should only be used with caution.

A systematic, but minor, mesh convergence study has been performed but not reported on here. The results indicate that there is a mesh sensitivity in the precipitous drop behavior where more elements (i.e. smaller) lead to a more distinct drop. With reference to the contour plots in Figs. 7 and 11, the mesh dependence will affect the details of how rapidly the region of elastic unloading widens after the band has formed. However, the mesh sensitivity is contained to this rapid softening region (cf. classical softening FEM-solutions, Zienkiewicz and Taylor (1991)) and as the solution progresses, and work hardening resumes, all levels of discretizations converge. The introduction of a nonzero saturation length scale limits the evolution of the length scale and stabilizes the feedback mechanism responsible for the rapid work softening. The width of the band of interrupted plastic straining, d, is unaffected by the discretization, except for very coarse meshes. The number of elements used in Section 4 was judged to be sufficiently good to avoid most discretization errors.

5.1. *Connection to small-scale bending experiments*

All the data points in Stölken and Evans (1998) are collected at bending strains of 2.44%, or larger, and therefore even the first data point is beyond the range explored in this paper. As noted by Moreau et al. (2005) and Ehrler et al. (2008) it is notoriously hard to get good data around the yield point for small test specimens but they have managed to develop the experimental setup to alleviate this problem. The constant curvature bending experiments on Ni foils reported therein all track the behavior close to the yield point. There is no indication of a pronounced drop in bending moment in any of the tests, ranging from 10 μm to 125 μm in foil thickness. It can be concluded that the larger values of the evolution parameter C (i.e. those that lead to a large drop in bending moment) are probably not physically reasonable in the context of annealed and comparatively soft metals.

The reduction in strain hardening due to a modest length scale evolution could however still be compatible with experimental data. When SGP-theories are fitted to data from thicker beams they tend to over-predict the stress-strain response of the thinner beams and the reduced hardening predicted with the proposed models would alleviate this to some extent. The problem of an unreasonably high predicted yield point would still persist, however.

In micro-cantilever beam experiments performed by Kapp et al. (2015) it was observed that for a single crystal cantilever most of the slip steps would terminate close to the neutral axis. This is consistent with a pile-up of GND around the neutral axis as discussed in Motz et al. (2008). Some of the more unconventional numerical results presented in this paper are not inconsistent with these experimental findings. First, the region of interrupted plastic straining is similar to the region in which slip traces disappear (or are severely reduced). Secondly, a pile-up of GND corresponds to the peak in plastic strain gradients that develops at the boundary between region (*i*) and (*ii*), which also corresponds to the spike in the length scale.

5.2. *Work softening and band formation in irradiated metals*

Drastic work softening has been observed in many metals and has been linked to various causes. For aluminum tensile specimens Cottrell and Stokes (1955) reported a sharp yield point drop after pre-straining at a low temperature and resumed straining at a higher temperature. In Luft (1991) a similar work softening or yield point drop effect is present in precipitation hardened molybdenum and quenched or neutron irradiated metals (both BCC and FCC). A higher radiation dose translates to an increased initial yield stress coupled with a more pronounced initial drop in stress right after the yield point and a reduced ductility, as shown in Farrell et al. (2004). It should be emphasized that these experiments are all in uniaxial tension but the qualitative behavior of a pronounced, or even sharp, yield point drop and reduced hardening are in tentative agreement with the numerical results presented here. For moderate to high irradiation doses in Zircaloy-4 and 316 stainless steel there is an initial portion of the stress-strain curve after yielding where the material work softens and then changes to work hardening.

The mechanism behind work softening in irradiated reactor structural alloys is linked to dislocation channel deformation where plastic deformation will concentrate into distinct bands in the microstructure. Inside these bands, also called clear channels, the irradiation-induced obstacles to dislocation motion have been cleared away by previous dislocation motion. They present much less resistance to dislocation motion than the surrounding material and plastic deformation tends to localize there.

In Dahlberg and Faleskog (2014) models of columnar grain structures were investigated using SGP. While the focus was on grain boundary models and the effect of size distributions a banded plastic strain field appeared for some combinations of grain structure and loading. The bands were diffuse, i.e. gradients were small, and the magnitude of plastic strain inside the bands was not much larger than outside. An additional motivation, besides the arguments put forward in Section 3, for pursuing the model development presented here is that with a length scale that decreases with plastic deformation, the gradients are allowed to become larger locally. Such a model could then predict more distinct plastic strain features similar to those found in irradiated metals.

6. Conclusions and final remarks

Equating the microstructural length scale in (1) to the constitutive length scale, ℓ, in SGP gives a monotonically decreasing ℓ with increased plastic deformation. This makes sense from a microstructural perspective as the dislocation mean free path, and related quantities, should decrease as the dislocation density increases. However, in phenomenological SGP the size-effects are proportional to $(\ell/D)^{\alpha}$ where D is some relevant spatial dimension of the domain and $\alpha > 0$. This implies that size-effects (e.g. strengthening) are reduced if the constitutive length scale decreases with accumulation of plastic strain. This effect can then be interpreted as a reduced, or even negative, work hardening. If ℓ is viewed on a purely phenomenological basis then it could be argued that, based on some of the available experimental evidence, it would make more sense if it increased instead of decreased, as already explored by Abu Al-Rub and Voyiadjis (2006) and Evans and Hutchinson (2009). In this study a single length scale theory have been used and consequently there is no room to include aspects of both the microstructural and the phenomenological interpretation of ℓ.

We have presented several suggestions on incremental evolution laws for the constitutive length scale, ℓ, in the SGP theory by Gudmundson (2004). The implications of these evolution laws have been explored numerically by solving the plane strain pure bending boundary value problem. For the macroscopic moment–curvature response there are two distinct effects. At first, the moment response is reduced as compared to an SGP reference solution without any length evolution. This behavior can very well be consistent with experimental data on thin beams and may even help to better reconcile theoretical predictions with experimental observations. A second and much more dramatic effect, where the moment will drop rapidly over a small increase in curvature may appear for thin beams and/or a strong length evolution. By comparison to the available experimental results, the conclusion is that for well-annealed metals this behavior is likely not compatible with observations. A rapid work softening phenomena, sometimes called a “yield point drop”, is often observed in quenched, precipitation hardened and neutron irradiated metals. For such material systems, a strong length scale evolution is a viable candidate to model, or at least (in a phenomenological sense) capture, the plastic deformation modes that are believed to give rise to this behavior.

Regarding the details of solution fields, the most conspicuous effect is the band, straddling the neutral axis, where plastic strain stops accumulating. This event is associated with the distinct drop in bending moment and the absence of one implies the absence of the other. Localized and banded structures are well known to appear in conjunction with plastic deformation but it is usually a reversed situation. Meaning that it is usually inside these bands that plastic deformation is accelerated, not depleted. The boundary conditions of the present problem may preclude a fully relevant solution once this band has formed. It is however concluded that the present formulation allows for a localization of plastic strain gradients, which can be interpreted as a pile-up of GND. It is shown that the proposed extension to SGP has the ability to predict patterning in the plastic strain field. This type of model could, therefore, be a precursor to models that aim to predict dislocation density cell formation.

A different approach by El-Naaman et al. (2016) where the back-stress in a non-work conjugate gradient crystal plasticity formulation was modified to investigate dislocation density patterning showed results reminiscent of dislocation cell formation. However, as pointed out by the authors, the results are strongly dependent on the size of the problem compared to the constant material length scale. A possibly very interesting approach would be to combine elements of their model with a low to moderate length scale evolution that would then be triggered and accentuated by the patterns emerging due to the back-stress modification but leave most of the beam almost unaffected by the length scale evolution. Another gradient crystal plasticity analysis of beam bending can be found in Öztop et al. (2013) where the ρ^{G} distribution shows a cusp at the neutral axis of the beam, in tentative agreement with the results presented here. To trigger fluctuations in the ρ^{G} -field a random variation of the saturation density was introduced whereas in the present paper all material parameters are the same everywhere in the domain.

Acknowledgements

C.F.O. Dahlberg gratefully acknowledges financial support from Vetenskapsrådet (VR E0566901) and the VINN Excellence Center Hero-m funded by Vinnova. M. Boåsen gratefully acknowledges financial support from The Swedish Radiation Safety Authority (SSM).

Appendix. Length scale update and consistent tangent stiffness

The procedure to update the length scale during increment $n \to n+1$ will here be demonstrated in relation to the specific evolution law (21),

$$\mathrm{d}\ell = -C\ell^{3}\left(\theta^{\mathrm{G}}\mathrm{d}\eta^{\mathrm{p}} + \theta^{\mathrm{S}}\frac{\mathrm{d}\varepsilon^{\mathrm{p}}}{\ell}\right). \tag{32}$$

Given (effective) increments in plastic strain $\Delta\varepsilon^{\mathrm{p}}$ and its gradient $\Delta\eta^{\mathrm{p}}$ the goal is to find the increment $\Delta\ell$ that satisfies the function

$$F(\Delta\ell) = \Delta\ell + C(\ell_n + \Delta\ell)^3\left(\theta^{\mathrm{G}}\Delta\eta^{\mathrm{p}} + \theta^{\mathrm{S}}\frac{\Delta\varepsilon^{\mathrm{p}}}{\ell_n + \Delta\ell}\right) = 0, \tag{33}$$

where ℓ_n is the length scale from the previously converged increment. The solution to $F = 0$ can be found by Newton's method or some other nonlinear equation solver. A restriction should be imposed such that $\ell_n + \Delta\ell > 0$. However in the current implementation, this restriction is handled by the introduction of the saturation length scale ℓ_{sat} and the fact that relatively small load increments are taken. The algorithm for finding $\Delta\ell$ for the other proposed evolution laws follow exactly the same procedure as outlined above.

Following the work and notation in Dahlberg and Faleskog (2013), the algorithmic tangent stiffness can be written as

$$\mathbb{D}_{\Omega} = \begin{bmatrix} \mathbb{D}_{\mathrm{e}} & \mathbb{O} \\ \mathbb{O} & \mathbb{D}_{\mathrm{p}} \end{bmatrix}, \tag{34}$$

where the sub-matrix $\mathbb{D}_{\mathrm{e}}$ is given directly from standard linear elasticity. The plastic stiffness matrix can be constructed by the following operation

$$\mathbb{D}_{\mathrm{p}} = \begin{bmatrix} \mathbb{Q}^{\alpha\alpha} & \mathbb{Q}^{\alpha\beta} \\ \mathbb{Q}^{\beta\alpha} & \mathbb{Q}^{\beta\beta} \end{bmatrix}^{-1} \begin{bmatrix} \mathbb{P}^{\alpha a} & \mathbb{P}^{\alpha b} \\ \mathbb{P}^{\beta a} & \mathbb{P}^{\beta b} \end{bmatrix}. \tag{35}$$

The matrices $\mathbb{Q}^{IJ}$ and $\mathbb{P}^{IJ}$ results from the linearization of the equilibrium equations and the constitutive description and are consistent with the update procedure for the stresses. The introduction of evolution laws for the length scale will only result in contributions to the $\mathbb{P}^{IJ}$ -matrices and only in an additive fashion as

$$\begin{aligned}
\mathbb{P}^{\alpha a} &\rightarrow \mathbb{P}_L^{\alpha a} = \mathbb{P}^{\alpha a} + \mathbb{L}^{11} \\
\mathbb{P}^{\alpha b} &\rightarrow \mathbb{P}_L^{\alpha b} = \mathbb{P}^{\alpha b} + \mathbb{L}^{12} \\
\mathbb{P}^{\beta a} &\rightarrow \mathbb{P}_L^{\beta a} = \mathbb{P}^{\beta a} + \mathbb{L}^{21} \\
\mathbb{P}^{\beta b} &\rightarrow \mathbb{P}_L^{\beta b} = \mathbb{P}^{\beta b} + \mathbb{L}^{22}.
\end{aligned} \tag{36}$$

The new matrices $\mathbb{P}_L^{IJ}$ only differ from previous results in Dahlberg and Faleskog (2013) by the addition of the $\mathbb{L}^{IJ}$ -matrices. Due to this, only the contributions from the length scale update to the tangent will be presented here.

In the following, several tensors, denoted in bold face, will be used to construct the $\mathbb{L}^{IJ}$ -matrices. In component notation they are written as

$$\begin{aligned}
\alpha_{ij} &= \frac{3}{2}\frac{q_{ij}}{\Sigma}, & \beta_{ijk} &= \frac{3}{2\ell}\frac{m_{ijk}}{\Sigma} \\
a_{ij} &= \frac{2}{3}\frac{\Delta\varepsilon_{ij}^{p}}{\Delta E^{p}}, & b_{ijk} &= \frac{2\ell}{3}\frac{\Delta\eta_{ijk}^{p}}{\Delta E^{p}} \\
E_{ij} &= \frac{2}{3}\frac{\Delta\varepsilon_{ij}^{p}}{\Delta\varepsilon^{p}}, & N_{ijk} &= \frac{2}{3}\frac{\Delta\eta_{ij}^{p}}{\Delta\eta^{p}}.
\end{aligned} \tag{37}$$

GND-approach

$$\begin{aligned}
\mathbb{L}^{11} &= \mathbb{O} \\
\mathbb{L}^{12} &= \pounds\left(\frac{\partial\Phi}{\partial\Sigma}\frac{\mathrm{d}\sigma_{\mathrm{f}}}{\mathrm{d}E^{\mathrm{p}}}\frac{\Sigma}{\sigma_{\mathrm{f}}}\boldsymbol{b}\colon \boldsymbol{\Delta\eta} + \frac{1}{\ell^2}\left(\frac{\partial\Phi}{\partial\Sigma} - \frac{\Phi}{\Sigma}\right)\boldsymbol{\beta}\colon \boldsymbol{m}\right)\boldsymbol{\alpha}\boldsymbol{N}^{\mathrm{T}} \\
\mathbb{L}^{21} &= \mathbb{O} \\
\mathbb{L}^{22} &= \pounds\left(\frac{\partial\Phi}{\partial\Sigma}\frac{\mathrm{d}\sigma_{\mathrm{f}}}{\mathrm{d}E^{\mathrm{p}}}\frac{\Sigma}{\ell\sigma_{\mathrm{f}}}\boldsymbol{b}\colon \boldsymbol{\Delta\eta} + \frac{\Phi}{\ell^2}\left(2 - \frac{\boldsymbol{\beta} : \boldsymbol{m}}{\ell\Sigma}\right)\right)\boldsymbol{\beta}\boldsymbol{N}^{\mathrm{T}},
\end{aligned} \tag{38}$$

where $\mathbb{O}$ is the zero matrix of appropriate dimension and

$$\pounds = \frac{-C\ell^3\,\Delta t\dot{\varepsilon}_0}{1 + 3C\ell^2\Delta\eta^{\mathrm{p}}}. \tag{39}$$

Incrementally additive approach

$$\begin{aligned}
\mathbb{L}^{11} &= \pounds\theta^{\mathrm{S}}\left(\frac{\partial\Phi}{\partial\Sigma}\frac{\mathrm{d}\sigma_{\mathrm{f}}}{\mathrm{d}E^{\mathrm{p}}}\frac{\Sigma}{\sigma_{\mathrm{f}}}\boldsymbol{b}\colon \boldsymbol{\Delta\eta} + \frac{1}{\ell^2}\left(\frac{\partial\Phi}{\partial\Sigma} - \frac{\Phi}{\Sigma}\right)\boldsymbol{\beta}\colon \boldsymbol{m}\right)\boldsymbol{\alpha}\boldsymbol{E}^{\mathrm{T}} \\
\mathbb{L}^{12} &= \pounds\theta^{\mathrm{G}}\left(\frac{\partial\Phi}{\partial\Sigma}\frac{\mathrm{d}\sigma_{\mathrm{f}}}{\mathrm{d}E^{\mathrm{p}}}\frac{\ell\Sigma}{\sigma_{\mathrm{f}}}\boldsymbol{b}\colon \boldsymbol{\Delta\eta} + \frac{1}{\ell}\left(\frac{\partial\Phi}{\partial\Sigma} - \frac{\Phi}{\Sigma}\right)\boldsymbol{\beta}\colon \boldsymbol{m}\right)\boldsymbol{\alpha}\boldsymbol{N}^{\mathrm{T}} \\
\mathbb{L}^{21} &= \pounds\theta^{\mathrm{S}}\left(\frac{\partial\Phi}{\partial\Sigma}\frac{\mathrm{d}\sigma_{\mathrm{f}}}{\mathrm{d}E^{\mathrm{p}}}\frac{\Sigma}{\ell\sigma_{\mathrm{f}}}\boldsymbol{b}\colon \boldsymbol{\Delta\eta} + \frac{1}{\ell^3}\left(\frac{\partial\Phi}{\partial\Sigma} - \frac{\Phi}{\Sigma}\right)\boldsymbol{\beta}\colon \boldsymbol{m} + \frac{2\Phi}{\ell^2}\right)\boldsymbol{\beta}\boldsymbol{E}^{\mathrm{T}} \\
\mathbb{L}^{22} &= \pounds\theta^{\mathrm{G}}\left(\frac{\partial\Phi}{\partial\Sigma}\frac{\mathrm{d}\sigma_{\mathrm{f}}}{\mathrm{d}E^{\mathrm{p}}}\frac{\Sigma}{\sigma_{\mathrm{f}}}\boldsymbol{b}\colon \boldsymbol{\Delta\eta} + \frac{1}{\ell^2}\left(\frac{\partial\Phi}{\partial\Sigma} - \frac{\Phi}{\Sigma}\right)\boldsymbol{\beta}\colon \boldsymbol{m} + \frac{2\Phi}{\ell}\right)\boldsymbol{\beta}\boldsymbol{N}^{\mathrm{T}},
\end{aligned} \tag{40}$$

where

$$£ = \frac{-C\ell^2\ \Delta t\dot{\varepsilon}_0}{1 + 3\theta^{\mathrm{S}}C\ell^2\Delta\eta^{\mathrm{p}} + 2\theta^{\mathrm{G}}C\ell\Delta\varepsilon^{\mathrm{p}}}. \tag{41}$$

Phenomenological approach

$$\begin{aligned}
\mathbb{L}^{11} &= £\left(\frac{\partial\Phi}{\partial\Sigma}\frac{\mathrm{d}\sigma_{\mathrm{f}}}{\mathrm{d}E^{\mathrm{p}}}\frac{\Sigma}{\sigma_{\mathrm{f}}}\boldsymbol{b}\colon \boldsymbol{\Delta\eta} + \frac{1}{\ell^2}\left(\frac{\partial\Phi}{\partial\Sigma} - \frac{\Phi}{\Sigma}\right)\boldsymbol{\beta}\colon \boldsymbol{m}\right)\boldsymbol{\alpha}\boldsymbol{a}^{\mathrm{T}}\\
\mathbb{L}^{12} &= £\left(\frac{1}{\ell}\left(\frac{\partial\Phi}{\partial\Sigma} - \frac{\Phi}{\Sigma}\right)\boldsymbol{\beta}\colon \boldsymbol{m}\right)\boldsymbol{\alpha}\boldsymbol{\beta}^{\mathrm{T}}\\
\mathbb{L}^{21} &= £\left(\frac{\partial\Phi}{\partial\Sigma}\frac{\mathrm{d}\sigma_{\mathrm{f}}}{\mathrm{d}E^{\mathrm{p}}}\frac{\Sigma}{\ell\sigma_{\mathrm{f}}}\boldsymbol{b}\colon \boldsymbol{\Delta\eta} + \frac{1}{\ell^3}\left(\frac{\partial\Phi}{\partial\Sigma} - \frac{\Phi}{\Sigma}\right)\boldsymbol{\beta}\colon \boldsymbol{m} + \frac{2\Phi}{\ell^2}\right)\boldsymbol{\beta}\boldsymbol{\alpha}^{\mathrm{T}}\\
\mathbb{L}^{22} &= £\left(\frac{\partial\Phi}{\partial\Sigma}\frac{\mathrm{d}\sigma_{\mathrm{f}}}{\mathrm{d}E^{\mathrm{p}}}\frac{\Sigma}{\sigma_{\mathrm{f}}}\boldsymbol{b}\colon \boldsymbol{\Delta\eta} + \frac{1}{\ell^2}\left(\frac{\partial\Phi}{\partial\Sigma} - \frac{\Phi}{\Sigma}\right)\boldsymbol{\beta}\colon \boldsymbol{m} + \frac{2\Phi}{\ell}\right)\boldsymbol{\beta}\boldsymbol{b}^{\mathrm{T}},
\end{aligned} \tag{42}$$

where

$$£ = \frac{-C\ell^r\ \Delta t\dot{\varepsilon}_0}{1 + rC\ell^{r-1}\Delta E^{\mathrm{p}} + C\ell^r\boldsymbol{b}\colon \boldsymbol{\Delta\eta}}, \tag{43}$$

with $r = 1,\ 2,\ 3$ according to which evolution law, of the three proposed, that is used.

References

Abu Al-Rub, R.K., Voyiadjis, G.Z., 2006. A physically based gradient plasticity theory. Int. J. Plast. 22, 654–684.

Ashby, M.F., 1970. Deformation of plastically non-homogeneous materials. Phil. Mag. 21, 399–424.

Castelluccio, G.M., McDowell, D.L., 2017. Mesoscale cyclic crystal plasticity with dislocation substructures. Int. J. Plast. 98, 1–26.

Cottrell, A.H., Stokes, R.J., 1955. Effects of temperature on the plastic properties of aluminium crystals. Proc. R. Soc. A 233, 17–34.

Dahlberg, C.F.O., Faleskog, J., 2013. An improved strain gradient plasticity formulation with energetic interfaces: theory and a fully implicit finite element formulation. Comput. Mech. 51, 641–659.

Dahlberg, C.F.O., Faleskog, J., 2014. Strain gradient plasticity analysis of the influence of grain size and distribution on the yield strength in polycrystals. Eur. J. Mech. Solid. 44, 1–16.

Dahlberg, C.F.O., Faleskog, J., Niordson, C.F., Legarth, B.N., 2013. A deformation mechanism map for polycrystals modeled using strain gradient plasticity and interfaces that slide and separate. Int. J. Plast. 54, 81–95.

Dahlberg, C.F.O., Saito, Y., Öztop, M., Kysar, J.W., 2014. Geometrically necessary dislocation density measurements associated with different angles of indentations. Int. J. Plast. 54, 81–95.

Dahlberg, C.F.O., Saito, Y., Öztop, M.S., Kysar, J.W., 2017. Geometrically necessary dislocations density measurements at a grain boundary due to wedge indentation into an aluminum bicrystal. J. Mech. Phys. Solid. 105, 131–149.

Demir, E., Raabe, D., Roters, F., 2010. The mechanical size effect as a mean-field breakdown phenomenon: example of microscale single crystal beam bending. Acta Mater. 58, 1876–1886.

Devincre, B., Hoc, T., Kubin, L., 2008. Dislocation mean free paths and strain hardening of crystals. Science 320, 1745–1748.

Dunstan, D.J., Bushby, A.J., 2013. The scaling exponent in the size effect of small scale plastic deformation. Int. J. Plast. 40, 152–162.

Dunstan, D.J., Bushby, A.J., 2014. Grain size dependence of the strength of metals: the Hall-Petch effect does not scale as the inverse square root of grain size. Int. J. Plast. 53, 56–65.

Ehrler, B., Hou, X., P'Ng, K.M.Y., Walker, C.J., Bushby, A., Dunstan, D.J., 2008. Grain size and sample size interact to determine strength in a soft metal. Phil. Mag. 88, 3043–3050.

El-Awady, J.A., 2014. Unravelling the physics of size-dependent dislocation-mediated plasticity. Nat. Commun. 6, 1–9.

El-Naaman, S.A., Nielsen, K.L., Niordson, C.F., 2016. On modeling micro-structural evolution using a higher order strain gradient continuum theory. Int. J. Plast. 76, 285–298.

Evans, A.G., Hutchinson, J.W., 2009. A critical assessment of theories of strain gradient plasticity. Acta Mater. 57, 1675–1688.

Farrell, K., Byun, T.S., Hashimoto, N., 2004. Deformation mode maps for tensile deformation of neutron-irradiated structural alloys. J. Nucl. Mater. 335, 471–486.

Fleck, N.A., Hutchinson, J.W., 1997. Strain gradient plasticity. In: In: Hutchinson, J.W., Wu, T.Y. (Eds.), Advances in Applied Mechanics, vol 33. Elsevier, pp. 295–361.

Fleck, N.A., Hutchinson, J.W., 2001. A reformulation of strain gradient plasticity. J. Mech. Phys. Solid. 49, 2245–2271.

Gao, H., Huang, Y., 2003. Geometrically necessary dislocation and size-dependent plasticity. Scripta Mater. 48, 113–118.

Gudmundson, P., 2004. A unified treatment of strain gradient plasticity. J. Mech. Phys. Solid. 52, 1379–1406.

Gurtin, M.E., 2008. A finite-deformation, gradient theory of single-crystal plasticity with free energy dependent on densities of geometrically necessary dislocations. Int. J. Plast. 24, 702–725.

Gurtin, M.E., Anand, L., Lele, S.P., 2007. Gradient single-crystal plasticity with free energy dependent on dislocation densities. J. Mech. Phys. Solid. 55, 1853–1878.

Holt, D.L., 1970. Dislocation cell formation in metals. J. Appl. Phys. 41, 3197–3201.

Idiart, M.I., Deshpande, V.S., Fleck, N.A., Willis, J.R., 2009. Size effects in the bending of thin foils. Int. J. Eng. Sci. 47, 1251–1264.

Jakobsen, B., Poulsen, H.F., Lienert, U., Almer, J., Shastri, S.D., Sorensen, H.O., Gundlach, C., Pantleon, W., 2006. Formation and subdivision of deformation structures during plastic deformation. Science 312, 889–892.

Jiang, J., Britton, T.B., Wilkinson, A.J., 2013. Evolution of dislocation density distributions in copper during tensile deformation. Acta Mater. 61, 7227–7239.

Kapp, M.W., Kirchlechner, C., Pippan, R., Dehm, G., 2015. Importance of dislocation pile-ups on the mechanical properties and the bauschinger effect in microcantilevers. J. Mater. Res. 30, 791–797.

Koneva, N.A., Starenchenko, V.A., Lychagin, D.V., Trishkina, L.I., Popova, N.A., Kozlov, E.V., 2008. Formation of dislocation cell substructure in face-centered cubic metallic solid solutions. Mater. Sci. Eng. 483–484, 179–183.

Kysar, J.W., Saito, Y., Öztop, M.S., Lee, D., Huh, W.T., 2010. Experimental lower bounds on geometrically necessary dislocation density. Int. J. Plast. 26, 1097–1123.

Littlewood, P.D., Britton, T.B., Wilkinson, A.J., 2011. Geometrically necessary dislocations density distributions in Ti–6Al–4V deformed in tension. Acta Mater. 59, 6489–6500.

Liu, D., Dunstan, D.J., 2017. Material length scale of strain gradient plasticity: a physical interpretation. Int. J. Plast. 98, 156–174.

Luft, A., 1991. Microstructural processes of plastic instabilities in strengthened metals. Prog. Mater. Sci. 35, 97–204.
Martínez-Pañeda, E., Niordson, C.F., Bardella, L., 2016. A finite element framework for distortion gradient plasticity with applications to bending of thin foils. Int. J. Solid Struct. 96, 288–299.
Moreau, P., Raulic, M., P'Ng, K.M.Y., Gannaway, G., Anderson, P., Gillin, W.P., Bushby, A.J., Dunstan, D.J., 2005. Measurement of the size effect in the yield strength of nickel foils. Phil. Mag. Lett. 85, 339–343.
Motz, C., Weygand, D., Senger, J., Gumbsch, P., 2008. Micro-bending tests: a comparison between three-dimensional discrete dislocation dynamics simulations and experiments. Acta Mater. 56, 1942–1955.
Niordson, C.F., 2008. On higher-order boundary conditions at elasticplastic boundaries in strain-gradient plasticity. Phil. Mag. 88, 3731–3745.
Niordson, C.F., Legarth, B.N., 2010. Strain gradient effects on cyclic plasticity. J. Mech. Phys. Solid. 58, 542–557.
Nix, W.D., Gao, H., 1998. Indentation size effects in crystalline material: a law for strain gradient plasticity. J. Mech. Phys. Solid. 46, 411–425.
Oudriss, A., Feaugas, X., 2016. Length scales and scaling laws for dislocation cells developed during monotonic deformation of (001) nickel single crystal. Int. J. Plast. 78, 187–202.
Öztop, M.S., 2011. Multiscale Experimental Analysis in Plasticity: Linking Dislocation Structures to Continuum Fields. Ph.D. thesis. Columbia University.
Öztop, M.S., Niordson, C.F., Kysar, J.W., 2013. Length-scale effect due to periodic variation of geometrically necessary dislocation densities. Int. J. Plast. 41, 189–201.
Peerlings, R.H.J., 2007. On the role of moving elasticplastic boundaries in strain gradient plasticity. Model. Simulat. Mater. Sci. Eng. 15, 109–120.
Petryk, H., Stupkiewicz, S., 2016a. A minimal gradient-enhancement of the classical continuum theory of crystal plasticity. Part I: the hardening law. Arch. Mech. 68, 459–485.
Petryk, H., Stupkiewicz, S., 2016b. A minimal gradient-enhancement of the classical continuum theory of crystal plasticity. Part II: size effects. Arch. Mech. 68, 487–513.
Stölken, J.S., Evans, A.G., 1998. A microbend test method for measuring the plasticity length scale. Acta Mater. 46, 5109–5115.
Tarleton, E., Balint, D.S., Gong, J., Wilkinson, A.J., 2015. A discrete dislocation plasticity study of the micro-cantilever size effect. Acta Mater. 88, 271–282.
Taylor, G.I., 1934a. The mechanism of plastic deformation of crystals. Part I. Theoretical. Proc. R. Soc. Lond. - Ser. A 145, 362–387.
Taylor, G.I., 1934b. The mechanism of plastic deformation of crystals. Part II. Comparison with observations. Proc. R. Soc. Lond. - Ser. A 145, 388–404.
Voyiadjis, G.Z., Abu Al-Rub, R.K., 2005. Gradient plasticity theory with a variable length scale parameter. Int. J. Solid Struct. 42, 3998–4029.
Wang, M.Y., Voisin, T., McKeown, J.T., Ye, J., Calta, N.P., Li, Z., Zeng, Z., Zhang, Y., Chen, W., Roehling, T.T., Ott, R.T., Santala, M.K., Depond, P.J., Matthews, M.J., Hamza, A.V., Zhu, T., 2018. Additively manufactured hierarchical stainless steels with high strength and ductility. Nat. Mater. 17, 63–71.
Zhou, J., Odqvist, J., Ruban, A., Thuvander, M., Xiong, W., Ågren, J., Olson, G.B., Hedström, P., 2017. Effect of solution treatment on spinodal decomposition during aging of an Fe-46.5 at.% Cr alloy. J. Mater. Sci. 52, 326–335.
Zienkiewicz, O.C., Taylor, R.L., 1991. 4 edition. The Finite Element Method, vol. 2. McGraw-Hill Book Company, pp. 266 (Chapter 7), section 15.

Paper II

Engineering Fracture Mechanics 214 (2019) 590–608

Contents lists available at ScienceDirect

Engineering Fracture Mechanics

journal homepage: www.elsevier.com/locate/engfracmech

A generalized probabilistic model for cleavage fracture with a length scale – Influence of stress state and application to surface cracked experiments

Magnus Boåsen[a,*], Mateusz Stec[b], Pål Efsing[a], Jonas Faleskog[a]

[a] Department of Solid Mechanics, Royal Institute of Technology (KTH), Teknikringen 8D, SE-100 44 Stockholm, Sweden
[b] Swedish Defence Research Agency (FOI), SE-164 90 Stockholm, Sweden

ARTICLE INFO

Keywords:
Cleavage fracture
Brittle fracture
Non-local stress
Weakest link
Semi-elliptic surface crack

ABSTRACT

A probabilistic model for the cumulative probability of failure by cleavage fracture with a material related length scale is further developed in this study. A new generalized effective stress measure is proposed, based on a normal stress decomposition of the stress tensor, capable of describing a state of normal stress in the range from the mean stress to the maximum principal stress. The effective stress measure associated with a material point is evaluated from the stress tensor averaged over the material related length scale. The model is shown to be well capable to predict both the fracture toughness at loss of both in-plane and out-of-plane constraint by model application to two different datasets from the open literature. The model is also shown to be well capable of predicting the probability of failure of discriminating experiments on specimens containing semi-elliptic surface cracks. A comparison where the master curve methodology is used to predict the probability of failure of the experiments is also included.

1. Introduction

A great effort and progress has been made to the advancement of the understanding of failure by cleavage fracture in ferritic steels, its micro mechanisms and the transition into ductile failure with increasing temperature see Pineau et al. [1] and references therin. There are a number of industrial applications driving the effort. An important driver for the development is the nuclear industry where the reactor pressure vessel is the key component to analyze. Experimental characterization of cleavage fracture toughness encompasses several factors that needs to be addressed, among these are: influence of the statistical size effect and the associated scatter, temperature dependence, geometrical or constraint dependence. All these factors depend on the underlying microstrutural properties and possible inhomogeneities of the material in question.

The micro mechanisms related to cleavage fracture have been extensively studied in the literature. The initiation of cleavage fracture can be traced back to the initiation of a single microcrack which grows unstable and propagates into neighboring grains and onward through other barriers in the microstructure [2]. Microcracks are primarily nucleated from brittle second phase particles such as grain boundary carbides, which is a consequence of plastic deformation of the surrounding ferrite composed matrix [3]. The effect of the carbide size distribution on the resulting fracture toughness was studied for ferritic, bainitic, and martensitic microstructures, by Bowen et al. [4,5]. It was found that in all the microstructures, fracture toughness is primarily controlled by the coarsest carbide. In this process the rate-sensitivity of the ferritic microstructure also seems to play an important role as indicated by the numerical

---

[*] Corresponding author.
E-mail address: boasen@kth.se (M. Boåsen).

https://doi.org/10.1016/j.engfracmech.2019.03.041
Received 9 November 2018; Received in revised form 11 February 2019; Accepted 26 March 2019

Nomenclature

A	parameter in master curve methodology
$A*$	partial area of unit sphere
$a,\ c$	crack depth, width
B	thickness of SEN(B) test specimen
B_0	reference crack front length, master curve
c	material parameter in weakest link model
h	random function in weakest link model
E	Young's modulus
$J,\ J_c$	the J-integral, fracture toughness defined by the J-integral
K_I	mode I stress intensity factor
$K_{J\Phi}$	local fracture toughness, master curve
$K_{min},\ K_{0\Phi}$	minimum and local reference fracture toughness, master curve
L	length parameter in weakest link model
$\overline{L}$	lode parameter of non local stress tensor $\bar{\sigma}_{ij}$
m	material hardening exponent
$N_A,\ N_B$	number of experimental data points in estimation of weakest link parameters, subset A and B.
N_e	number of elements in stress integration
N_{CF}	number of elements in crack front integration
n	effective normal stress parameter
P	applied force in experiments
$P_f,\ P_{rank}$	failure probability, ranked failure probability
$R,\ R_A,\ R_B$	error function minimized when estimating weakest link parameters, sub-functions A and B
R_{p02}	0.2% offset yield strength
s	test specimen roller span
T	thickness of surface cracked test specimen
T_0	reference temperature for ferritic steels in the transition region, master curve
$\overline{T}$	stress triaxiality of non local stress tensor $\bar{\sigma}_{ij}$
$u_1,\ u_2,\ u_3$	displacement in the X_1, X_2 and X_3 directions
$V,\ V_0$	volume, reference volume in weakest link model
V_L	integration volume for non-local stress tensor $\bar{\sigma}_{ij}$
W	width of test specimen
X, $\hat{X}$	element centroid coordinates used in stress integration

Greek symbols

$\delta_p,\ \delta_f$	displacement of piston, displacement at clip gauge
ε_0	power law hardening reference strain
ε_e^p	effective plastic strain
η	distribution parameter in weakest link model
ν	Poisson's ratio
ξ	crack front length, crack front coordinate
ρ	stress distribution function
σ_0	power law hardening yield stress
σ_b	maximum nominal bending stress over crack plane
σ_f	power law hardening flow stress
σ_{th}	threshold stress in weakest link model
σ_Y	yield strength, master curve
$\bar{\sigma}$	non-local effective normal stress in weakest link model
$\bar{\sigma}_e$	non-local effective stress
$\bar{\sigma}_I,\ \bar{\sigma}_{II},\ \bar{\sigma}_{III}$	non-local principal stresses, $\bar{\sigma}_I \geqslant \bar{\sigma}_{II} \geqslant \bar{\sigma}_{III}$
$\bar{\sigma}_{ij}$	non-local stress tensor
$\bar{\sigma}_m$	non-local mean stress
$\bar{\sigma}_n$	non-local normal stress
$\varphi,\ \theta$	polar and azimuthal angles

Abbreviations

EBSD	Electron backscatter diffraction
DBTT	Ductile to brittle transition temperature
RKR	Ritchie, Knott, Rice
Temp	Temperature

study by Kroon and Faleskog [6].

A nucleated microcrack that propagates will do so along the {1 0 0}-planes, also called the cleavage planes in ferrite [7]. These cleavage planes can be illustrated as three orthogonal planes along the sides of the commonly depicted BCC-cube. A microcrack that propagates along a cleavage plane through the first grain, must propagate unhindered across the high-angle boundaries within the microstructure before it can develop into a cleavage fracture. As an example, using EBSD-measurements of interupted fracture tests, Lambert-Perlade et al. [8] observed that crack arrest had occured at high-angle bainite packet boundaries. Cleavage planes will significantly differ in orientation across a high-angle boundary. This difference in orientation is commonly quantified by the tilt and twist angles and affects the toughness locally cf. [9,10]. Numerical investigations of microcrack propagation from one grain into another has been carried out by Stec and Faleskog [11,12]. For more in-depth reviews on brittle cleavage fracture in ferritic steels, the reader is referred to the extensive review papers by Pineau [1] and Pineau et al. [7].

In the quest of establishing a reliable method for conducting both quantitative and qualitative integrity assessments of real components, several models has been developed based either on the local field quantities such as stress and strain ahead of a crack front, commonly referred to as local models, or models based on global crack front quantities such as the stress intensity factor K_I and the T-stress. Both types of models can favorably be incorporated into a framework based on probabilistic modelling by assuming a weakest link mechanism for cleavage fracture. Although not being a probabilistic model, a good starting point for modelling of cleavage fracture is the one developed by Ritchie et al. [13]. The underlying assumption in the so called RKR-model is that the stress ahead of the crack front must exceed the critical cleavage stress of the material over a critical distance in order for a cleavage fracture to develop, this clearly illustrates that cleavage fracture is associated with a length scale.

Cleavage fracture of ferritic steels is a failure mode with an inherent randomness. This can be accounted for by use of extreme value statistics, assuming that a weakest link mechanism governs failure by cleavage fracture.

Among the so called local weakest link models, the Beremin model [14] pioneered the field in the 1980s by accounting for the statistical scatter in the critical cleavage stress in ferritic steels. The model is based on an assuption of the probability of propagating a microcrack subjected to the stress field ahead of a deforming crack front. Moreover, the model assumes that the size of the cleavage triggering sites can be described according to a power law distribution. Only the volume deforming plastically ahead of the crack front contributes to the failure probability through the maximum principal stress, assuming the nucleation of active microcracks able to partake in triggering cleavage fracture at the onset of plastic deformation, independent of the level of plastic strain. The main drawbacks of the Beremin model is that it predicts a minimum fracture toughness of zero and as a consequence the exponent generally becomes very high in order to reduce the excessive scatter of fracture toughness that otherwise would result from model predicitons. The original Beremin model is a two-parameter Weibull distribution. Other authors have extended the model to three parameters. One such extension is the one by Gao et al. [15] which includes the incorporation of a threshold stress σ_{th} below which cleavage fracture is assumed to not occur. As the Beremin model is based on the assumption that all microcracks are being nucleated at the onset of plastic deformation (independent of magnitude) and remains then active throughout the entire loading history, the model only considers propagation of microcracks. In the model by Bordet et al. [16,17], the probability of failure requires simultaneous fulfillment of microcrack nucleation and propagation, which are treated as statistically independent events. The probability of nucleated microcracks that also are able to trigger cleavage fracture is taken to be a function of plastic strain.

Recognizing that cleavage fracture develops from microcracks nucleated as a consequence of slip induced cracking of a microstructural entity, e.g. a second phase brittle particle such as a grain boundary carbide, Kroon and Faleskog [18] proposed a weakest link model that accounts for both plastic straining and high stress levels. In their model, it is assumed that sustained growth of a microcrack that eventually triggers a macroscopic failure by cleavage fracture requires a high level of stress over a sufficiently large distance. This since a nucleated microcrack needs to propagate unhindered across several microstructural barriers, such as high angle grain boundaries, before it can become a cleavage crack. This has been handled by the introduction of a non-local scalar stress measure, which is formed over the volume defined by the radius L. As a consequence, their model predicts a macroscopic threshold toughness. The model has been successfully applied to experiments of stationary cracks [19], and experiments where cleavage fracture was preceded by ductile crack growth [20]. The importance of a threshold stress for reliable predictions of the effects of crack tip constraint is illustrated in experimental study by Hohe et al. [21], where several models were scrutinized. In another study by Hohe et al. [22], a cleavage fracture model is developed around a failure curve for micro crack nucleation based on plastic strain and stress triaxiality.

In a study by Williams et al. [23] on fracture toughness of shallow cracks under biaxial loading conditions, different fracture criteria were explored in combination with a three-parameter Weibull model, i.e. different stress measures were used to calculate the Weibull stress. Among the six criteria evaluated, the use of the hydrostatic stress (mean stress) gave the most consistent results when applied to cruciform bending fracture tests. This indicates that a cleavage fracture criterion based on the maximum principal stress is not necessarily always the most appropriate one.

One of the most widely used weakest link models for describing cleavage fracture in ferritic steels is the model commonly referred to as the master curve. This model, proposed by Kim Wallin and co-workers [2,24,25], relies on the self-similar stress fields ahead of a sharp crack governed by the elastic stress intensity factor K_{I}. This results in a 3-parameter Weibull distribution with a constant shape parameter for the cumulative failure probability which emerges as a result from the self-similar elastic crack tip fields. In the master curve methodology, the elastic T-stress quantifies the effect of crack tip constraint through a connection to the reference temperature T_0 and the assumption that the shape of the master curve remains unchanged by loss of constraint. The effect of a positive T-stress was found to be insignificant with respect to the cleavage fracture toughness, whereas negative T-stress appears to affect the master curve in a nearly linear relation with respect to T_0 where the T-stress at the plastic limit load is to be used as explored by Wallin [26].

The purpose of this work is to further develop the probabilistic model for cleavage fracture proposed in [18], in recognition of that there is no unambiguous scalar measure of stress for modelling of cleavage fracture in complex geometries. Therefore, the non-local scalar measure of stress in [18] will be generalized in a consistent manner to represent an effective normal stress acting over a volume containing potential cleavage triggering sites. This is done to account for the propagation of variously oriented nucleated microcracks and associated cleavage planes and the effective loading on these. The predictive capability of the model containing the generalization of the stress state will be tested against two sets of published experiments pertaining to constraint loss in SEN(B)-specimens, and one set of un-published experiments on semi-elliptic surface cracked bending specimens. The latter experiments were originally included in the PhD-thesis of Stec [27], and as these experiments have not yet been published in the open literature they will therefore be carefully described and analyzed. The outline of the paper is as follows: in Section 2 the extended probabilistic model is described. In Section 3 the influence of the generalized effective normal stress is explored using two experimental data sets from the open literature. Section 4 treats the four-point bending experiments of specimens with semi-elliptic surface cracks, and the evaluation and application of the probabilistic model to these.

2. A non-local weakest link model accounting for a generalized normal stress state

As it has been observed from the evaluation of the experiments in [23], it may in some cases be more relevant to use the mean stress rather than the maximum principal stress in the evaluation of cleavage fracture. The model by Kroon and Faleskog [18] can be generalized for this purpose which will be outlined in this section. First a short account of the model will be given.

In [18], the failure probability is defined as

$$P_{\mathrm{f}} = 1 - \exp\left(-\int_V h_{\max}\frac{\mathrm{d}V}{V_0}\right), \tag{1}$$

where $h_{\max}$ is the maximum value of the random function experienced throughout the loading history, V is the volume of the structure, and V_0 is the reference volume. The random function $h = h(\varepsilon_{\mathrm{e}}^{\mathrm{p}}, \bar{\sigma})$ is taken as

$$h(\varepsilon_{\mathrm{e}}^{\mathrm{p}}, \bar{\sigma}) = h_1(\varepsilon_{\mathrm{e}}^{\mathrm{p}})h_2(\bar{\sigma}), \tag{2}$$

where

$$h_1(\varepsilon_{\mathrm{e}}^{\mathrm{p}}) = c\varepsilon_{\mathrm{e}}^{\mathrm{p}}, \tag{3}$$

$$h_2(\bar{\sigma}) = \exp\left(-\left(\frac{\eta\sigma_{\mathrm{th}}}{\bar{\sigma}}\right)^2\right) - \exp(-\eta^2) \text{ for } \bar{\sigma} > \sigma_{\mathrm{th}}. \tag{4}$$

In (3) and (4), $\varepsilon_{\mathrm{e}}^{\mathrm{p}}$ is the effective plastic strain, $\bar{\sigma}$ is a non-local measure of stress, c, σ_{th} and η are material parameters, where the influence of η has been observed to be weak in practical applications. The parameter η is related to the microcrack distribution, and is taken to be unity in all following calculations as suggested in [18]. The first part of the random function relates to the nucleation of microcracks, which is a primarily strain driven process, where the linear dependence on $\varepsilon_{\mathrm{e}}^{\mathrm{p}}$ represents the number of triggering sites present in the material. The second part, depending on $\bar{\sigma}$, relates to the fraction of these triggering sites that will be potential cleavage initiators. Furthermore, it is assumed that the stress level must be high enough over a sufficiently large volume. Hence, $\bar{\sigma}$ represents the average stress over this volume. The underlying size distribution of the potential triggering sites within the material is assumed to follow an exponential distribution.

In [19,20], the non-local stress measure is calculated as the volume average of the maximum principal stress over a spherical volume V_{L} with radius L. To pave the way for the generalization of the non-local stress measure entering (4), a volume average stress tensor is introduced according to

$$\bar{\sigma}_{ij} = \frac{1}{V_{\mathrm{L}}}\int_{V_{\mathrm{L}}} \sigma_{ij}\left(\hat{X}_k - X_k\right)\mathrm{d}\hat{V}, \tag{5}$$

where $\mathbf{X} = (X_1, X_2, X_3)$ are the coordinates of the center of V_{L}, as illustrated in Fig. 1. From the non-local stress tensor, the non-local principal stresses can be calculated with preserved orthogonality, rather than being an integration of the magnitude of the maximum principal stress.

From the non-local principal stresses, a non-local effective normal stress measure can be constructed. For this purpose, the normal stress acting on a plane defined by the polar angle φ and the azimuthal angle θ from the principal stress system as illustrated in Fig. 1 is expressed as

$$\bar{\sigma}_{\mathrm{n}}(\varphi, \theta) = \bar{\sigma}_{\mathrm{I}}\cos^2\varphi + \bar{\sigma}_{\mathrm{II}}\sin^2\varphi\cos^2\theta + \bar{\sigma}_{\mathrm{III}}\sin^2\varphi\sin^2\theta. \tag{6}$$

The average normal stress over the unit sphere combined with a stress distribution function $\rho(\varphi, \theta)$ can be calculated from the integral

$$\bar{\sigma} = \frac{1}{4\pi}\int_0^{2\pi}\int_0^{\pi} \bar{\sigma}_{\mathrm{n}}\left(\varphi, \theta\right)\rho\left(\varphi, \theta\right)\sin\varphi\mathrm{d}\varphi\mathrm{d}\theta. \tag{7}$$

If $\rho(\varphi, \theta)$ is set to unity, (7) becomes the mean stress $\bar{\sigma}_{\mathrm{m}} = (\bar{\sigma}_{\mathrm{I}} + \bar{\sigma}_{\mathrm{II}} + \bar{\sigma}_{\mathrm{III}})/3$. However, the stress distribution function $\rho(\varphi, \theta)$, can be chosen more carefully, but must for physical reasons satisfy

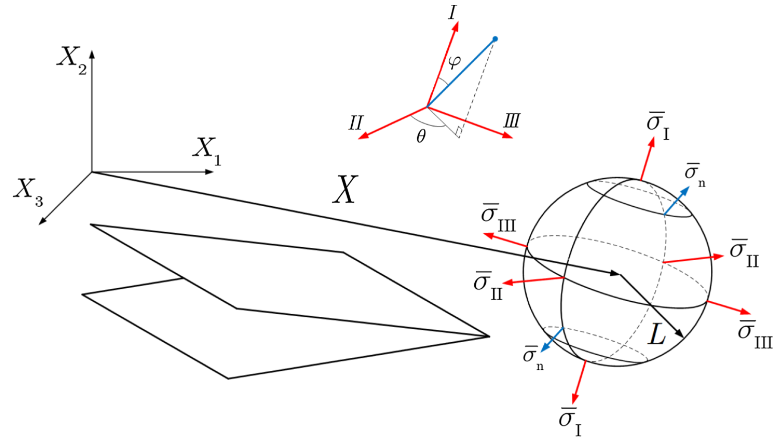

Fig. 1. A non-local stress tensor $\bar{\sigma}_{ij}$ is integrated over a spherical volume with radius L from which the principal stresses are calculated. The normal stress $\bar{\sigma}_{\mathrm{n}}$, and the polar φ and the azimuthal θ angles from the principal stress system are schematically shown.

$$\frac{1}{4\pi}\int_0^{2\pi}\int_0^{\pi}\rho\left(\varphi,\,\theta\right)\sin\varphi\mathrm{d}\varphi\mathrm{d}\theta = 1. \tag{8}$$

By choosing $\rho(\varphi, \theta)$ to be a function solely of the polar angle φ according to

$$\rho(\varphi) = (n+1)\cos^n\varphi \text{ where } n \geqslant 0, \tag{9}$$

the integral for the non-local scalar measure of stress in (7) can be evaluated as

$$\bar{\sigma} = \frac{(n+1)\bar{\sigma}_{\mathrm{I}} + \bar{\sigma}_{\mathrm{II}} + \bar{\sigma}_{\mathrm{III}}}{n+3}. \tag{10}$$

This results in a non-local stress measure that is able to express a state of normal stress over the volume V_{L}, ranging from the mean stress $\bar{\sigma}_{\mathrm{m}}$ when $n = 0$ to the maximum principal stress $\bar{\sigma}_{\mathrm{I}}$ when $n \to \infty$.

The principal stresses may be expressed in terms of the von Mises effective stress $\bar{\sigma}_{\mathrm{e}}$, the stress triaxiality $\bar{T} = (\bar{\sigma}_{\mathrm{I}} + \bar{\sigma}_{\mathrm{II}} + \bar{\sigma}_{\mathrm{III}})/(3\bar{\sigma}_{\mathrm{e}})$ and the Lode parameter $\bar{L} = (2\bar{\sigma}_{\mathrm{II}} - \bar{\sigma}_{\mathrm{I}} - \bar{\sigma}_{\mathrm{III}})/(\bar{\sigma}_{\mathrm{I}} - \bar{\sigma}_{\mathrm{III}})$. This may be used to recast the effective normal stress measure on the form

$$\bar{\sigma} = \bar{\sigma}_{\mathrm{e}}\left[\bar{T} + \frac{n}{n+3}\cdot\frac{(3-\bar{L})}{3\sqrt{3+\bar{L}^2}}\right]. \tag{11}$$

From (11), it is seen that the average value between the two extremes, the maximum principal and the mean stress, respectively, of the effective normal stress measure is obtained for $n = 3$ as also shown in Fig. 2. In this figure, $\bar{\sigma}/\bar{\sigma}_{\mathrm{e}}$ is plotted versus parameter n for three distinctly different stress states: generalized tension $\bar{L} = -1$, generalized shear $\bar{L} = 0$ and generalized biaxial tension $\bar{L} = 1$, at a constant triaxiality $\bar{T} = 2.5$. It can also be seen how the most rapid changes to the effective normal stress occurs in the interval $0.3 \leqslant n \leqslant 30$. An illustration of how the effective normal stress changes with the parameter n is shown in Fig. 3.

To connect with cleavage planes in a microstructure, consider three orthogonal planes equally susceptible for cleavage fracture. Assume that the distribution of these planes is random, i.e. the microstructure is homogeneous. Onset of crack propagation is then likely to occur on the plane that is subjected to the largest normal stress. The orientation of the most critical plane with reference to Fig. 1 can due to symmetry reasons be represented by the solid angular sector: $0 \leqslant \varphi \leqslant \pi/4,\ 0 \leqslant \theta \leqslant \pi/2$. The average normal stress on the most critical cleavage plane can then be calculated as

$$\bar{\sigma}^* = \frac{1}{A^*}\int_0^{\pi/2}\int_0^{\pi/4}\bar{\sigma}_{\mathrm{n}}\left(\varphi,\,\theta\right)\sin\varphi\mathrm{d}\varphi\mathrm{d}\theta, \tag{12}$$

where A^* is the unit sphere area over which the integration occurs. Evaluation of (12) and equating the result to the effective normal stress measure in (10) gives a relation to the effective normal stress parameter n as

$$n = \frac{12\sqrt{2}+15}{7} \approx 4.57. \tag{13}$$

Microcracks will not always nucleate on a cleavage plane aligned with the maximum principal stress. Therefore, the effective normal stress measure derived in (10) is introduced as a phenomenological way of treating the potential triggering of cleavage initiation from a distribution of variously oriented microcracks and associated cleavage planes.

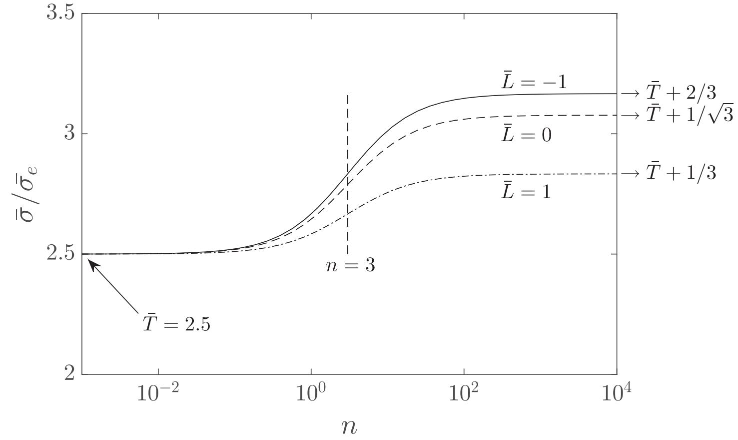

Fig. 2. The effective normal stress measure $\bar{\sigma}/\bar{\sigma}_e$ as a function of the n-parameter explored for three distinctly different stress states defined by a fixed triaxiality $\bar{T} = 2.5$ and the Lode parameter set to $\bar{L} = \{-1,\ 0,\ 1\}$. Note that the maximum principal stress is obtained for the stress states as $n \to \infty$.

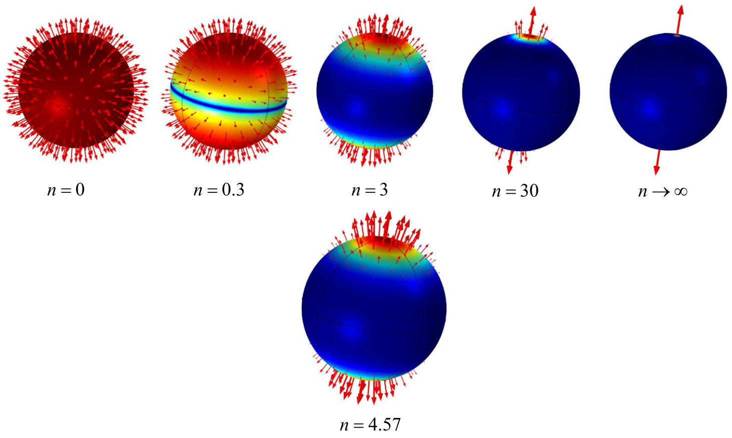

Fig. 3. Visualization of how the effective normal stress changes with the parameter n, the principal directions follows from Fig. 1. The effective normal stress is here represented by $\bar{\sigma}_\mathrm{n}(\varphi, \theta)\rho(\varphi, \theta)$. Note that the mean stress is obtained when $n = 0$ and the maximum principal stress when $n \to \infty$. Color coding of the sphere represents iso-contours of $\cos^n \varphi$. (For interpretation of the references to colour in this figure legend, the reader is referred to the web version of this article.)

3. Influence of model parameters

The influence of the effective normal stress on the predictive capabilities of the weakest link model laid out above will now be explored. Two sets of experiments taken from the literature have been chosen to illustrate the influence of the non-local effective normal stress.

The first set of experiments is taken from Faleskog et al. [19], where three point bending experiments were carried out at three different temperatures across the ductile to brittle transition temperature region. These experiments are characteristic of loss of *in-plane constraint*, and will here be denoted as the Faleskog dataset. The second set of experiments is taken from Rathbun et al. [28] where three point bending experiments were conducted in order to study constraint loss and statistical size effects on fracture

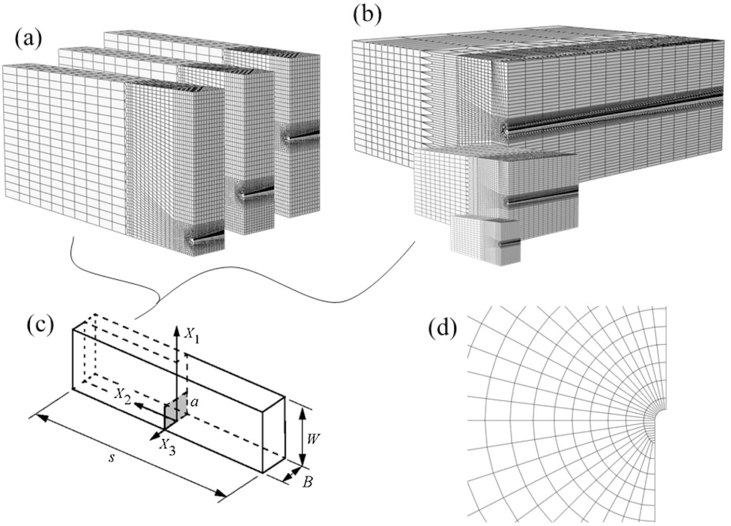

Fig. 4. Illustration of the finite element models used to study the influence of the effective normal stress in the non-local weakest link model. (a) Faleskog dataset, (b) Rathbun dataset, (c) schematic specimen overview (d) close-up of the crack tip, which was modelled as a small notch. Only solutions with a crack tip opening at least three times the original notch or larger, was considered.

toughness of a typical low alloy steel. These experiments are characteristic of loss of *out-of-plane constraint*, and will here be denoted as the Rathbun dataset. The choice of nomenclature of in- and out-of-plane constraint is due to how the crack size to specimen width is varied within the datasets. In the Faleskog dataset the width W and the ratio B/W are kept constant while the ratio a/W is varied, while in the Rathbun dataset the ratio a/W is kept constant while the width W and thickness B are varied. This creates two types of constraint loss where the Faleskog dataset constraint loss is related to effects of shallow cracks (in-plane), and the Rathbun dataset is rather related to thickness (out-of-plane) and loss of constraint due to size effects.

3.1. Numerical computation of the failure probability and parameter estimation

Models of the experiments for estimating model parameters and predicting the probability of failure was set up as finite element models. These were generated with meshes containing between 27 000 and 35 000, 20 noded hexahedral elements with quadratic shape functions and reduced integration. Due to symmetry, only a quarter of the three point bending specimens was modelled with 12–15 elements through the thickness of the model. Examples of the finite element models employed can be seen in Fig. 4. A high mesh density was used in the close vicinity of the crack front in order to resolve the stress and strain fields for the probabilistic calculations of the weakest link model, transition from fine to coarse mesh was obtained with the meshing method described in [29]. In all simulations, the elastic modulus E and Poisson's ratio ν were taken as 210 GPa and 0.3, respectively. All models were solved using a large deformation framework. The elastic–plastic material was assumed to obey the J_2 flow theory of plasticity with isotropic hardening. Tensile test data from the experimental datasets were fitted to a power law hardening equation on the form

$$\sigma_{\mathrm{f}} = \sigma_0\left(1 + \frac{\varepsilon_{\mathrm{e}}^{\mathrm{p}}}{\varepsilon_0}\right)^m, \tag{14}$$

for which the parameters of the investigated materials can be found in Table 1.

The failure probability is calculated by evaluating the stress and strain fields in the centroid of the finite elements. The integral in (1) was numerically determined according to a one Gauss point integration scheme as

$$\int_V h_{\max}\frac{\mathrm{d}V}{V_0} \approx \sum_{i=1}^{N_e} h_{\max}(\varepsilon_{\mathrm{e}}^{\mathrm{p}}(\mathbf{X}^i),\, \bar{\sigma}(\mathbf{X}^i))\frac{V_i}{V_0}, \tag{15}$$

where $\mathbf{X}^i$ and V_i denote the position of the centroid and the volume of element i in the undeformed configuration, N_e is the number of elements over which the integration occurs, and $h_{\max}$ is the maximum value of h throughout the loading history up to the current load level.

In order to calculate the non-local stress tensor at a point $\mathbf{X}$, a similar integration scheme as for the failure probability is utilized as

$$\bar{\sigma}_{ij} \approx \frac{1}{\sum_k V_k}\sum_k \sigma_{ij}(\mathrm{X}^k)\, V_k, \quad \text{for} \quad \left|\mathbf{X}^k - \mathbf{X}\right| \leqslant L, \tag{16}$$

where V_k is the element volume of the element in which the Cauchy stress tensor, σ_{ij} is evaluated at the points $\mathbf{X}^k$ which satisfies the inequality above, and L is the length scale over which the non-local stress state is formed.

In order to appropriately estimate the model parameters, two data sets of experimental fracture tests with differing crack-tip constraint are needed. In the estimation of the weakest link model parameters, an unconstrained minimization using the Nelder-Mead simplex algorithm [30] was carried out. For the purpose of minimization, two partial residuals are introduced as

$$R_{\mathrm{A}} = \sum_{i=1}^{N_{\mathrm{A}}} [P_{\mathrm{rank}}^i - P_{\mathrm{f}}(J_c^i)]^2,\ R_{\mathrm{B}} = \sum_{i=1}^{N_{\mathrm{B}}} [P_{\mathrm{rank}}^i - P_{\mathrm{f}}(J_c^i)]^2 \tag{17}$$

where A and B relates to the two experimental sets needed for parameter estimation, and N_{A} and N_{B} are the number of specimens in each set. The model parameters $c/V_0,\ \sigma_{\mathrm{th}},\ n$ and L are found from minimization of the total residual $R = R_{\mathrm{A}} + R_{\mathrm{B}}$. The parameter fitting was carried out by firstly finding a suitable value for the length scale parameter L and secondly choosing $n = \{0,\ 3,\ \infty\}$, and then estimating $c/V_0,\ \sigma_{\mathrm{th}}$ by minimization of R. The probability of failure could then readily be calculated by enforcing the parameters found from the fitting procedure.

Table 1
Parameters of the power law hardening function and the yield strength of the used materials in this study.

Dataset	σ_0/MPa	$\varepsilon_0/10^{-6}$	m	$R_{\mathrm{p0.2}}$/MPa
Faleskog Temp = − 30 °C	265.4	1.96	0.118	597
Faleskog Temp = 25 °C	275.3	2.16	0.107	557
Faleskog Temp = 55 °C	280.7	2.02	0.102	552
Rathbun	438.7	3280	0.194	600

3.2. In-plane constraint

The experiments by Faleskog et al. [19] was carried out on a modified A508-steel with a reference temperature re-evaluated to $T_0 = 47$ °C. (in [24], T_0 was evaluated to 48 °C) The fracture tests were conducted on three point bend specimens (SEN(B)) with specifications according to $W = 40$ mm, $B = 20$ mm, $s = 4W$ and $a/W = \{0.5,\ 0.25,\ 0.1\}$. Testing was carried out at the temperatures $\{-30,\ 25,\ 55\}$ °C, i.e. a study of in-plane constraint fracture toughness over a wide range of temperatures in the DBTT-region. In the fitting of the model parameters, the experiments from the specimens with crack length to specimen width ratios $a/W = \{0.5,\ 0.1\}$ were used, as this gives the largest difference in crack tip constraint and thus also the best estimate of the model parameters. In the previous studies of this material, using the same weakest link framework, the length scale parameter was found to be $L = 150$ μm, which also has been used in this study. The other model parameters that were fitted from the experiments can be found in Appendix B.

The results from the investigation of the effective stress parameter n is presented as plots of the failure probability as a function of the crack front averaged J-integral in Figs. 5–7, for the three chosen values of n. It is clearly displayed that a low value of the effective stress parameter n yields a lower failure probability at high levels of loading as compared to that of a high value of n. In other words, the non-local mean stress yields a lower failure probability at high levels of the J-integral as compared to the non-local maximum principal stress. Regarding the parameter estimation for the three datasets, it appears that there is no obvious trend over the range of temperatures considered as to what value of n gives the best fit. For the lowest and highest temperatures of the dataset Temp = $\{-30,\ 55\}$ °C, the non-local maximum principal stress at $n \to \infty$ clearly gives the best prediction of the three curves presented. On the other hand, a low value of n appears to give a better prediction of the failure probability for the dataset pertaining to room temperature (25 °C) in both the calibration and validation subsets. In Figs. 5–7, estimation of model parameters is carried out on the $a/W = \{0.5,\ 0.1\}$ specimen subset, while model validation is carried out on the $a/W = 0.25$ specimen subset. Both $a/W = \{0.25,\ 0.1\}$ are geometries where loss of constraint will occur, but as $a/W = 0.25$ lies in between crack sizes used for calibration, one would expect the model prediction to be quite good. True model validation would however require calibration and then transfer to an entirely different geometry. Such a validation will be presented in Section 4 where the model is applied to experiments of surface cracked specimens.

To investigate specimen size effects, geometrically self similar SEN(B)-specimens with $a/W = \{0.5,\ 0.1\}$ have been utilized with parameters calibrated for Temp = 25 °C. The result is presented in Fig. 8, which shows predicted fracture toughness at a failure probability of 50% as a function of specimen thickness. As a reference, predictions from the master curve methodology is included, where the solid line represents the toughness at a failure probability of 50%, and the dashed lines corresponds to the 5–95% fractiles. The master curve predictions for the $a/W = 0.1$ specimens is adjusted by the T-stress at the plastic limit load for a SEN(B)-specimen taken from [26]. As displayed in Fig. 8, the predicted fracture toughness increases with decreasing specimen size as expected, however, this increase is emphasized for small values of n. For the deeply cracked $a/W = 0.5$ specimens, all of the P_f predictions fall within the 5–95% fractiles of the master curve. By contrast, the predictions for shallow cracked $a/W = 0.1$ specimens, the effect of n on the predicted fracture toughness is significant. As the specimen size is decreased, the case $n = 0$ predicts a fracture toughness that differs by almost a factor two from the case of $n \to \infty$. It should be observed that predictions that employs the maximum principal stress lie closest to the master curve predictions.

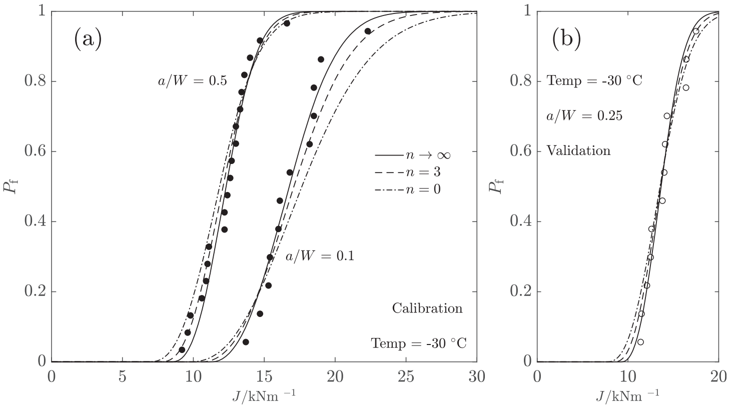

Fig. 5. Comparison of the predicted failure probability for different values of the effective stress parameter n with rank probabilities for the fracture tests (circles) in the Faleskog Temp = −30 °C dataset. (a) Subsets where a/W = {0.5, 0.1} used for calibration of the model parameters, (b) subset where a/W = 0.25 used for validation of the probabilistic model.

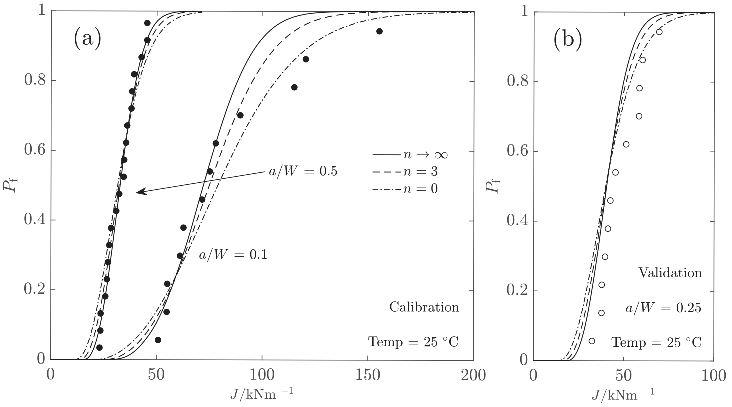

Fig. 6. Comparison of the predicted failure probability for different values of the effective stress parameter *n* with rank probabilities for the fracture tests (circles) in the Faleskog Temp = 25 °C dataset. (a) Subsets where $a/W = \{0.5, 0.1\}$ used for calibration of the model parameters, (b) subset where $a/W = 0.25$ used for validation of the probabilistic model.

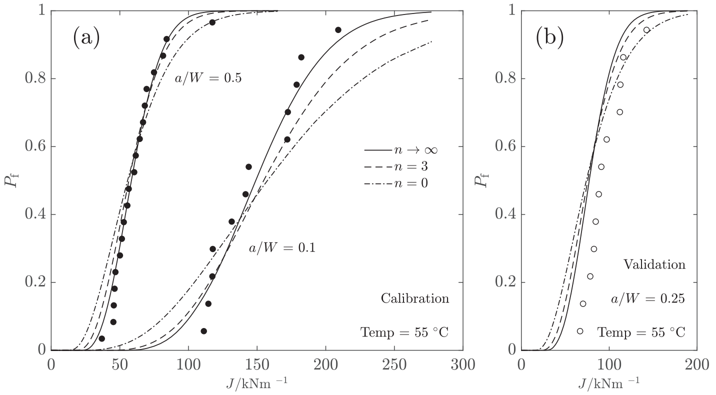

Fig. 7. Comparison of the predicted failure probability for different values of the effective stress parameter *n* with rank probabilities for the fracture tests (circles) in the Faleskog Temp = 55 °C dataset. (a) Subsets where $a/W = \{0.5, 0.1\}$ used for calibration of the model parameters, (b) subset where $a/W = 0.25$ used for validation of the probabilistic model.

3.3. Out-of-plane constraint

The comprehensive experimental study conducted by Rathbun et al. [28,31,32] was made on a A533-steel. The material has a reference temperature $T_0 = -93$ °C and the chemical composition listed in Table 2. The fracture tests were conducted on three point bend specimens where the crack size to specimen width ratio was fixated at $a/W = 0.5$, but where the width *W* was varied over the wide range $W = \{6.4 - 50.8\}$ mm and the thickness *B* to width ratio was varied as $B/W = \{0.16 - 40\}$. All the tests were conducted at a temperature of − 91 °C and was carried out in order to study size effects on loss of crack tip constraint and its implications to the apparent fracture toughness. The specimens chosen for modelling in this study were selected to represent a wide range of fracture toughness for the material in question. The specimens included in this study have dimensions $W = \{6.4, 12.7, 25.4\}$ mm with the corresponding thickness to width ratios $B/W = \{1.25, 2.5, 5\}$. This choice represents one of the most discriminating and extreme combination of *W* and *B* in the Rathbun dataset. In the estimation of the model parameters, the experiments from the specimens widths of $W = \{25.4, 6.4\}$ mm were used, as this gives the largest difference in crack tip constraint. A suitable length scale of $L = 100$ μm was found in the parameter estimation procedure, the other model parameters that were estimated from the experiments can be found in Appendix B.

In Fig. 9, the failure probability from the model predictions is compared to the ranked probability from the experiments. It can be noted that the model predictions show an excellent agreement with the experimental data, both in terms of the calibration and the

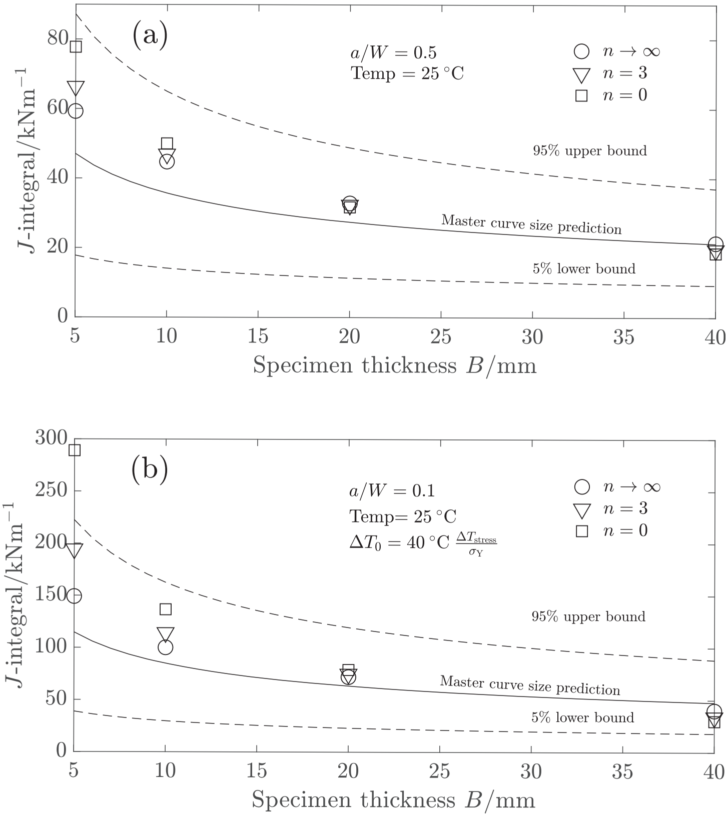

Fig. 8. The influence of the effective stress parameter *n*on the predicted size effect on the cleavage fracture toughness at a failure probability of $P_{\mathrm{f}} = 50\%$. (a) Size effect predictions on specimens where $a/W = 0.5$, (b) size effect predictions on specimens where $a/W = 0.1$.

Table 2
Chemical composition of the material investigated in Rathbun et al./wt.%.

C	Al	Si	P	S	Cr	Mn	Ni	Cu	Mo
0.21	0.04	0.24	0.004	0.008	0.09	1.23	0.63	0.08	0.53

validation subsets. The effect of the effective stress parameter *n* on the prediction of the failure probability is negligible.

4. Evaluation of fracture tests on surface cracked specimens

This section presents the preparation, execution and evaluation of four-point bending fracture experiments of specimens with a semi-elliptic surface crack.

4.1. Material and experimental method

Fracture experiments were performed on bending specimens with a semi-elliptic surface crack made from a modified A508 steel at 25 °C. The modification consisted of a heat treatment that raised the ductile to brittle transition region to a temperature interval of 0–80 °C, which resulted in a reference temperature $T_0 = 47$ °C. This steel is the same as the one used in the tests reported by Faleskog et al. [19] and Kroon et al. [20]. The chemical composition of the material can be found in Table 3.

Each test specimen consisted of three parts of A508 steel that were welded together. The three parts were taken from the broken fracture specimens of the tests performed by Faleskog et al. [19]. Only the specimens with the deepest crack tested at room

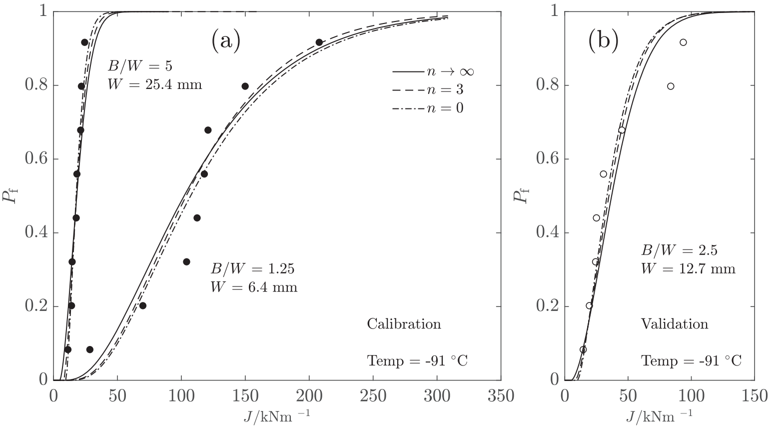

Fig. 9. Comparison of the predicted failure probability for different values of the effective stress parameter $n$with rank probabilities for the fracture tests (circles) in the Rathbun dataset. (a) Subsets where $W =$ {25.4, 6.4} mm and B/W = {5, 1.25} used for calibration of the model parameters, (b) subset where $W = 12.7$ mm and B/W = 2.5 used for validation of the probabilistic model.

Table 3
Chemical composition of the investigated material/wt.%.

C	S	Cr	Mn	Ni	Cu	Mo
0.18	0.003	0.46	0.57	0.79	0.11	0.92

temperature and below were re-purposed, since the plastic deformation in those specimens only developed in the proximity of the crack tip. Some of the material closest to the previous crack tip was also removed through mechanical machining in order to ensure not using plastically deformed material in the new specimens, i.e. only using material that has been subjected to elastic deformation. A schematic picture of the specimens used in the experiments is shown in Fig. 10(a).

The goal of the manufacturing process was to create specimens with target dimensions (mm): $W = 40$, $T = 20$, $L = 240$, $l_w = 70$, $a = 6$ and $c = 10$, with the dimensions detailed in Fig. 10. The width, W, and the thickness, T, were measured before the experiments in the vicinity of the cross section containing the crack and can be found in Table A1 in Appendix A. The desired shape of the crack was obtained through prefatigue.

Load was transferred to the specimen by a servo-hydraulic testing machine, where the load P and the displacement δ_p of the piston were recorded during the tests. To facilitate a direct measurement of specimen deformation, a specific fixture was used, where the displacement between the two parts of the fixture, δ_f, was recorded using a clip gauge. This is schematically shown in Fig. 11.

4.2. Analysis of fracture tests

The onset of cleavage fracture in the thirteen specimens tested was characterized by two distinct events: (i) complete failure of the specimen (10 specimens) and (ii) pop-in (3 specimens). A pop-in was recognized as the occurrence of a discontinuity in the load-displacement curve. All discontinuities were regarded to be significant, a plot of the load-displacement curves showing pop-in events can be seen in Fig. 12.

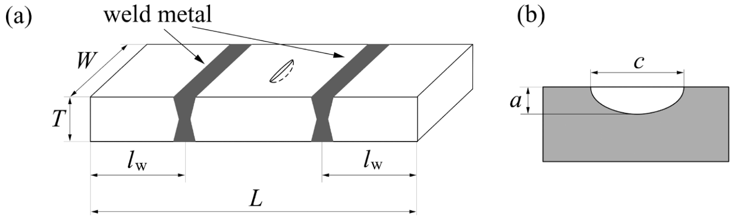

Fig. 10. (a) Schematic description of a test specimen. (b) Cross section of a pre-cracked specimen along a crackplane with the initial crack dimensions of a half ellipse.

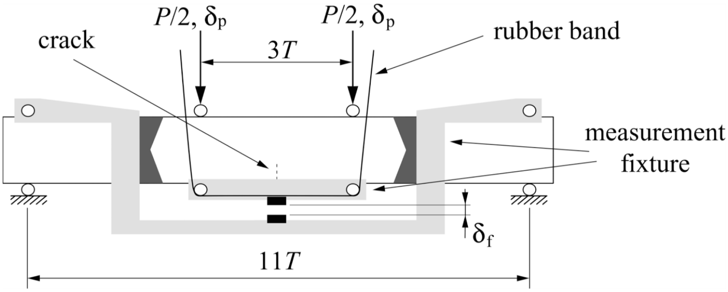

Fig. 11. Schematic description of test assembly.

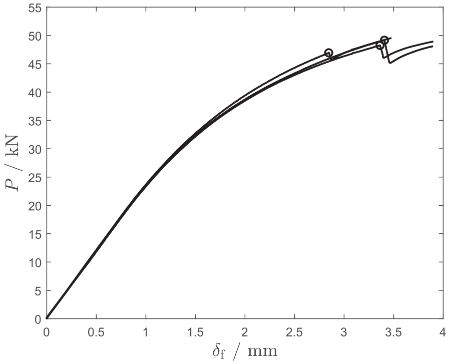

Fig. 12. Load-displacement curves showing the effects of the pop-in events. Open circles marks the point at which failure was considered.

The displacement recorded by the clip gauge, δ_f, (see Fig. 11) was used to calculate the displacement of the specimen in the direction of the applied load at the loading contact points on the specimen. After the fracture tests, the crack geometry was measured by the use of seventeen data points with equal angular distribution for each test specimen, as seen in Fig. 13. In order to obtain the major and the minor axes, a least square fit of the coordinates of the initial crack front to an elliptic equation was performed. The results of this analysis can be found in Appendix A. Evaluation of the J-integral at the onset of cleavage fracture is detailed in Section 4.2.

In order to evaluate a representative value of the J-integral at cleavage fracture, several finite element models of the specimens in the experimental series were used. Measurements of the specimens showed variations in the specimen dimensions and crack geometry, as can be seen in Table A1 of Appendix A. Due to this variation, the specimens were divided into four groups based on the stress intensity factor solution for a semi-elliptical surface crack in a flat plate subjected to bending, Anderson [33]. The inter-group difference in the stress intensity factor solutions was less than 1%.

For each group, the crack geometry used in the finite element modelling of the fracture tests was taken as the mean of the respective minor and major axis of the semi elliptical surface crack in the specimens. This is illustrated along with the crack front measurements in Fig. 13. The geometrical dimensions and crack size used for the model of each group can be found in Table A2. The finite element models were solved using a large deformation framework and discretized using 20 noded quadratic hexahedral elements with reduced integration and consisted of 32000 elements modelling one quarter of the specimen with 22 element layers along the crack front as illustrated in Fig. 14. Symmetry boundary conditions were applied on the planes $X_2 = 0$ and $X_3 = 0$ by setting $u_2 = 0$ and $u_3 = 0$, respectively. The load was applied through prescribing the displacement $u_1 = \bar{u}_1$ at $\{X_1 = t,\ X_2 = 1.5T,\ X_3\}$ combined with the fixed boundary condition $u_1 = 0$ at $\{X_1 = 0,\ X_2 = 5.5T,\ X_3\}$. The vertical displacement δ_f was calculated as $\delta_f = u_3(t,\ 1.5T,\ X_3) - u_3(0,\ 5.5T,\ X_3)$. Note, the distinctions made between the model dimensions as described by the lower case letters (Table A2 in Appendix A) and the nominal specimen dimensions as described by capital letters (defined above). The elastic-plastic material parameters were set to be the same as in the Faleskog Temp = 25 °C dataset.

The J-integral was evaluated as a domain integral in the employed finite element software, and since the value varies along the curved semi elliptical crack front, an effective J-integral was evaluated over the element layers along the crack front of length ξ as

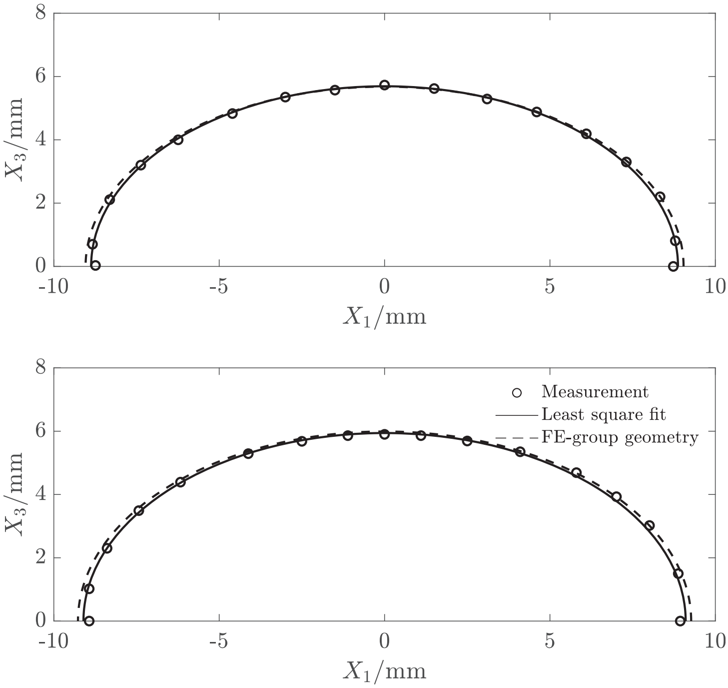

Fig. 13. Crack shape at fracture with the corresponding approximations. (a) Specimen 2 (b) specimen 6.

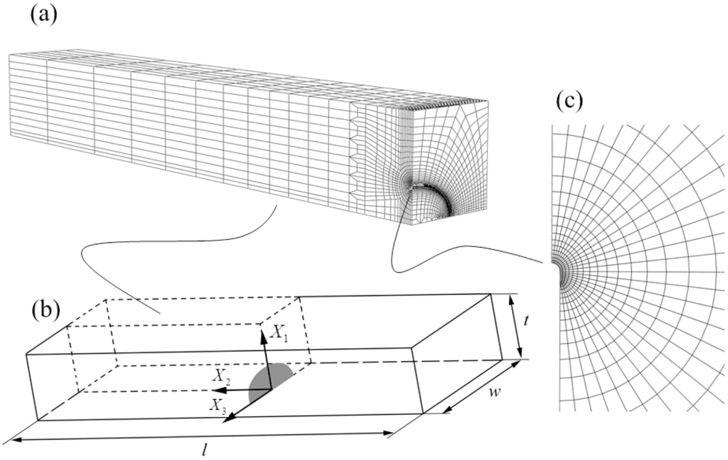

Fig. 14. Illustration of the finite element model used for evaluating the fracture toughness of the experiments and used in the weakest link evaluation of the probability of failure. (a) Discretization of the specimen, (b) specimen orientation and model parameters, (c) close-up of the crack tip.

$$\bar{J} = \frac{1}{\xi}\int_{\xi} J(\xi)\mathrm{d}s \approx \frac{1}{\sum_{i=1}^{N_{\mathrm{CF}}} \xi_i} \sum_{i=1}^{N_{\mathrm{CF}}} J(\xi_i)\xi_i. \tag{18}$$

Here, ξ_i is the length of element i along the crack front, N_{CF} is total number of elements along the crack front, and $J(\xi_i)$ is the value of the J-integral in that element layer. The cleavage fracture toughness J_{c} of the specimens, was taken as the $\bar{J}$-integral of the finite element analysis corresponding to the specimen displacement δ_{f} at the point of failure by cleavage fracture. The resulting fracture toughness from the evaluation described here can be found in Table A1 in Appendix A.

The failure probability of a test, P_{f}, was calculated using a rank probability P^{i}_{rank} where i denotes the specimen with the rank number i. According to Wallin [34], the most accurate description of the rank probability is

$$P^{i}_{\mathrm{rank}} = \frac{i - 0.3}{N + 0.4} \tag{19}$$

where N denotes the number of specimens in the experimental set.

4.3. Weakest link model

By employing the non-local weakest link model laid out in Section 2, together with the finite element model described in Section 4.2, the failure probability was calculated. In these calculations, the model parameters calibrated from the room temperature dataset in Section 3.2 was used. The resulting failure probability differs very little in-between the four groups, therefore, the predictions shown here pertain to the group containing the largest amount of specimens, i.e. group 2. The results is shown in Fig. 15, where the failure probability is plotted versus the effective J-integral defined in (18).

As can be seen in Fig. 15, the predicted failure probability shows a good conformity with the ranked probability of the experiments. The effective normal stress parameter tends to yield a slightly better prediction if $n = 0$ and slightly worse if $n \to \infty$. The same trend was also observed for the SEN(B)-specimens in Fig. 6 as discussed in Section 3.2.

4.4. Master curve method

The master curve can be used to make a prediction of the probability of failure of structures with three dimensional crack fronts where loss of crack tip constraint occurs. The governing equations for this can be found in Appendix C. By using an elastic finite element model of the four point bending experiments, the local elastic crack field quantities can be readily calculated for use with the master curve methodology. The model was made with the same boundary and symmetry conditions as for the elastic-plastic model, but with a small strain linear elastic material model and a sharp crack front. The stress intensity factor and T-stress solutions from the model can be seen in Fig. 16 where it can be clearly noted that the T-stress is negative along the entire crack front, indicating a loss of crack tip constraint. The stress intensity factor K_{I} and the T-stress in Fig. 16 are normalized by $\sigma_{\mathrm{b}}\sqrt{\pi a}$, and σ_{b}, respectively, where $\sigma_{\mathrm{b}} = 6P/T^2$ is the maximum nominal bending stress acting over the crack plane.

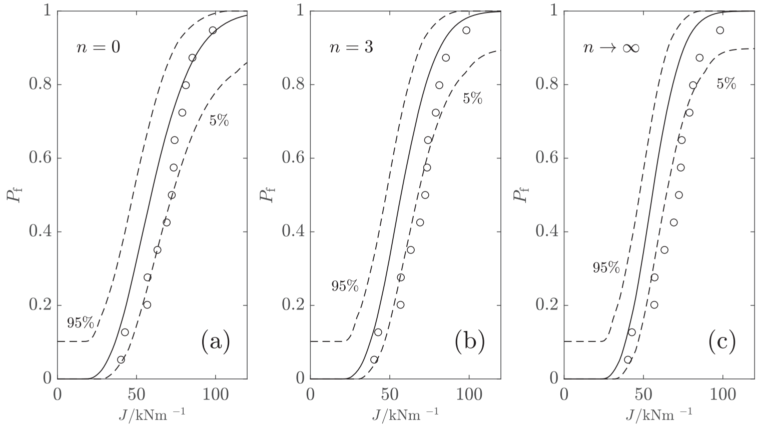

Fig. 15. Application of the non-local weakest link model to predict the failure probability of the surface cracked four point bending specimens (circles), compared to the rank probabilities for the experimental J-integral values at failure. (a) Prediction with $n = 0$, (b) Prediction with $n = 3$, (c) Prediction where $n \to \infty$. In the PhD-thesis of Stec, P_{f} is plotted versus the maximum J-integral along the crack front.

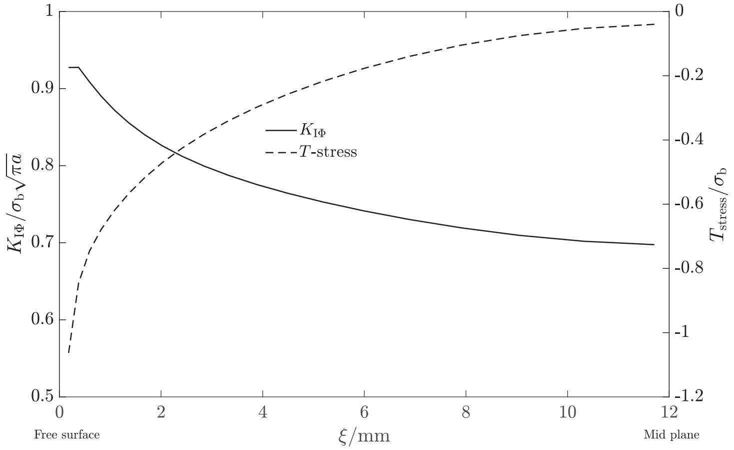

Fig. 16. Variation of the elastic crack tip fields K_I and T-stress along the crack front of the finite element model of the four point bending specimen with a geometry from group 2. Note that the crack tip fields are plotted from the free surface up to the mid plane where the symmetry condition prevails.

For crack front lengths that greatly exceedes the reference length of 25.4 mm, Wallin [35] recommends that a second re-scaling should be made to avoid an unnecessary over conservatism. However in this case, the crack front lengths of the four groups are $\xi = \{25.8, 23.7, 23.9, 24.5\}$ mm, therefore it was judged that the suggested re-scaling was unnecessary. The T-stress adjustment of T_0 for the master curve in (C2) was evaluated at the limit load using the solution presented in Fig. 16, where the limit load solution proposed by Sattari-Far and Dillström in [36] was utilized, which gave $\sigma_\mathrm{b} \approx 1.45R_{\mathrm{p}02}$. For details of the constraint adjustment using the T-stress and the calculation of the failure probability using the master curve methodology, see Appendix C.

Fig. 17 shows the failure probability evaluated from the crack front quantities of the elastic finite element model and the master curve. The failure probability, Eq. (C1) in Appendix C, was calculated using the solutions presented in Fig. 16. Here, two T-stress adjusted master curve predictions are presented alongside an un-adjusted prediction. Clearly, the master curve predicts an over-

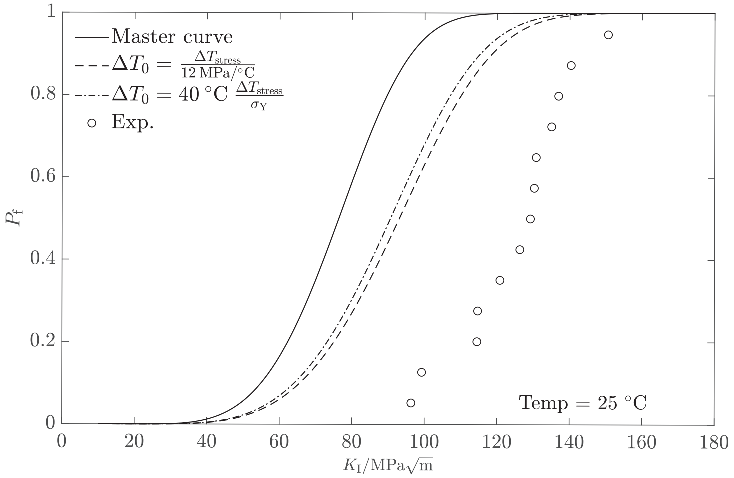

Fig. 17. Predictions of the failure probability using the master curve methodology of the four point bending experiments with a semi elliptic surface flaw.

conservative estimate of the fracture toughness as compared to the experiments. For instance at $P_f = 0.5$ the measured fracture toughness is approximately 40% higher than what is predicted by the T-stress adjusted master curve methodology.

5. Discussion

The model proposed in [18] may be seen as a way to address the combined events of nucleation of a microcrack and its propagation over microstructural barriers into a macroscopic cleavage fracture. Here, this model has been further developed by introducing a generalized non-local effective normal stress measure. This adds an extra parameter to the model, the effective normal stress parameter n, which sets the relative influence of the mean stress and the maximum principal stress on the effective normal stress measure, respectively. From Eq. (11) and Fig. 2 it can be understood that n controls the relative contribution from the stress triaxiality and the deviatoric stress state in terms of the Lode parameter on the effective normal stress measure. Hence, when the stress triaxiality decreases, e.g. by loss of constraint ahead of a crack front, the relative difference between the mean stress $n = 0$ and the maximum principal stress $n \to \infty$ increases, as the Lode dependent second term in Eq. (11) becomes more dominant. As observed from Figs. 5–8, a low value of n tends to increase the predicted scatter of the failure probability. Not shown above, but the increase in scatter can to some extent be mediated by a larger length scale L, however not in full. The length scale itself will apart from introducing a threshold toughness value also affect the impact of macroscopic stress field due to boundary interaction as the size of a specimen becomes small.

Following the remark in Section 2, the introduction of the effective normal stress parameter n may be seen as a phenomenological way of handling the triggering of cleavage fracture from a microcrack propagating on the most critical plane in a set of randomly oriented cleavage planes. From the analysis in Eqs. (12) and (13), it is seen that under these assumptions the effective normal stress parameter becomes $n \approx 4.57$. A random distribution of cleavage planes would relate to an isotropic microstructure. In Section 3 the influence of the effective normal stress parameter n is studied. It is shown for the Rathbun dataset that the influence of n is insignificant as compared to that for the Faleskog datasets. For the Faleskog Temp = $\{-30, 55\}^\circ$ C datasets, the best predictions obtained with $n \to \infty$, while for the 25° C dataset it appears that the $n = \{0, 3\}$ would give a better prediction. However for the 25 °C dataset, the residual is minimized for $n = 4.93$, which is close to the value 4.57. It should be noted that both parameters n and L affects the predicted scatter in fracture toughness; an increasing value of L has a rather strong effect of decreasing the scatter, whereas an increasing n has a moderate effect.

For high constraint geometries where primarily one parameter can be used to characterize the crack tip fields (e.g. K_I or J), the influence of n appears to diminish. This was observed in the failure probability predictions for the Rathbun dataset as seen in Fig. 9. In their dataset, the T-stress is positive for all tests and the influence of the n-parameter is expected to be low. Indeed this is the case as can be concluded from Fig. 9. Another aspect of the Rathbun dataset that decreases the influence of out-of-plane constraint loss is the high hardening of the material cf. [18]. It should be mentioned that the model parameters resulting from calibration will to some extent depend on the datasets used. If a combination of deep and shallow cracked specimens had been used in the calibration of the Rathbun material, the importance of might have been larger.

Based on the datasets evaluated in this study, it is not entirely clear how the effective normal stress parameter n may improve predictions of the failure probability. For some datasets, a clear improvement can be observed, cf. Fig. 6. A very large impact of parameter n of the failure predictions was observed for small shallow cracked SEN(B)-specimens, cf. Fig. 8. To clarify this, new experiments combining in-plane and out-of-plane constraint loss would be needed.

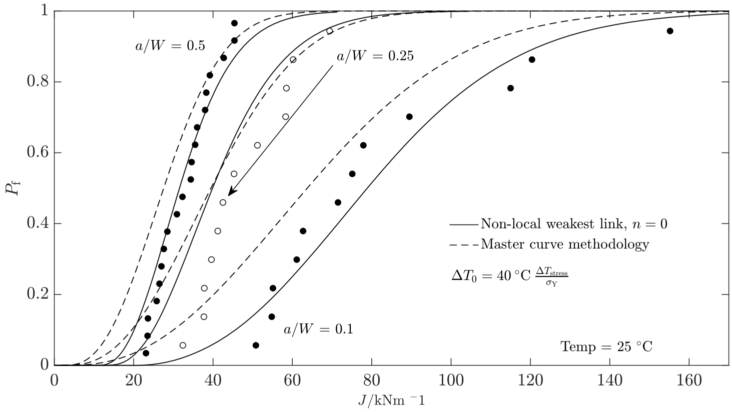

Fig. 18. Comparison of predictions using the non-local weakest link model with $n = 0$, and predictions from the master curve methodology.

For the case of $n \rightarrow \infty$, the non-local maximum principal stress enters the probabilistic model, however, in this study a slight difference in the threshold stress σ_{th} is found from the original study of the same material that was published by Faleskog et al. in [19]. In their study, the threshold stress is found to be $\sigma_{\text{th}} = \{1432.8, 1657.3, 1771.9\}$ MPa, and in this study the corresponding $\sigma_{\text{th}} = \{1395.8, 1551.8, 1642.2\}$ MPa was found. The difference is due to how the non-local stress measure is calculated, in [19] the non-local stress measure is calculated by averaging the maximum principal stress in the volume defined by the length scale L. While in this study, the maximum principal stress is evaluated by use of the non-local stress tensor.

Regarding the four-point bending experiments presented in this study that was part of a PhD-thesis of Stec [27], this study presents a re-visit of these experiments with new evaluation of both the fracture tests and the probabilistic modelling. The probabilistic modelling has been done using the recent developments in the non-local weakest link model developed originally by Kroon and Faleskog [18]. As can be seen in Fig. 15, the model well reproduces the probability of failure, where $n = 0$ appears to give a slightly better prediction than $n \rightarrow \infty$ does. However, results for all n are within the range of what is judged satisfactory. The SEN(B) and the surface cracked four point bending experiments performed at room temperature, constitute a large set of discriminating fracture tests. The non-local weakest link model investigated in this study well captures the rank probability of these tests. It is of interest to compare the outcome of this model to that of the master curve methodology, which from an engineering point of view is significantly easier to use. This comparison is shown in Fig. 18. For practical purposes, the master curve methodology gives acceptable predictions for the SEN(B)-specimens in this study. However, for the more complicated surface cracked geometry, the predicted fracture toughness is considerably over estimated. This suggests that the procedure to adjust T_0 for loss of constraint in more complicated geometries may be improved. If accurate predictions of the failure probability in more complicated geometries are desired, it seems necessary that the master curve assessment should be complimented by an evaluation based on a more sophisticated model of the type proposed in this study.

6. Concluding remarks

The probabilistic model for failure by cleavage fracture proposed by Kroon and Faleskog [18] has been further developed. Specifically, the non-local scalar measure of stress has been adequately generalized and now has a clear microstructural interpretation related to existing cleavage planes.

The proposed generalized probabilistic model has been validated against two experimental datasets which are discriminating with respect to loss of in-plane and out-of-plane crack tip constraint. Furthermore, the model was verified against a dataset consisting of four-point bending experiments containing semi-elliptic surface cracks.

Acknowledgements

Mr. Hans Öberg is acknowledged for carrying out the experiments of the four-point bending fracture tests. Dr. Erik Olsson is acknowledged for providing the meshing tools used for the SEN(B)-specimens. The Swedish Radiation Safety Authority SSM and the Swedish Centre for Nuclear Technology (SKC) is acknowledged for financial support.

Appendix A. Experimental fracture test data

See Tables A1 and A2.

Table A1

Cleavage fracture toughness of the semi-elliptic surface cracked specimens subjected to four-point bending, evaluated according to the details in Section 4.2.

ID	Group	W/ mm	T/ mm	a/ mm	c/ mm	J_c/ kNm^{-1}
1	1	38.5	19.0	6.45	9.66	63.2
2	2	38.5	19.1	5.69	8.87	98.3
3	2	38.55	19.1	5.66	9.04	85.3
4	2	38.4	19.0	5.75	9.01	79.0
5	2	38.5	19.0	5.69	9.18	72.3
6	2	38.6	19.1	5.65	9.09	69.1
7	2	38.45	18.9	5.64	9.03	42.7
8	3	38.5	19.1	5.83	9.00	81.2
9	3	38.5	19.05	5.80	8.92	74.1
10	3	38.6	19.0	5.85	9.14	73.5
11	3	38.5	19.0	5.78	9.24	56.8
12	4	38.5	19.1	5.94	9.10	57.0
13	4	38.55	19.1	6.05	9.44	40.2

Table A2
Geometry parameters used for finite element modelling of the fracture tests.

Group	w/mm	t/mm	a/mm	c/mm
1	38.5	19.0	6.45	9.66
2	38.5	19.0	5.68	9.05
3	38.5	19.0	5.82	9.07
4	38.5	19.0	5.99	9.27

Appendix B. Weakest link parameters

Weakest link model parameters found from the fitting procedure conducted in Section 3 (see Table B1).

Table B1
Parameters for the weakest link model for the datasets (a) Faleskog Temp = −30 °C, (b) Faleskog Temp = 25 °C, (c) Faleskog Temp = 55 °C, (d) Rathbun.

Dataset	$c/V_0/[10^{10}\,\mathrm{m}^3]$	σ_{th}/MPa	n
(a)	314.94	988.0	0
	634.93	1192.2	3
	1135.3	1395.8	∞
(b)	44.088	1101.2	0
	87.324	1328.4	3
	157.80	1551.8	∞
(c)	13.150	1120.0	0
	40.127	1400.4	3
	76.300	1642.2	∞
(d)	17.019	1048.6	0
	10.277	1160.3	3
	4.2488	1197.8	∞

Appendix C. Master curve methodology for three dimensional cracks

In a general three diminsional case, the stress intensity factor and constraint will vary along a crack front. To account for this, Wallin has extended the master curve methodology [35]. The probability distribution function is given by

$$P_{\mathrm{f}} = 1 - \exp\left[-\int_0^{\xi}\left(\frac{K_{J\Phi}-K_{\min}}{K_{0\Phi}-K_{\min}}\right)^4\frac{\mathrm{d}\xi}{B_0}\right], \tag{C1}$$

where B_0 is the reference crack front length of 25.4 mm, ξ is the length of the curved crack front, and where the local stress intensity factor $K_{J\Phi}$ and the temperature and constraint dependent reference fracture toughness $K_{0\Phi}$ are integrated along the crack front. $K_{0\Phi}$ is defined as the fracture toughness at a failure probability of 63.2% and is described by

$$K_{0\Phi} = 31 + 77\exp[0.019(T - T_0 - \Delta T_0)]\,\mathrm{MPa}\sqrt{\mathrm{m}}, \tag{C2}$$

where T is the temperature, note that Temp is used for temperature throughout the of the paper. The ΔT_0 constraint correction is given by

$$\Delta T_0 = A\frac{\Delta T_{\mathrm{stress}}}{\sigma_{\mathrm{Y}}}. \tag{C3}$$

Where the T-stress at the plastic limit load is to be used, as developed by Wallin [26]. The factor A has been found to be yield strength dependent, for $\sigma_{\mathrm{Y}} < 600$ MPa, A can be taken as a constant parameter equal to 40 °C. Another choice is $A = \frac{\sigma_{\mathrm{Y}}}{12\,\mathrm{MPa}\,/\,^{\circ}\mathrm{C}}$ which is valid for T-stresses below 300 MPa [2]. Both constraint corrections are used in this paper.

References

[1] Pineau A. Modeling ductile to brittle fracture transition in steels – micromechanical and physical challenges. Int J Fract 2008;150:129–56.
[2] Wallin K. Fracture toughness of engineering materials. first ed. EMAS Publishing; 2011.

[3] McMahon C, Cohen M. Initiation of cleavage fracture in polycrystalline iron. Acta Metall 1965;13:591–604.
[4] Bowen P, Druce S, Knott J. Effects of microstructure on cleavage fracture in pressure vessel steel. Acta Metall 1986;34:1121–31.
[5] Bowen P, Druce S, Knott J. Micromechanical modelling of fracture toughness. Acta Metall 1987;35:1735–46.
[6] Kroon M, Faleskog J. Micromechanics of cleavage fracture initiation in ferritic steels by carbide cracking. J Mech Phys Solids 2005;53:171–96.
[7] Pineau A, Benzerga A, Pardoen T. Failure of metals I: brittle and ductile fracture. Acta Mater 2016;107:424–83.
[8] Lambert-Perlade A, Gourgues A, Besson J, Sturel T, Pineau A. An enhanced probabilistic model for cleavage fracture assessment accounting for local constraint effects. Metall Mater Trans A 2004;35A:1039–53.
[9] Qiao Y, Argon A. Cleavage crack-growth-resistance of grain boundaries in polycrystalline Fe–2%Si alloy: experiments and modeling. Mech Mater 2003;35:129–54.
[10] Qiao Y, Argon A. Cleavage cracking resistance of high angle grain boundaries in Fe–3%Si alloy. Mech Mater 2003;35:313–31.
[11] Stec M, Faleskog J. Influence of grain size on arrest of a dynamically propagating cleavage crack in ferritic steels – micromechanics. Int J Fract 2009;158:51–71.
[12] Stec M, Faleskog J. Micromechanical modeling of grain boundary resistance to cleavage crack propagation in ferritic steels. Int J Fract 2009;160:151–67.
[13] Ritchie R, Knott J, Rice J. On the relationship between critical tensile stress and fracture toughness in mild steel. J Mech Phys Solids 1973;21:395–410.
[14] Beremin FM, Pineau A, Mudry J, Devaux F, D'Escatha Y, Ledermann P. A local criterion for cleavage fracture of a nuclear pressure vessel steel. Metall Trans A 1983;14:2277–87.
[15] Gao X, Faleskog J, Fong Shih C. Analysis of ductile to cleavage transition in part – through cracks using a cell model incorporating statistics. Fatigue Fract Eng Mater Struct 1998;22:239–50.
[16] Bordet S, Karstensen A, Knowles D, Wiesner C. A new statistical local criterion for cleavage fracture in steel. Part I: model presentation. Eng Fract Mech 2005;72:435–52.
[17] Bordet S, Karstensen A, Knowles D, Wiesner C. A new statistical local criterion for cleavage fracture in steel. Part II: application to an offshore structural steel. Eng Fract Mech 2005;72:453–74.
[18] Kroon M, Faleskog J. A probabilistic model for cleavage fracture with a length scale – influence of material parameters and constraint. Int J Fract 2002;118:99–118.
[19] Faleskog J, Kroon M, Öberg H. A probabilistic model for cleavage fracture with a length scale – parameter estimation and predictions of stationary crack experiments. Eng Fract Mech 2004;71:57–79.
[20] Kroon M, Faleskog J, Öberg H. A probabilistic model for cleavage fracture with a length scale – parameter estimation and predictions of growing crack experiments. Eng Fract Mech 2008;75:2398–417.
[21] Hohe J, Friedmann V, Wenck S, Siegele D. Assessment of the role of micro defect nucleation in probabilistic modeling of cleavage fracture. Eng Fract Mech 2008;75:3306–27.
[22] Hohe J, Hardenacke V, Luckow S, Siegele D. An enhanced probabilistic model for cleavage fracture assessment accounting for local constraint effects. Eng Fract Mech 2010;77:3573–91.
[23] Williams P, Bass B, McAfee W. Shallow flaws under biaxial loading conditions – Part II: application of a Weibull stress analysis of the cruciform bend specimen using a hydrostatic stress criterion. J Pressure Vessel Technol 2000;123:25–31.
[24] Wallin K. The Scatter in k_{IC}-Results. Eng Fract Mech 1984;19:1084–93.
[25] ASTM, Standard Test Method for Determination of Reference Temperature, T_0, for Ferritic Steels in the Transition range, ASTM West Conshohocken, U.S., ASTM International, Geneva, Switzerland; 2018.
[26] Wallin K. Quantifying Tstress controlled constraint by the master curve transition temperature T_0. Eng Fract Mech 2001;68:303–28.
[27] Stec M. Micromechanical modeling of cleavage fracture in polycrystalline materials. first ed. Department of Solid Mechanics; 2008.
[28] Rathbun H, Odette G, Yamamoto T, Lucas G. Influence of statistical and constraint loss size effects on cleavage fracture toughness in the transition – a single variable experiment and database. Eng Fract Mech 2006;73:134–58.
[29] Schneiders R, Schindler R, Weiler F. Octree-based generation of hexahedral element meshes. Int Mesh Roundt 1996;5:205–16.
[30] Nelder J, Mead R. A simplex method for function minimization. Comput J 1965;7:308–13.
[31] Rathbun H, Odette G, Yamamoto T, Lucas G. Influence of statistical and constraint loss size effects on cleavage fracture toughness in the transition – a model based analysis. Eng Fract Mech 2006;73:2723–47.
[32] Rathbun H, Odette G, Yamamoto T, Lucas G. Statistical and constraint loss size effects on cleavage fracture – implications to measuring toughness in the transition. Eng Fract Mech 2006;73:134–58.
[33] Anderson TL. Fracture mechanics fundamentals and applications. third ed. Taylor & Francis; 2005.
[34] Wallin K. Statistical aspect of constraint with emphasis on testing and analysis of laboratory specimens in the transition region. Constraint effects in fracture, ASTM 1993;1171:264–88.
[35] Wallin K. Use of the master curve methodology for real three dimensional cracks. Nucl Eng Des 2007;237:1388–94.
[36] Sattari-Far I, Dillström P. Local limit load solutions for surface cracks in plates and cylinders using finite element analysis. Int J Press Vess Pip 2004;81:57–66.

Paper III

Analysis of thermal embrittlement of a low alloy steel weldment using fracture toughness and microstructural investigations

Magnus Boåsen[a] *, Kristina Lindgren[b], Martin Öberg[a],
Mattias Thuvander[b], Jonas Faleskog[a], Pål Efsing[a]

[a] *Solid Mechanics, Department of Engineering Mechanics, KTH Royal Institute of Technology,*
SE-100 44 Stockholm Sweden

[b] *Department of Physics, Chalmers University of Technology, SE-412 96 Göteborg, Sweden*

Abstract

A thermally aged low alloy steel is investigated in terms of its fracture toughness and microstructural evolution and compared to a reference. The main purpose of the study is to investigate the effects of thermal embrittlement on the brittle fracture toughness, and its effects on the influence of loss of crack tip constraint. Ageing appears to enable brittle fracture initiation from grain boundaries besides initiation from second phase particles, making the fracture toughness distribution bimodal as a result. The consequence is that the constraint effect is significantly reduced when grain boundary initiation dominates the toughness distribution, as compared to the reference material where the constraint effect is significant. The microstructure is investigated at the nano scale using atom probe tomography where nanometer sized Cu-rich clusters are found primarily situated on dislocation lines.

---

* Corresponding author.
Address: KTH Solid Mechanics, Teknikringen 8D, SE-100 44 Stockholm Sweden
Email address: boasen@kth.se (M. Boåsen)

1. Introduction

When assessing degradation due to ageing in low alloy steels used as structural materials in pressure vessel components both base and weld metals must be considered, as for example in reactor pressure vessels in nuclear power plants. In this type of materials in nuclear applications, ageing mainly occurs by neutron irradiation and thermal ageing, and generally manifests itself as a hardening effect and an increase in the ductile-to-brittle transition temperature, or in another word *embrittlement*. In pressurized water reactors (PWRs), the pressurizer regulates the pressure and thereby the temperature within the primary loop so that the water is kept from boiling. Following the replacement of the pressurizer in Ringhals unit 4 (R4) in 2011, material extraction was carried out in order to study potential ageing effects on the materials after 28 years of operation. Initial investigations of two of the welds from the pressurizer material displayed a noteworthy increase in the transition temperature $\Delta T_{41\mathrm{J}} = \{78 \text{ and } 71\}$ ˚C and an increase of the yield strength $\Delta R_{\mathrm{p02}} = \{128 \text{ and } 59\}$ MPa, displaying a clear indication of embrittlement due to thermal ageing at the operating temperature of 345 ˚C (no irradiation present in the pressurizer).

Embrittlement is a key aspect in the structural integrity ageing assessment of any structure. Therefore, understanding the changes in the fracture toughness and all its features for a material that undergoes embrittlement is necessary. The cleavage fracture toughness of ferritic steels is strongly dependent on temperature, size and crack tip constraint. Generally, it can be said that higher temperature endorses a more ductile behavior, larger specimens or components will be more brittle, and high constraint will produce a lower fracture toughness than low constraint. To our knowledge, no studies have been published concerning the constraint effect on fracture toughness after the material has undergone embrittlement and how this relates to the behavior of a reference material.

The prevailing explanation to embrittlement due to thermal ageing of low alloy steels in nuclear applications is impurity segregation towards prior austenite grain boundaries, e.g. phosphorus, commonly referred to as grain boundary embrittlement. Studies of thermal ageing include a wide spectra of base and weld metals from reactor types such as the VVER-1000 [1], [2], [3], [4], as well as the western PWRs featuring the typical steels A508 and A533 or its equivalents [5], [6], [7], [8], [9], [10], [11]. All studies referenced here, reports on intergranular fracture due to impurity segregation caused by thermal ageing.

In the extensive review of intergranular failure in steels by Briant and Banerji [12], it is noted that some distinguishable phenomena appear to be related to intergranular failure. One being that segregation of elements from groups IV-VI in the periodic system appears to yield the most potent grain boundary embrittlement, which is also mentioned by McMahon [13]. These groups include elements such as Si, Sn, P and S, which are not uncommon impurities or alloying elements in the steels of interest. Another is that a grain size effect appears to emerge where microstructures with larger grains yields more intergranular fracture than for the case of smaller grains. The authors of [12] speculate that this could be due to a dilution of the impurity elements due to the difference in grain boundary area in relation to grain volume, for the case of smaller grains. This implies that a microstructure with smaller grains would result in a larger degree of dilution of impurity across the grain boundaries and thus less embrittlement, than in a microstructure with larger grains *ceteris paribus*. Another notable phenomenon is the effect of co-segregation of elements such as Ni and Mn, which is indicated to yield a faster and more potent embrittlement [12], [14], [15]. In a study by Banerji et al. [16] concerning the effects of impurities and hydrogen on intergranular fracture in a commercial steel, several heats were tempered at different temperatures in the range 50-625 ˚C and then subjected to Charpy impact testing at room temperature. One of the findings in the study was that the largest decrease of the absorbed energy appeared after tempering at ~350 ˚C with resulting intergranular facets covering the fracture surfaces. Also, a similar grain size dependency as reported in [12] could be observed, i.e. larger grains yielding more embrittlement at the same conditions.

Grain boundary embrittlement as a result of thermal ageing will act as a non-hardening embrittlement since it, in general, does not impede dislocation motion, and gives rise to a fracture morphology with a large incidence of grain boundary facets. It also appears to have several commonalities with the phenomenon called reversible temper embrittlement [12], [17]. The hardening effect that is typically observed in irradiated low alloy steels comes to a large extent from the formation of solute clusters during irradiation. The hardening effect is due to that the solute clusters act as obstacles to dislocation motion, thereby increasing the resistance to plastic flow. In the case of the welds of the Swedish reactor pressure vessels, the irradiation induced solute clusters consists mainly of Mn, Ni, Si and Cu [18], [19], [20]. The formation of similar clusters in a thermally aged weld metal has also been observed by Lindgren et al. [21]. In that study, solute clusters are noted to have been formed preferentially on dislocations as observed by atom probe tomography (APT) and is related to the thermally ageing induced hardening of the weld metal. It should be noted that the weld investigated in this study and the one investigated by Lindgren et al. were extracted from the same pressurizer but from different welds. However, both welds were manufactured with the same welding specifications. In other atom probe studies of thermally aged low alloy steels [22], [23], [24], [25], solute clusters of similar composition as the ones in [21] were found, however these findings were not connected to any changes in mechanical properties.

The weld investigated in this study is a multi-layer weld, which signifies that the weld is built up by several layers of weld beads. This gives rise to a complex microstructure where three distinct grain zones will emerge. These zones are:

I. the as-welded zone, consisting of elongated dendritic grains,
II. the once reheated zone, consisting of small equiaxed grains, and
III. the multiple reheated zone, also consisting of small equiaxed grains.

This will give rise to variations in several properties such as local chemistry, fracture toughness and other mechanical properties. An interesting study of the fracture toughness of multi-layer welds was made by Viehrig et al. [26].

The main purpose of the testing conducted in this paper is to investigate the effects of thermal ageing on the brittle fracture toughness, and its effects on the influence of loss of constraint. Due to the fact that ageing also may lead to weakened grain boundaries, it is also of interest to investigate to what extent this may contribute to the embrittlement, where weakened grain boundaries then will introduce a second mechanism for brittle fracture initiation besides initiation from particle cracking. Thus, the core of this paper is an investigation of the fracture toughness of an in-service thermally aged weld metal from a Swedish nuclear power plant. This is compared to a reference material from a replaced reactor pressure vessel head, which has been in operation at a lower temperature than the pressurizer and where the effects of ageing therefore are considered minor. The study presents the results from an extensive experimental program where effects of ageing on the constraint sensitivity has been a focal point. Moreover, results from ductile fracture toughness testing, and tensile as well as hardness testing are presented along with an examination of the materials microstructure on the nano scale.

The outline of the paper is as follows: Section 2 presents the materials used in this study in terms of chemical composition, as-manufactured mechanical properties, along with the experimental set-up used. Section 3 presents the outcome of the experimental program including fractography and results from APT.

2. Materials and experiments

2.1. Materials

The thermally aged material investigated in this study has been extracted from the decommissioned and replaced pressurizer of the Ringhals unit 4 reactor. The pressurizer was manufactured by Uddcomb from plates of low alloy steel of the type A-533 Gr B Cl. The weld metal comes from the circumferential weld connecting the lower head to the first cylindrical structure of plates in the pressurizer. The studied weld was manufactured using submerged-arc welding employing a weld wire with a low Cu – high Mn-Ni content, characteristic for several of the nuclear pressure vessels manufactured by Uddcomb. The measured chemical composition of the welding wire and flux combination can be found in Table 1. A post weld heat treatment was conducted for residual stress relief at 620 ˚C as part of the fabrication procedure. The pressurizer was in operation from 1983 to 2011, gathering 215 000 h at an operating temperature of 345 ˚C. The pressurizer was well insulated during its operation and consequently the temperature gradient through the thickness can be considered negligible. The check-in mechanical testing of the weld metal can be found in Table 2. The material from the pressurizer will henceforth be denoted as *R4PRZ*.

A reference material extracted from the replaced reactor pressure vessel head of Ringhals unit 3 was also included in the testing program for comparison purposes. This material was chosen since there was no archive material available for the pressurizer. A weld with similar Cu-Mn-Ni-Si content and check-in mechanical properties as the pressurizer was chosen. The reactor pressure vessel head was manufactured from forgings of A-508 cl 2 by Uddcomb and was welded using the same manufacturing specifications as the R4PRZ. The measured chemical composition of the reference material can be found in Table 1, and the check-in mechanical properties in Table 2. The reference material was in operation between 1981 and 2005 accumulating 176 000 h at 310-315 ˚C. Preliminary testing (not presented here) showed that the effects of thermal ageing at this operating temperature were minor in comparison to those of the pressurizer. The reference material will be denoted as *R3RPVH* throughout this paper.

Table 1. Chemical composition of the investigated weld metals from the manufacturing documentation.

Wt. %	C	Si	P	S	V	Cr	Mn	Co	Ni	Cu	Mo	Sn	Fe
R4PRZ	0.082	0.20	0.013	0.006	0.004	0.14	1.62	0.008	1.61	0.06	0.45	0.005	Bal.
R3RPVH	0.08	0.22	0.008	0.006	0.000	0.03	1.66	0.019	1.57	0.07	0.49	0.002	Bal.

Table 2. Check-in mechanical properties of the investigated weld metals.

	R_{p02}/MPa	T_{41J}/°C
R4PRZ	579	-53
R3RPVH	575	-59

2.2. Fracture testing

The fracture toughness testing in the investigation of the constraint effect utilizes SEN(B)-specimens with the same overall dimensions but with different crack depth, deep for a state of high constraint and shallow for low constraint, for an illustration see Figure 1. Also included in the study is a small, deeply cracked SEN(B)-specimen as a reference specimen. All specimens were extracted as T-S oriented with dimensions $W = \{30 \text{ and } 14\}$ mm, $B = \{15 \text{ and } 7\}$ mm, $a/W = \{0.5 \text{ and } 0.1\}$, and were manufactured such that the weld was centered in the specimen with base metal on each side. All specimens for investigation of the brittle fracture toughness were manufactured without side-grooves.

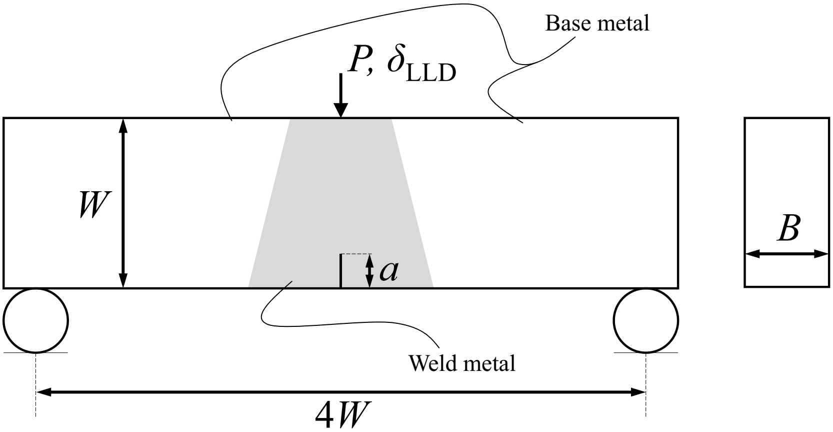

Figure 1. Schematic illustration of a SEN(B)-specimen used in the experiments.

The testing for the brittle fracture toughness was conducted in accordance with ASTM E1921 [27], with the exception that the standard does not cover testing of specimens containing shallow cracks. The cracks were created using fatigue pre-cracking at room temperature according to the recommendations in E1921, which resulted in straight crack fronts in all specimens. When pre-cracking the shallow specimens, the crack length was estimated using a strain measurement technique. Testing was carried out in a computer controlled cooling chamber utilizing liquid nitrogen to cool the specimen. The fracture toughness testing was carried out in displacement control with a loading rate corresponding to 1 $\mathrm{MPa}\sqrt{\mathrm{m}}/\mathrm{s}$ during the initial elastic region of the test. The fracture toughness was evaluated from the load line displacement. The J-integral at failure was calculated from the load line displacement (LLD) where the plastic η-factor valid for shallow cracks in SEN(B)-specimens was taken from Faleskog et al. [28].

The brittle fracture toughness results were interpreted by means of the master curve standard ASTM E1921 [27]. The ductile-to-brittle reference temperature T_0 was evaluated according to that standard. The master curve concept is based on a probabilistic weakest link model for brittle cleavage fracture assuming small-scale yielding conditions and self-similar crack tip fields [29]. The probability of failure at K_{Jc} is expressed by

$$P_f = 1 - \exp\left(-\frac{B}{B_0}\left[\frac{K_{Jc} - K_{\min}}{K_0 - K_{\min}} \right]^4 \right), \tag{1}$$

where B is the thickness of the specimen (or crack front width), B_0 is a reference thickness which is set to 1T = 25.4 mm, $K_{\min}$ is a threshold fracture toughness, and $K_0 = K_0\,(T,\, T_0)$ is a temperature dependent reference fracture toughness that is referenced to 100 $\mathrm{MPa}\sqrt{\mathrm{m}}$ for a 1T specimen at T_0. More specifically, K_0 is well described by

$$K_0 = 31 + 77\exp\left(0.019\left[T - T_0\right]\right)\ \mathrm{MPa}\sqrt{\mathrm{m}}. \tag{2}$$

For the master curve to give a good description of a material´s brittle cleavage fracture toughness the material itself needs to be homogeneous. In the case of a large degree of scatter due to material inhomogeneity, ASTM E1921 supplies additional methodology of T_0-evaluation so that a conservative estimate of the fracture toughness can be ensured. One example of such a method is the SINTAP-methodology, which now has been included in E1921, where an additional safety factor is included in the evaluation of T_0. Such methods may be needed in the evaluation of the fracture toughness of weld metals, where the scatter may be larger than that of more microstructurally homogeneous base metals. Another example is the case where the material displays a bimodal toughness distribution, where the bimodal master curve [30] can be utilized, which is expressed as

$$P_f = 1 - p_a \exp\left(-\frac{B}{B_0}\left[\frac{K_{J\mathrm{c}} - K_{\min}}{K_0^A\left(T_0^A\right) - K_{\min}} \right]^4 \right) - \left(1 - p_a\right)\exp\left(-\frac{B}{B_0}\left[\frac{K_{J\mathrm{c}} - K_{\min}}{K_0^B\left(T_0^B\right) - K_{\min}} \right]^4 \right). \quad (3)$$

The bimodal master curve requires three parameters that needs to be estimated, where $T_0{}^A$ and $T_0{}^B$ correspond to the reference temperature for each mechanism (mode in the distribution), respectively, and p_a is a probability scaling parameter that defines the contribution of each mechanism.

As the original master curve model is based on self-similar crack tip fields (small-scale yielding, high constraint), it is not capable of handling the effect of loss of constraint. In order to incorporate the effect of constraint, an empirical correction of T_0 by the T-stress is proposed by Wallin [31], [32], as

$$T_0 = T_0^{\text{high constraint}} + \Delta T_0^{\text{constraint}}, \text{ where } \Delta T_0^{\text{constraint}} = A\frac{\Delta T_{\text{stress}}}{\sigma_{\text{y}}}. \quad (4)$$

Here, the difference in T-stress at the limit load between the predicted geometry and the geometry used to determine $\mathrm{T}_0^{\text{high constraint}}$ should be used, where $\mathrm{T}_0^{\text{high constraint}}$ normally is referred to as T_0, as the standard test method prescribes the use of deeply cracked specimens that produce a state of high constraint. In (4), the factor A is a yield strength dependent parameter that is empirically found to be approximately $\sigma_{\text{y}}/10\,\text{MPa/°C}$ [31] for $\sigma_{\text{y}} > 600$ MPa and constant equal to 40 ˚C [32] when σ_{y} is below 600 MPa. It should be noted that the constraint correction of the master curve is still partially developed for more complex geometries [33].

As the main purpose of this study is to investigate the sensitivity to the constraint effect on the fracture toughness of the thermally aged weld metal from the pressurizer and compare those results to the reference material available, a well-grounded approach is needed. An objective way to compare the constraint sensitivity of two materials is to choose the testing temperatures such that the median of the high constraint fracture toughness coincides. The next step is to conduct low constraint testing at the same temperatures, elucidating potential differences in the constraint effect on the fracture toughness between the two materials.

The testing was therefore conducted in the following steps:

i. Initial test series according to ASTM E1921 to find the reference temperature T_0 for the two materials

ii. use T_0 to determine temperatures where the high constraint fracture toughness will be the same for the two materials

iii. conduct remaining test series at the chosen temperature, high and low constraint as well as small specimens.

From the test results in step *i*, T_0 was evaluated to determine the testing temperatures to be used in step *iii*. The testing temperatures that would yield the same high constraint brittle fracture toughness was chosen to be -50 ˚C for R4PRZ and -90 ˚C for R3RPVH. Both materials were tested in series of 12 specimens in step *iii*.

Alongside the tests for the brittle fracture toughness, tests for the ductile fracture toughness were also conducted. These were carried out at a temperature of 75 ˚C to avoid brittle fracture altogether, i.e. clearly being on the upper shelf. The testing was performed with SEN(B)-specimens with side-grooves to promote uniform growth across the thickness of the specimens. The specimens were extracted from the T-S orientation with dimensions W = 30 mm, B = 15 mm, B_N = 12 mm, and a/W = 0.5, which is the same as used for the specimens in the brittle fracture tests. All testing was conducted in accordance with ASTM E1820 [34]. The J-integral was calculated from the crack mouth opening displacement (CMOD).

2.3. Tensile and hardness testing

Uniaxial tensile testing was also carried out on round bar specimens of both the weld and the base metal. In addition, hardness testing was performed on the weld metal, before and after heat treatments at 430 ˚C and 600 ˚C, respectively. Note that different samples were used for the different temperatures. The hardness tests were performed to investigate the recovery of the ageing induced hardening during heat treatments. Hardness testing according to Vickers with an indentation load of 10 kgf was chosen as the test method. The specimens used were manufactured into blocks measuring 15 mm × 8 mm × 4 mm. An initial grid of indents was made to map out the initial hardness of the two materials, R4PRZ and R3RPVH, were the samples displayed a slight variation of hardness across the surface intended for measurement, as a result of the varying microstructure inherent to the weld. Hardness was also measured across and along the centerline of the weld in both materials.

2.4. Atom Probe Tomography and Transmission Electron Microscopy

The nanostructure of the material has been investigated by APT, which was performed in a LEAP 3000X HR from Imago Scientific Instruments. From the results of the study in [21], it was expected that unevenly distributed Ni-Mn-Cu-Si rich clusters would be found. Due to this, large volumes of material were analysed, and thus laser pulsing was used in addition to voltage pulsed analysis. However, laser pulsing affects the Si position due to surface diffusion [35] and thus both pulsing modes were used. For voltage pulsed analysis, a temperature of 50 K and pulse fraction of 20 % was used. For laser pulsed analysis, the temperature was 30 K and the laser energy 0.3 nJ. In both cases the laser pulse frequency was 200 kHz. The sample preparation was done using a standard two-step electropolishing method [36], finishing with millisecond pulsing to get rid of surface oxides. The reconstructions were made in the IVAS 3.6 software, using reconstruction parameters k between 4.0 and 5.3, and evaporation field of 33 V/nm in the case of voltage pulsed analysis and 23 V/nm for laser pulsed analysis. The image compression factor was set to 1.65 for all reconstructions.

The cluster analysis was performed using the maximum separation method (MSM) [37], [38], a method that requires a careful choice of parameters in order to get relevant and comparable results [39], [40]. Cluster parameters were chosen by comparing the data set to a randomised version, and aiming to avoid defining random fluctuations in composition as clusters. Solute elements were chosen to be Cu, Ni, and Mn. The maximum solute atom distance in order for two atoms to be considered being in a cluster, $d_{\max}$, was set to 0.45 nm, and the smallest number of solute atoms defining a cluster, $N_{\min,}$ was chosen to 20. Cluster sizes were determined by calculating the number of solute atoms in the clusters, assuming α-Fe body centred cubic structure and a detection efficiency of the LEAP of 37 %. The amount of Fe in the cluster is uncertain, since local magnification effects focus Fe atoms into the clusters during field evaporation [41], [42]. Thus, the 50 % Fe detected in clusters in these APT reconstructions is probably considerably lower in the actual material. Here, the Fe content is excluded from the clusters when calculating the size. This might give a slight underestimation if there is any Fe in the clusters. Cluster compositions were determined using MSM as well. For the number density, clusters on the edge of the analysis were identified and counted as half a cluster. It should be noted that the terms precipitate and cluster is used interchangeably in this paper, as the characterisation method (APT) does not give any crystallographic information.

3. Experimental results

3.1. Fracture toughness tests

In the evaluation of the reference temperature T_0, it was observed that the two materials behaved differently, which was due to the degree of inhomogeneity. The thermally aged R4PRZ displays a larger degree of inhomogeneity and has therefore been evaluated with the more conservative SINTAP-evaluation than that of the reference material R3RPVH, which was evaluated according to the normal procedure of E1921. The deeply cracked specimens of both data sets are shown as a function of testing temperature in Figure 2 together with the master curve predictions based on the respective materials' T_0. It is clear that the thermally aged R4PRZ is more brittle than R3RPVH, with a difference in T_0, ΔT_0 = 45 ˚C. Estimating the T_{41J} from the T_0 of R3RPVH by the empirical relation supplied in E1921 ($T_{41J} = T_0 + 24$ ˚C) yields T_{41J} = -54 ˚C, which agrees well with the check-in values for T_{41J} listed in Table 2, giving justification to using R3RPVH as a (fracture toughness) reference to R4PRZ.

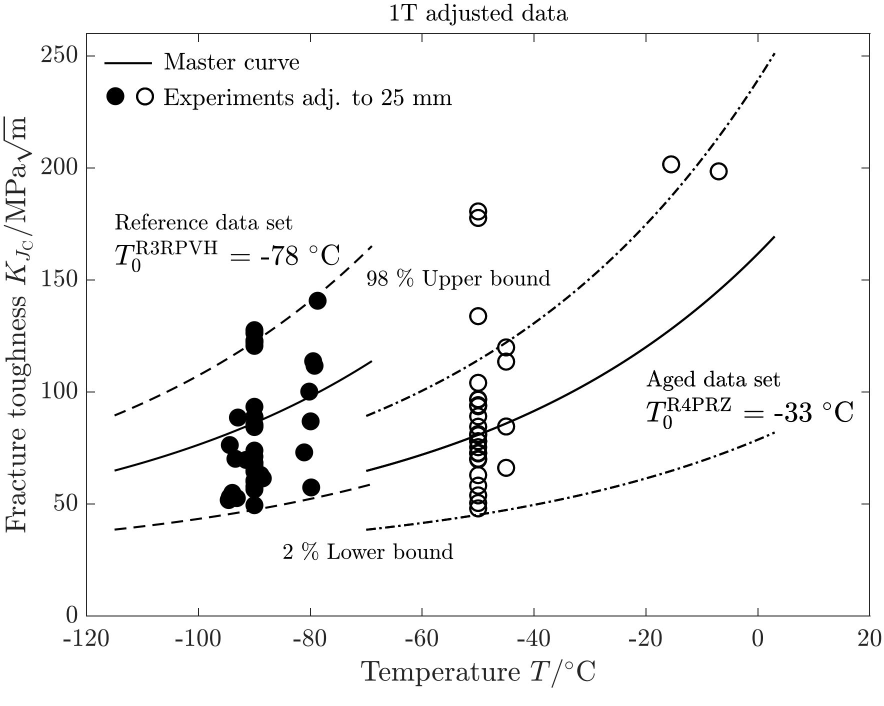

Figure 2. Fracture toughness of individual specimens belonging to both R3RPVH and R4PRZ against testing temperature, and the predicted temperature dependence from the master curve model.

By looking at the ranked probability of the single temperature tests, i.e. the constraint sensitivity tests, it appears that the R4PRZ displays a bimodal toughness distribution as seen in Figure 3, while R3RPVH does not, as seen in Figure 4. The rank probability is here computed as the median rank by Benard's approximation $P^i_{\mathrm{rank}} \approx (i - 0.3)/(N + 0.4)$.

Especially noticeable is that the low constraint R4PRZ specimens (*a/W* = 0.1) behave very similar to high constraint R4PRZ specimens (*a/W* = 0.5) at rank probability levels below 0.4, where the fracture toughness essentially coincide (Figure 3). While at higher levels of rank probability, the low constraint R4PRZ specimens (*a/W* = 0.1) are subject to ductile crack growth up to 1 mm prior to brittle failure. Consequently, the scatter in fracture toughness becomes extreme and is found in the range 9.6 kN/m to 785 kN/m.

As seen in Figure 5, the chosen temperatures for the constraint sensitivity tests were appropriate as the resulting fracture toughness distribution of the high constraint specimens (Figure 5 a) shows a close similarity for both materials. In Figure 5 (b), the low constraint results for both materials are compared, which clearly shows the difference between the thermally aged R4PRZ and the reference R3RPVH. In Figure 5 (c), a comparison of the fracture toughness of the small specimens is shown, which aligns well, once again displaying the conformity of fracture toughness pertinent to high constraint geometries.

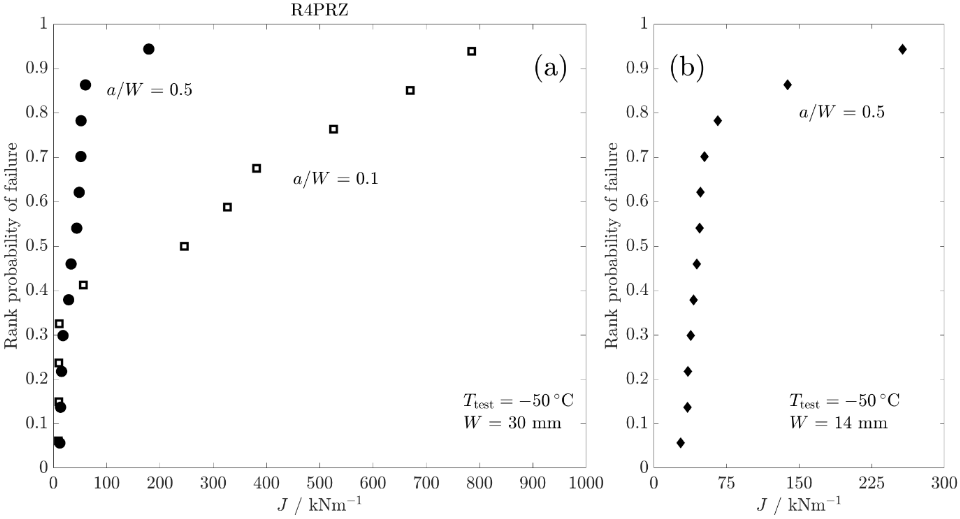

Figure 3. Rank probabilities for the fracture tests of R4PRZ at the test temperature -50 ˚C. (a) Data sets where *W* = 30 mm and *a/W* = {0.5, 0.1}. (b) Data set where *W* = 14 mm and *a/W* = 0.5.

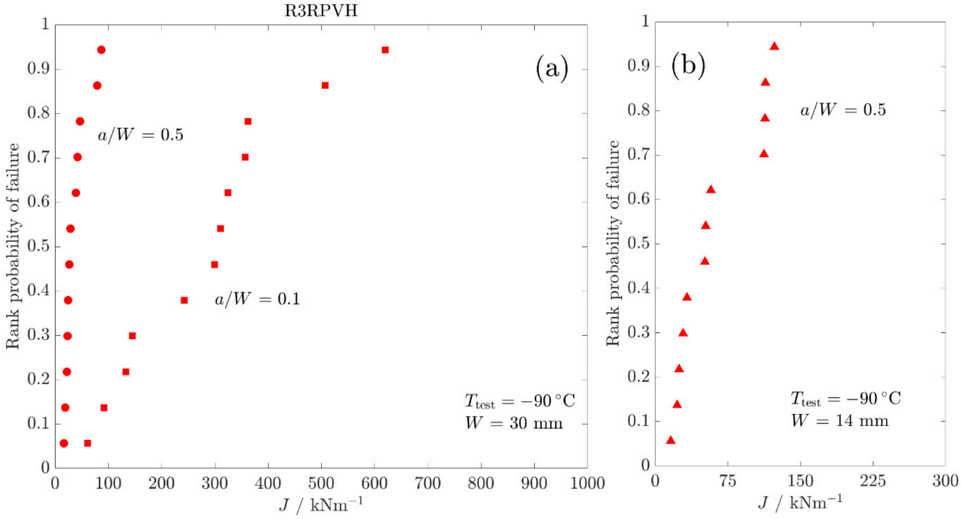

Figure 4. Rank probabilities for the fracture tests of R3RPVH at the test temperature -90 ˚C. (a) Data sets where $W = 30$ mm and $a/W = \{0.5, 0.1\}$. (b) Data set where $W = 14$ mm and $a/W = 0.5$.

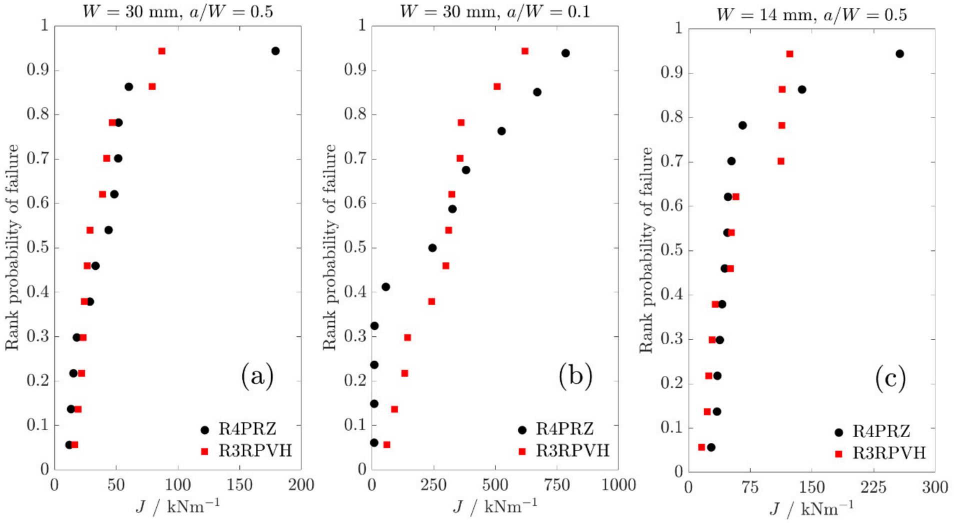

Figure 5. Rank probabilities for the fracture tests of R4PRZ and R3RPVH for comparison of fracture toughness distribution. (a) Data set where $W = 30$ mm and $a/W = 0.5$. (b) Data set where $W = 30$ mm and $a/W = 0.1$. (c) Data set where $W = 14$ mm and $a/W = 0.5$.

Fractography of the single temperature fracture tests presented in Figure 3-Figure 5 reveals that initiation of brittle fracture in the *low toughness specimens* from the thermally aged R4PRZ has occurred by grain boundary cracking. Here, the fracture surfaces are consistently riddled with intergranular facets in direct connection to the crack front. This with no evidence of brittle fracture initiation from a second phase particle, as is commonly observed for cleavage fracture in ferritic steels. Observations of the *higher toughness specimens* unveil transgranular features and subsequently fracture initiation from second phase particles in tandem with intergranular features. For instance, low toughness brittle fracture appears to be solely associated with intergranular fracture while at higher levels of toughness, a mixture of both inter- and transgranular fracture appears to be the underlying cause of brittle fracture. Some examples of this is shown in Figure 6 and Figure 7 where low and high toughness specimens containing deep and shallow cracks are shown. For clarity, a low magnification image (uppercase) is associated with one of higher magnification (lowercase) per level of fracture toughness shown.

Turning to the fracture morphology of the reference material R3RPVH. In this material, virtually unaffected by ageing, transgranular fracture is dominating the entire specimen population with few exceptions, where traces of intergranular fracture can be found in low toughness specimens. It should be noted that R3RPVH is not a perfect reference material, since it has been in operation during a significant number of years, however at a lower temperature and shorter time than R4PRZ.

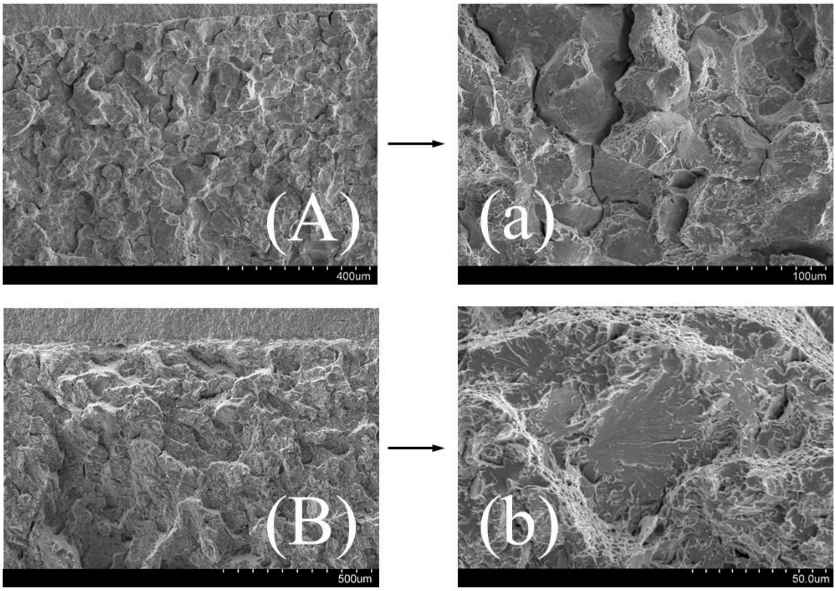

Figure 6. Fractography of deeply cracked specimens (*a/W* = 0.5) from the R4PRZ data set. Specimen {(A), (a)} fractured at a *low* toughness of K_{JC} = 52 MPa$\sqrt{\text{m}}$, displays intergranular fracture, note secondary cracks in (a). Specimen {(B), (b)} fractured at a *higher* toughness of K_{JC} = 108 MPa$\sqrt{\text{m}}$, displays transgranular fracture, probable initation point in (b).

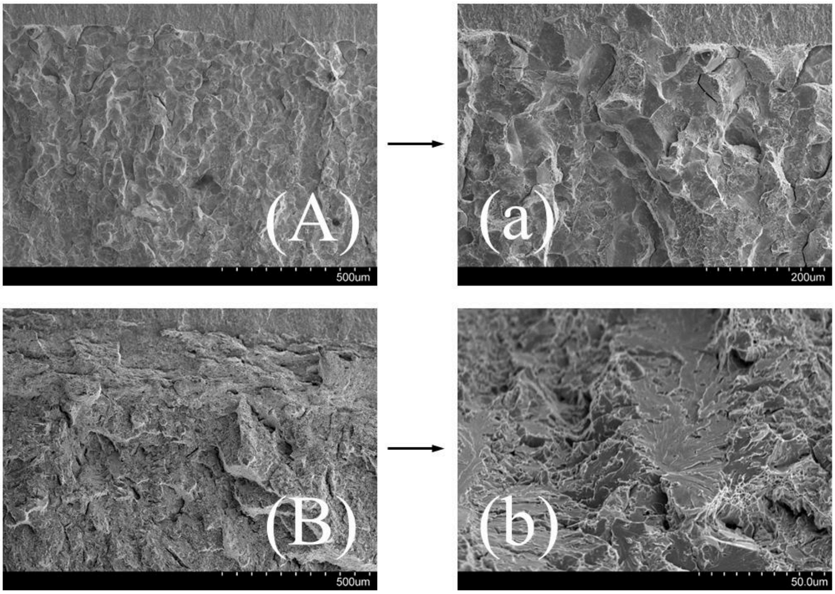

Figure 7. Fractography of shallowly cracked specimens (*a/W* = 0.1) from the R4PRZ data set. Specimen {(A), (a)} fractured at a *low* toughness of K_{JC} = 50 MPa$\sqrt{\text{m}}$, displays intergranular fracture, note secondary cracks in (a). Specimen {(B), (b)} fractured at a *higher* toughness of K_{JC} = 270 MPa$\sqrt{\text{m}}$, displays transgranular fracture, probable initation point in (b).

The results from the ductile fracture toughness testing is shown in Figure 8, where both the force-CMOD relation and the J_R-behavior for the two materials are shown. From these results it can be clearly distinguished that the ductile initiation fracture toughness J_{IC} = 337 kN/m is the same for both materials while the resistance to crack growth differs such that the thermally aged R4PRZ offers less resistance to crack growth after approximately 1 mm of growth.

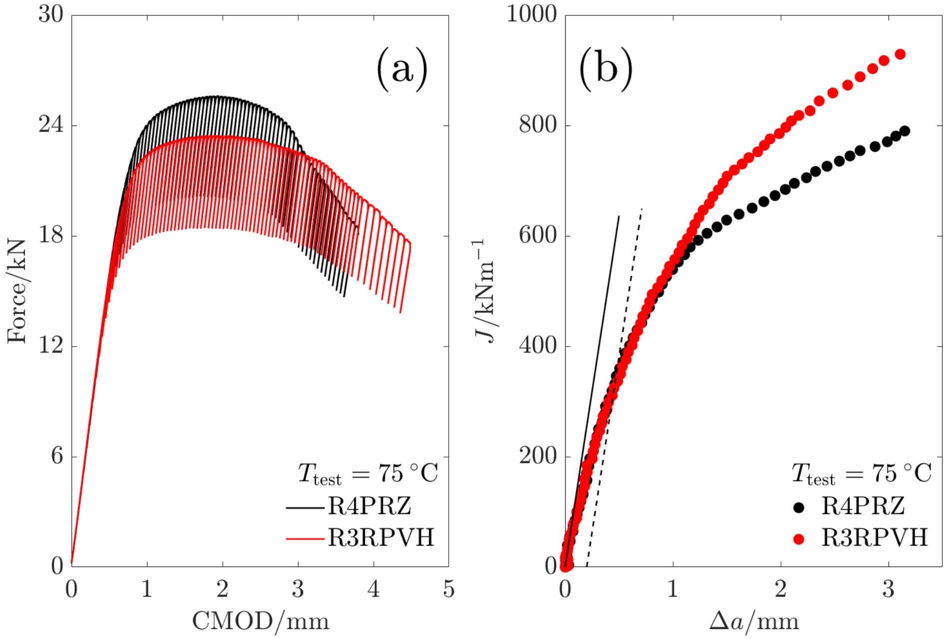

Figure 8. Results from ductile fracture toughness testing. (a) Force-CMOD relation. (b) J-Δa relation.

3.2. Tensile and hardness tests

Figure 9 shows a selection of the tensile tests that were carried out in this investigation. Figure 9 (a) shows the tensile results at the testing temperatures pertinent to the constraint sensitivity fracture tests and it can be seen that the yield and ultimate tensile strength are virtually the same. Figure 9 (b) displays the tensile results at room temperature, where it can be seen that the thermally aged R4PRZ appears to be slightly stronger than the reference R3RPVH. The tensile testing indicates that both materials are subjected to some hardening due to operation as the yield strength from the current investigation is higher than that of the check-in testing, a comparison is shown in Table 3.

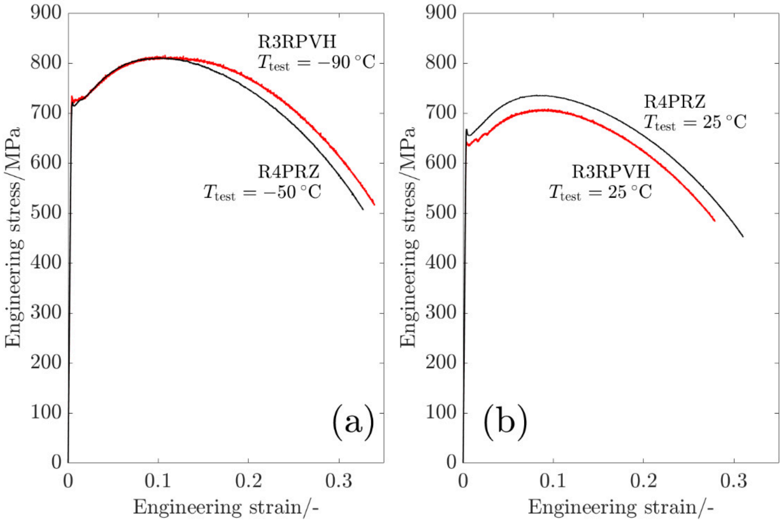

Figure 9. Tensile tests of R4PRZ and R3RPVH. (a) At constraint sensitivity test temperatures. (b) At room temperature.

Table 3. Comparison between check-in yield strength and the results obtained in this investigation.

R_{p02}/MPa	Check-in	Current	Difference
R4PRZ	579	656	77
R3RPVH	575	637	62

The results from the Vickers hardness tests are shown in Figure 10, where the hardness measured across and along the weld centerline in one of the R4PRZ and R3RPVH SEN(B)-specimens used for brittle fracture testing is plotted. It can clearly be seen that the hardness corresponds well with the results from the tensile tests in Figure 9 for the two materials. For the hardness tests combined with heat treatments, annealing at 430 ˚C gave no change in hardness for times up to 50 h. However, annealing at 600 ˚C gave the results shown in Figure 11, where normalized hardness is presented for both materials against annealing time. The error bars represent the range in hardness from the measurements after annealing. The initial hardness of the specimens used in Figure 11 can be represented by 248 kgf/mm^2 and 254 kgf/mm^2, which decreased to 220 kgf/mm^2 and 213 kgf/mm^2 after 25 h of annealing for R4PRZ and R3RPVH, respectively. It should be noted that a significant variability in hardness exists in the specimens, hence the wide range of the error bars.

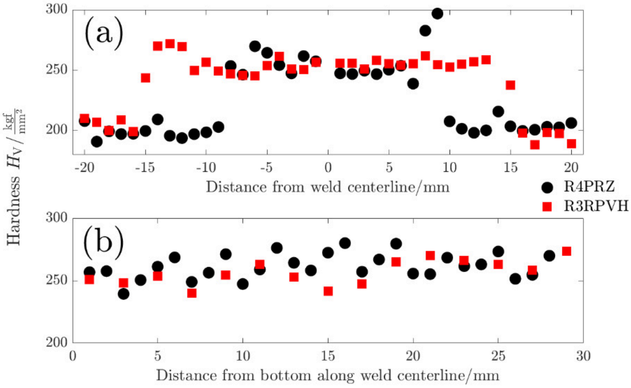

Figure 10. Hardness measured on SEN(B)-specimens of R4PRZ and R3RPVH. (a) Shows the hardness across the weld centerline, from base metal to weld metal into base metal. (b) Shows the hardness along the weld centerline.

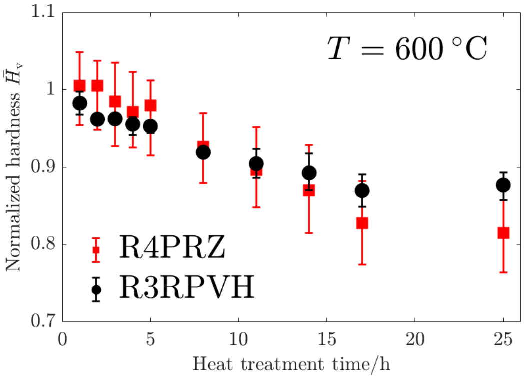

Figure 11. Hardness of R4PRZ and R3RPVH against heat treatment time. Error bars represent the range in hardness measurement at each annealing.

3.3. Master curve analysis of single temperature fracture tests

By estimating the parameters of the bimodal master curve relevant to the single temperature fracture tests of R4PRZ, the results in Figure 12 are obtained. When the three parameters are estimated for the high constraint specimen in Figure 12 (a), it appears to yield a consistent prediction of the size effect in Figure 12 (c). However, there is no ambiguous manner in which a constraint adjustment can be made to reliably predict the experimental rank probabilities of the low constraint specimen in Figure 12 (b). Therefore, the results presented in Figure 12 (b) correspond to the low constraint specimen without corrections for loss of constraint. Furthermore, the bimodal master curve prediction in Figure 12 (b) was based on a new set of parameters that were estimated to fit the experimental results shown in this graph. Thus, one set of bimodal parameters cannot be used to capture the experimental results of both the high and low constraint specimens displayed in Figure 12. It should be noted that the master curve methodology, unimodal and bimodal, is based on self-similar crack tip fields related to a stationary crack, while the results in Figure 12 (b) are subject to significant ductile crack growth prior to brittle failure. This will have an impact on the accuracy of the master curve with regards to parameter estimation and model predictions around and above the ductile initiation fracture toughness, $J_{\mathrm{IC}} = 337$ kN/m, $K_{\mathrm{IC}} = 272$ MPa$\sqrt{\mathrm{m}}$.

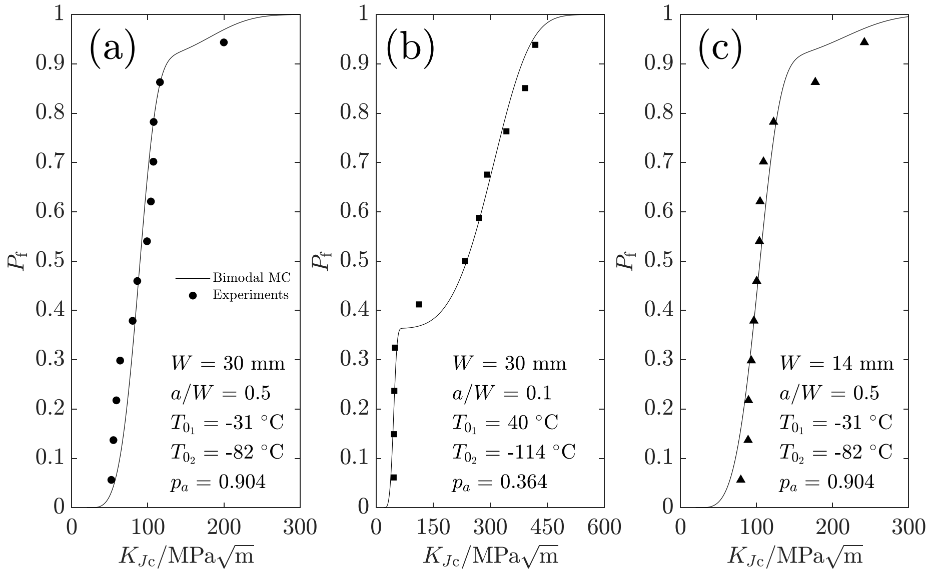

Figure 12. Comparison of predicted failure probabilities (solid lines) from the bimodal master curve with rank probabilities for the experimental fracture tests pertaining to R4PRZ (symbols). (a) Data set where W = 30 mm and a/W = 0.5. (b) Data set where W = 30 mm and a/W = 0.1. (c) Data set where W = 14 mm and a/W = 0.5.

Note, no constraint correction using e.g. T-stress has been used, the low constraint data has been used for both prediction and parameter estimation.

In Figure 13, master curve predictions of the probability of failure of the fracture tests of the reference material, R3RPVH are shown. Clearly, there is no need to use the bimodal master curve to describe the fracture toughness distribution of the reference material. The results presented in Figure 13 (a) corresponding to the low constraint specimens (a/W = 0.1) are successfully constraint corrected using Eq. (4) where $A = \sigma_y / 10\,\mathrm{MPa/°C}$.

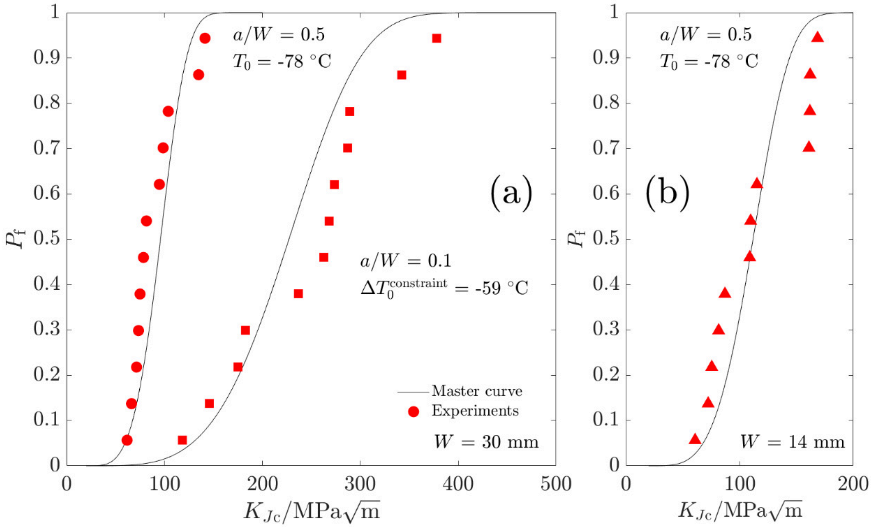

Figure 13. Comparison of predicted failure probabilities (solid lines) from the (unimodal) master curve with rank probabilities for the experimental fracture tests pertaining to R3RPVH (symbols). (a) Data set where W = 30 mm and a/W = 0.5 and data set where W = 30 mm and a/W = 0.1. (c) Data set where W = 14 mm and a/W = 0.5. Note, T_0 has been subject to constraint correction using the T-stress for the low constraint specimens, a/W = 0.1 presented in (a).

3.4. Atom Probe Tomography and Transmission Electron Microscopy

Regarding the results from the APT investigation, the measured chemical compositions can be seen in Table 4. The standard deviation between the different analyses of the same material is given, as APT is a local method and the welded material is chemically heterogeneous on the considered length scale. The average Ni content of the R4PRZ is slightly higher than that of R3RPVH. The average compositions (at.%) are generally close to the nominal composition (given in wt.% in Table 1).

Table 4. Chemical compositions as measured by APT. The standard deviation between the runs are given as an estimate of the local variation in composition. N and S are omitted due to their overlaps with Si and O, respectively, in the APT spectrum.

At. %	R4PRZ	R3RPVH
C	0.03±0.03	0.03±0.01
Si	0.42±0.09	0.47±0.04
P	0.02±0.01	0.01±0.01
V	0.004±0.003	0.002±0.001
Cr	0.13±0.01	0.05±0.01
Mn	1.33±0.15	1.35±0.07
Co	0.01±0.01	0.02±0.01
Ni	1.69±0.58	1.36±0.08
Cu	0.05±0.01	0.05±0.01
Mo	0.12±0.07	0.19±0.07
Fe	Bal.	Bal.

In the R4PRZ material, clusters were found using APT, see Figure 14. The analyzed material was found to be heterogeneous; some of the smaller analyses did not contain any features whereas some contained many. Solute clusters containing Ni, Mn, Cu, and Si, were found in the reconstruction seen in Figure 14. Some of these appear to have nucleated on carbonitrides. The carbonitrides contain V, Cr, Mo and some Mn, and some are found on dislocations, decorated with Mo,C, and Mn. As seen in the figure, not all carbonitrides contain all elements. The reconstruction in Figure 14 also contain a boundary layer with Mo, C, some Ni, Si and Mn, and a few clusters/precipitates, out of which two appear to contain Cu and two does not.

A difficulty when analyzing the clusters and carbonitrides was the overlap in the mass spectrum at 32.5 Da. Both $^{65}Cu^{2+}$ and VN^{2+} have peaks here in the voltage pulsed analyses. This was handled by using the peak at 31.5 Da to identify Cu^{2+} atoms, comparing with the local natural abundance of ^{65}Cu and ^{63}Cu. An example of this is shown in Figure 15, where the top precipitate is a carbonitride and the peak at 32.5 Da is mainly VN^{2+}. The 32.5 Da peak atoms then mainly coincide with the V atoms, whereas there are Cu atoms spread out outside the carbonitride. In the lower cluster, that consists of mainly Ni, Mn, Si and Cu, the 32.5 Da peak is mainly $^{65}Cu^{2+}$, and the ions coincide with the $^{63}Cu^{2+}$ atoms at 31.5 Da. In laser pulsed runs the field is lower and thus most of the Cu evaporates as 1+ ions [43]. In this case, the overlap problem is less prominent as VN still evaporates as VN^{2+}.

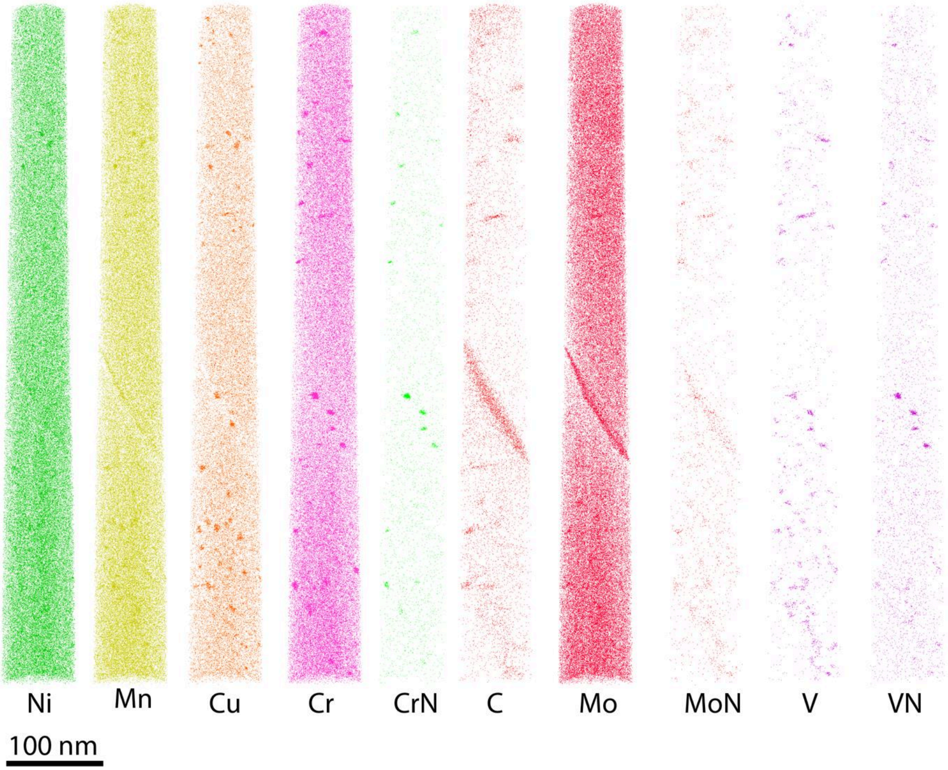

Figure 14. APT reconstruction of thermally aged R4PRZ material. Only ions that are not randomly distributed are shown. This analysis was run in laser pulsed mode.

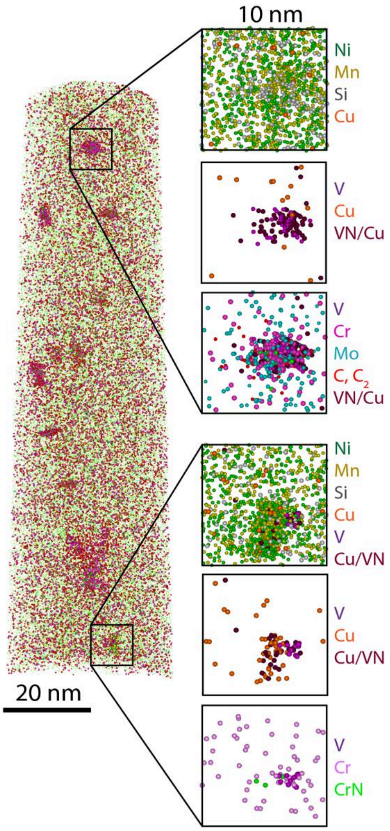

Figure 15. Atom probe reconstruction of the thermally aged R4PRZ material. Two precipitates are cut out in boxes of 10×10×10 nm^3, with different elements shown. The top V and Cr-rich carbonitride does not contain any Ni or Cu, and only small amounts of Mn. The ions marked VN/Cu are mainly VN. The lower precipitate contains mainly Ni, and Mn, and some Cu. There is also some V in one part of the precipitate. Most of the Cu/VN ions are probably Cu. This analysis was run in voltage pulsed mode.

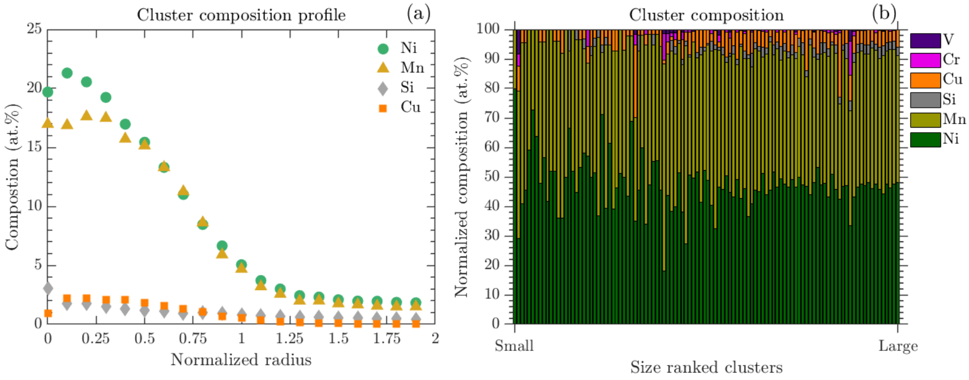

Figure 16. The composition profile, and the cluster composition cluster by cluster, normalized by Fe in R4PRZ. The composition profile is not normalized in terms of composition, but the radius is. Zero corresponds to the cluster center, and unity to the edge of the cluster. The cluster composition cluster by cluster is sorted in increasing size.

In Figure 16, the normalized composition profile and the individual cluster compositions of one analysis are shown. The clusters contain mainly Ni and Mn, and smaller amounts of Cu and Si. It was found that the cluster Cu content varied between the different analyses, and that the example in Figure 16 is low in Cu. The clusters have similar composition within the same analysis. Many of the clusters contain some V or Cr. The average size of the Cu-rich clusters was also varying between the analyses, but the average was found to be 2.1±0.3 nm, and the number density $0.13 \pm 0.05 \cdot 10^{23}$ /m^3.

The reference material from the RPVH of Ringhals R3, R3RPVH, was also analysed using APT. One reconstruction can be found in Figure 17. In general, this material contained a lower density of small carbonitrides than the pressurizer. Still, some were found, and also Mo and C enriched dislocations, and boundaries. In Figure 17 a Mo-rich carbide is sitting on the boundary.

Interestingly, occasional clusters containing Cu, Ni, and Mn were found in the R3RPVH material. In Figure 17, one is present on the boundary layer. In other reconstructions, a few clusters were found on dislocations. The number density of the precipitates was very low, and they were not homogeneously distributed.

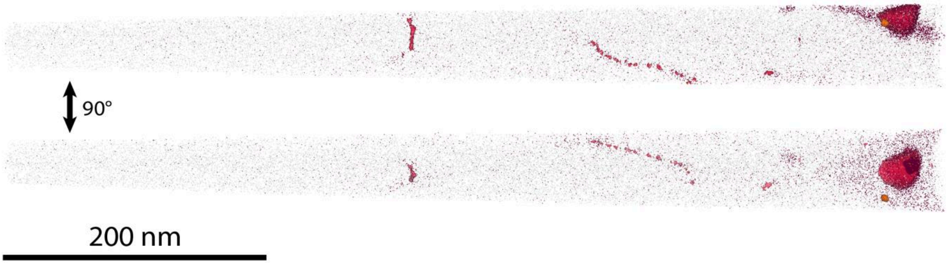

Figure 17. APT reconstruction of the R3RPVH. Red isoconcentration surfaces correspond to Mo 1.9%, orange to Cu 1%, and brown dots are C atoms. A few dislocations are visible as well as a boundary layer containing a Mo-rich carbide and a Cu-rich precipitate. The outline of the analysis is shown in grey. The reconstruction is turned 90°.

4. Discussion

The in-service thermal ageing of the pressurizer weld metal from Ringhals unit 4 appears to manifest through both hardening and non-hardening embrittlement mechanisms. That is, both by an increase in yield strength and by a weakening of the grain boundaries of the material. The effects of the embrittlement due to thermal ageing are profound in that they both give a significant change in the reference temperature T_0 and affects the fracture toughness distribution. As seen in Figure 3-5 the comparison between the fracture toughness distributions of R4PRZ and R3RPVH reveals that there are some apparent differences at conditions that should be equal in terms of the high constraint fracture toughness. The most notable difference being that the low constraint specimens of R4PRZ shows a very wide range in the test data, where the most brittle specimens display fracture initiation through intergranular fracture and the tougher specimens appear to experience brittle fracture initiation from both grain boundaries and second phase particles, where the latter appears to bring out transgranular fracture features.

The toughness distribution of the R4PRZ appears to be bimodal where the bimodality has its origin in the multiple initiation mechanisms. This indicates that failure initiated from a grain boundary is weaker than that of failure initiated from a second phase particle in this material. The upper part of the distribution for the R4PRZ appears to be tougher than that of R3RPVH, which is likely an effect of ductile crack growth that occurs prior to the final brittle fracture.

For describing the toughness distribution of the thermally aged R4PRZ, the bimodal master curve is required and appears to be able to describe the material well under conditions of high constraint. The reference material R3RPVH is well described by the standard master curve, i.e. the *unimodal* model. However, the transition between the high and low constraint geometries is not trivial. For the case of R3RPVH, the correction of T_0 for the low constraint $a/W = 0.1$ appears to work well using Wallin's empirical relation [31]. But, a constraint correction for the bimodal master curve that ideally should be used to describe the R4PRZ is currently ambiguous due to the complex interactions of the initiation mechanisms and the number of parameters included in the model.

Separating the effects from hardening and non-hardening contributions to the change in fracture toughness is not straight forward. From the fractography of the thermally aged R4PRZ, the effects of non-hardening embrittlement can be distinguished from the presence of intergranular features. The hardening contribution was elucidated by the combination of hardness tests and heat treatments. From the measurements presented in Figure 11, the hardness in both materials can be seen to decrease by 12-18 % which is similar to the difference between the yield strengths obtained in the current investigation and the check-in data. It should also be noted that the decrease in hardness is to a level judged to be relevant to the as-manufactured hardness of the weld. This implies that there is a hardening effect present in both the R4PRZ and the R3RPVH materials, i.e. hardening due to thermal ageing at the operating temperatures.

Concerning the ductile fracture tests presented in Figure 8, the fracture toughness plotted against crack growth aligns well for crack growth up to ~1 mm, thereafter it deviates so that the R4PRZ has less resistance than R3RPVH. This is accompanied with a change in the fracture surface appearance where the morphology changes notably. A possible explanation would be that the crack grows into a different part of the microstructure, which presents different requisites for void growth and coalescence, the main operating mechanism for ductile crack growth in these materials. As an example, if the crack starts growing in a zone with a reheated microstructure (small equiaxed grains), it is likely that the ductile fracture resistance will change once the crack grows into an as-welded zone (elongated dendritic grains), or vice versa.

The obvious material to compare the APT-results of the R4PRZ material with is the pressurizer weld analysed by APT by the authors in [21] and [44]. This weld comes from the same component, but is slightly different in terms of composition. The clusters containing Cu, Ni, Mn, and Si are relatively similar in appearance. The Cu content is higher in the clusters reported in [21] and [44], but the measured Cu content is also higher in that weld (0.10 at. % compared to the 0.05 at. % in the weld in this paper). The lower Cu content makes the core-shell structure (Cu-rich core) less prominent in the clusters of this paper. The cluster size and number density of the two materials are within the estimated errors considering the heterogeneous distribution.

As mentioned earlier, the terms cluster and precipitate are used interchangeably in this paper, as APT does not provide enough crystallographic information to reveal the crystal structure of these small clusters/precipitates. Generally, bcc Cu-clusters in α-Fe are believed to transform into 9R precipitates when they have a diameter of at least around 4 nm, and into fcc at larger sizes [45], [46]. Here, the Ni and Mn content of the clusters is high, and thus the question is what type of precipitate is formed, and at which diameter.

The most significant difference from the other weld of the same pressurizer is the amount of small carbonitrides. In the other material, occasional V and Cr-containing carbonitrides were found. They were also found in the reference material used in that paper and in the Ringhals RPV weld metal [20]. It is assumed that the carbonitrides are present before ageing, and are thus not affecting the shift of mechanical properties in a direct way. They appear to act as nucleation point for the Cu-rich clusters, as many of them are found in connection to each other (see Figure 14-16). The higher number of carbonitrides does, however, not seem to give a significant increase in the number of Ni-Mn-Si-Cu clusters as the number density of 0.13 10^{23} $/m^3$ here is close and within the uncertainty to the 0.16 10^{23} $/m^3$ as measured in [21]. Also, there are carbonitrides were Cu, Ni, Mn and Si have not precipitated/clustered, see Figure 14 and 15.

The fact that Ni-Mn-Cu-Si clusters could be found in the R3RPVH material that was used as reference material is interesting. Such clusters were not found in similar un-aged reference materials used by the authors in similar high Ni and Mn, low Cu weld metals [21], [20]. Despite the diffusion of these elements in α-Fe being very slow at the relevant temperature (310-315 °C), some clustering still seems to be possible, although to a very limited degree.

5. Conclusions

The effects of embrittlement due to thermal ageing on the weldments from a pressurizer of a Swedish nuclear power plant, more specifically the effect of ageing on the constraint sensitivity of the fracture toughness has been investigated and compared to a reference material. Testing revealed a $\Delta T_0 = 45\ ^\circ\mathrm{C}$ between the materials, indicating a significant embrittlement. The thermally aged material displays a bimodal fracture toughness distribution, which is pronounced at low constraint, and is due to brittle fracture being initiated from weakened grain boundaries as well as second phase particles. To describe the fracture toughness distribution, the bimodal master curve is needed and no constraint correction for the low constraint specimens can unambiguously be made. The reference material is well described by the unimodal master curve and the constraint effect is well predicted within the same framework.

The nanostructure of both materials is characterized using atom probe tomography. In-homogeneously distributed solute clusters of Ni-Mn-Cu-Si situated on dislocations and on carbonitrides, which are also present within the material, were observed.

A hardening due to thermal ageing is apparent in both the studied materials. It is investigated using uniaxial tensile tests as well as hardness tests in combination with heat treatments. After annealing at 600 ˚C for 25 h it appears that the ageing induced hardening is restored, most likely due to dissolution of solute clusters formed due to thermal ageing.

Acknowledgements

The Swedish Radiation Safety Authority (SSM) and the Swedish Centre for Nuclear Technology (SKC) are acknowledged for their financial support. Ringhals AB is acknowledged for supplying the material that was used in the experimental investigation. Jenny Roudén is greatly acknowledged for her support in this study and for constructive comments on the manuscript.

References

[1] L. Debarbis, B. Acosta, A. Zeman, S. Pirfo och P. Moretto, ”Ductile-to-brittle transition temperature of thermally segregated WWER-1000 base metal,” *International Journal of Microstructure and Materials Properties,* vol. 2, pp. 326-338, 2007.

[2] B. A. Gurovich , A. A. Chernobaeva, D. Yu Erak, E. A. Kuleshova, D. A. Zhurko, V. B. Papina, M. A. Skundin och D. A. Maltsev, ”Chemical composition effect on VVER-1000 RPV weld metal thermal ageing,” *Journal of Nuclear Materials,* vol. 465, pp. 540-549, 2015.

[3] A. A. Chernobaeva, E. A. Kuleshova, B. A. Gurovich, D. Yu Erak, O. O. Zabusov, D. A. Maltsev, D. A. Zhurko, V. B. Papina och M. A. Skundin, ”Thermal ageing effects of VVER-1000 weld metal under operation temperature,” i *Fontevraud 8*, Avignon, 2014.

[4] Y. I. Shtrombakh, B. A. Gurovich, E. A. Kuleshova, D. A. Maltsev, S. V. Fedotova och A. A. Chernobaeva, ”Thermal ageing mechanisms of VVER-1000 reactor pressure vessel steels,” *Journal of Nuclear Materials,* vol. 452, pp. 348-358, 2014.

[5] P. Joly, F. Roch och C. Primault, ”Effect of thermal ageing on properties of pressure vessel low alloy steel,” i *Proceedings of the ASME 2013 Pressure Vessels and Piping Conference*, Paris, 2013.

[6] R. Pelli och J. Forstén, ”Effect of thermal ageing on impact ductility of the nuclear pressure vessel steel SA533B and its weld metal,” *Theoretical and Applied Fracture Mechanics,* vol. 8, pp. 25-31, 1987.

[7] J. Kameda och Y. Nishiyama, ”Combined effects of phosphorus segregation and partial intergranular fracture on the ductile-brittle transition temperature in structural alloy steels,” *Materials Science and Engineering A,* vol. 528, pp. 3705-3713, 2001.

[8] A. Andreiu, A. Pineau, P. Joly, F. Roch och D. Ryckelynck, ”Influence of P and C intergranular segregation during manufacturing and ageing on the fracture toughness of nuclear pressure vessel steels,” *Procedia Materials Science,* vol. 3, pp. 655-660, 2014.

[9] S. G. Druce, G. Gage och J. G., ”Effect of ageing on properties of pressure vessel steels,” *Acta Metallurgica,* vol. 34, nr 4, pp. 641-652, 1986.

[10] I. A. Vatter, C. A. Hippsley och S. G. Druce, ”Review of Thermal Ageing Data and its Application to Operating Reactor Pressure Vessels,” *International Journal of Pressure Vessels and Piping,* vol. 54, pp. 31-48, 1993.

[11] C. Naudin, J. M. Frund och A. Pineau, ”Intergranular fracture stress and phosphorus grain boundary segregation of a Mn-Ni-Mo steel,” *Scripta Materialia,* vol. 40, nr 9, pp. 1013-1019, 1999.

[12] C. L. Briant och S. K. Banerji, ”Intergranular failure in steel: the role of grain boundary composition,” *International Metal Reviews,* pp. 164-199, 1978.

[13] C. J. McMahon, ”Intergranular Fracture in Steels,” *Materials Science and Engineering,* vol. 25, pp. 233-239, 1976.

[14] M. Guttmann, ”Equilibrium segregation in a ternary solution: a model for temper embrittlement,” *Surface Science,* vol. 53, pp. 213-227, 1975.

[15] M. Guttmann, ”Temper Embrittlement and Ternary Equilibrium Segregation,” *Materials Science and Engineering ,* vol. 42, pp. 227-232, 1980.

[16] S. K. Banerji, C. J. McMahon och H. C. Feng, ”Intergranular Fracture in 4340-Type Steels: Effects of Impurities and Hydrogen,” *Metallurgical Transactions A,* vol. 9A, pp. 237-247, 1978.

[17] D. F. Stein, ”Reversible temper embrittlement,” *Annual Review of Materials Research,* vol. 7, pp. 123-153, 1977.

[18] M. K. Miller, K. A. Powers, R. K. Nanstad och P. Efsing, ”Atom probe tomography characterizations of high nickel, low copper surveillance RPV welds irradiated to high fluences,” *Journal of Nuclear Materials,* vol. 437, pp. 107-115, 2013.

[19] P. D. Styman, J. M. Hyde, D. Parfitt, K. Wilford, M. G. Burke, C. A. English och P. Efsing, ”Post-irradiation annealing of Ni-Mn-Si-enriched clusters in a neutron-irradiated

RPV steel weld using Atom Probe Tomography,” *Journal of Nuclear Materials,* vol. 459, pp. 127-134, 2015.

[20] K. Lindgren, M. Boåsen, K. Stiller, P. Efsing och M. Thuvander, ”Evolution of precipitation in reactor pressure vessel steel welds under neutron irradiation,” *Journal of Nuclear Materials,* vol. 488, pp. 222-230, 2017.

[21] K. Lindgren, M. Boåsen, K. Stiller, P. Efsing och M. Thuvander , ”Cluster formation in in-service thermally aged pressurizer welds,” *Journal of Nuclear Materials,* vol. 504, pp. 23-28, 2018.

[22] J. M. Hyde, G. Sha, E. A. Marquis, A. Morley, K. B. Wilford och T. J. Williams, ”A comparison of the structure of solute clusters formed during thermal ageing and irradiation,” *Ultramicroscopy,* vol. 111, pp. 664-671, 2011.

[23] P. D. Styman, J. M. Hyde, K. Wilford, A. Morley och G. D. W. Smith, ”Precipitation in long term thermally aged high copper, high nickel model RPV steel welds,” *Progress in Nuclear Energy,* vol. 57, pp. 86-92, 2012.

[24] P. D. Styman, J. M. Hyde, K. Wilford och G. D. W. Smith, ”Quantitative methods for the APT analysis of thermally aged RPV steels,” *Ultramicroscopy,* vol. 132, pp. 258-264, 2013.

[25] P. D. Styman, J. M. Hyde, K. Wilford, D. Parfitt, N. Riddle och G. D. W. Smith, ”Characterisation of interfacial segregation to Cu-enriched precipitates in two thermally aged reactor pressure weld steels,” *Ultramicroscopy,* vol. 159, pp. 292-298, 2015.

[26] H.-W. Viehrig, M. Housaka, D. Kalkhof och H.-J. Schindler, ”Fracture mechanics characterisation of reactor pressure vessel multi-layer weld metal,” *International Journal of Pressure Vessels and Piping,* Vol. %1 av %2135-136, pp. 36-51, 2015.

[27] ASTM International, ”E1921 Standard Test Method for Determination of Reference Temperature, T0, for Ferritic Steels in the Transition Range,” ASTM International, West Conshohocken, 2019.

[28] J. Faleskog, M. Kroon och H. Öberg, ”A probabilistic model for cleavage fracture with a length scale - parameter estimation and predictions of stationary crack experiments,” *Engineering Fracture Mechanics,* vol. 71, pp. 57-79, 2004.

[29] K. Wallin, ”The scatter in KIC-results,” *Engineering Fracture Mechanics,* vol. 19, nr 6, pp. 1085-1093, 1984.

[30] K. Wallin, P. Nevasmaa, A. Laukkanen och T. Planman, ”Master Curve analysis of inhomogeneous ferritic steels,” *Engineering Fracture Mechanics,* vol. 71, pp. 2329-2346, 2004.

[31] K. Wallin, ”Quantifying T-stress controlled constaint by the master curve transition temperature T0,” *Engineering Fracture Mechanics,* vol. 68, pp. 303-328, 2001.

[32] K. Wallin, Fracture Tougness of Engineering Materials - Estimation and Application, Croydon: EMAS Publishing, 2011.

[33] M. Boåsen, M. Stec, P. Efsing och J. Faleskog, ”A generalized probabilistic model for cleavage fracture with a length scale - Influence of stress state and application to surface cracked experiments,” *Engineering Fracture Mechanics,* vol. 214, pp. 590-608, 2019.

[34] ASTM International, ”E1820 Standard Test Method for Measurement of Fracture Toughness,” ASTM International, West Conshohocken, 2019.

[35] J. M. Hyde, M. G. Burke, B. Gault, D. W. Saxey, P. Styman, K. B. Wilford och T. J. Williams, ”Atom probe tomography of reactor pressure vessel steels: an analysis of data integrity,” *Ultramicroscopy,* vol. 111, nr 6, pp. 676-682, 2011.

[36] M. K. Miller, Atom Probe Tomography: Analysis at the Atomic Level, Academic/Plenum Publishers: 2000, 200.

[37] J. M. Hyde och C. A. English, ”An Analysis of the Structure of Irradiation induced Cu-enriched Clusters in Low and High Nickel Welds,” i *Materials Research Society Symposium*, Boston, 2000.

[38] D. Vaumousse, A. Cerezo och P. J. Warren, ”A procedure for quantification of precipitate microstructures from three-dimensional atom probe data,” *Ultramicroscopy,* vol. 95, pp. 215-221, 2003.

[39] Y. Dong, A. Etienne, A. Frolov, S. Fedotova, K. Fujii, K. Fukuya, C. Hatzoglou, E. Kuleshova, K. Lindgren, A. London, A. Lopez, S. Lozano-Perez, Y. Miyahara, Y. Nagai, K. Nishida, B. Radiquet, D. K. Schreiber, N. Soneda, M. Thuvander, T. Toyama, J. Wang, F. Sefta, P. Chou och E. A. Marquis, ”Atom Probe Tomography Interlaboratory Study on Clustering Analysis in Experimental Data Using the Maximum Separation Distance Approach,” *Microscopy and Microanalysis,* vol. 25, nr 2, pp. 356-366, 2019.

[40] K. Lindgren, K. Stiller, P. Efsing och M. Thuvander, ”On the Analysis of Clustering in an Irradiated Low Alloy Reactor Pressure Vessel Steel Weld,” *Microscopy and Microanalysis,* vol. 23, nr 2, pp. 379-384, 2017.

[41] E. A. Marquis och J. M. Hyde, ”Applications of atom-probe tomography to the characterization of solute behaviours,” *Materials Science and Engineering: R: Reports ,* vol. 69, nr 4-5, pp. 37-62, 2010.

[42] P. D. Edmondson, C. M. Parish och R. K. Nanstad, ”Using complimentary microscopy methods to examine Ni-Mn-Si-precipitates in highly-irradiated reactor pressure vessel steels,” *Acta Materialia,* vol. 134, pp. 31-39, 2017.

[43] D. R. Kingham, ”The Post-Ionization of Field Evaporated Ions: a Theoretical explanation of Multiple Charged States,” *Surface Science,* vol. 116, pp. 273-301, 1982.

[44] K. Lindgren, M. Boåsen, K. Stiller, P. Efsing och M. Thuvander, ”Thermal ageing of low alloy steel weldments from a Swedish nuclear power plant - the evolution of the microstructure,” i *Fontevraud 9*, Avignon, 2018.

[45] A. Deschamps, M. Militzer och W. J. Poole, ”Comparison of Precipitiation Kinetics and Strengthening in an Fe-0.8%Cu Alloy and a 0.8% Cu-containing Low-carbon Steel,” *ISIJ International ,* vol. 43, pp. 1826-1832, 2003.

[46] P. J. Othen, M. L. Jenkins och G. D. W. Smith, ”High-resolution electron microscopy studies of the studies of the structure of Cu precipitates in α-Fe,” *Philosophical Magazine A,* vol. 70, pp. 1-24, 1994.

[47] R. Xing, D. Yu, G. Xie, Z. Yang, X. Wang och X. Chen, ”Effect of thermal aging on mechanical properties of a bainitic forging steel for reactor pressure vessel,” *Materials Science and Engineering A,* vol. 720, pp. 169-175, 2018.

[48] K. Lindgren, M. Boåsen, K. Stiller, P. Efsing och M. Thuvander, ”Evolution of precipitation in reactor pressure vessel steel welds under neutron irradiation,” *Journal of Nuclear Materials,* vol. 488, pp. 222-230, 2017.

Paper IV

A weakest link model for multiple mechanism brittle fracture - Model development and application

Magnus Boåsen*, Carl F.O. Dahlberg, Pål Efsing, Jonas Faleskog

Solid Mechanics, Department of Engineering Mechanics, KTH Royal Institute of Technology, Teknikringen 8D, SE-100 44 Stockholm, Sweden.

Abstract

A multiple mechanism weakest link model for intergranular and transgranular brittle fracture is developed on the basis of experimental observations in a thermally aged low alloy steel. The model development is carried out in tandem with micro mechanical analysis of grain boundary cracking using crystal plasticity modeling of polycrystalline aggregates with the purpose to inform the weakest link model. The fracture modeling presented in this paper is carried out by using a non-local porous plastic Gurson model where the void volume fraction evolution is regularized over two separate length scales. The ductile crack growth preceding the final brittle fracture is well predicted using this type of modeling. When applied to the brittle fracture tests, the weakest link model predicts the fracture toughness distribution remarkably well, both in terms of the constraint and the size effect. Included in the study is also the analysis of a reference material.

Keywords: Brittle fracture, cleavage fracture, intergranular, transgranular, crystal plasticity, weakest link

---

*Corresponding author. E-mail: boasen@kth.se

Preprint submitted to Journal of the Mechanics and Physics of Solids *August 6, 2020*

1. Introduction

The structural integrity of a component is fundamentally dependent on the mechanical properties of the material of which it is made. In the case of components of ferritic steels, cleavage fracture is an adverse failure mode that generally occurs at low temperatures. At higher temperatures, such materials progressively become more ductile until the cleavage failure mode is suppressed in its entirety. This transition is typically called the ductile-to-brittle transition and needs to be accounted for in the design and operation of components made from ferritic steels. For components with a long design life, the risk of embrittlement of structural materials by ageing due to environmental factors is increased. Such factors could be operating temperature, irradiation or a reactive chemical environment. Embrittlement of ferritic steels, which typically exhibit cleavage fracture at low temperatures, will cause an increase in the temperature at which cleavage fracture can occur. This phenomena is a characteristic for ageing of low alloy steels in nuclear power plants whereby ageing is primarily induced by neutron irradiation [1] and high operating temperatures [2]. Embrittlement by ageing in this sense is commonly divided in two groups; hardening and non-hardening embrittlement. Hardening embrittlement occurs due to the formation of microstructural features such as solute clusters or fine scale precipitates that impede dislocation motion, thereby increasing the yield strength of the material, resulting in embrittlement. Non-hardening embrittlement works by decreasing the cohesive strength of prior austenite grain boundaries by impurity segregation, thus altering the fracture path from the cleavage planes to the grain boundaries. The most common impurity elements known to cause this phenomenon belongs to groups IV-VI in the periodic system, e.g. P, S, Sn and Si, commonly found as trace elements in the steels considered [3], [4]. Briant and Banerji [3] also observed that with larger grain size came a larger fraction of intergranular failure, which they discussed in terms of dilution of segregants for the case of smaller grains, i.e. less impurities per unit grain boundary area. Both the hardening and non-hardening mechanisms can appear exclusive of the other or simultaneously. A recent study [5] of a weld metal from a decommissioned component from a Swedish nuclear power plant subjected to thermal ageing concluded that the material had been subject to both hardening as well as non-hardening embrittlement. Fracture toughness testing of the material revealed that multiple mechanisms for cleavage initiation existed, giving rise to a complex bimodal toughness distribution.

For cleavage fracture to be possible, several pre-requisites needs to be fulfilled. The first being the nucleation of a micro crack, this event typically occurs by the cracking of a second phase particle due to plastic straining of the matrix surrounding the particle [6]. For a nucleated micro crack to transition into a fully developed cleavage crack experiencing unstable propagation it must grow in size and overcome microstructural barriers such as grain boundaries. This progression from nucleus to self-sustained growth will only be completed when a high enough stress level is reached over a sufficiently large region around the nucleation site. As cleavage fracture exhibits a large degree of inherent scatter, probabilistic modeling is needed to describe its behavior. Weakest link modeling has been shown to be well suited to describe the fracture toughness associated with cleavage fracture, examples of such models include the ones by Beremin et al. [7], Wallin [8], [9], Bordet et al. [10], [11], and Kroon and Faleskog [12], [13], [14], [15]. These models have varying degree of complexity and different strengths, e.g. the *master curve* model by Wallin is based on the intensity, K_{I}, of the crack tip stress field and has been shown in numerous cases to well describe the strong effect of temperature on the cleavage fracture toughness. The model by Kroon and Faleskog has been shown to capture the effects of crack tip constraint in a promising way. However, all of the mentioned models pertain to single mechanism cleavage failure, i.e. brittle cleavage fracture initiated by one mechanism.

Models incorporating multiple mechanism brittle fracture include the one by Yahya et al. [16] where the studied material displayed intergranular failure initiated at MnS-inclusions and transgranular failure initiated from a second population of microstructural features. The probabilistic model employed in their study is an extension of the Beremin model [7]. Another multiple mechanism model is the one by Wallin et al. [17] which is an extension of the master curve model, making it capable of describing bimodal toughness distributions.

The material considered in this study is a multi-layer weld of a low alloy steel, where an understanding of the grain structures is of importance. As a multi-layer weld is formed, zones of different grain structures will emerge due to the solidification and subsequent reheating of the weld beads. As a weld bead solidifies during welding, a dendritic grain structure emerges transverse to the welding direction. When the multi-layer weld is built up, subsequent weld beads will be laid on top of the already existing beads, thus effectively heat treating the upper part of the weld bead below. This gives rise to a region with smaller equiaxed grains in the bead below due to recrystallization from the locally increased temperature. As this process continues, the weld will achieve a microstructure that has regions of dendritic grains, regions with finer grains that have been reheated once (equiaxed) and regions that have been reheated several times (equiaxed).

This paper is concerned with a probabilistic model for multiple mechanism brittle fracture where initiation is possible from both particle cracking as well as grain boundary failure. The model will be shown capable of handling crack tip constraint as well as incorporating multiple mechanisms for brittle fracture initiation. The model will be applied and compared to fracture tests of thermally aged welds from a decommissioned pressurizer from a Swedish nuclear power plant [5] and its main features will be explored. The outline of the paper is as follows, Section 2 gives a brief account of the fracture tests, as well as the modeling of the same, Section 3 presents the foundation of the probabilistic model and the model assumptions, Section 4 presents a micro mechanical study of polycrystalline aggregates in order to motivate the failure characteristics of grain boundaries, Section 5 presents an application of the model to experiments and explores the model behavior, and finally the paper is concluded by a discussion of the model and the results in Section 6.

2. Material, experiment and fracture modeling

2.1. Material and experiment

The experimental series considered in this study can be found detailed in [5], however a brief review will also be given here.

The materials considered in this paper are two low alloy steel welds from the Ringhals nuclear power plant in Sweden, one thermally aged material subjected to 345 °C for ∼215 000 h, and a reference material that has been subjected to 310-315 °C for ∼176 000 h. Even though the difference in operating temperature and time may appear minute, the effects of ageing are distinct, the embrittlement due to operation of the reference material is considered small or close to negligible in comparison to the thermally aged material. From here onward the thermally aged material will be denoted *R4PRZ* and the reference material *R3RPVH*.

The main emphasis of the experiments was the constraint effect on the brittle fracture toughness and how the constraint sensitivity would be impacted by embrittlement due to thermal ageing. To elucidate this, fracture test series with different crack tip constraint were conducted at temperatures where the high constraint fracture toughness of the two materials would coincide. The fracture test series was composed of T-S oriented, SEN(B)-specimens with dimensions $W = 30$ mm, $B = 15$ mm, and $a/W = \{0.5\,\text{and}\,0.1\}$ i.e. both deep and shallow cracks. Deep corresponding to a state of high crack tip constraint and shallow for low crack tip constraint. Also included was a series of smaller specimens to be used as a size effect reference with, $W = 14$ mm, $B = 7$ mm, and $a/W = 0.5$. The temperatures that were chosen to yield similar brittle fracture toughness were -50 °C and -90 °C for R4PRZ and R3RPVH respectively.

The reference temperature T_0 was determined from the fracture test results according to ASTM E1921 [9] to be $T_0^{\text{R4PRZ}} = -33$ °C and $T_0^{\text{R3RPVH}} = -78$ °C, i.e. a $\Delta T_0 = 45$ °C. The fracture tests of R4PRZ revealed a bimodal toughness distribution as seen in Figure 1, where the effect on the specimens with shallow cracks was strong, as can be seen in the rank probabilities for the experimental data in Figure 1. The rank probability of failure was estimated using the median rank according to Benard's approximation as $P^i_{\text{rank}} = (i - 0.3)/(N + 0.4)$. Fractographical investigations revealed that initiation of fracture in the more brittle specimens (low toughness) of R4PRZ, e.g. the first five specimens in Figure 1(b), was exclusively from grain boundaries. In the specimens with higher fracture toughness, the brittle/cleavage fracture was preceded by ductile growth and was initiated partly from second phase particles and partly from grain boundaries. This revealed that two mechanisms exist in the microstructure and both can initiate brittle fracture. The testing of R3RPVH uncovered a unimodal toughness distribution with cleavage fracture initiation from second phase particles. It should be mentioned that small portions of intergranular features was found in a few specimens of the R3RPVH as well.

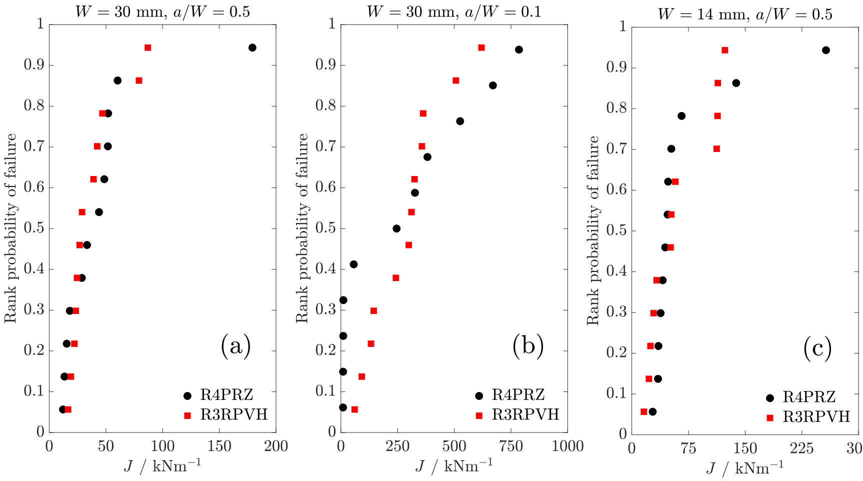

Figure 1: Experimental fracture test results of the thermally aged R4PRZ and the reference R3RPVH. Results pertaining to high constraint specimens (a), low constraint specimens (b), and small specimens (c).

The experimental series also included ductile fracture tests that were conducted on the upper shelf at a temperature of 75 °C using SEN(B)-specimens with side-grooves to promote uniform growth along the crack front. The specimen dimensions were $W = 30$ mm, $B = 15$ mm, $B_{\mathrm{N}} = 12$ mm, and $a/W = 0.5$. The ductile initiation fracture toughness was determined to $J_{\mathrm{IC}} = 338$ kN/m for both materials at 75 °C.

2.2. Fracture modeling

Models of the experiments for both the development of the multiple mechanism weakest link model and the ductile failure tests were set up as finite element (FE) models. These were generated with meshes containing 32 500 - 47 000 elements for models pertinent to both the ductile fracture and brittle fracture experiments. Eight noded hexahedral elements with reduced integration was used in all models, and due to symmetry, only a quarter of the three point bend specimen was modeled with 12 elements through the thickness. An overview of the FE-models can be seen in Figure 2. The elastic-plastic material behavior was modeled using the Gurson model for porous plasticity [18] with the plastic potential under isotropic strain hardening as

$$\Phi = \left(\frac{\sigma_{\mathrm{e}}}{\sigma_{\mathrm{f}}}\right)^2 + 2\, q_1 f \cosh\left(\frac{3}{2}\frac{q_2\, \sigma_{\mathrm{m}}}{\sigma_{\mathrm{f}}}\right) - \left(1 + (q_1\, f)^2\right) = 0. \tag{1}$$

Here σ_{e} is the von Mises equivalent stress, σ_{m} is the mean stress, σ_{f} is the material flow strength, f is the void volume fraction, and q_1 and q_2 are parameters introduced by Tvergaard [19], [20] to improve model predictions. The parameters q_1 and q_2 will here be taken as proposed by Faleskog et al. [21]. The evolution of the void volume fraction during plastic straining is divided in two terms, one defined by dilatational deformation $\dot{f}_{\mathrm{m}}$ and one defined by deviatoric deformation $\dot{f}_{\mathrm{s}}$, i.e. $\dot{f} = \dot{f}_{\mathrm{m}} + \dot{f}_{\mathrm{s}}$. Contributions from nucleation due to plastic straining is also included but is split into the aforementioned categories as will be shown below. The evolution of the void volume fraction due to dilatational deformation is given by

$$\dot{f}_{\mathrm{m}} = (1 - f)\, \dot{\varepsilon}^{\mathrm{p}}_{\mathrm{kk}} + \dot{f}^{\mathrm{nucleation}}_{\mathrm{m}}, \tag{2}$$

where $\dot{\varepsilon}^{\mathrm{p}}_{\mathrm{kk}}$ is the volumetric part of the plastic strain increment. The evolution of the void volume fraction due to devatoric deformation was first introduced by Nahshon and Hutchinson [22] as a shear modification to the original Gurson model and is given by

$$\dot{f}_{\mathrm{s}} = k_{\omega} f \omega \frac{s_{ij}\dot{\varepsilon}^{\mathrm{p}}_{ij}}{\sigma_{\mathrm{e}}} \varphi\left(T\right) + \dot{f}^{\mathrm{nucleation}}_{\mathrm{s}}. \tag{3}$$

Here k_{ω} is a model parameter that sets the strength of the deviatoric damage evolution, s_{ij} is the stress deviator, $\dot{\varepsilon}^{\mathrm{p}}_{ij}$ is the incremental plastic strain tensor,

ω is a measure of the stress state that is unity for a pure shear stress state with a smooth transition to zero as the stress state transitions to pure tension or compression. It is given by

$$\omega = 1 - \left(\frac{27 J_3}{2\sigma_{\mathrm{e}}^3}\right)^2, \tag{4}$$

where J_3 is the third invariant of the stress deviator. The function $\varphi\left(T\right)$ penalizes the deviatoric damage evolution for high stress triaxialities T and was introduced by Nielsen and Tvergaard [23] as the shear modification of the void volume fraction tends to overestimate the contribution at moderate to high stress triaxialities T. The function $\varphi\left(T\right)$ is here taken as

$$\varphi\left(T\right) = \frac{1}{2} - \frac{1}{2}\tanh\left(\kappa\left(T - T_0\right)\right), \tag{5}$$

which is unity for low values of T and transitions smoothly to zero depending on κ and T_0. In this case, κ was calculated so that 90 % of the transition from unity to zero would occur over the interval specified by ΔT_{90}, the relation becomes $\kappa = 1.4722195/\Delta T_{90}$.

The contribution to the void growth as a result of nucleation due to plastic straining is expressed as

$$\dot{f}^{\mathrm{nucleation}} = D\dot{\bar{\varepsilon}}^{\mathrm{p}}, \tag{6}$$

where $\dot{\bar{\varepsilon}}^{\mathrm{p}}$ is the matrix equivalent strain rate which is related to the aggregate equivalent strain rate as $\dot{\bar{\varepsilon}}^{\mathrm{p}} = \sigma_{ij}\dot{\varepsilon}_{\mathrm{ij}}^{\mathrm{p}}/\left[\left(1-f\right)\sigma_{\mathrm{f}}\right]$. This enables the separation into dilatational and deviatoric contributions as

$$\dot{f}_{\mathrm{m}}^{\mathrm{nucleation}} = D\frac{\sigma_{kk}\dot{\varepsilon}_{\mathrm{kk}}^{\mathrm{p}}}{3\left(1-f\right)\bar{\sigma}}, \tag{7}$$

$$\dot{f}_{\mathrm{s}}^{\mathrm{nucleation}} = D\frac{s_{ij}\dot{\varepsilon}_{\mathrm{ij}}^{\mathrm{p}}}{\left(1-f\right)\bar{\sigma}}. \tag{8}$$

Here D is the parameter for strain-controlled void nucleation at the current accumulated level of plastic strain $\bar{\varepsilon}^{\mathrm{p}}$, which in this case is taken as a log-normal distribution as

$$D = \frac{f_{\mathrm{N}}}{\bar{\varepsilon}^{\mathrm{p}} s_{\mathrm{N}}\sqrt{2\pi}}\exp\left(-\frac{1}{2}\left[\frac{\ln\left(\bar{\varepsilon}^{\mathrm{p}}/\varepsilon_{\mathrm{N}}\right)}{s_{\mathrm{N}}}\right]^2\right). \tag{9}$$

The parameter f_{N} is related to the volume fraction available for nucleation, ε_{N} and s_{N} are the distribution parameters and relates to the mean and the standard

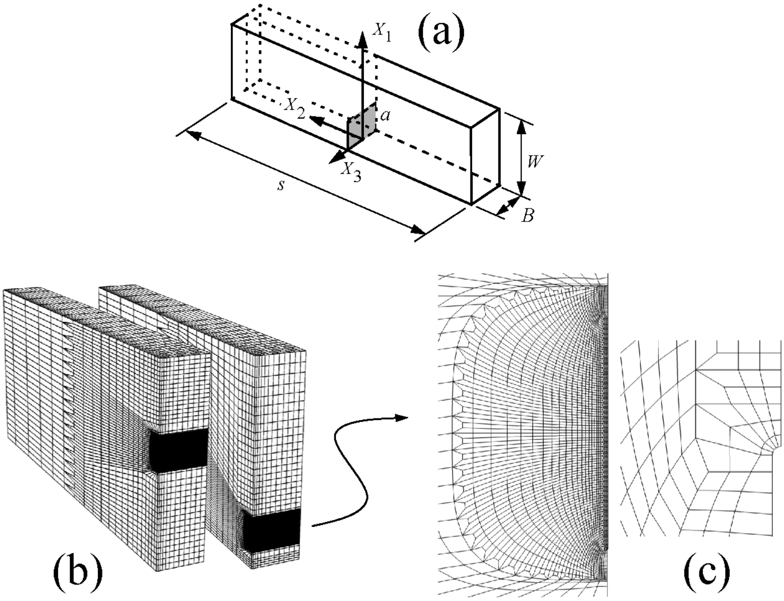

Figure 2: (a) Schematic illustration of model symmetries and dimensions corresponding to experimental specimens, (b) illustration of finite element discretization, (c) close up of fine mesh region surrounding the vicinity of the crack tip.

deviation as $\varepsilon_{\mu} = \varepsilon_{\mathrm{N}} \exp\left(s_{\mathrm{N}}^2\right)$ and $s_{\mathrm{D}} = \varepsilon_{\mathrm{N}} \exp\left(s_{\mathrm{N}}^2\right) \sqrt{\exp\left(s_{\mathrm{N}}^2\right) - 1}$, respectively. In the first formulation of strain controlled nucleation of voids by Chu and Needleman [24] a normal distribution was employed. The present choice was made for two reasons (i) the normal distribution is defined for infinitely large negative plastic strains, and (ii) the underlying distributions of potential void forming features, such as second phase particles e.g. carbides, tend to be well described by a log-normal distribution.

As the void volume fraction f increases, the load carrying capacity will be reduced due to a material softening. This will give rise to mesh dependent solutions (cf. Zienkiewicz and Taylor [25]). One solution to this issue in earlier studies of fracture modeling employing the Gurson model has been by use of careful mesh design where the element size becomes a material parameter, cf. Xia and Fong Shih [26], and Gao et al. [27]. Another solution to this issue is suggested by Tvergaard and Needleman [28] where the void volume fraction is regularized by integration over a certain length scale which yields mesh independent results. A third solution is examplified by Nguyen et al. [29] where a non-local micromorphic continuum theory is used in conjunction with the Gurson model, in their model the plastic strains are non-local variables which are then used to form the increment in the void volume fraction.

In the formulation presented here, the integration of void volume fraction is used where the dilatational and deviatoric components of the increment in the void volume fraction are regularized over separate length scales, R_{m} and R_{s} respectively. This is carried out as

$$\dot{\bar{f}}_{\mathrm{m}} = \frac{1}{V_{\mathrm{m}}} \int_V \dot{f}_{\mathrm{m}} \left(X_k - \hat{X}_k \right) \mathrm{d}V, \tag{10a}$$

$$\dot{\bar{f}}_{\mathrm{s}} = \frac{1}{V_{\mathrm{s}}} \int_V \dot{f}_{\mathrm{s}} \left(X_k - \hat{X}_k \right) \mathrm{d}V. \tag{10b}$$

Here $\mathbf{X} = \{X_1, X_2, X_3\}$ are the coordinates of the center of $V_{R_{\mathrm{i}}}$, and $R_{\mathrm{i}} \geqslant |\hat{X}_k - X_k|$. Note that $\dot{\bar{f}}_i$ will be equal to the local $\dot{f}_i$ in the limit where $R_{\mathrm{i}} \to 0$, where subscript i corresponds to the dilatational and deviatoric damage processes. The integration is carried out in the reference configuration. The increment in void volume fraction used in all computations is the sum of the non-local increments as $\dot{f} = \dot{\bar{f}}_{\mathrm{m}} + \dot{\bar{f}}_{\mathrm{s}}$.

The reason for choosing this modeling approach was due to the mesh refinement needed for resolving the crack tip fields appropriately for the weakest link modeling. For instance, incorporating the constitutive length scale in the mesh design will not be able to resolve the fields accurately enough as this would yield to large elements for weakest link calculations, making the integration method more suited for the problem. The non-local regularization was initially carried out using a single length scale for the increment in void volume fraction. However, this proved to be problematic since the crack growth would consistently initiate some distance ahead of the crack tip and, in some cases depending on the choice of parameters, leave a small ligament of load carrying elements close to the crack tip. By separating the regularization into dilatational and deviatoric contributions to the void volume fraction, these problems could be avoided altogether.

As voids grow to a critical size during plastic straining, the load carrying capacity of the material point is diminished due to the coalescence of voids. This final process of void growth and failure is not captured by the Gurson model, instead the yield condition is evaluated using the modified void volume fraction f^* as introduced by Tvergaard and Needleman [30] to account for the rapid increase in the void volume fraction during coalescence as

$$f^* = \begin{cases} f & \text{for } f \leqslant f_\mathrm{C} \\ f_\mathrm{C} + \frac{1/q_1 - f_\mathrm{C}}{f_\mathrm{E} - f_\mathrm{C}} \left(f - f_\mathrm{C} \right) & \text{for } f > f_\mathrm{C} \end{cases} \tag{11}$$

where f_C is the critical void volume fraction at the onset of coalescence and f_E is the void volume fraction at total loss of load carrying capacity.

The constitutive model has been implemented in the commercial software Abaqus as a VUMAT, i.e. an explicit user material subroutine. Further details about the model implementation and behavior will be not be elaborated on here. Regarding the boundary conditions of the FE-models, symmetry conditions were prescribed on the planes $X_2 = 0$ and $X_3 = 0$ by enforcing $u_2 = 0$ and $u_3 = 0$, respectively. The top roller support of the SEN(B)-specimen set up was modeled by enforcing $u_1 = 0$ at the three top node rows in the plane $X_2 = 0$. The load was introduced by applying a constant velocity $v_1 = \bar{v}_1$ at $\{X_1 = 0, X_2 = 2W\}$, $\bar{v}_1$ was specified at a level to achieve a solution judged to be close to quasi-static. In Abaqus Explicit, the J-integral cannot be calculated by the built in routines. Instead, the J-integral was calculated from the force-load line displacement relation according to the methodology supplied in ASTM E1820 [31] along with the relation for the plastic η-factor for shallow cracks from Faleskog et al. [13].

The material flow strength was inferred from tensile tests of the weld metals and was fitted to a Voce-like hardening law on the form

$$\sigma_\mathrm{f} = \sigma_0 \left[1 + \alpha_\mathrm{f}\, \bar{\varepsilon}^\mathrm{p} + \beta_\mathrm{f}\, \left(1 - \exp\left(-\gamma_\mathrm{f}\, \bar{\varepsilon}^\mathrm{p} \right) \right) \right], \tag{12}$$

where σ_0, α_f, β_f and γ_f are parameters that can be found in Table 1.

The parameters of the porous plastic model were calibrated from the ductile fracture tests at 75 °C, and then used to make predictions which were compared to the fracture test results at -50 and -90 °C. The parameters can be found in Table 2. The same model parameters pertinent to the porous plastic models were used for both materials. The comparison between experimental results and model predictions can be seen in Figure 3 and Figure 4 for the ductile fracture tests and the brittle specimens subjected to ductile growth prior to final brittle failure, respectively. A comparison between the force-displacement relation of

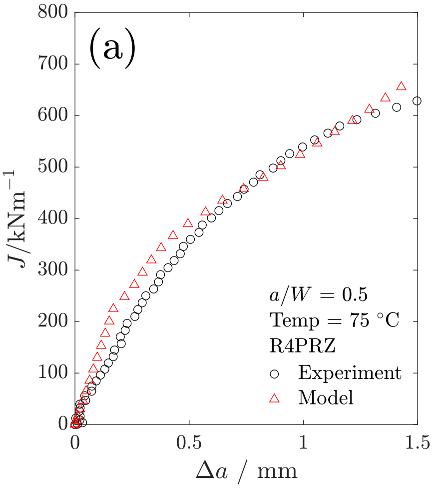

Figure 3: Comparison of crack growth predictions and experimental fracture test results at test temperature 75 °C. (a) Thermally aged R4PRZ, (b) reference R3RPVH. Note, these data sets were used for parameter calibration.

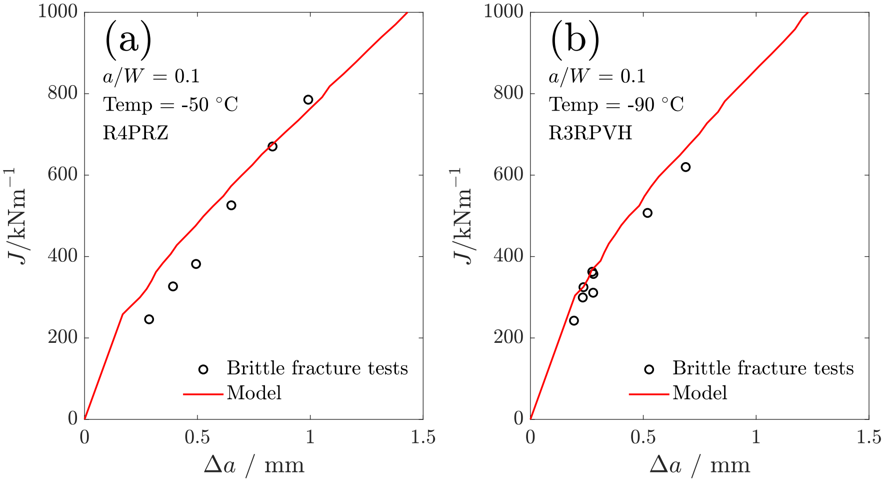

Figure 4: Comparison of crack growth predictions and experimental fracture test results at test temperatures $-50\,^{\circ}$C and $-90\,^{\circ}$C. (a) Thermally aged R4PRZ, (b) reference R3RPVH.

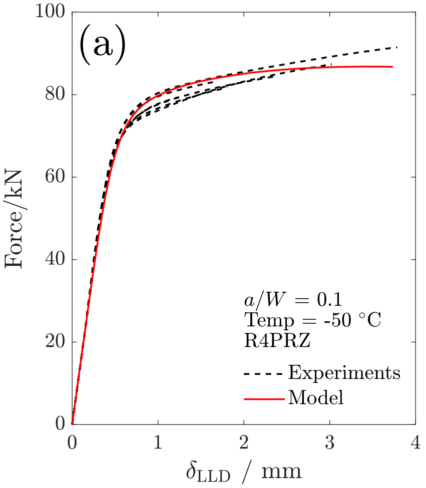

Figure 5: Comparison of force-displacement predictions and experimental fracture test results at test temperatures $-50\,^{\circ}$C and $-90\,^{\circ}$C. (a) Thermally aged R4PRZ, (b) reference R3RPVH.

the brittle fracture specimens can be seen in Figure 5. Models of different levels of discretization were used in the modeling of the pure ductile fracture tests and the brittle fracture tests. The pertinent issue here is to note the resolution in the integrals of (10a) and (10b). For the length scales in Table 2, the model used for the pure ductile models has a level of discretization that gives ∼20 elements/element for the dilatiational length scale and ∼3 elements/element for the deviatoric length scale, along the axis of crack propagation in the fine mesh zone respectively. The corresponding numbers for the finer models used in the modeling of the brittle fracture tests are ∼28 elements/element for the dilatiational length scale and ∼5 elements/element for the deviatoric length scale, along the axis of crack propagation in the fine mesh zone.

Table 1: Model parameters used in the Voce-like hardening law.

Material	$T/^{\circ}$C	σ_0/MPa	α_{f}	β_{f}	γ_{f}
R4PRZ	75	662.0	0.3143	0.1541	20.97
R3RPVH	75	617.8	0.3393	0.1772	24.89
R4PRZ	-50	717.5	0.4098	0.2900	16.09
R3RPVH	-90	694.4	0.4772	0.3600	21.6

Table 2: Model parameters used in the porous plastic model.

Parameter	Value	Parameter	Value	Parameter	Value
q_1	1.57	q_2	0.974	f_0	0.003
k_ω	3.0	T_ω	0.9	ΔT_{90}	0.2
f_N	0.001	ε_N	0.03	S_N	0.5
f_C	0.15	f_E	0.2		
$R_\mathrm{m}/\mu\mathrm{m}$	280	$R_\mathrm{s}/\mu\mathrm{m}$	50		
E/GPa	200	ν	0.3		

In order to supply relevant boundary conditions for the micromechanical model in Section 4, the stress state ahead of the crack tip in the relevant models will be analyzed. Any stress state can be described by its three principal stresses, or correspondingly by a combination of the von Mises effective stress σ_{e}, the Triaxiality parameter, $T = (\sigma_{\mathrm{I}} + \sigma_{\mathrm{II}} + \sigma_{\mathrm{III}})/(3\sigma_{\mathrm{e}})$, and the Lode parameter, $L = (2\sigma_{\mathrm{II}} - \sigma_{\mathrm{I}} - \sigma_{\mathrm{III}})/(\sigma_{\mathrm{I}} - \sigma_{\mathrm{III}})$, where the characteristics of the stress state is determined by the combination of T and L. The maximum principal stress, the stress triaxiality and the Lode parameter were extracted ahead of the crack tip from the models of the specimens used in the testing in order to understand the characteristics of the stress state. The maximum principal stress was extracted rather than the von Mises effective stress since understanding of the highest stress and its location ahead of the crack tip is central for brittle fracture. To capture the effect of crack tip constraint on the stress state ahead of the crack tip, models with the crack size to width ratio $a/W = \{0.5,\ 0.1\}$ were used.

The stress state in terms of the maximum principal stress σ_{I}, the stress triaxiality T, and the Lode parameter L was extracted ahead of the crack tip along the centerline of the specimen and can be seen plotted against the normalized crack tip coordinate in Figure 6 (a-c). The specimen was loaded to levels that would not cause ductile crack growth, i.e. the solutions presented in Figure 6 are representative for those of a stationary crack. Figure 6 (d-f) shows the same quantities averaged over the interval $0.5 \leqslant r\sigma_0/J \leqslant 2.0$, i.e. around the stress peak in Figure 6 (a-c), against the level of loading as defined through the J-integral. The difference in crack tip constraint is clearly shown in Figure 6 (a) and (b) where the shallow cracked specimen has a less intense stress state than the deeply cracked specimen. From subfigures (d-f) it is seen how the stress state undergoes a build-up period, reaching a close to constant level over the load levels depicted. From this analysis it was found that the stress state in the region around the stress peak in deeply and shallowly cracked SENB specimens could be characterized by $T = \{2.2,\ 1.9\}$ and $L = \{\text{-}0.25,\ \text{-}0.4\}$, respectively.

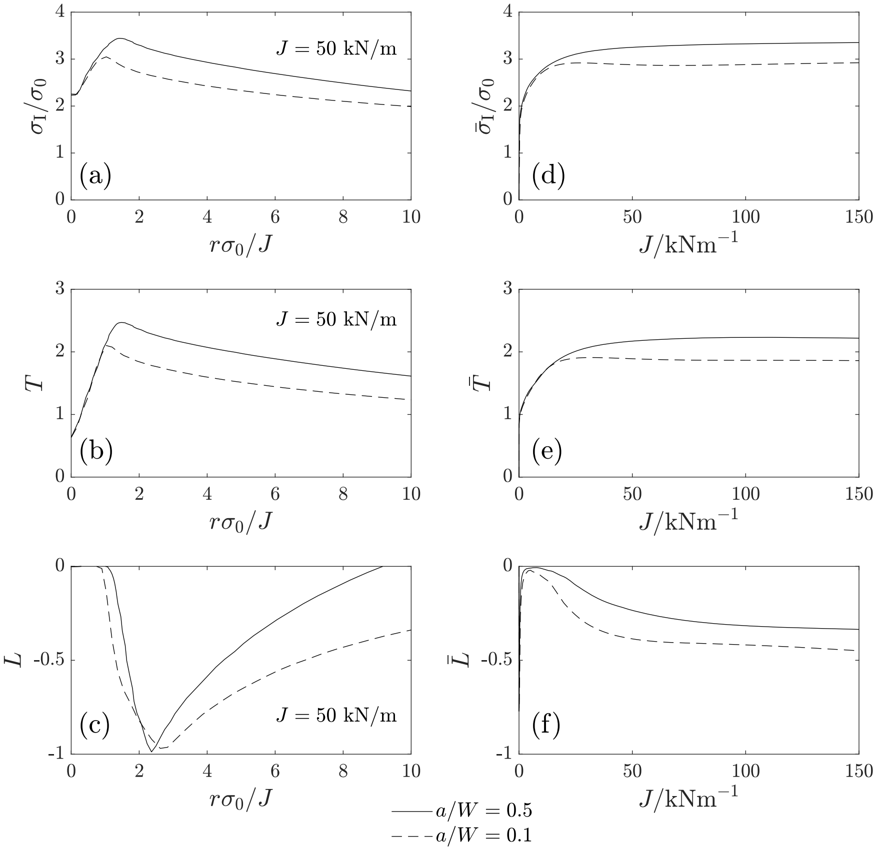

Figure 6: Stress state characteristics along the centerline in the crack plane of the SEN(B)-specimen. (a) Maximum principal stress normalized with σ_0 from Eq. (12), (b) stress triaxiality T, and (c) Lode parameter L, (a-c) plotted at $J = 50$ kN/m. (d) Normalized averaged maximum principal stress, (e) averaged stress triaxiality $\bar{T}$, (f) averaged Lode parameter $\bar{L}$, (d-f) averaged over $0.5 \leqslant r\sigma_0/J \leqslant 2.0$ and plotted throughout the loading history.

3. Probabilistic model incorporating multiple failure mechanisms

In this chapter a weakest link model capable of handling multiple mechanisms for brittle fracture will be developed.

As brittle failure typically can be traced back to a single micro crack nucleus that developes into a self-sustaining brittle fracture, weakest link modeling is considered appropriate here. The basic weakest link assumption can be summarized as: the volume of a structure can be divided into infinitesimal elements, complete failure of the structure occurs if one of these elements fail. It will be assumed that one of two possible failure mechanisms may be activated within each element, specifically grain boundary or particle initiated failure. However, the following framework can readily be extended to a multitude of mechanisms. The nature of the problem allows for the expression of the probability of failure to be derived by assuming either statistical independence or mutual exclusivity among the failure mechanisms. Mutual exclusivity implies that even though multiple mechanisms are probable to cause brittle fracture initiation, only one mechanism will initiate and cause the resulting failure, i.e. either the one or the other. Due to the independence between the mechanisms the probability of failure of an infinitesimal element can be written as $P\left(A \cup B\right) = P\left(A\right) + P\left(B\right)$, and thus $P\left(A \cap B\right) = 0$. This results in a weakest link expression as

$$P_{\mathrm{f}} = 1 - \exp\left(-\int_V \left(h^{\mathrm{A}} + h^{\mathrm{B}}\right) \frac{\mathrm{d}V}{V_0}\right), \tag{13}$$

where h^{A} and h^{B} are the hazard functions for the different micro mechanisms of failure. The connection between the physical behavior of the micro mechanism and the probabilistic model is described through the functions $h^i\left(\sigma, \varepsilon\right)$, which can be interpreted to be related to the number of potential brittle crack initiators available at the current load level. The superscript i is used to signify a specific micro mechanism. The model developed here takes inspiration from the work by Kroon and Faleskog [12] and can be seen as a development of that model. In their work, the function h was divided into two separate parts as $h = h_1\left(\bar{\varepsilon}^{\mathrm{p}}\right) h_2\left(\sigma\right)$, where h_1 is related to the formation of micro cracks and is representative of the number of micro cracks at that level of plastic strain, while h_2 is related to the propagation of a critical micro crack leading to macroscopic failure. In previous studies [13], [14], [15] where this model has been applied, the failure probability was calculated from the maximum value of h during the load history leading up to the current load step. This choice makes the implementation straight forward and relatively simple, however it leaves the interpretation of h ambiguous in some cases. For example, if the micro crack nucleation rate would decrease with increasing plastic strain, the model would still predict an increasing probability of failure. Also, a micro crack needs to be nucleated in a region of high stress such that it keeps propagating until it can become self-sustaining. It is less likely that brittle fracture will occur from an arrested micro crack, which a model with $h_{\max}$ suggests. For this reason, an incremental formulation for h_1 is proposed as

$$h_1^i = \int_0^{\bar{\varepsilon}^{\mathrm{p}}} g_1^i \left(\bar{\varepsilon}^{\mathrm{p}}\right) \mathrm{d}\bar{\varepsilon}^{\mathrm{p}}, \tag{14}$$

where g_1 is related to the rate of nucleation of micro cracks. Combined with h_2, the expression for h becomes

$$h^i = \int_0^{\bar{\varepsilon}^{\mathrm{p}}} g_1^i \left(\bar{\varepsilon}^{\mathrm{p}}\right) h_2^i \left(\sigma \left(\bar{\varepsilon}^{\mathrm{p}}\right)\right) \mathrm{d}\bar{\varepsilon}^{\mathrm{p}}. \tag{15}$$

This expression allows for unambiguous interpretations of the nucleation rate and that a micro crack must indeed nucleate in a region of high stress in order to propagate as a cleavage crack. Experimental observations by McMahon and Cohen [6], Lindley et al. [32], and Gurland [33] prompted Kroon and Faleskog to use a linear function for h_1 which in this framework translates to a constant g_1. The case of a linear function has been shown to work well in the case of particle initiated cleavage. A viable choice of g_1 for intergranular failure, will be developed in Section 4. The function h_2 will for both mechanisms be taken to be on the same form as in the original model i.e. through an assumption of an exponential micro crack size distribution as

$$h_2^i \left(\bar{\sigma}\right) = \begin{cases} \exp\left(-\left(\frac{\eta \sigma_{\mathrm{th}}^i}{\bar{\sigma}}\right)^2\right) - \exp\left(-\eta^2\right) \text{ for } \bar{\sigma} > \sigma_{\mathrm{th}}^i, \\ 0 \text{ for } \bar{\sigma} \leqslant \sigma_{\mathrm{th}}^i. \end{cases} \tag{16}$$

Here, σ_{th}^i is the threshold stress below which brittle fracture is not possible, $\bar{\sigma}$ is a non-local measure of stress. The parameter η is a distribution parameter which has been shown to have little significance in practical applications, η will be taken as unity throughout this study as per the suggestions in [12]. The non-local stress measure $\bar{\sigma}$ in (16) is calculated from the non-local stress tensor $\bar{\sigma}_{ij}$, which is calculated as the volume average over the volume V_{L} with radius L as

$$\bar{\sigma}_{ij} = \frac{1}{V_{\mathrm{L}}} \int_{V_{\mathrm{L}}} \sigma_{ij}(\hat{X}_k - X_k)\, \mathrm{d}\hat{V}, \tag{17}$$

where $\mathbf{X} = \{X_1, X_2, X_3\}$ are the coordinates of the center of V_{L} and $L \geqslant |\hat{X}_k - X_k|$. Note that $\bar{\sigma}_{ij}$ will be equal to the local σ_{ij} in the limit of $L \to 0$ or if the stress state in V_{L} is homogeneous. The non-local stress measure $\bar{\sigma}$ can then readily be calculated from the principal stresses of the non-local stress tensor as

$$\bar{\sigma} = \frac{(n+1)\bar{\sigma}_{\mathrm{I}} + \bar{\sigma}_{\mathrm{II}} + \bar{\sigma}_{\mathrm{III}}}{n+3}, \tag{18}$$

which is the effective normal stress measure, introduced in [15], where the parameter n can be used to obtain a measure of normal stress that ranges between the mean stress when $n = 0$ and the maximum principal stress when $n \to \infty$. Note the ordering of the principal stresses $\bar{\sigma}_{\mathrm{I}} \geqslant \bar{\sigma}_{\mathrm{II}} \geqslant \bar{\sigma}_{\mathrm{III}}$. In this study, $n \to \infty$ was chosen, resulting in the maximum principal stress in order to reduce the parameter space.

At significant plastic straining related to the ductile failure process, potential brittle fracture initiators may cause a void to form rather than initiating a brittle fracture nucleus, either by particle debonding or by microcrack arrest of a grain boundary crack. A method to account for this process in the modeling of brittle fracture was laid out by Xia and Fong Shih [34]. By considering the conditional probability of brittle fracture occurring given that no void has nucleated, the brittle fracture probability given the probability of void nucleation can be written as

$$P^i_{\mathrm{brittle}} = P^i_{\mathrm{brittle}_{\mathrm{novoid}}} \left(1 - P_{\mathrm{void}}\right), \tag{19}$$

where P^i_{brittle} is the brittle fracture probability, $P^i_{\mathrm{brittle}_{\mathrm{novoid}}}$ is the brittle fracture probability where no account is taken of void nucleation, and P_{void} is the void nucleation probability. Taking this into account for the total failure probability alters the expression in Eq. (13) to

$$P_{\mathrm{f}} = 1 - \exp\left(- \int_V \left(h^A + h^B\right) \left(1 - P_{\mathrm{void}}\right) \frac{\mathrm{d}V}{V_0} \right). \tag{20}$$

Here it is assumed that both brittle mechanisms are affected in the same way where, P_{void} is related to the nucleation of voids due to plastic straining as introduced in Section 2.2 which is expressed as

$$P_{\mathrm{void}} = \frac{1}{f_{\mathrm{N}}} \int_{0}^{\bar{\varepsilon}^{\mathrm{p}}} D\left(\bar{\varepsilon}^{\mathrm{p}}\right)\, \mathrm{d}\bar{\varepsilon}^{\mathrm{p}}. \tag{21}$$

4. Modeling of grain boundary failure

Micro mechanical modeling of polycrystalline aggregates has been considered in order to study and motivate the micro crack nucleation rate from grain boundaries subjected to a stress state relevant to that of a material point ahead of a deforming crack tip. As a multi-layer weld is considered in this study, the grain structures have been divided into representative volume elements (RVEs) of equiaxed grains and dendritic grains. The grain structure models considered here were made using the open-source software Neper [35]. The equiaxed grain structures were made using a constrained tesselation to yield a log-normal grain size distribution with a specific coefficient of variation $c_v = s/\mu$, and a log-normal grain sphericity distribution in order to achieve the equiaxed structure. The dendritic grain structures were constructed from tessellations with specific grain aspect ratios, asp = width/length. The grain structures considered in this study contain 1000 or 800 grains with random crystallographic orientation. For simplicity the equiaxed and dendritic structures were separated into individual models as depicted in Figure 7.

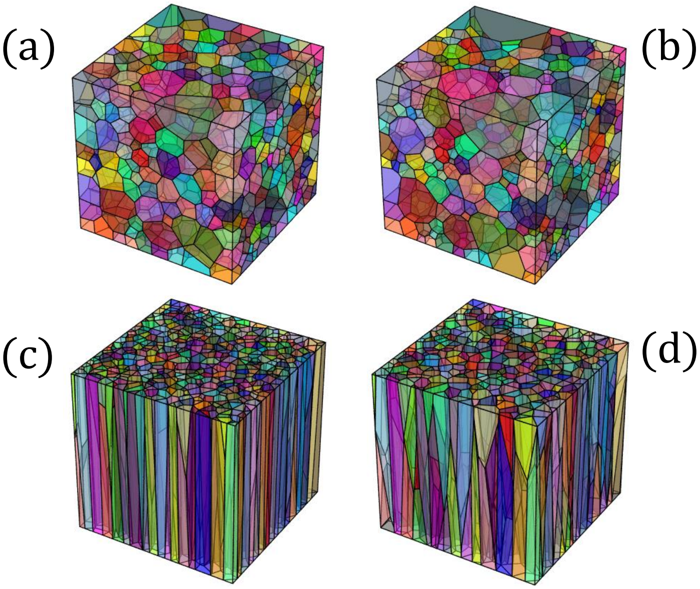

Figure 7: Tesselations of grain structures. (a) and (b) corresponds to the equiaxed grain structures, where $c_v = \{0.2, 0.4\}$ respectively. (c) and (d) corresponds to the dendritic grain structures, where the aspect ratio of the grains corresponds to 0.05 and 0.1 respectively.

4.1. Crystal plasticity

The analysis of the RVEs has been carried out using the crystal plasticity framework offered in the open-source software DAMASK [36]. The crystal plastic framework in DAMASK is a modification of the phenomenological model introduced by Hutchinson [37] to accommodate the slip systems of bcc crystals. The framework incorporates slip on 12 $\{110\}\langle 111\rangle$ and 12 $\{112\}\langle 111\rangle$ systems, respectively, which are parameterized by the slip resistances s^{α} $(\alpha = 1, 2, ..., 24)$. The resistance is asymptotically increased towards the saturation stress s^{α}_{∞} due to shearing on the slip systems γ^{β} $(\beta = 1, 2, ..., 24)$ as

$$\dot{s}^{\alpha} = \sum_{\beta=1}^{24} h_0 |\dot{\gamma}^{\beta}| \left|1 - \frac{s^{\beta}}{s^{\alpha}_{\infty}}\right|^{a} \operatorname{sgn}\left(1 - \frac{s^{\beta}}{s^{\alpha}_{\infty}}\right) h^{\alpha\beta}, \tag{22}$$

where h_0 and a are model parameters and $h^{\alpha\beta}$ are slip interaction parameters. Given a set of current slip resistances and a resolved shear stress, the shear on each slip system evolves at a rate of

$$\dot{\gamma}^{\alpha} = \dot{\gamma}_0 \left|\frac{\tau^{\alpha}}{s^{\alpha}}\right|^{n} \operatorname{sgn}(\tau^{\alpha}), \tag{23}$$

where $\dot{\gamma}_0$ is the reference shear rate and n is the viscoplastic stress exponent. The resolved shear stress, τ^{α}, on a specific slip system is calculated as

$$\tau^{\alpha} = \mathbf{M}_{\mathrm{p}} \left(s^{\alpha}_{\mathrm{s}} \otimes n^{\alpha}_{\mathrm{s}}\right), \tag{24}$$

where $\mathbf{M}_{\mathrm{p}}$ is the Mandel stress in the intermediate plastic configuration, s^{α}_{s} and n^{α}_{s} are the unit vectors along the slip direction and the slip plane normal, respectively. The sum of all individual shear contributions on all slip systems defines the plastic velocity gradient, $\mathbf{L}_{\mathrm{p}}$, as

$$\mathbf{L}_{\mathrm{p}} = \sum_{i=1}^{24} \dot{\gamma}^{\alpha} \left(s^{\alpha}_{\mathrm{s}} \otimes n^{\alpha}_{\mathrm{s}}\right). \tag{25}$$

The elastic behavior is described by the generalized Hooke's law subjected to cubic symmetry, hence three independent parameters c_{11}, c_{12} and c_{44} describes the elastic properties of the microstructure. The elastic properties were chosen with anisotropy according to Hirth and Lothe [38], but scaled to yield a homogenized Young's modulus of 200 GPa.

To study the crack initiation from grain boundaries using the models depicted in Figure 7, appropriate boundary conditions relevant to the analysis are needed. However, applying displacement boundary conditions to achieve such a state in a finite deformation elastic-plastic analysis poses a problem as the volumetric behavior will change when the plastic deformation starts to dominate the solution. To overcome this issue, the RVEs are subjected to straining such that the macroscopic stress ratios over the RVE are kept constant through nonlinear kinematic constraints. Moreover, the sides of the model are constrained to remain straight and perpendicular during deformation. This is achieved through constraining the RVEs by a multi point constraint (MPC) in Abaqus. The procedure for this type of constraint was introduced by Faleskog et al. [21] since then the methodology has been successfully applied in various formulations in several studies such as [39], [40], [41], [42], [43], [44]. This methodology makes it possible to supply the characteristics of the stress state in terms of the triaxiality parameter T and the Lode parameter L.

In order to estimate the crystal plastic model material parameters in Table 3, a model with $T = 1/3$ and $L = -1$ was utilized and compared to uniaxial tensile test data (before necking). The von Mises effective stress and strain used for the comparison was readily calculated from the macroscopic principal stresses and strain increments acting over the RVE as

$$\Sigma_{\mathrm{e}} = \frac{1}{\sqrt{2}}\sqrt{\left(\Sigma_{\mathrm{I}} - \Sigma_{\mathrm{II}}\right)^2 + \left(\Sigma_{\mathrm{II}} - \Sigma_{\mathrm{III}}\right)^2 + \left(\Sigma_{\mathrm{I}} - \Sigma_{\mathrm{III}}\right)^2}, \tag{26}$$

$$E^{\mathrm{p}}_{\mathrm{e}} = \int_0^t \frac{\sqrt{2}}{3}\sqrt{\left(\dot{E}^{\mathrm{p}}_{\mathrm{I}} - \dot{E}^{\mathrm{p}}_{\mathrm{II}}\right)^2 + \left(\dot{E}^{\mathrm{p}}_{\mathrm{II}} - \dot{E}^{\mathrm{p}}_{\mathrm{III}}\right)^2 + \left(\dot{E}^{\mathrm{p}}_{\mathrm{I}} - \dot{E}^{\mathrm{p}}_{\mathrm{III}}\right)^2}\,\mathrm{d}t, \tag{27}$$

where the principal axes are illustrated in Figure 8. The constitutive crystal plastic model parameters were tuned until the model response was comparable to uniaxial tensile test data, the comparison between model response and tensile test data can be seen in Figure 9. All parameters used in DAMASK can be found in Table 3.

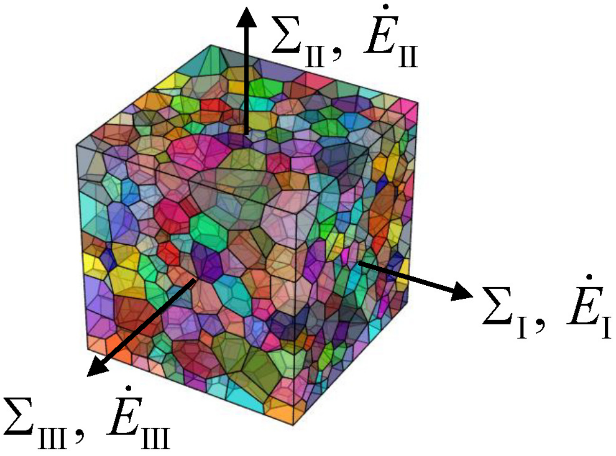

Figure 8: Illustration of the principal axes of the RVE.

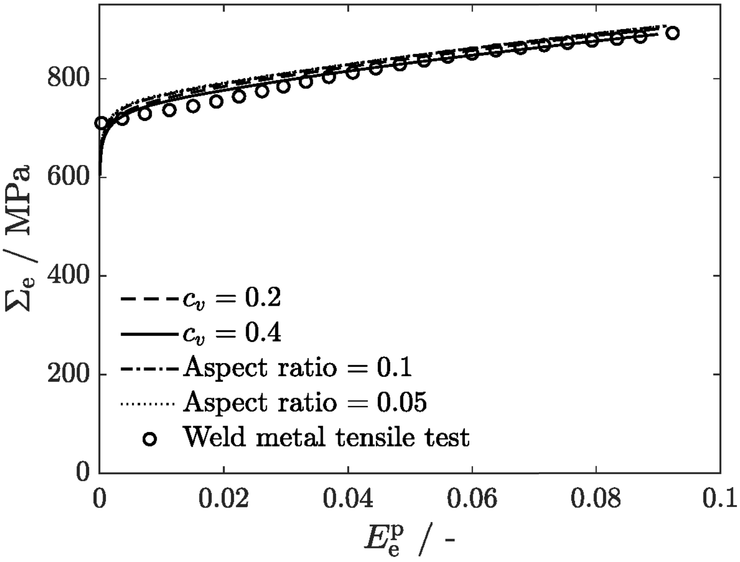

Figure 9: Comparison between homogenized Σ_{e}-$E_{\mathrm{e}}^{\mathrm{p}}$ over the RVE and the experimental flow stress-strain relation as inferred from a tensile test.

Table 3: Model parameters used in crystal plasticity model.

Parameter	Value	Parameter	Value
h_0/MPa	2700.0	n	50.0
$h^{\alpha\beta}$	1.4	a	15.0
$s_0^{\alpha}/\mathrm{MPa}$	290.0	c_{11}/GPa	184.0
$s_{\infty}^{\alpha}/\mathrm{MPa}$	1850.0	c_{12}/GPa	107.0
$\dot{\gamma}_0/\mathrm{s}^{-1}$	0.001	c_{44}/GPa	93.0

4.2. Grain boundary stress state and micro crack nucleation

The simulations pertinent to the investigation of the grain boundary cracking were run with boundary conditions enforcing $T = \{2.35, 2.2, 2.05, 1.9, 1.75\}$ and $L =$ -0.25. Early on in the investigation it was realised that the stress triaxiality T had a significant influence on the grain boundary stress state while the Lode parameter L had a negligible influence. Therefore, a range of stress triaxialites was chosen to enclose the values found in the analysis in Section 2.2 to be used as boundary conditions in the analysis of the polycrystalline aggregates.

The initiation of a micro crack from a grain boundary capable of participating in a brittle failure event has been analysed through assuming that the grain boundary strength can be associated to a surface energy, γ_{s}. The driving force to nucleate a micro crack at a grain boundary facet is assumed to be governed by the Griffith criterion [45], [46], which relates the surface energy γ_{s} to a critical stress σ_{c}. Here, γ_{s} is viewed as an effective surface energy also including some plastic dissipation representative of grain boundary separation. For practical purposes, the shape of the grain boundary crack will be in the form of an internal elliptic crack, characterized by A_{GB} and its aspect ratio $\kappa = a/c$, where a and c is the minor and major axis respectively. This yields the following expression for the grain boundary strength,

$$\sigma_{\mathrm{c}} = \left(\frac{2\left(1/\sqrt{\kappa} + 1.464\kappa^{1.15}\right) E\gamma_{\mathrm{s}}}{\pi\left(1-\nu^2\right)} \right)^{1/2} \left(\frac{\pi}{A_{\mathrm{GB}}} \right)^{1/4}, \tag{28}$$

where the stress intensity solution was taken from Newman and Raju [47]. The surface energy used to compute the critical stress will be presented normalized according to $\bar{\gamma} = \gamma_{\mathrm{s}}/(E\bar{d})$, where $\bar{d}$ is the mean radius of the grains calculated from the volume by assuming grains of spherical shape.

As detailed in Section 3, the relation between the incremental failure probability in a sub-volume of the structure and the physical process resulting in brittle fracture is described through the function h, which itself is divided into two parts, $h = h_1\left(\bar{\varepsilon}^{\mathrm{p}}\right) h_2\left(\bar{\sigma}\right)$. The first part is related to the number of micro cracks at a given level of plastic strain, which here will be formed on the basis of the nucleation rate, being the key issue in this analysis. Thus in the post-processing of the grain structure models, the normal stress component of the tractions between two grains is compared to the strength, σ_{c}, of that specific grain boundary to determine whether failure has occurred. If failure occurs, then that specific grain boundary is added to the cumulative number of failed grain boundaries not to be regarded in the subsequent load history. If failure does not occur, then it will be eligible for failure at a later stage in the load history. The main drawback of such an analysis it that even though a boundary has failed it will continue to carry load, as opposed to cohesive zone modelling where a load redistribution would occur at the moment of failure. However, it is presumed that this type of analysis can be justified for the understanding of h as long as the number fraction of grain boundaries considered to be critical is low. To achieve this, $\bar{\gamma} = 35$ was chosen and used throughout.

The fraction of critical grain boundaries, i.e. the accumulated number of grain boundaries that has exceeded the critical stress, normalized by the total number of grain boundaries in the analysis for all the considered models can be seen in Figure 10. It is clear that the fraction of critical grain boundaries appears to accumulate with the same characteristic in all models. That is, no critical grain boundaries during initial elastic straining followed by a rapid increase which more or less stabilizes at increased plastic straining. The overall accumulated number of critical grain boundaries is directly dependent to the surface energy $\bar{\gamma}$. However, the characteristic of the accumulation of critical grain boundaries remains, to a large extent, the same. The data plotted in Figure 10 is considered to be proportional to the h_1-function of the weakest link model, i.e. the resulting g_1-function would need to be decreasing with respect to plastic strain. By choosing a form of g_1 that results in the following expression for h_1

$$h_1 = c \int_{\varepsilon^{\mathrm{p}}} \frac{1}{\varepsilon_0 \left(1 + \varepsilon^{\mathrm{p}}/\varepsilon_0\right)} \,\mathrm{d}\varepsilon^{\mathrm{p}}, \tag{29}$$

a least square fit of c and ε_0 with a resulting $R^2 = 0.99$ or better is achieved for all levels of triaxiality. Indicating that $g_1 = c/\left(\varepsilon_0 \left(1 + \varepsilon^{\mathrm{p}}/\varepsilon_0\right)\right)$ is a good candidate for the grain boundary failure mechanism.

In Figure 11 the average normal stress σ_{n} acting on each grain boundary in the equiaxed model is visualized, where the model with $c_v = 0.4$ has been used. The stress state is plotted at a global plastic strain $\varepsilon^{\mathrm{p}} = 0.005$. In Figure 11 (a), σ_{n} is plotted against the grain boundary misorientation θ, calculated according to Randle [48]. In Figure 11 (b), σ_{n} is plotted against the

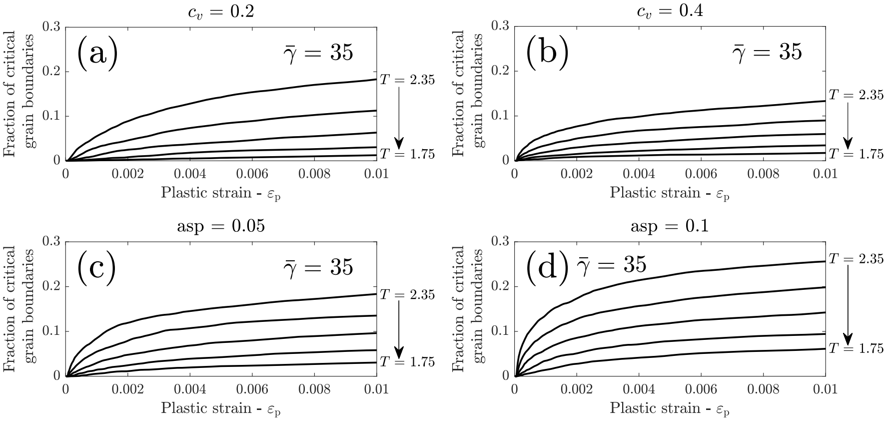

Figure 10: The accumulated number fraction of critical grain boundaries in the models pertaining to (a) $c_v = 0.2$, (b) $c_v = 0.4$, (c) asp = 0.05, and (d) asp = 0.1. Each line represents a solution where the stress triaxiality T belongs to the set {2.35, 2.2, 2.05, 1.9, 1.75}.

polar angle between the grain boundary normal and the normal of the global maximum principal stress acting over the RVE. Lastly, in Figure 11 (c), σ_n is plotted against the grain boundary area normalized with the mean grain boundary area. In Figure 11 (c), the Griffth criterion is also illustrated where grain boundaries exceeding the critical stress are colored red as opposed to the non critical which are colored black. This color coding applies to all subfigures. Clearly, the results in Figure 11 (b) shows that grain boundaries with a normal aligning with the maximum principal stress appears to be more prone to failure. The results in Figure 11 (a) are not as clear, i.e. no strong coupling between the failed grain boundaries and the grain boundary misorientation appears to be seen. The results for the other models considered are similar to the results shown in Figure 11, which is why they are not shown here.

At this juncture, it is of interest to find out how the crystal microstructure influences the local normal stress at the grain boundaries in relation to the corresponding normal stress obtained from the global stress state. This is shown in Figure 12 where the average normal stress at each grain boundary is normalized by the normal stress obtained from the global stress state. This means, if the ratio $\sigma_\mathrm{n}/\Sigma_\mathrm{N}$ is unity, the grain boundary stress is fully controlled by the global stress state, while any deviation from unity indicates an influence of the crystal microstructure. From this figure, it can be observed that the ratio does not de-

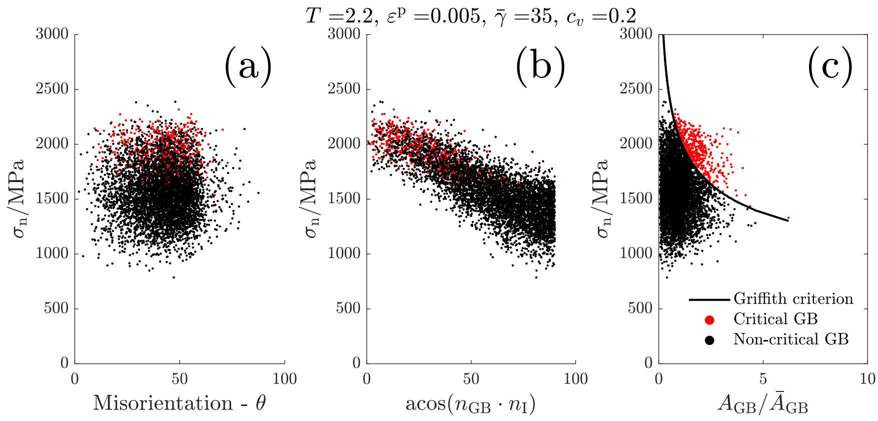

Figure 11: Illustration of the grain boundary normal stress σ_{n} as a function of (a) grain boundary misorientation, (b) the polar angle from the maximum principal stress direction, and (c) the grain boundary area normalized by the mean grain boundary area, here is also the Griffith criterion illustrated. Note the color coding where red indicates a critical grain boundary and black indicates a non-critical grain boundary.

viate much from unity in the vast majority of the grain boundaries in the model. If the variation around unity in Figure 12 can be neglected, an analytical model for grain boundary failure may suffice. Such a model will be developed next.

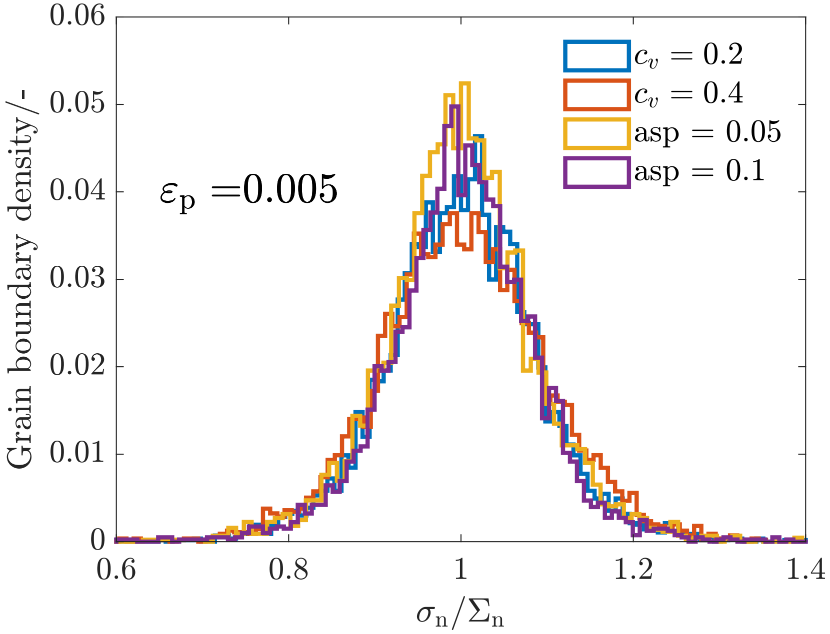

Figure 12: Histogram of the distribution of the grain boundary stress normalized by the global stress (over RVE) projected on the grain boundary normal. In perfect isotropy, all bars would align at unity. The standard deviation of the datasets is $\sigma_{\mathrm{GB}} = \{0.087, 0.097, 0.087, 0.084\}$, respectively for $c_v = 0.2$, $c_v = 0.4$, asp = 0.05 and asp = 0.1.

4.3. Analytical model for grain boundary crack nucleation

Consider a volume akin to the models in Section 4.2 subjected to a stress state defined by T, L and σ_e. Then, the principal stresses can be expressed as

$$\sigma_\mathrm{I} = \sigma_\mathrm{e}\left(T + \frac{3-L}{3\sqrt{L^2+3}}\right), \tag{30}$$

$$\sigma_\mathrm{II} = \sigma_\mathrm{e}\left(T + \frac{2L}{3\sqrt{L^2+3}}\right), \tag{31}$$

$$\sigma_\mathrm{III} = \sigma_\mathrm{e}\left(T - \frac{3+L}{3\sqrt{L^2+3}}\right). \tag{32}$$

The effective stress σ_e is specified as a flow strength relation on the form $\sigma_\mathrm{e} = \sigma_\mathrm{ref}\left(\varepsilon^\mathrm{p}/\varepsilon_\mathrm{ref}\right)^m$ where the plastic strain ε^p is used as a loading parameter. The parameters were estimated to yield an as-similar response as the crystal model as possible. The grain boundary areas are randomly drawn from a log-normal distribution (to emulate the same distribution as in the crystal models) and the normals are taken as uniformly distributed over the unit sphere. The critical stress of each grain boundary is calculated in the same manner as in the crystal models and the post processing regarding the accumulation of critical grain boundaries occurs in the same way.

Considering a case with 5000 grain boundaries and distribution parameters for the area distribution corresponding to the crystal models, the outcome seen in Figure 13 results, which is compared to the outcome of the crystal models. It can be clearly seen that the results from the crystal model is reproduced by the analytical model. By using the analytical model to investigate a wider range of stress triaxialites the results in Figure 14 are obtained. Interestingly, a threshold in the triaxiality below which no critical grain boundaries can be found appears to emerge. By inferring a g_1-function from these results, the following expression can be be used to reproduce the behavior with a $R^2 = 0.996$

$$h_1 = \begin{cases} c\int_{\varepsilon^\mathrm{p}} \frac{(T-T_\mathrm{th})^2}{\varepsilon_0(1+\varepsilon^\mathrm{p}/\varepsilon_0)}\,\mathrm{d}\varepsilon^\mathrm{p} & \text{for } T > T_\mathrm{th}, \\ 0 & \text{for } T \leqslant T_\mathrm{th}. \end{cases} \tag{33}$$

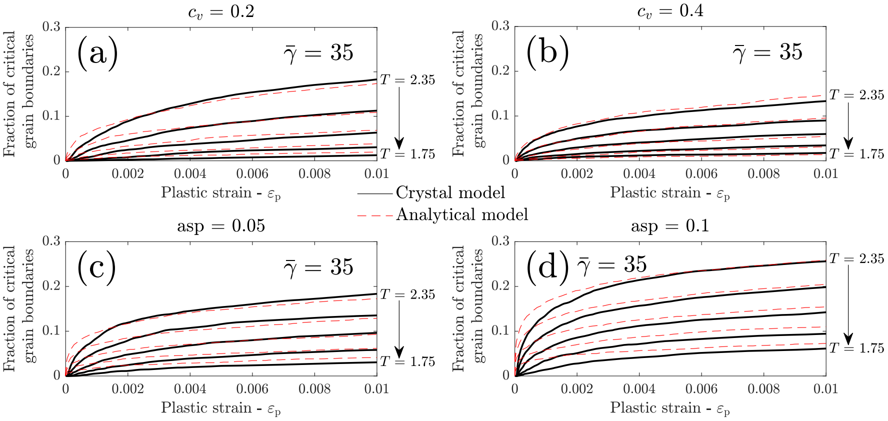
$c_v = 0.2$

$c_v = 0.4$

asp = 0.05

asp = 0.1

Figure 13: Comparison of the accumulated number fraction of critical grain boundaries between analytical model and the crystal models pertaining to (a) $c_v = 0.2$, (b) $c_v = 0.4$, (c) asp = 0.05, and (d) asp = 0.1. Each line represents a solution where the stress triaxiality T belongs to the set {2.35, 2.2, 2.05, 1.9, 1.75}.

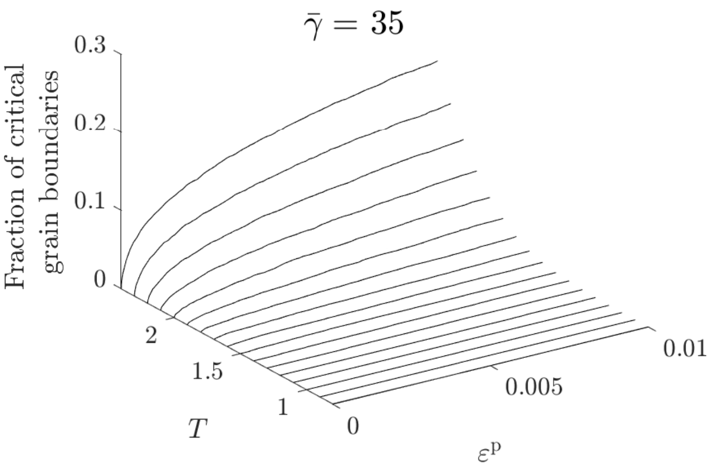
$\bar{\gamma} = 35$

Figure 14: The accumulated number fraction of critical grain boundaries calculated by the analytical model with the purpose of exploring the influence of the stress triaxiality. Note the threshold effect in the lower end of the triaxiality axis.

5. Application of probabilistic model to experiments

From the micro mechanical investigation in Section 4, two candidates for the g_1-function could be inferred for the grain boundary mechanism in the weakest link framework detailed in Section 3. This section presents the estimation of parameters and application to experiments of the micro mechanically informed weakest link model for multiple mechanism brittle fracture. The estimation of parameters was carried out by minimzing the residual $R = R_{\mathrm{I}} + R_{\mathrm{II}}$ using the Nelder-Mead simplex algorithm [49], where superscript I and II relates to the high and low constraint experiments used in the estimation of model parameters. The partial residuals R_{I} and R_{II} were computed as

$$R_{\mathrm{I}} = \sum_{i=1}^{N_{\mathrm{I}}} [P^i_{\mathrm{rank}} - P_{\mathrm{f}}\left(J^i_{\mathrm{c}}\right)]^2,\ R_{\mathrm{II}} = \sum_{i=1}^{N_{\mathrm{II}}} [P^i_{\mathrm{rank}} - P_{\mathrm{f}}\left(J^i_{\mathrm{c}}\right)]^2. \tag{34}$$

For details regarding the calculations pertinent to the weakest link model, the reader is referred to [13] and [15].

The length scales used to compute the non-local stress in (17) needs to be properly resolved over the mesh used in the FE-models. With the models used for the weakest link calculations, the length scales reaches over ∼5 elements per element along the axis of crack propagation in the fine mesh region. The length scales used can be found in Table 4 and an overview of the models used can be seen in Figure 2.

Concerning the material used as a reference in this study, R3RPVH, the fracture toughness distribution appears to be unimodal. Also, the cleavage initiation mechanism in the reference material was traced back to second phase particles. Therefore, a single mechanism weakest link framework has been applied to the fracture tests of R3RPVH, i.e. a single, constant g_1-function was used. The outcome of the parameter estimation and application of the model to the reference material, R3RPVH, can be seen in Figure 15. It is clearly seen that a single mechanism weakest link framework including the effect of potential void formation, is capable of describing the fracture toughness distribution for the cases considered.

Regarding the aged material, R4PRZ, where two initiation mechanisms are able to initiate brittle fracture, i.e. grain boundaries and second phase particles, the multiple mechanism weakest link framework needs to be used. Concerning

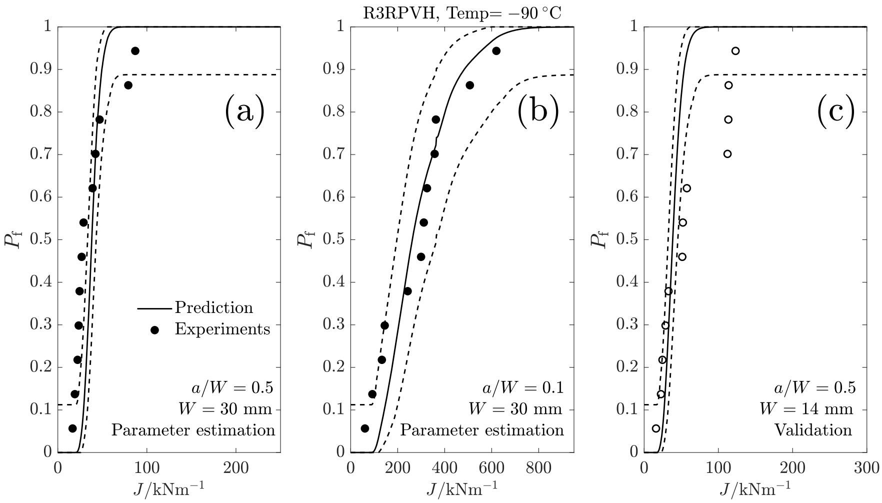

Figure 15: Comparison of the predicted failure probability with rank probabilities for the fracture tests (circles) of the reference material R3RPVH data set tested at a temperature of −90 °C. (a) subset where $a/W = 0.5$ and $W = 30$ mm, (b) subset where $a/W = 0.1$ and $W = 30$ mm, and (c) subset where $a/W = 0.5$ and $W = 14$ mm. Subsets (a) and (b) were used for parameter estimation, subset (c) were used as validation of model predictions.

the choice of g_1 for the grain boundary mechanism, the following two candidates have been found in Section 4 to describe the rate of critical grain boundaries per plastic strain

$$g_1 = c\frac{1}{\varepsilon_0\left(1+\varepsilon^\mathrm{p}/\varepsilon_0\right)}, \tag{35a}$$

$$g_1 = \begin{cases} c\frac{(T-T_\mathrm{th})^2}{\varepsilon_0(1+\varepsilon^\mathrm{p}/\varepsilon_0)} & \text{for } T > T_\mathrm{th}, \\ 0 & \text{for } T \leqslant T_\mathrm{th}. \end{cases} \tag{35b}$$

Here Eq. (35a) only depends on plastic strain and has two parameters to describe the rate of micro crack nucleation. Eq. (35b) depends of both plastic strain and the stress triaxiality and has three parameters, where two are the same as the previous case and the third is a threshold parameter in the stress triaxiality T_th. The importance of resolving the integral for the hazard function in (15) throughout the loading history should be noted. Especially for the grain boundary mechanism, even with 500 load steps in the FE-models, additional steps had to be added by linear interpolation of the pertinent fields before convergence was reached in the weakest link predictions. By considering both Eq.

Table 4: Model parameters used in the weakest link model. (a) Single mechanism model for R3RPVH. (b) Multiple mechanism model for R4PRZ.

	Parameter	Value	Parameter	Value	Parameter	Value
(a)	$c/V_0/10^9$	2.0519	$\sigma_{\mathrm{th}}/\mathrm{MPa}$	2019.5	$L/\mu\mathrm{m}$	50.0
(b)	$c^{\mathrm{A}}/V_0/10^8$	1.3300	$\sigma_{\mathrm{th}}^{\mathrm{A}}/\mathrm{MPa}$	1921.6	$L/\mu\mathrm{m}$	50.0
			$\sigma_{\mathrm{th}}^{\mathrm{B}}/\mathrm{MPa}$	1008.9	$L/\mu\mathrm{m}$	50.0
(35a)	$c^{\mathrm{B}}/\ln(1/\varepsilon_0)/V_0$	3054.0	$\varepsilon_0/10^{-8}$	1.1		
(35b)	$c^{\mathrm{B}}/\ln(1/\varepsilon_0)/V_0$	25040.0	$\varepsilon_0/10^{-8}$	1.1	T_{th}	0.808

(35a) and (35b) the parameters pertinent to the weakest link model for multiple mechanisms can be estimated. The parameters of the model can be found in Table 4, note the normalization of the parameter c in Eq. (35a) and (35b). Interestingly, parameter estimates comes out the same with the exception of the parameter c in Eq. (35a) and (35b). It was found that the prediction of the fracture toughness distribution appears to be rather insensitive to the choice of g_1 with respect to the proposed functions in this study. The model predictions are shown together with the experimental fracture test results in Figure 16, where (35a) was used. In Figure 17 the model predictions together with the underlying mechanisms are illustrated, where each mechanism is calculated as if being the sole mechanism, i.e. by a single mechanism weakest link expression. It appears that the microstructurally informed weakest link model with multiple mechanisms for brittle fracture is able to describe the bimodal toughness distribution of the thermally aged material with a remarkable accuracy. Figure 18 shows model predictions for SEN(B)-specimens with different sizes to illustrate the effect of size on the outcome of the model. It is clear that the intergranular fracture mechanism is subject to a distinct size effect where it may be suppressed in its entirety if the specimen size is small enough. On the other hand, if the specimen size is increased, the intergranular mechanism becomes more likely and will dominate given a large enough geometry.

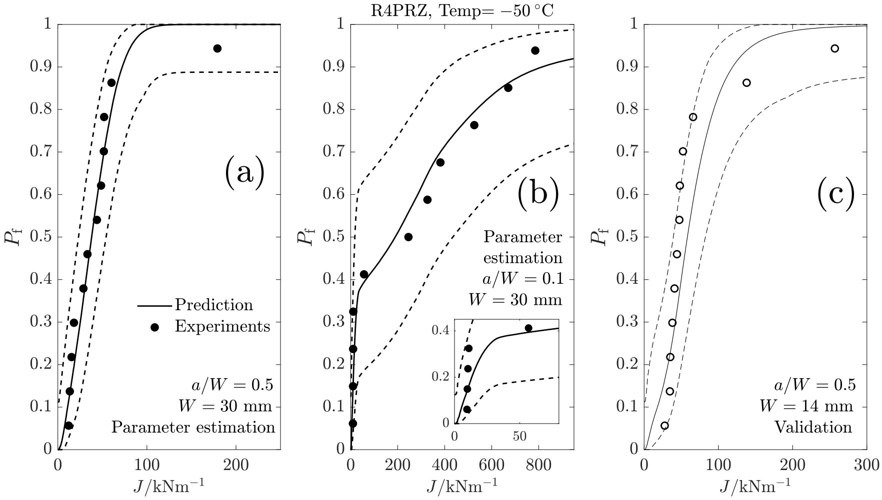

Figure 16: Comparison of the predicted failure probability with rank probabilities for the fracture tests (circles) of the thermally aged R4PRZ data set tested at a temperature of −50 °C. (a) subset where $a/W = 0.5$ and $W = 30$ mm, (b) subset where $a/W = 0.1$ and $W = 30$ mm, and (c) subset where $a/W = 0.5$ and $W = 14$ mm. Subsets (a) and (b) were used for parameter estimation, subset (c) were used as validation of model predictions. Note, in (b) figure inset shows steep initial region of model prediction.

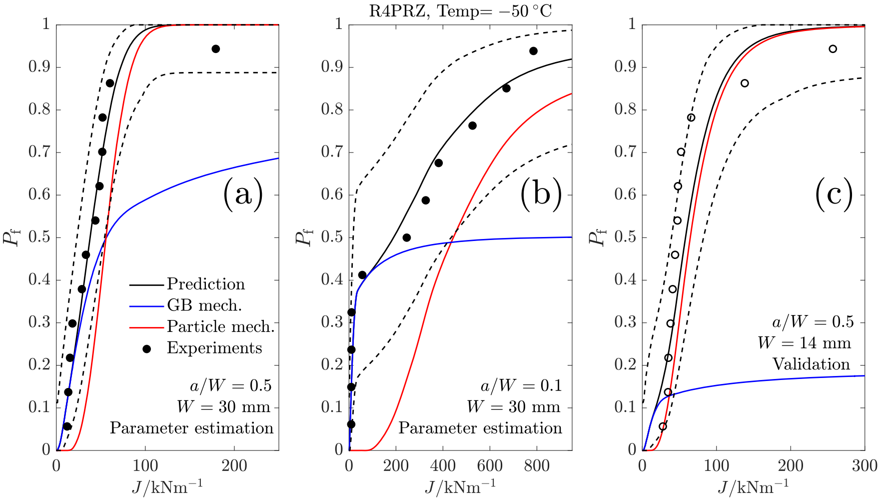

Figure 17: Comparison of the predicted failure probability with rank probabilities for the fracture tests (circles) of the thermally aged R4PRZ data set tested at a temperature of $-50\,^\circ$C. Shown here is also the individual mechanisms calculated as if being single mechanism predictions. Note that the individual mechanisms as illustrated here does not sum up to the actual multi mechanism prediction since they are computed as single mechaism predictions and are for illustration purposes only.

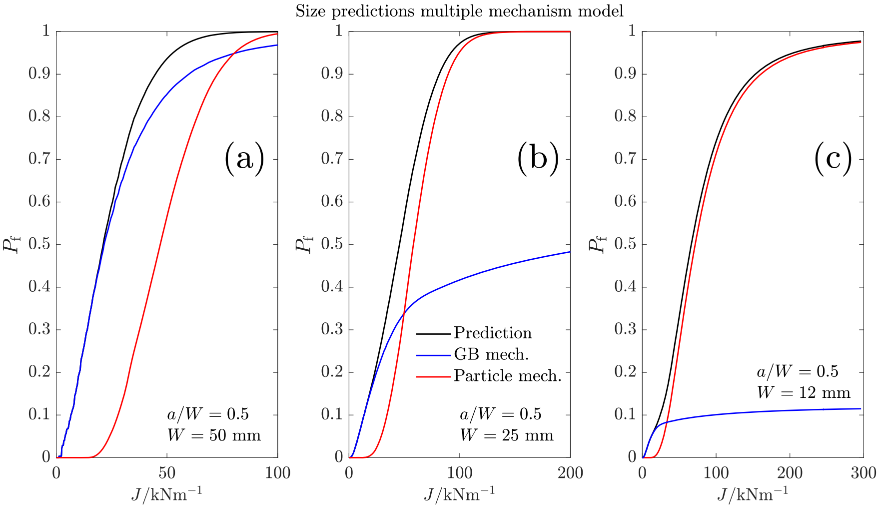

Figure 18: Model predictions showcasing the size effect of the multiple mechanism weakest link model. Note that the intergranular mechanism is suppressed for the smaller geometry, and vice versa for the larger geometry. (a) Large specimen, $W = 50$ mm, (b) medium sized specimen, $W = 25$ mm, (c) small specimen, $W = 50$ mm.

6. Discussion and concluding remarks

The study presented in this paper is pertinent to modeling brittle failure of ferritic steels with multiple failure mechanisms. More specifically, aged low alloy steels in the case where the ageing introduces a second mechanism of brittle failure that alters the fracture toughness distribution from being unimodal to bimodal. In this paper it is shown how a multiple mechanism weakest link framework can be constructed to account for both intergranular and transgranular fracture. The mechanism for grain boundary controlled fracture has been inferred from crystal plastic simulations, which when introduced into the weakest link model, has been shown to be able to reproduce the fracture toughness distribution with a remarkable accuracy.

Regarding the crystal plastic models presented in Section 4, the modeling effort was carried out in order to motivate the choice of the g_1-function that governs the nucleation behavior of grain boundary micro cracks in the weakest link model. This was carried out by investigation of the grain boundary stress state which has been compared to a Griffith criterion for the critical stress. Another modeling approach for similar problems is using a cohesive zone methodology for the grain boundaries. This makes it possible to account for the local unloading due to the opening of a grain boundary crack, and its subsequent propagation in connecting grain boundaries. It was judged that such a sophisticated model would be overreaching for the cases in this study, on one hand, the investigation of the propagation would complicate the separation of nucleation and propagation. On another hand, the goal was to investigate the accumulation of grain boundaries that would be prone to nucleate micro cracks as function of the overall stress and strain state, where simplicity in the modeling effort was sought after. The Griffith criterion is normally used in analysis of crack propagation. Here it is regarded to represent the first barrier that needs to be overcome in the process that triggers the formation of a macroscopic brittle fracture, i.e. nucleation. It is here deemed that the transition from a micro crack to a self-sustaining macroscopic brittle crack is subject to dissipation on a higher level than that related to the nucleation of the micro crack itself.

From the results of accumulated number fraction of critical grain boundaries, the characteristic of the accumulation as function of plastic strain is the key result that is used in the choice of the g_1-function. The fact that all models appear to yield the same characteristic stems from that the global stress state dictates the local grain boundary stress state, and also from the distribution of the grain boundary areas. Both act to make it possible to construct the analytical model presented in Section 4.3. The analytical model permits the investigation of a wider range of stress states, as the crystal models are very computational intensive and yields only one stress state per simulation.

In Section 2.2 of this paper, the modeling of fracture toughness tests using FE-models and a porous plastic constitutive model is presented. Even though by calibrating the model parameters at the higher temperature ductile tests at 75 °C, the model is able to predict the crack growth preceding the brittle fracture in the data sets at the temperatures $-50°$C and $-90°$C with satisfactory accuracy. Indicating that the model parameters of the porous plastic model is quite insensitive to temperature in this range. Regarding the void contribution from the strain controlled nucleation, which also controls the interplay between the ductile and brittle fracture in this framework, it is assumed to include the contribution from both mechanisms capable of participating in the brittle failure event. Second phase particles may either form a void due to particle cracking and subsequent crack arrest or by particle debonding and the grain boundaries may also form a void by cracking followed by crack arrest. This is why the void mechanism acts on both mechanisms in the final expression for the failure probability in Eq. (20). The parameter f_{N} could likely be divided in two parts, one for the contribution of second phase particles and one for grain boundaries. However, as these contributions would be small and close to inaccessible through physical measurements on the microstructure, it is deemed unnecessary and impractical to make such a division.

The reference material appears to be well described by a single mechanism weakest link framework, with the inclusion of the effect of the ductile mechanism. One key feature in the weakest link model developed by Kroon and Faleskog [12] is the non-local stress, which is intended to account for the barriers that must be overcome by a microcrack (e.g. grain boundaries) before it develops into a self-sustaining macroscopic brittle fracture. In the estimation of parameters for the reference material and the aged material, the length scale that is used in the non-local integration is the same for both materials. Something which appears reasonable since the reference material should describe the aged material in an as manufactured state, having more or less the same microstructure and thereby barriers to propagation.

The weakest link model describes the fracture toughness distribution with a remarkable accuracy and is well fitted to two data sets used for parameter estimation. The fact that close to equal toughness predictions can be obtained with both g_1-functions presented in (35a) and (35b) is most likely due to that the range in stress triaxiality T is too narrow in the experiments presented here. This also indicates that solely relying on fracture test for calibrating the triaxiality threshold T_{th} might not he reliable. To elucidate the effect of the stress triaxiality more clearly, experiments with specimen sets pertaining to more distinct differences in T are deemed necessary. Thus for the predictions on fracture tests as presented here, the function $g_1 = c/\left(\varepsilon_0\left(1+\varepsilon^{\mathrm{p}}/\varepsilon_0\right)\right)$ is deemed sufficient in order to reduce the parameter space.

An interesting feature that emerges from the model is a significant size effect on the grain boundary mechanism such that the grain boundary mechanism could be suppressed in its entirety. This comes out in such a way that larger specimens will be more prone to result in grain boundary failure while smaller specimens might be close to or entirely without the mechanism. As is the case in this study, the grain boundary mechanism is more brittle than the particle mechanism, which indicates that fracture toughness testing on small specimens might be non-conservative, as the most brittle fracture mode might be obscured by the test method.

Acknowledgements

The Swedish Radiation Safety Authority (SSM) and the Swedish Centre for Nuclear Technology (SKC) are acknowledged for their finanical support. Ringhals AB is acknowledged for supplying the material that was used in the experimental investigation.

References

[1] G. S. Was, *Fundamentals of Radiation Materials Science: Metals and Alloys*, vol. 1. Springer Science & Business Media, 1 ed., 2007. Chapter 13.

[2] R. K. Nanstad, M. A. Sokolov, S. R. Ortner, and P. D. Styman, “Neutron and Thermal Embrittlement of RPV Steels: An Overview,” *ASTM STP 1603*, pp. 68–106, 2018.

[3] C. L. Briant and S. K. Banerji, “Intergranular failure in steel: the role of grain boundary composition,” *International Metals Reviews*, vol. 4, pp. 164–199, 1978.

[4] J. F. Knott, “Micro-mechanisms of fracture and the fracture toughness of engineering alloys,” *International Journal of Fracture*, vol. 1, pp. 61–82, 1977.

[5] M. Boåsen, K. Lindgren, M. Öberg, M. Thuvander, J. Faleskog, and P. Efsing, “Analysis of thermal embrittlement of a low alloy steel weldment using fracture toughness and microstructural investigations,” tech. rep., Solid Mechanics, Dept. of Engineering Mechanics, KTH, 2020.

[6] C. J. McMahon and M. Cohen, “Initiation of cleavage fracture in polycrystalline iron,” *Acta Metallurgica*, vol. 13, pp. 591–604, 1965.

[7] F. M. Beremin, A. Pineau, J. C. Mudry, F. Devaux, Y. D' Escatha, and P. Ledermann, “A local criterion for cleavage fracture of a nuclear pressure vessel steel,” *Metallurgical Transactions A*, vol. 14, pp. 2277–2287, 1983.

[8] K. Wallin, “The Scatter in k_{IC}-Results,” *Engineering Fracture Mechanics*, vol. 19, pp. 1084–1093, 1984.

[9] ASTM, “Standard Test Method for Determination of Reference Temperature, T_0, for Ferritic Steels in the Transition range,” ASTM West Conshohocken, U.S., ASTM International, Geneva, Switzerland, 2019.

[10] S. R. Bordet, A. D. Karstensen, D. M. Knowles, and C. S. Wiesner, “A new statistical local criterion for cleavage fracture in steel. Part I: model presentation,” *Engineering Fracture Mechanics*, vol. 72, pp. 435–452, 2005.

[11] S. R. Bordet, A. D. Karstensen, D. M. Knowles, and C. S. Wiesner, “A new statistical local criterion for cleavage fracture in steel. Part II: application to an offshore structural steel,” *Engineering Fracture Mechanics*, vol. 72, pp. 453–474, 2005.

[12] M. Kroon and J. Faleskog, “A probabilistic model for cleavage fracture with a length scale – influence of material parameters and constraint,” *International Journal of Fracture*, vol. 118, pp. 99–118, 2002.

[13] J. Faleskog, M. Kroon, and H. Öberg, “A probabilistic model for cleavage fracture with a length scale parameter estimation and predictions of stationary crack experiments,” *Engineering Fracture Mechanics*, vol. 71, pp. 57–79, 2004.

[14] M. Kroon, J. Faleskog, and H. Öberg, “A probabilistic model for cleavage fracture with a length scale - parameter estimation and predictions of growing crack experiments,” *Engineering Fracture Mechanics*, vol. 75, pp. 2398–2417, 2008.

[15] M. Boåsen, M. Stec, P. Efsing, and J. Faleskog, “A generalized probabilistic model for cleavage fracture with a length scale influence of stress state and application to surface cracked experiments,” *Engineering Fracture Mechanics*, vol. 214, pp. 590–608, 2019.

[16] O. M. L. Yahya, F. Borit, R. Piques, and A. Pineau, “Statistical modelling of intergranular brittle fracture in low alloy steel,” *Fatigue & Fracture of Engineering Materials & Structures*, vol. 21, pp. 1485–1502, 1998.

[17] K. Wallin, P. Nevasmaa, A. Laukkanen, and T. Planman, “Master Curve analysis of inhomogeneous ferritic steels,” *Engineering Fracture Mechanics*, vol. 71, pp. 2329–2346, 2004.

[18] A. L. Gurson, “Continuum theory of ductile rupture by void nucleation and growth: Part iyield criteria and flow rules for porous ductile media,” *J. Eng. Mater. Technol.*, vol. 99, pp. 2–15, 1977.

[19] V. Tvergaard, “Influence of voids on shear band instabilities under plane strain conditions,” *International Journal of Fracture*, vol. 17, pp. 389–407, 1981.

[20] V. Tvergaard, “Ductile fracture by cavity nucleation between larger voids,” *Journal of the Mechanics and Physics of Solids*, vol. 30, pp. 265–286, 1982.

[21] J. Faleskog, G. Xiaosheng, and C. Fong Shih, “Cell model for nonlinear fracture analysis I. Micromechanics calibration,” *International Journal of Fracture*, vol. 89, pp. 355–373, 1998.

[22] K. Nahshon and J. W. Hutchinson, “Modification of the Gurson Model for shear failure,” *European Journal of Mechanics A/Solids*, vol. 27, pp. 1–17, 2008.

[23] K. L. Nielsen and V. Tvergaard, “Ductile shear failure or plug failure of spot welds modelled by modified gurson model,” *Engineering Fracture Mechanics*, vol. 77, pp. 1031–1047, 2010.

[24] C. C. Chu and A. Needleman, “Void Nucleation Effects in Biaxially Streched Sheets,” *Journal of Engineering Materials and Technology*, vol. 102, pp. 249–256, 1980.

[25] O. C. Zienkiewicz and R. L. Taylor, *The Finite Element Method*, vol. 2. McGraw-Hill Book Company, 4 ed., 1991. Chapter 7, section 15. pp.266.

[26] L. Xia and C. Fong Shih, “Ductile crack growth - i. a numerical study using computational cells with microstructurally-based length scales,” *Journal of the Mechanics and Physics of Solids*, vol. 43, pp. 233–259, 1995.

[27] X. Gao, J. Faleskog, and C. Fong Shih, “Cell model for nonlinear fracture analysis - ii. Fracture-process calibration and verification,” *International Journal of Fracture*, vol. 89, pp. 375–398, 1998.

[28] V. Tvergaard and A. Needleman, “Effects of nonlocal damage in porous plastic solids,” *International Journal of Solids and Structures*, vol. 32, pp. 1063–1077, 1995.

[29] V.-D. Nguyen, T. Pardoen, and L. Noels, “A nonlocal approach of ductile failure incorporating void growth, internal necking, and shear dominated coalescence mechanisms,” *Journal of the Mechanics and physics of solids*, vol. 137, no. 103891, 2020.

[30] V. Tvergaard and A. Needleman, “Analysis of the cup-cone fracture in a round tensile bar,” *Acta Metallurgica*, vol. 32, pp. 157–169, 1984.

[31] ASTM, “Standard Test Method for Measurement of Fracture Toughness,” ASTM West Conshohocken, U.S., ASTM International, Geneva, Switzerland, 2019.

[32] T. C. Lindley, G. Oates, and C. E. Richards, “A critical appraisal of carbide cracking mechanisms in ferrite/carbide aggregates,” *Acta Metallurgica*, vol. 18, pp. 1127–1136, 1970.

[33] J. Gurland, “Observations on the fracture of cementite particles in a spheriodized 1.05%c steel deformed at room temperature,” *Acta Metallurgica*, vol. 20, pp. 735–741, 1972.

[34] L. Xia and C. Fong Shih, “Ductile crack growth - iii. transition to cleavage fracture incorporating statistics,” *Journal of the Mechanics and Physics of Solids*, vol. 44, pp. 603–639, 1996.

[35] R. Quey, P. R. Dawson, and F. Barbe, “Large-scale 3D random polycrystals for finite element method: Generation, meshing and remeshing,” *Comput. Methods Appl. Mech. Engrg.*, vol. 200, pp. 1729–1745, 2011.

[36] F. Roters, M. Diehl, P. Shanthraj, P. Eisenlohr, C. Reuber, S. L. Wong, T. Maiti, A. Ebrahimi, T. Hochrainer, H.-O. Fabritius, S. Nikolov, M. Friak, N. Fujita, N. Grilli, K. G. F. Janssens, N. Jia, P. J. J. Kok, D. Ma, F. Meier, E. Werner, M. Stricker, D. Weygand, and D. Raabe, “Damask – the düsseldorf advanced material simulation kit for modelling multi-physics crystal plasticity, damage, and thermal phenomena from the single crystal up to the component scale,” *Computational Materials Science*, vol. 158, pp. 420–478, 2019.

[37] J. W. Hutchinson, “Bounds and self-consistent estimates for creep of polycrystalline materials,” *Proc. R. Soc. Lond. A.*, vol. 348, pp. 101–127, 1976.

[38] J. P. Hirth and J. Lothe, *Theory of dislocations*, vol. 1. Krieger publishing company, 2 ed., 1982. Appendix 1.

[39] J. Kim, G. Xiaosheng, and S. S. Tirumalai, "Modeling of void growth in ductile solids: effects of stress triaxiality and initial porosity," *Engineering Fracture Mechanics*, vol. 71, pp. 379–400, 2004.

[40] I. Barsoum and J. Faleskog, "Rupture mechanisms in combined tension and shear - Micromechanics," *International Journal of Solids and Structures*, vol. 44, pp. 5471–5498, 2007.

[41] G. Vadillo and J. Fernández-Sáez, "An analysis of Gurson model with parameters dependent on triaxiality based on unitary cells," *European Journal of Mechanics A/Solids*, vol. 28, pp. 417–427, 2009.

[42] L. E. B. Dæhli, T. Børvik, and O. S. Hopperstad, "Influence of loading path on ductile fracture of tensile specimens made from aluminium alloys," *International Journal of Solids and Structures*, vol. 88-89, pp. 17–34, 2016.

[43] Z. G. Liu, W. H. Wong, and T. F. Guo, "Void behaviors from low to high triaxialities: Transition from void collapse to void coalescence," *International Journal of Plasticity*, vol. 84, pp. 183–202, 2016.

[44] L. E. B. Dæhli, J. Faleskog, T. Børvik, and O. S. Hopperstad, "Unit cell simulations and porous plasticity modelling for strongly anisotropic FCC metals," *European Journal of Mechanics A/Solids*, vol. 65, pp. 360–383, 2017.

[45] A. A. Griffith, "The phenomena of rupture and flow in solids," *Philosophical Transactions of the Royal Society of London. Series A, Containing Papers of a Mathematical or Physical Character*, vol. 221, pp. 163–198, 1921.

[46] T. L. Anderson, *Fracture Mechanics Fundamentals and Applications.* Taylor & Francis, third ed., 2005.

[47] J. C. J. Newman and I. S. Raju, "An empirical stress-intensity factor equation for the surface crack," *Engineering Fracture Mechanics*, vol. 15, pp. 185–192, 1981.

[48] V. Randle, *The measurement of grain boundary geometry.* Bristol : Institute of Physics, 1993.

[49] J. A. Nelder and R. Mead, “A simplex method for function minimization,” *The Computer Journal*, vol. 7, pp. 308–313, 1965.